

UNIDAD IZTAPALAPA
DIVISION DE CIENCIAS BASICAS E INGENIERIA
POSGRADO EN CIENCIAS (INGENIERIA QUIMICA)

TESIS

**“INNOVATIONS IN HYDROCARBON VALORIZATION: A
COMPREHENSIVE STUDY OF THE OXIDATIVE CONVERSION OF
METHANE AND THE OXIDATIVE DEHYDROGENATION OF ETHANE”**

PARA OBTENER EL GRADO DE:
DOCTOR EN CIENCIAS (INGENIERIA QUIMICA)

PRESENTA:
M. en C. ALEJANDRO ROMERO LIMONES
MATRICULA: 2153804698
ORCID: 0000-0002-7404-8440
romero1992@hotmail.com

ASESOR: DR. CARLOS OMAR CASTILLO ARAIZA
ASESOR: DR. JORIS THYBAUT

JURADO:
PRESIDENTE: DR. RICHARD STEVE RUIZ MARTINEZ
SECRETARIO: HECTOR FERNANDO PUEBLA NUÑEZ
VOCAL: GAMALIEL CHE GALICIA
VOCAL: KAI-OLAF HINRICHSEN
VOCAL: MARK SAEYS

IZTAPALAPA, CIUDAD DE MEXICO, 20 DE AGOSTO 2024

Members of the Examination Board

Chair

Prof. Richard Steve Ruiz Martínez, PhD, Metropolitan Autonomous University

Co-chair

Prof. Patrick De Baets, PhD, Ghent University

Other members entitled to vote

Prof. Mark Saeys, PhD, Ghent University

Prof. Kai-Olaf Hinrichsen, PhD, Technical University of Munich

Prof. Gilberto Espinosa Paredes, PhD, Metropolitan Autonomous University

Prof. Gamaliel Che Galicia, PhD, Meritorious Autonomous University of Puebla

Prof. Héctor Fernando Puebla Núñez, PhD, Metropolitan Autonomous University

Supervisors

Prof. Carlos O. Castillo Araiza, PhD, Metropolitan Autonomous University

Prof. Joris W. Thybaut, PhD, Ghent University

Jeroen Poissonnier, PhD, Ghent University

Metropolitan Autonomous University – Iztapalapa
Department of Process Engineering and Hydraulics
Division of Basic Sciences and Engineering
Laboratory of Catalytic Reactor Engineering Applied to Chemical and Biological Systems
Av. San Rafael Atlixco No. 186
C.P. 09340, Iztapalapa, Mexico City, Mexico

Ghent University
Faculty of Engineering and Architecture
Department of Materials, Textiles and Chemical Engineering
Laboratory for Chemical Technology
Technologiepark 125
B-9052 Ghent, Belgium
Tel.: +32 (0)9 331 17 57
Fax: +32 (0)9 331 17 59
<http://www.lct.ugent.be>

This work was supported by the European Union's Horizon 2020 research and innovation programme under grant agreement No 837733 and CONACYT providing a postgraduate fellowship.

Acknowledgments

Through these years of researching at both *Universidad Autónoma Metropolitana* and *Universiteit Gent*, I would like to thank all the researchers, my peers, friends and family who supported me indirectly and directly. Disclaimer: It is a “big” list and the following paragraphs are a mix of English and Spanish.

Primero que nada, a mi mamá y mi papá. De no haber sido por todo el esfuerzo extraordinario que han realizado, yo no hubiera tenido la oportunidad de haber llegado a estas instancias. Cada uno de mis logros es también de ustedes. Además, quisiera mencionar también a mi hermana (Abi), por su apoyo incondicional. ¡Gracias infinitas, familia!

A mis compañeros y amigos de la Universidad Autónoma Metropolitana – Iztapalapa y el Laboratorio de Ingeniería de Reactores Catalíticos. Conforme fueron pasando los años, esta lista iba incrementando considerablemente. No quisiera olvidar mencionar a alguno de ustedes. Si compartimos alguna plática en los pasillos o laboratorios de la UAM-I, pero especialmente, si tomamos una chela o jugamos fútbol juntos, estoy agradecido por compartir tan buenos momentos durante las etapas difíciles y no tan difíciles de este doctorado. Particularmente, quisiera agradecer al Dr. Alberto Aguirre Hernandez y al Dr. Gerardo Gómez Ramos, del Laboratorio de Ingeniería de Reactores Catalíticos, que a lo largo de los años de este doctorado, siempre han estado con la mejor disposición para discutir temas relevantes de investigación (y no tan relevantes de la vida cotidiana), así como también me han mostrado su apoyo en diversas cuestiones académicas y profesionales.

Un especial agradecimiento al Dr. Roel Hernández Rodríguez. Desde que empezamos juntos la maestría, siempre has mostrado un profundo interés por saber más y hacer investigación de manera rigurosa y ética. Además de la gran amistad que hemos forjado en estos años, directa e

Acknowledgments

indirectamente, siempre me has apoyado, y me has inspirado a hacer investigación lo mejor posible.

Al Dr. Luis Ramos Huerta y a la M. C. Jocelyn Carmona. Desde que empezó esta travesía del posgrado, y hasta la fecha, ustedes siempre estuvieron ahí con la mejor disposición de ayudar de manera desinteresada en temas académicos y no tan académicos. Sin importar que tan complicado lucía el panorama durante los diferentes inconvenientes que acontecían en el posgrado (paro, huelga, pandemia, etc.), ustedes siempre han estado ahí.

To my peers and friends from the LCT and CaRe group. In the beginning, the cultural shock, being in a new country, and a huge challenge to face was hard for me. Since the first weeks, I was (un)lucky to attend the *Chemical Research in Flander 2*, where I truly met some of my peers, who later became my friends, and then things in the lab became “less hard”. I am deeply grateful to my coffee-break mates and friends: Anoop, Beruk, Reza, Sébastien, and Adi, from whom I learned a lot about different cultures and every time they were available to talk about any “hot topic” of the moment. Also, I would like to thank my office mates: Servaas, María, Klaus, Lukas, and Raman. Thank you for the nice atmosphere in the office, even when we had “hot topic” discussions.

I would like to thank all the C123 consortium partners. I am grateful for having participated in a project of enormous magnitude, but above all for having learned a lot professionally from all of you. Special thanks to Andreas and Hans-Jörg from Linde, Izabel from TotalEnergies, and Mohamed from PDC. Every meeting and discussion we had improved the way I do research.

Of course, I cannot leave out my “LCT minivoetbal” teammates: Parvis, Yihan, Siavash, Steven, Soroush, Yentl, and Carlos. I’m pretty sure the motivation to write this thesis wouldn’t have been possible without “refreshing my mind” with football, especially winning the league for the first time for the LCT. Those memories will be with me forever.

Acknowledgments

Un agradecimiento especial para César Pernaletе (el chamo). Pana, empezamos casi al mismo tiempo en el LCT, y casi al instante de conocernos se sintió la buena vibra y la calidez latina que aminora la nostalgia de estar lejos de casa. A pesar de que (casi) siempre estás ocupado trabajando duro, viendo la forma de resolver cualquier situación académica (y no académica), siempre estuviste disponible para una plática agradable acompañada de una buena cerveza. Extrañaré aquellos buenos momentos en Ter Hagen 37. Gracias por todo pana.

A Carlos Alvarado Camacho. ¿Qué puedo decir que no sepas ya? Hemos vivido casi lo mismo en este doctorado en conjunto entre UAM-I y UGent. Sabemos todo lo que esto implica y no me queda más que agradecer por el apoyo que me has mostrado en estos últimos años, particularmente las tarde-noches de fútbol y chelas.

I want to express my sincere gratitude to the examination committee, comprised of Dr. Richard Steve Ruiz Martínez, Dr. Patrick De Baets, Dr. Mark Saeys, Dr. Kai-Olaf Hinrichsen, Dr. Gilberto Espinosa Paredes, Dr. Gamaliel Che Galicia, Dr. Héctor Fernando Puebla Núñez, for their dedication in evaluating this work. Their expertise, insights and recommendations have significantly contributed to its refinement.

To Jeroen Poissonnier for his mentorship during my PhD. Since the first day at the LCT, you have been really patient and tolerant with me, even when I was (totally/a little bit) lost with my research. I believe you were the one with the highest iterations and feedback I received on the writing of my manuscripts. Without your recommendations, I wouldn't have achieved the writing skills I reached at this final stage of my PhD. Moreover (just a small detail), thank you for all the (very nice) recommendations on the Belgian beers, definitively the best beers in the world.

My deepest gratitude to professors Carlos Omar Castillo Araiza and Joris Thybaut for having allowed me to do this joint PhD between Mexico and Belgium, which has changed and

Acknowledgments

improved my mindset and point of view of what I understood of “chemical engineering research”. Without their support, guidance, invaluable mentorship, and (a lot of) feedback this thesis and publications wouldn’t have reached the level of high rigor of which I am very proud.

Por último, a mi compañera de vida y esposa Gabriela. Me faltarían palabras para describir lo agradecido que estoy por todo el apoyo que me has dado (sí, aquí aplica el “no sé qué decir”). Sé que esta etapa del doctorado no ha sido fácil, y estar lejos, la pandemia, y otras situaciones adversas lo han hecho más difícil de lo que ya lo era. A pesar de todo, siempre estuviste ahí para mí, y sin importar lo que pase yo siempre estaré ahí para ti. Te amo.

Y bueno, ahora sí por último y no menos importante, quisiera dejar en claro mi agradecimiento a mi gatita, Ónix, quien me hizo compañía los últimos dos años en Bélgica, y mantuvo mi salud mental y emocional lo mejor posible.

Alejandro Romero Limones

August 2024

Table of Contents

Acknowledgments	i
Table of Contents	viii
List of Figures	xi
List of Tables	xvii
List of Symbols	xviii
List of Abbreviations.....	xxiv
Summary	xxv
Samenvatting.....	xxviii
Resumen	xxxii
Chapter 1 – Introduction.....	1
1.1 Circular economy for hydrocarbons.....	1
1.2 The role of natural gas.....	2
1.3 Methane conversion technologies	4
1.3.1 Steam and autothermal reforming of methane.....	5
1.3.2 Exploring new frontiers.....	5
1.4 The C123 European Horizon 2020 integrated project.....	7
1.4.1 Oxidative Conversion of Methane (OCoM).....	8
1.4.2 Hydroformylation of ethylene (HF).....	9
1.5 Ethane conversion technologies.....	9
1.5.1 Steam cracking of ethane.....	10
1.5.2 Ethane Dehydroaromatization (EDA).....	11
1.5.3 Oxidative Dehydrogenation of Ethane (ODH)	11
1.6 Packed bed reactor	12
1.6.1 Fluid Dynamics.....	14
1.6.2 Heat transfer.....	14
1.7 Scope and outline of the thesis.....	16
1.8 References.....	18
Chapter 2 – Oxidative Conversion of Methane (OCoM)	36
2.1 Introduction.....	37
2.2 Procedures.....	37
2.2.1 Experimental.....	37
2.2.2 Definitions	38
2.2.3 Reactor model.....	38

2.2.4	Contribution analysis.....	39
2.3	Kinetic model construction.....	40
2.3.1	Reaction network	40
2.3.2	Catalyst testing experiments - effect of the methane to oxygen inlet molar ratio.....	42
2.3.3	Catalyst testing experiments – effect of temperature.....	44
2.3.4	Rate equations.....	45
2.3.5	Model performance	45
2.4	The C123 process.....	48
2.4.1	General concept.....	48
2.4.2	OCoM reactor - temperature assessment.....	49
2.4.3	OCoM reactor – space time assessment.....	52
2.4.4	OCoM reactor - methane to oxygen inlet molar ratio assessment.....	55
2.4.5	OCoM reactor - co-feeding ethane assessment.....	57
2.4.6	Realistic feedstocks assessment.....	60
2.4.7	(Once-through) OCoM reactor performance.....	60
2.4.8	Process considerations.....	62
2.5	Conclusions.....	63
2.6	References.....	64
	Appendices	67
	Appendix 2A Effect of CO ₂ in the feedstock.....	67
	Appendix 2B Reaction rates analysis.....	67
Chapter 3	– Transport phenomena within a packed bed reactor with low d_t/d_p	69
3.1	Introduction.....	71
3.2	Experimental systems (bench-scale and industrial-scale)	71
3.3	Fluid dynamics.....	73
3.3.1	Pressure drop.....	73
3.3.2	Viscous and inertial frictional forces	75
3.3.3	Axial velocity profiles within a packed bed	78
3.4	Heat transfer (no reaction).....	81
3.4.1	Qualitative description of the axial and radial temperature gradients.....	81
3.4.2	Determination of $k_{eff,z}$ at adiabatic conditions (radial isothermicity).....	83
3.4.3	Pseudo-local heat transfer approach.....	86
3.4.4	Determining the radial effective thermal conductivity.....	88
3.4.5	Determination of the wall heat transfer coefficient.....	94
3.4.6	Heat transfer resistance analysis	96
3.5	Conclusions.....	97

3.6	References.....	99
	Appendices	105
	Appendix 3A Heat transfer mechanisms captured by the effective thermal conductivity ..	105
	Appendix 3B Literature correlations for the calculation of $k_{\text{eff},z}$	106
	Appendix 3C Estimated $k_{\text{eff},r}$ from KWT-BC.....	106
	Appendix 3D Conventional heat transfer approaches for wall-cooled packed beds	108
	Appendix 3E 1-D Pseudo-homogeneous heat transfer model.....	110
Chapter 4	– Oxidative dehydrogenation of ethane packed bed reactor.....	111
4.1	Reactor model	112
4.2	The role of PLA on the description of the ODH reactor	115
4.3	The impact of $k_{\text{eff},z}$ on the description of the ODH reactor	117
4.4	Conclusions.....	120
4.5	References.....	122
	Appendices	124
	Appendix 4A ODH kinetic model.....	124
Chapter 5	– Conclusions and perspectives	125
5.1	Conclusions.....	125
5.2	Perspectives	127
5.3	References.....	129

List of Figures

Figure 1.1. Global methane emissions from the energy sector, 2000 – 2022 [1]	1
Figure 1.2. Gas reserves, 2020. Proven reserves, measured in cubic meters, are those quantities that can be recovered in the future from known reservoirs under existing economic and operating conditions, according to geological and engineering information [2,3]	3
Figure 1.3. C123 project overview, starting from unused methane resources valorization through OCoM. Then, after achieving an optimal CO and C ₂ H ₄ molar mixture, the ethylene hydroformylation produces C ₃ species	8
Figure 1.4. Natural gas withdrawals in the U.S. from difference well sources between 2007 – 2022 [4].....	10
Figure 2.1. Simplified reaction network describing OCoM focusing on the carbon containing components	40
Figure 2.2. (a) Methane and oxygen conversion and selectivities towards ethane, ethylene, C ₂ , CO and CO ₂ as a function of the CH ₄ /O ₂ inlet molar flow ratio. (b) Molar flow rates of H ₂ and water as a function of the CH ₄ /O ₂ inlet molar flow ratio. T = 800 °C, p _{tot} = 100 kPa, W _{cat} /F _{CH₄,in} = 2.50 kgcat s mol ⁻¹ . Lines are added to guide the eye	43
Figure 2.3. (a) Methane and oxygen conversion and selectivities towards ethane, ethylene, C ₂ , CO and CO ₂ as a function of the temperature. (b) Molar flow rates of H ₂ and water as a function of the temperature. CH ₄ /O ₂ = 4 mol mol ⁻¹ , p _{tot} = 100 kPa, W _{cat} /F _{CH₄,in} = 2.50 kgcat s mol ⁻¹ . Lines are added to guide the eye.....	45
Figure 2.4. Parity diagram of the observed and calculated molar flow rates for the 8-steps kinetic model. Full line is the first bisector and dashed lines represent the 10% deviation....	48
Figure 2.5. Carbon species selectivity as a function of the methane conversion. Symbols represent the experimental data and full lines the simulations from the kinetic model.....	48
Figure 2.6. Representation of unit-operations in the C123 process. Depending of the methane source, natural gas, shale gas or biogas is considered. The C123 process consists of a mixer	

List of Figures

unit, an Oxidative Conversion of Methane (OCoM) reactor, the Hydroformylation of Ethylene reactor (HF), and a separation unit. The separation unit separates the C3 liquid species (propanal) and the gas species from the HF outlet stream. Gas species are recycled towards the mixer.....49

Figure 2.7. Temperature effect on: (a) Methane and oxygen conversion, (b) carbon species yields, (c) reaction rates, (d) CH₄ conversion distribution, (e) relative reaction rates towards CO production, (f) reconverted ethane distribution, and (g) relative reaction rates towards ethylene production. CH₄/O₂ inlet molar ratio of 4 mol mol⁻¹ and $W_{cat}/F_{CH_4,in}$ of 2.5 kg_{cat} s⁻¹ mol⁻¹. Symbols are added to distinguish between the reactions.....52

Figure 2.8. $W_{cat}/F_{CH_4,in}$ effect on: (a) Methane and oxygen conversion, (b) carbon species yields, (c) reaction rates, (d) CH₄ conversion distribution, (e) relative reaction rates towards CO production, (f) reconverted ethane distribution, and (g) relative reaction rates towards ethylene production. CH₄/O₂ inlet molar ratio of 4 mol mol⁻¹ and temperature of 850 °C. Symbols are added to distinguish between the reactions54

Figure 2.9. CH₄/O₂ inlet molar ratio effect on: (a) Methane and oxygen conversion, (b) carbon species yields, (c) reaction rates, (d) CH₄ conversion distribution, (e) relative reaction rates towards CO production, (f) reconverted ethane distribution, and (g) relative reaction rates towards ethylene production. $W_{cat}/F_{CH_4,in}$ of 2.5 kg_{cat} s⁻¹ mol⁻¹ and temperature of 850 °C. Symbols are added to distinguish between the reactions..... 57

Figure 2.10. Effect of co-feeding ethane on: (a) Methane and oxygen conversion, (b) carbon species yields, (c) reaction rates, (d) CH₄ conversion distribution, (e) relative reaction rates towards CO production, (f) reconverted ethane distribution, and (g) relative reaction rates towards ethylene production. $W_{cat}/F_{CH_4,in}$ of 6.5 kg_{cat} s⁻¹ mol⁻¹, CH₄/O₂ inlet molar ratio of 10 mol mol⁻¹, and temperature of 850 °C. Symbols are added to distinguish between the reactions..... 59

Figure 2.11. (a) Carbon conversion, and (b) carbon species yields at different OCoM feedstock compositions. Operating conditions of the (once-through) OCoM reactor: CH₄/O₂ = 10 mol mol⁻¹, $W_{cat}/F_{CH_4,in}$ = 6.5 kg_{cat} s⁻¹ mol⁻¹, and T = 850 °C.....61

List of Figures

- Figure 2A.1. Conversion and selectivity as a function of the CO₂ content in feedstock. CH₄/O₂ = 4 molCH_{4,in} molO_{2,in}⁻¹, p_{tot} = 1 bar, W_{cat}/FCH_{4,in} = 2.50 kg s molCH_{4,in}⁻¹. Lines are added to show experimental trends..... 67
- Figure 2B.1. Computed reaction rates from the OCoM kinetic model as function of the (a) CH₄/O₂ inlet molar ratio with a fixed temperature of 800 °C and W_{cat}/FCH_{4,in} of 2.5 kg s molCH_{4,in}⁻¹, and as a function of the (b) temperature with a fixed CH₄/O₂ inlet molar ratio of 4 molCH_{4,in} molO_{2,in}⁻¹ and W_{cat}/FCH_{4,in} of 2.5 kg s molCH_{4,in}⁻¹. Symbols are added to distinguish between thereactions.....68
- Figure 3.1. Schematic diagram of the packed bed showing the different kind of operations depending on the targeted parameters. Left, industrial-scale and bench-scale non-adiabatic operation (bed length in blue and red letters, respectively). Right, bench-scale adiabatic operation. 73
- Figure 3.2. Pressure drop within the packed bed. A comparison between the experimental data (full symbols) and simulations with, the parameters estimated in this work (continuous line), Ergun’s parameters [14] ($\alpha = 150$ and $\beta = 1.75$), Limberg’s parameters [16] ($\alpha = 260$ and $\beta = 0.9$), Morcom’s parameters [17] ($\alpha = 245$ and $\beta = 2.4$), and Eisfeld’s correlation [18] 74
- Figure 3.3. (a) Void fraction, Darcy and Forchheimer number for the bench and industrial-scale packed bed; and (b) Void fraction and apparent permeability in the packed bed obtained in this work and reported in the literature from a particle resolved simulation (PRS) [15]..... 77
- Figure 3.4. Axial velocity profiles within the packed bed. Rep ranging from 700 to 1700..... 80
- Figure 3.5. Schematic diagram of the qualitative axial temperature distribution within a packed bed reactor with low dt/dp ratio (< 8 mr ms⁻¹) when a highly exothermic reaction is considered..... 82
- Figure 3.6. Schematic diagram of the relevant radial zones in a packed bed: core zone (blue), internal wall zone (green), external wall zone (yellow) and heat transfer medium (red)..... 83
- Figure 3.7. (a) keff,z variation with the Rep. Symbols represent the keff,z obtained in this work, the green continuous line represents the correlation developed in this work, the red dashed line shows Votruba et al. correlation [52], the blue dotted line shows Yagi et al. [10], and the non-

List of Figures

continuous black lines show the $k_{eff,z}$ obtained by different correlations from the literature [53–55]. (b) Axial temperature profiles for the bench-scale packed bed obtained in absence of flow and at Re_p between 210 and 1260 in absence of reaction. Dotted lines show the simulations considering the $k_{eff,z}$ from Yagi et al., full lines represent the $k_{eff,z}$ estimated in this work, and the dashed lines show the $k_{eff,z}$ from Votruba et al..... 85

Figure 3.8. Pseudo-local $k_{eff,r,PLA}$ within the packed bed at Re_p from 210 to 1400. Estimations considering and neglecting $k_{eff,z}$ are presented as continuous lines and dashed lines, respectively. Void fraction is shown as reference with a yellow dotted line.....90

Figure 3.9. Temperature profiles within the bench-scale packed bed. a) Axial temperature profiles at the center of the bed assessing the pseudo-local $k_{eff,r}$. b) Radial temperature profiles at 13 cm from the inlet assessing the pseudo-local $k_{eff,r}$. c) Axial temperature profiles at the center of the bed assessing the $k_{eff,z}$. d) Radial temperature profiles at 13 cm from the inlet assessing the $k_{eff,z}$. e) Radial temperature profiles at 43 cm from the inlet assessing the $k_{eff,z}$ 92

Figure 3.10. Temperature profiles within the industrial-scale packed bed. a) Axial temperature profiles at the center of the bed assessing the pseudo-local $k_{eff,r}$. b) Radial temperature profiles at 10 cm from the inlet with a Re_p of 700, 1050 and 1400 assessing the pseudo-local $k_{eff,r}$. c) Radial temperature profiles at 10, 20, and 30 cm from the inlet with a Re_p of 1400 assessing the pseudo-local $k_{eff,r}$. d) Axial temperature profiles at the center of the bed assessing the $k_{eff,z}$. e) Radial temperature profiles at 10 cm from the inlet with a Re_p of 700, 1050 and 1400 assessing the $k_{eff,z}$. f) Radial temperature profiles at 10, 20, and 30 cm from the inlet with a Re_p of 1400 assessing $k_{eff,z}$ 94

Figure 3.11. Temperature profiles within the industrial-scale packed bed. Axial temperature profiles at the center of the bed. Radial temperature profiles at 10 from the inlet with a Re_p of 700, 1050 and 1400. c) Radial temperature profiles at 10, 20, and 30 cm from the inlet with a Re_p of 1400. 96

Figure 3.12. Percentage of external and internal heat transfer resistances within the industrial-scale packed bed at Re_p from 210 to 1400 Re_p 97

Figure 3A.1. Schematic diagram of the heat transfer mechanisms captured by the effective thermal conductivity. Independent of fluid flow: (1) Conduction through motionless fluid, (2)

List of Figures

Conduction through pellet contact, (3) Radiation between void fraction, (4) Radiation between solid surfaces, (5) Conduction through the pellet. Dependent on fluid flow: (6) Convection in the fluid flow direction, (7) Conduction in the boundary layer between pellets, (8) Heat transfer by mixing, and (9) Heat transfer by convection solid-fluid-solid. 105

Figure 3C.1. Radial effective conductivity estimated for the bench and industrial-scale packed bed and determined from literature correlations [32,58,86,87] 108

Figure 3D.1. Heat transfer parameters estimated for the bench and industrial-scale packed bed and determined from correlations from the literature [15,45,100,103–108] 109

Figure 4.1. Axial temperature profiles predicted from PLA, CLA and BLA for the industrial-scale packed bed reactor at a Re of 1400, $T_b = 440$ °C and inlet $C_2H_6/O_2/N_2 = 9/7/84$. The parameters h_w [$W\ m^{-2}\ K^{-1}$] and $keff_r$ [$W\ m^{-1}\ K^{-1}$] from literature [6] are 91.5 and 1.17, respectively, for the CA, while for the BLA they are 155 and 1.65, respectively. 116

Figure 4.2. Axial temperature profiles predicted from PLA for the industrial-scale packed bed reactor at a Re_p of 1400 and inlet $C_2H_6/O_2/N_2 = 9/7/84$. The bath temperature ranges from 400 – 480 °C. Dashed lines describes fluid temperature and continuous lines the solid temperature 117

Figure 4.3. Axial temperature profiles predicted for the industrial-scale packed bed reactor, inlet molar ratio $C_2H_6/O_2/N_2 = 9/7/84$, $T_0 = 200$ °C. (a) At $T_b = 440$ °C. (b) At $T_b = 480$ °C. Dotted lines refer to $Re_p = 700$, and continuous lines refer to $Re_p = 1400$. Blue lines refer to considering $keff_z$ from Yagi et al. [16], green lines refer to the $keff_z$ estimated in this work, and red lines to $keff_z$ from Votruba et al. [17] 118

Figure 4.4. Axial temperature profiles predicted for the industrial-scale packed bed reactor, $T_0 = 200$ °C, $Re_p = 1400$. (a) At $T_b = 440$ °C. (b) At $T_b = 480$ °C. Dashed lines refer to an inlet molar ratio $C_2H_6/O_2/N_2 = 13/3/84$, and continuous lines refer to inlet molar ratio $C_2H_6/O_2/N_2 = 9/7/84$. Blue lines refer to considering $keff_z$ from Yagi et al. [16], green lines refer to the $keff_z$ estimated in this work, and red lines to $keff_z$ from Votruba et al. [17] 119

Figure 4.5. Axial temperature profiles predicted for the industrial-scale packed bed reactor, inlet molar ratio $C_2H_6/O_2/N_2 = 9/7/84$, $Re_p = 1400$. (a) At $T_b = 440$ °C. (b) At $T_b = 480$ °C.

List of Figures

Continuous lines refer to $T_0 = 200\text{ }^\circ\text{C}$, and non-continuous lines refer to $T_0 = 300\text{ }^\circ\text{C}$. Blue lines refer to considering $k_{eff,z}$ from Yagi et al. [16], green lines refer to the $k_{eff,z}$ estimated in this work, and red lines to $k_{eff,z}$ from Votruba et al.[17]

.....120

List of Tables

Table 2.1. Operating conditions of the OCoM experiments.....	38
Table 2.2. Reactions considered for the kinetic model.....	41
Table 2.3. Parameter estimates and corresponding 95% confidence intervals from the OCoM kinetic model over the MnNaW/SiO ₂ catalyst.	46
Table 2.4. Molar composition of the three different feedstocks considered for OCoM.....	60
Table 3.1. Estimated μ_{eff} values with their 95% probability confidence intervals and the μ_{eff}/μ_f ratio. Note that μ_f equals $222 \text{ kg}_f \text{ m}_r^{-2} \text{ s}^{-1}$	81
Table 3.2. Heat transfer parameter estimates and their corresponding 95% confidence intervals for the PL-IHTA (see Eqs. (3.33) – (3.34)).	89
Table 3.3. External heat wall transfer coefficient estimates and their corresponding 95% confidence intervals.....	95
Table 3.4. Internal and external heat transfer resistances	97
Table 3C.1. $k_{\text{eff},r}$ estimates and their corresponding 95% confidence intervals for KWT-CA and KWT-BLA	107
Table 3D.1. Heat wall transfer coefficient estimates and their corresponding 95% confidence intervals for CA and BLA.....	109
Table 4.1. Reactor and catalyst dimensions, operating conditions, and transport phenomena parameters used in the reactor model.	114

List of Symbols

Symbol	Description	Units
a_s	External surface to particle volume ratio	$m_s^2 m_r^{-3}$
C_i	Molar concentration of species i in the fluid phase	$kmol m_f^{-3}$
$C_{i,s}$	Molar concentration of species i in the solid phase	$kmol m_f^{-3}$
$C_{i,s,ss}$	Molar concentration of species i in the solid phase at steady state	$kmol m_f^{-3}$
$C_{i,ss}$	Molar concentration of species i in the fluid phase at steady state	$kmol m_f^{-3}$
CH_4/O_2	Methane to oxygen inlet molar ratio	$mol mol^{-1}$
$C_{p,f}$	Specific heat capacity of the fluid at constant pressure	$kJ kg_f^{-1} K^{-1}$
$C_{p,s}$	Specific heat capacity of the solid at constant pressure	$kJ kg_s^{-1} K^{-1}$
d_p	Particle diameter	m_s
d_t	Tube diameter	m_r
$\mathbf{D}(\mathbf{r})$	Solid-fluid resistance vector	$kg m_r^{-2} s^{-2}$
$D(\mathbf{r})_z$	z -component of the solid-fluid resistances vector	$kg m_r^{-2} s^{-2}$
	$\mathbf{D}(\mathbf{r})$	
$D_{eff,r}$	Radial mass dispersion coefficient	$m_r^2 h^{-1}$
$D_{eff,z}$	Axial mass dispersion coefficient	$m_r^2 h^{-1}$
$E_{a,j}$	Activation energy of reaction j	$kJ mol^{-1}$

List of Symbols

$\hat{F}_{k,i}$	Predicted responses	
$F_{k,i}$	Experimental responses	
F_i	Molar flow rate of the species i	mol s^{-1}
$F_{C,in}$	Molar flow rate of carbons fed as reactant	mol s^{-1}
$F_{C,out}$	Molar flow rate of carbons at the outlet	mol s^{-1}
g_z	Axial component of gravity	$\text{m}_r \text{ h}^{-2}$
G	Superficial mass flow rate	$\text{kg m}_r^{-2} \text{ h}^{-1}$
h_g	Interfacial heat transfer coefficient	$\text{W m}_s^{-2} \text{ K}^{-1}$
h_w	Wall heat transfer coefficient	$\text{W m}_r^{-2} \text{ K}^{-1}$
$h_{w,ext}$	External wall heat transfer coefficient	$\text{W m}_r^{-2} \text{ K}^{-1}$
$h_{w,in}$	Internal wall heat transfer coefficient	$\text{W m}_r^{-2} \text{ K}^{-1}$
$\underline{\mathbf{H}}$	Apparent permeability tensor	m_r^2
$H(r)_{zz}$	z -component of the tensor $\underline{\mathbf{H}}$	$\text{kg m}_r^{-2} \text{ s}^{-2}$
$k_{0,j}$	Pre-exponential factor of reaction j	$\text{mmol s}^{-1} \text{ kg}_{cat}^{-1} \text{ Pa}^{-2}$
$k_{1,h}$	Slope parameter of the $k_{eff,r,PLA}$	
$k_{2,h}$	Damping parameter of the $k_{eff,r,PLA}$	
$k_{eff,r}$	Radial effective thermal conductivity	$\text{W m}_r^{-1} \text{ K}^{-1}$
$k_{eff,r}^0$	Static contribution of the radial effective conductivity,	$\text{W m}_r^{-1} \text{ K}^{-1}$
$\langle k_{eff,r} \rangle_{core}$	Averaged radial effective thermal conductivity of the packed bed core zone	$\text{W m}_r^{-1} \text{ K}^{-1}$
$k_{eff,r,PLA}$	Pseudo-local radial effective thermal conductivity	$\text{W m}_r^{-1} \text{ K}^{-1}$

List of Symbols

$k_{\text{eff},z}$	Axial effective thermal conductivity	$\text{W m}_r^{-1} \text{K}^{-1}$
k_j	Rate coefficient of reaction j	$\text{mmol g}_{\text{cat}}^{-1} \text{h}^{-1}$
k_g	Interfacial mass transfer coefficient	$\text{m}_f^3 \text{m}_s^{-2} \text{h}^{-1}$
K	Packed bed permeability	m_r^2
K_z	Packed bed pseudo-permeability	m_r
K_n	Adsorption equilibrium coefficient for component n	Pa^{-1}
L	Reactor length	m_r
m_j	Partial reaction order of reaction j	
M	Number of independent observations	
N	Number of responses	
$N_{\text{C,in}}$	Number of carbon atoms of species i at the inlet	
p_i	Partial pressure of component i	Pa
p_{tot}	Total pressure	Pa
p_z	Axial component of pressure	Pa
Pr	Prandtl number, $Pr = C_p \mu_f / k_f$	
q_0	Heat flux from the infra-red lamp	W m_r^{-2}
R	Radial position	m_r
r_j	Specific reaction rate of reaction j	$\text{mmol g}_{\text{cat}}^{-1} \text{h}^{-1}$
R	Universal gas constant	$\text{J mol}^{-1} \text{K}^{-1}$
R_i	Net production rate of species i	mmol s^{-1}
R_t	Tube radius	m_r
Re_p	Particle Reynolds; $Re_p = d_p u_z \rho_f / \mu_f$	

List of Symbols

S_i	Selectivity towards species i	mol mol^{-1}
T	Time	h
T	Fluid temperature	K
T_0	Feed temperature	K
T_b	Salt bath temperature	K
T_s	Solid temperature	K
T_{ss}	Fluid temperature at steady state	K
$T_{w,in}$	Temperature at the internal surface of the tube wall	K
T_δ	Temperature at the internal heat boundary layer surface	K
u_z	Superficial velocity	$\text{m}_r^3 \text{ m}_r^{-2} \text{ h}^{-1}$
$u_{z,0}$	Superficial velocity at the bed inlet	$\text{m}_r^3 \text{ m}_r^{-2} \text{ h}^{-1}$
U_w	Global heat transfer coefficient	$\text{kJ m}_r^{-2} \text{ h}^{-1} \text{ K}^{-1}$
v_z	Axial component of the interstitial velocity	$\text{m}_r \text{ h}^{-1}$
$v_{z,ss}$	Axial component of the interstitial velocity at steady state	$\text{m}_r \text{ h}^{-1}$
W_{cat}	Catalyst mass	kg_{cat}
$W_{cat}/F_{CH_4,in}$	Space time: ratio of catalyst mass and methane inlet molar flow	$\text{kg}_{cat} \text{ s mol}^{-1}$
W_i	weight factor assigned to the i-collocation point	
X_i	Conversion of component i	
Y_i	Yield of component i	
z	Axial position	m_r

List of Symbols

Greek letters

α	Ergun's coefficient related to viscous solid-fluid contributions	
β	Ergun's coefficient related to inertial solid-fluid contributions	
$\delta_{HT,in}$	Internal heat boundary layer thickness	m_r
$\delta_{HT,ext}$	External heat boundary layer thickness	m_r
ΔH_j	Reaction enthalpy	kJ mol^{-1}
ΔP_z	Axial pressure drop	$\text{kg m}_r^{-1} \text{h}^{-2}$
ε	Void fraction,	$m_f^3 m_r^{-3}$
ε_0	Averaged void fraction,	$m_f^3 m_r^{-3}$
θ_i	Fractional surface coverage of component i	
μ_f	Dynamic viscosity	$\text{kg}_f m_r^{-1} \text{h}^{-1}$
μ_{eff}	Effective viscosity	$\text{kg}_f m_r^{-1} \text{h}^{-1}$
$\nu_{i,j}$	Stoichiometric number of component i in reaction j	
ρ_b	Packed bed density	$\text{kg}_s m_r^{-3}$
ρ_f	Fluid density	$\text{kg}_f m_r^{-3}$
ρ_s	Solid density	$\text{kg}_s m_s^{-3}$
Φ	Optimal parameter vector	
$\nu_{i,j}$	Stoichiometric number of component i in reaction j	

Subscripts

C	Number of carbons
---	-------------------

List of Symbols

cat	Catalyst
eff	Effective
exp	Experimental
f	Fluid
i	i-species
in	Inlet
j	Reaction j
n	Component n
0	Inlet
out	outlet
P	Particle
R	Reactor
S	Solid
ss	Steady state
t	Tube
*	Density of vacant sites

Superscript

0	Static, inlet
---	---------------

List of Abbreviations

Acronym	Description
BG	Biogas feedstock considering CO ₂ and methane
BLA	Boundary Layer Approach
CA	Classical Approach
d_t/d_p	tube to particle diameter ratio
ER	Eley-Rideal
HF	Hydroformylation of ethylene
KWT-BC	Know Wall-Temperature Boundary Condition
KWT-BLA	Known Wall-Temperature Boundary Layer Approach
NG	Natural gas feedstock considering only methane
OCM	Oxidative Coupling of Methane
OCoM	Oxidative Conversion of Methane
ODH	Oxidative Dehydrogenation of Ethane
POE	Partial Oxidation of Ethane
POEt	Partial Oxidation of Ethylene
POM	Partial Oxidation of Methane
PLA	Pseudo-Local Approach
PL-IHTA	Pseudo-local Internal Heat Transfer Approach
RSS	Residual Sum of Squares
SG	Shale Gas feedstock consisting of methane, CO ₂ and ethane
SRM	Steam Reforming of Methane
TDE	Thermal Dehydrogenation of Ethane
TOCO	Total Oxidation of CO
TOE	Total Oxidation of Ethane
TOEt	Total Oxidation of Ethylene
TOM	Total Oxidation of Methane
WGSR	Water Gas Shift Reaction

Summary

Today, unused carbon resources, such as natural gas, are widely available, and most of the time they are wasted through venting or flaring, contributing to global warming. It is imperative to validate an efficient and selective transformation of it into higher value products for industrial implementation, while reducing the carbon footprint from the petrochemical industry, and to transition to a less energy-intensive methane and ethane conversion technology than the conventional processes, i.e., steam reforming of methane and thermal cracking of ethane. Within the framework of the circular economy for hydrocarbons, two fundamental processes have been assessed in this thesis: the Oxidative Conversion of Methane (OCoM) and the Oxidative Dehydrogenation of Ethane (ODH).

On the one hand, from a lab-scale perspective, OCoM is proposed in this work as a novel process concept for methane valorization into a product stream with a molar $C_2H_4/CO/H_2$ composition of 1/1/1, i.e., suitable for further ethylene hydroformylation, as an alternative of the Oxidative Coupling of Methane (OCM). OCoM, by exploiting other methane and ethane conversion reactions, i.e., Steam Reforming of Methane (SRM) and the Thermal Dehydrogenation of Ethane (TDE), overcomes the limitations traditionally encountered during OCM in the pursuit of a maximum ethylene yield. Some of these limitations are the high energy-intensive separation of ethylene from the product gas mixture, e.g., C_2H_4/C_2H_6 molar ratio of 2.5 mol mol⁻¹, and C_2 yields below 35% mol mol⁻¹ which is not enough for its industrialization.

The MnNaW/SiO₂ catalyst was selected for OCoM among other catalytic materials because of its good stability (> 90 h), high temperature performance (850 °C) without indications of deactivation and trade-off between methane conversion (30% mol mol⁻¹) and C_2 selectivity (80% mol mol⁻¹). Then, an experimental assessment was performed using this catalyst under industrially relevant conditions ($T = 800 - 850$ °C, $p_{tot} = 100$ kPa, $W_{cat}/F_{CH_4,in} = 2 - 2.5$ kg_{cat} s mol⁻¹, CH_4/O_2 inlet molar ratio = 3 – 5 mol mol⁻¹ and inlet CO₂ molar fraction < 20%). The experimental campaign was carried out as a basis for reaction network proposal and kinetic model development for the various relevant reactions in OCoM, such as the OCM, TDE, and SRM. It is noteworthy to mention that co-feeding CO₂ has no significant effect on the OCoM performance utilizing the MnNaW/SiO₂ catalyst. The impact of the operating

Summary

conditions on the OCoM performance was simulated with this model, while simultaneously pursuing a $C_2H_4/CO/H_2$ molar ratio of 1/1/1 and a maximum C_2 yield. Furthermore, total O_2 conversion is targeted to avoid more challenging downstream separations. Three different real feedstocks were considered for the assessment of OCoM: natural gas approximated as pure methane, shale gas which additionally includes CO_2 and ethane, and biogas, a mixture of essentially methane and CO_2 . Among the three different feedstocks, shale gas was found to exhibit the highest OCoM potential, with a carbon conversion of 31% $mol\ mol^{-1}$, an ethylene yield of 19% $mol\ mol^{-1}$, equivalent with a carbon yield (ethylene + CO) of 28% $mol\ mol^{-1}$, and a $C_2H_4/CO/H_2$ molar ratio amounted to 1/1.1/3.7. The optimal operating conditions were found as a temperature of 850 °C a $W_{cat}/F_{CH_4,in}$ of 6.5 $kg_{cat}\ s\ mol^{-1}$ and a CH_4/O_2 inlet molar ratio of 10 $mol\ mol^{-1}$.

On the other hand, the recent implementation of the multitubular ODH packed bed reactor in the industry demands for a reliable reactor model that accurately accounts for all the phenomena occurring during its performance, i.e., kinetics and transport phenomena. Hence, a generalized approach to model the temperature gradients in an industrial-scale wall-cooled packed bed with a low tube-to-particle diameter ratio ($< 8\ m_r\ m_s^{-1}$) is proposed and assessed in this work. The modeling approach is built on experiments carried out in absence of reaction in bench-scale as well as in industrial-scale packed beds for the adequate characterization of the heat transfer parameters. The methodology leads to the reliable determination of the external wall heat transfer coefficient ($h_{w,ext}$) and pseudo-local radial effective thermal conductivity ($k_{eff,r,PLA}$). This approach allows the quantification of heat transfer resistances through the core and the internal and the external wall of the bed indicating that approximately 30% of the resistances are located along the internal side of the packed bed when it was operated at particle Reynolds numbers ranging from 700 to 1400. Because of its complex impact on heat transfer, fluid dynamics is accounted for by implementing a methodology that uses pressure drop data and the mass conservation criterion to describe velocity profiles, including the determination of the viscous and inertial resistances caused by solid surfaces at the core and near the wall. The approximation developed in this work overcomes historical limitations identified when modeling radial heat transfer mechanisms by applying conventional heat transfer approaches. Moreover, the axial heat transfer conduction was characterized via the effective axial conductivity ($k_{eff,z}$) from adiabatic experiments in a bench-scale packed bed in the absence of reaction. Non-adiabatic and non-isothermal bench-scale and industrial-scale packed bed

Summary

experimental data were used in the assessment of the impact of axial heat conduction on the description of temperature gradients.

The heat transfer information is transferred to a pseudo-heterogenous model to simulate the performance of an industrial-scale wall-cooled packed-bed reactor with low tube-to-particle diameter ratio ($d_t/d_p < 8 \text{ m}_r \text{ m}_s^{-1}$) for the highly exothermic ODH. Simulations demonstrate the reliability of the proposed heat transfer approach, and the limitations of the conventional approximations when describing temperature profiles in a packed bed reactor.

Furthermore, the impact of axial conductive heat transfer on the prediction of hot spots and, more particularly, thermal runaway has been elucidated. When disregarding axial heat conduction or adopting literature-based values for $k_{\text{eff},z}$, determined from either experiments at low d_t/d_p ratios ($< 8 \text{ m}_r \text{ m}_s^{-1}$) and $\text{Re}_p \leq 1000$ or high d_t/d_p ratios ($> 8 \text{ m}_r \text{ m}_s^{-1}$) and $\text{Re}_p \leq 700$ at a wide panel of operating configurations, runaway is simulated at conditions where it has not been observed experimentally or a negligible hot-spot prediction is obtained. When considering the $k_{\text{eff},z}$ determined for the specific reactor configuration in this work, hot spots are predicted at Re_p of 700 and 1400, but no runaway. The discrepancies between experimental findings and temperature profiles simulated based on literature-based values for $k_{\text{eff},z}$ indicate the need for a specific determination of $k_{\text{eff},z}$ in packed bed reactors with low d_t/d_p ratio to more accurately predict hot spots, resulting in more reliable reactor design and operation.

Samenvatting

Vandaag de dag zijn ongebruikte koolstofbronnen, zoals aardgas, overal voorhanden, en meestal worden ze verspild door afblazen of affakkelen, wat bijdraagt aan de opwarming van de aarde. Het is absoluut noodzakelijk om hiervoor een gevalideerd model voor de efficiënte en selectieve transformatie in producten met een hogere economische waarde voor industriële toepassingen te hebben, dit verkleint de koolstofvoetafdruk van de petrochemische industrie, en om over te stappen naar een minder energie-intensieve methaan- en ethaanconversietechnologie dan de conventionele processen, zijnde de stoomreforming van methaan en het thermisch kraken van ethaan. Twee fundamentele processen binnen het kader van een circulaire economie voor koolwaterstoffen worden in dit proefschrift beschouwd: de Oxidatieve Conversie van Methaan (OCoM) en de Oxidatieve Dehydrogenering van Ethaan (ODH).

Eenzijds wordt OCoM in dit werk voorgesteld als een nieuw procesconcept voor de valorisatie van methaan in een productstroom met een molaire $C_2H_4/CO/H_2$ -samenstelling van 1/1/1, dit maakt het geschikt voor verdere hydroformylering van etheen, als alternatief voor de oxidatieve koppeling van methaan (OCM). OCoM overkomt, door gebruik te maken van andere methaan- en ethaanconversiereacties, namelijk Stoomreforming van Methaan (SRM) en de Thermische Dehydrogenering van Ethaan (TDE), de traditionele beperkingen van OCM bij het streven naar een maximale ethyleenopbrengst. Een van deze beperkingen is de zeer energie-intensieve afscheiding van ethyleen uit het gasvormig productmengsel. Een molaire verhouding C_2H_4/C_2H_6 van $2,5 \text{ mol mol}^{-1}$, en C_2 opbrengst van minder dan $35\% \text{ mol mol}^{-1}$ maken het proces economisch niet levensvatbaar. De MnNaW/SiO₂-katalysator werd geselecteerd voor OCoM vanwege zijn goede stabiliteit (> 90 uur), sterke prestaties bij hoge temperaturen (850 °C) zonder aanwijzingen van deactivering en het evenwicht tussen methaanomzetting ($30\% \text{ mol mol}^{-1}$) enerzijds en C_2 -selectiviteit ($80\% \text{ mol mol}^{-1}$) anderzijds. Vervolgens werd deze katalysator experimenteel getest onder industrieel relevante omstandigheden ($T = 800 - 850 \text{ °C}$, $p_{\text{tot}} = 100 \text{ kPa}$, $W_{\text{cat}}/F_{CH_4, \text{in}} = 2 - 2,5 \text{ kg}_{\text{cat}} \text{ s mol}^{-1}$, molaire verhouding CH_4/O_2 inlaat = $3 - 5 \text{ mol mol}^{-1}$ en molaire fractie CO_2 inlaat < 20%). De resultaten van deze experimenten waren de basis voor het opstellen van een reactienetwerken en de ontwikkeling van kinetische modellen voor de verschillende relevante reacties in OCoM, zoals

de OCM, TDE en SRM. Hierbij werd vastgesteld dat het gelijktijdig voeden van CO₂ geen significant effect heeft op de prestaties van het OCoM-proces bij gebruik van de MnNaW/SiO₂-katalysator. Met dit model werd de impact van de reactiecondities op de prestaties van het OCoM-proces gesimuleerd. Er werd steeds gestreefd naar een molaire C₂H₄/CO/H₂-verhouding van 1/1/1 en een maximale C₂-opbrengst werd. Bovendien is ook de totaleconversie van O₂ een doel, dit om meer complexe scheidingen te vermeiden. Drie verschillende, realistische grondstoffen zijn beschouwd: aardgas, ongeveer zuiver methaan; schaliegas dat bovendien CO₂ en ethaan omvat; en biogas, een mengsel van hoofdzakelijk methaan en CO₂. Van de drie verschillende grondstoffen bleek schaliegas het meest geschikt voor OCoM, met een koolstofomzetting van 31% mol mol⁻¹, een ethyleenopbrengst van 19% mol mol⁻¹, equivalent met een koolstofopbrengst (ethyleen + CO) van 28% mol mol⁻¹, en een molaire C₂H₄/CO/H₂-verhouding van 1/1,1/3,7. De optimale reactiecondities zijn een temperatuur van 850 °C, een W_{cat}/F_{CH₄,in} van 6,5 kg_{cat} s mol⁻¹ en in de voeding een molaire CH₄/O₂-verhouding van 10 mol mol⁻¹.

Aan de andere kant vraagt de recente implementatie van de multitubulaire, gepakte kolom ODH-reactor in de industrie om een betrouwbaar reactormodel dat nauwkeurig rekening houdt met alle verschijnselen die optreden tijdens de werking ervan, namelijk kinetiek en transportverschijnselen. In dit werk wordt een breed toepasbare benadering voorgesteld en getest om de temperatuurgradiënten in een wandgekoeld, gepakte kolom reactor op industriële schaal met een lage buis-tot-deeltjesdiameterverhouding ($< 8 m_r m_s^{-1}$) te modelleren voorgesteld en getest. Het model is gebaseerd op experimenten die zijn uitgevoerd in afwezigheid van reactie op zowel laboratoriumschaal als in gepakte kolom reactoren op industriële schaal voor een adequate bepaling van de warmteoverdrachtsparameters. De methodologie leidt tot de betrouwbare bepaling van de warmteoverdrachtscoëfficiënt van de buitenmuur ($h_{w,ext}$) en de effectieve radiale pseudo-lokale thermische geleidbaarheid ($k_{eff,r,PLA}$). Deze aanpak maakt de kwantificering van de weerstand tegen tegenwarmteoverdracht door de kern, en de binnen- en buitenwand van het bed mogelijk. Hieruit blijkt dat ongeveer 30% van de weerstand zich langs de binnenzijde van het gepakte kolom reactor bevindt wanneer de deeltjes-Reynoldsgetallen variëren van 700 tot 1400. Omdat vloeistofmechanica een complexe invloed heeft op warmteoverdracht wordt dit ook geïmplementeerd in het model door drukvalgegevens en het criterium voor massabehoud te gebruiken om snelheidsprofielen te beschrijven. Ook de viscositeits- en traagheidsweerstand, veroorzaakt door vaste oppervlakken in de kern en dichtbij de muur, worden in kaart gebracht. Deze benadering maakt

het modelleren van radiale warmteoverdracht, gebruik makende van traditionele technieken om warmteoverdracht te beschrijven, mogelijk. Bovendien werd de conductieve axiale warmteoverdracht in kaart gebracht met behulp van de effectieve axiale geleidbaarheid ($k_{\text{eff},z}$) afgeleid uit adiabatische experimenten in een gepakt kolom reactor op laboratoriumschaal bij afwezigheid van reactie. Niet-adiabatische en niet-isotherme experimentele gegevens op laboratoriumschaal en industriële schaal werden gebruikt bij het inschatten van de impact van axiale warmteoverdracht op de beschrijving van temperatuurgradiënten.

De informatie over de warmteoverdracht werd gebruikt in een pseudo-heterogeen model om de prestaties van een wandgekoelde, gepakt kolom reactor op industriële schaal met een lage verhouding tussen buis en deeltjesdiameter ($d_i/d_p < 8 m_r m_s^{-1}$) voor de zeer exotherme ODH te beoordelen. Simulaties tonen de betrouwbaarheid van de voorgestelde benadering en de beperkingen van de conventionele benaderingen bij het beschrijven van temperatuurprofielen in een gepakte kolom reactor aan.

Bovendien is de impact van conductieve axiale warmteoverdracht op de voorspelling van hotspots en, meer in het bijzonder, thermische runaway in kaart gebracht. Wanneer axiale warmtegeleiding buiten beschouwing wordt gelaten of op de literatuur gebaseerde waarden voor $k_{\text{eff},z}$ worden overgenomen, bepaald op basis van experimenten bij lage d_i/d_p -verhoudingen ($< 8 m_r m_s^{-1}$) en $Re_p \leq 1000$, of hoge d_i/d_p -verhoudingen ($> 8 m_r m_s^{-1}$) en $Re_p \leq 700$ bij een breed scala aan reactiecondities, wordt runaway gesimuleerd onder omstandigheden waarin dit experimenteel niet wordt waargenomen of waarbij verwaarloosbare hotspots worden voorspeld. Wanneer we de $k_{\text{eff},z}$ in beschouwing nemen die voor de specifieke reactorconfiguratie in dit werk is bepaald, worden er hotspots voorspeld bij Re_p van 700 en 1400, maar geen runaway. De discrepanties tussen experimentele bevindingen en temperatuurprofielen die zijn gesimuleerd op basis van waarden voor $k_{\text{eff},z}$ uit literatuur duiden op de noodzaak van een meer exacte bepaling van $k_{\text{eff},z}$ in gepakte kolom reactoren met een lage d_i/d_p -verhouding om hotspots nauwkeuriger te voorspellen, wat resulteert in meer betrouwbaar reactorontwerp en -werking.

Resumen

Actualmente, recursos de carbono no utilizados, como el gas natural, están ampliamente disponibles y la mayor parte del tiempo se desperdician mediante su ventilación al medioambiente o su quema, lo cual contribuye al calentamiento global. Es imperativo validar una transformación eficiente y selectiva de estos recursos en productos de mayor valor para su implementación industrial, reduciendo al mismo tiempo la huella de carbono de la industria petroquímica, y haciendo una transición hacia una tecnología de conversión de metano y etano que consuma menos energía que los procesos convencionales, es decir, el reformado de metano con vapor y el craqueo térmico de etano. Dentro del marco de la economía circular de los hidrocarburos, en esta tesis se han evaluado dos procesos fundamentales: la Conversión Oxidativa del Metano (OCoM) y la Deshidrogenación Oxidativa del Etano (ODH).

Por un lado, desde una perspectiva a escala de laboratorio, en este trabajo OCoM es propuesto como un concepto de proceso novedoso para la valorización de metano hacia una corriente de producto con una composición molar $C_2H_4/CO/H_2$ de 1/1/1, es decir, adecuado para una posterior hidroformilación de etileno, como alternativa al Acoplamiento Oxidativo de Metano (OCM). OCoM, al aprovechar otras reacciones de conversión de metano y etano, es decir, el reformado de metano con vapor (SRM) y la deshidrogenación térmica de etano (TDE), supera las limitaciones encontradas tradicionalmente durante la OCM en la búsqueda de un rendimiento máximo de etileno. Algunas de estas limitaciones son la separación de etileno de la mezcla de los gases producto que consume mucha energía, por ejemplo, una relación molar C_2H_4/C_2H_6 de 2.5 mol mol⁻¹, y rendimientos de C_2 inferiores al 35% mol mol⁻¹, lo que no es suficiente para su industrialización.

El catalizador MnNaW/SiO₂ fue seleccionado para OCoM, entre otros materiales catalíticos, debido a su buena estabilidad (> 90 h), rendimiento a altas temperaturas (850 °C) sin indicaciones de desactivación, y compensación entre conversión de metano (30% mol mol⁻¹) y selectividad de C_2 (80% mol mol⁻¹). Luego, se realizó una evaluación experimental utilizando este catalizador en condiciones industrialmente relevantes ($T = 800 - 850$ °C, $p_{tot} = 100$ kPa, $W_{cat}/F_{CH_4,in} = 2 - 2.5$ kg_{cat} s mol⁻¹, relación molar de entrada $CH_4/O_2 = 3 - 5$ mol mol⁻¹ y fracción molar de CO₂ de entrada < 20%). La campaña experimental se llevó a cabo como base para la propuesta de red de reacción y el desarrollo de modelos cinéticos para las diversas reacciones relevantes en OCoM, como OCM, TDE y SRM. Cabe mencionar que la

alimentación conjunta de CO_2 no tiene un efecto significativo sobre el rendimiento del OCoM utilizando el catalizador MnNaW/SiO_2 . Con este modelo se simuló el impacto de las condiciones de operación en el rendimiento de OCoM, buscando simultáneamente una relación molar $\text{C}_2\text{H}_4/\text{CO}/\text{H}_2$ de 1/1/1 y un rendimiento máximo de C_2 . Además, se buscó la conversión total de O_2 con el objetivo de evitar posteriores procesos de separación. Para la evaluación de OCoM se consideraron tres diferentes fuentes de alimentación reales: gas natural aproximado como metano puro, gas de lutita (*shale gas*) que además incluye CO_2 y etano, y biogás, una mezcla esencialmente de metano y CO_2 . Entre las tres diferentes fuentes de alimentación, se encontró que el gas de lutita presenta el mayor potencial para OCoM, con una conversión de carbono del 31% mol mol^{-1} , un rendimiento de etileno del 19% mol mol^{-1} , equivalente a un rendimiento de carbono (etileno + CO) del 28% mol mol^{-1} , y una relación molar $\text{C}_2\text{H}_4/\text{CO}/\text{H}_2$ de 1/1.1/3.7. Las condiciones de operación óptimas encontradas son temperatura de 850 °C, un espacio-tiempo de ($W_{\text{cat}}/F_{\text{CH}_4,\text{in}}$) de 6.5 $\text{kg}_{\text{cat}} \text{s mol}^{-1}$ y una relación molar de entrada de CH_4/O_2 de 10 mol mol^{-1} .

Por otro lado, la reciente implementación del reactor multitubular de lecho empacado para la ODH en la industria exige un modelo de reactor confiable que tenga en cuenta de manera precisa todos los fenómenos que ocurren durante su desempeño, es decir, la cinética y los fenómenos de transporte. Por lo tanto, en este trabajo se propone y evalúa un enfoque generalizado para modelar los gradientes de temperatura en un lecho empacado con enfriamiento en la pared a escala industrial con una baja relación de diámetro de tubo a partícula ($<8 m_r m_s^{-1}$). La aproximación del modelado se basa en experimentos llevados a cabo en ausencia de reacción, tanto a escala banco como en lechos empacados a escala industrial, para la caracterización adecuada de los parámetros de transferencia de calor. La metodología conduce a la determinación confiable del coeficiente de transferencia de calor de la pared externa ($h_{w,\text{ext}}$) y la conductividad térmica efectiva radial pseudo-local ($k_{\text{eff},r,\text{PLA}}$). Este enfoque permite la cuantificación de las resistencias de transferencia de calor a través del centro del lecho empacado y la pared interna y externa del lecho, lo que indica que aproximadamente el 30% de las resistencias están ubicadas a lo largo del lado interno del lecho empacado cuando se operó con números de Reynolds de partículas que van desde 700 a 1400. Debido a su complejo impacto en la transferencia de calor, la dinámica de fluidos es considerada mediante la implementación de una metodología que utiliza datos de caída de presión y el criterio de conservación de masa para describir los perfiles de velocidad, incluida la determinación de las resistencias viscosas e inerciales causadas por superficies sólidas en el centro del lecho y cerca

de la pared. La aproximación desarrollada en este trabajo supera las limitaciones históricas identificadas al modelar mecanismos de transferencia de calor radiales mediante la aplicación de enfoques convencionales de transferencia de calor. Además, la conducción de transferencia de calor axial se caracterizó mediante la conductividad térmica efectiva axial ($k_{\text{eff},z}$) de experimentos adiabáticos en un lecho empacado a escala de banco en ausencia de reacción. Se utilizaron datos experimentales de un lecho empacado a escala industrial en condiciones de operación no adiabáticas y no isotérmicas para evaluar el impacto de la conducción de calor axial en la descripción de los gradientes de temperatura.

La información de transferencia de calor se transfiere a un modelo pseudo-heterogéneo para simular el rendimiento de un reactor de lecho empacado con enfriamiento en la pared a escala industrial con una baja relación de diámetro de tubo a partícula ($d_t/d_p < 8 \text{ m}_r \text{ m}_s^{-1}$) para la altamente exotérmica ODH. Las simulaciones demuestran la confiabilidad de la aproximación de transferencia de calor propuesta y las limitaciones de las aproximaciones convencionales al describir los perfiles de temperatura en un reactor de lecho compacto.

Además, se ha dilucidado el impacto de la transferencia de calor por conducción axial en la predicción de puntos calientes y, particularmente, fuga térmica (*thermal runaway*). Al ignorar la conducción de calor axial o adoptar valores basados en la literatura para $k_{\text{eff},z}$, determinados a partir de experimentos con relaciones d_t/d_p bajas ($< 8 \text{ m}_r \text{ m}_s^{-1}$) y $\text{Re}_p \leq 1000$ o relaciones d_t/d_p altas ($> 8 \text{ m}_r \text{ m}_s^{-1}$) y $\text{Re}_p \leq 700$ en un amplio panel de configuraciones operativas, la fuga térmica se simula en condiciones en las que no se ha observado experimentalmente o se obtiene una predicción de punto caliente insignificante. Al considerar el $k_{\text{eff},z}$ determinado para la configuración específica del reactor en este trabajo, se predicen puntos calientes en Re_p de 700 y 1400, pero no fugas térmicas. Las discrepancias entre los hallazgos experimentales y los perfiles de temperatura simulados basados en valores de $k_{\text{eff},z}$ basados en la literatura indican la necesidad de una determinación específica de $k_{\text{eff},z}$ en reactores de lecho empacado con una relación d_t/d_p baja para predecir con mayor precisión los puntos calientes, lo que resulta en más diseño y operación confiables del reactor.

Chapter 1 – Introduction

1.1 Circular economy for hydrocarbons

Understanding and addressing greenhouse gas emissions is high on the agenda in our climate change dialogue. Nowadays, methane emissions are the second leading cause of global warming after carbon dioxide [20], and they account for approximately 30% of the global temperature increase since the Industrial Revolution [21]. This is primarily due to the global warming potential of methane, which exceeds that of CO₂ by a factor 25. As such, its heat-trapping capability in the atmosphere significantly influences global warming during its 12-year atmospheric life span. The oil and gas industry, particularly through the wastage of natural gas via venting (direct release into the atmosphere), flaring (intentional burning), and even via leaks (result during the production, processing, and transportation), serves as the principal source of methane(-related) emissions worldwide in the energy sector, see Figure 1.1 [1,22].

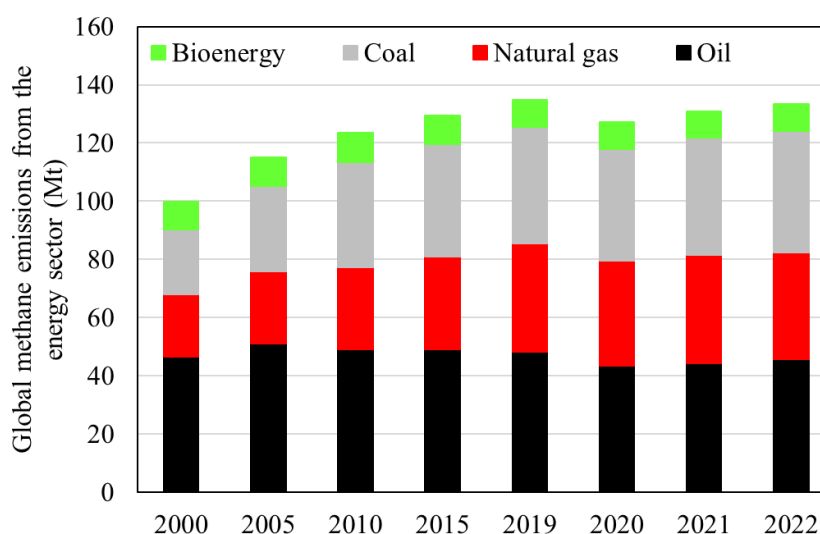


Figure 1.1. Global methane emissions from the energy sector, 2000 – 2022 [1].

Worldwide leaders in the gas and oil industry have been taking steps to promote a circular economy for hydrocarbons to reduce waste and greenhouse gas emissions, targeting innovative approaches to production (and consumption). This strives towards waste reduction by converting waste by-products into new functional products, i.e., reducing the total quantity of materials used and minimizing the production of hydrocarbons [23,24], and fostering a sustainable utilization of natural resources [25]. In the United States, laws have been promoted

toward a circular economy such as the Inflation Reduction Act (IRA), the Creating Helpful Incentives to Produce Semiconductors (CHIPS), the Science Act, and the Bipartisan Infrastructure Law. These laws encourage the investment in clean-energy and sustainable agriculture, next-generation industrial processes, and tools to measure and track the ingredients that go into products [26]. The Kingdom of Saudi Arabia, leading the world with the largest investment in green hydrogen [27], released a Circular Economy Roadmap in May 2018 outlining a plan to shift the country towards a more environmentally sustainable economy [28]. This roadmap identifies key areas for improvement, including waste management, recycling, renewable energy, and the use of recycled materials. In the European Union, the European Green Deal (EGD) was launched in 2019 as a package of policy initiatives aimed at transforming the EU into a modern, resource-efficient, and competitive economy. EGD targets reducing methane emissions from the energy sector at least 55% by 2030 and ensuring no net emissions of greenhouse gases by 2050 [29,30]. Within EGD, the Circular Economy Action Plan (CEAP) was established in 2020, comprising a comprehensive series of legislative and non-legislative initiatives aiming at transitioning the European economy from a linear to a circular model [31]. In addition, EU has launched various funding programs to encourage research innovation in the European industry, enhance international competitiveness, and promote research supporting EU policies [32,33].

1.2 The role of natural gas

In the global energy narrative natural gas play a significant role including power generation, heating, and transportation [34]. At the end of 2020 the total proven reserves of natural gas amounted to 188 trillion m³ worldwide [2,3,35], see Figure 1.2. Expert analysts foresee a steady annual growth of approximately 2% for natural gas, surpassing coal as the principal energy source within the next two decades [36]. This leads to the emergence of new opportunities in the methane and ethane market [37].

In the context of petroleum exploration and production, the term "natural gas" refers to the gases that are typically found in geological formations associated with crude oil reservoirs, i.e., associated gas. [38]. Depending on the composition and location, some kind of associated gases are wet natural gas, stranded gas and marginal gas. Wet natural gas is a mixture of hydrocarbon compounds and small quantities of various non-hydrocarbons existing in the gaseous phase or in solution with crude oil in porous rock formations at reservoir conditions [39]. It is called wet because it contains a significant amount (~15%) of liquid hydrocarbon

compounds, i.e., ethane, propane, and butane, in addition to methane gas [34]. Stranded gas is a natural gas that is difficult to exploit because of physical (remoteness of location, lack of pipeline infrastructure) or economic factors [40]. When this one is not economical to process and sell, it is often wasted via flaring or venting. However, there are increasing efforts to utilize this gas to increase oil recovery by re-injecting it into oil fields [41], or by using it as a feedstock in Gas-to-Liquid (GTL) processes that convert natural gas into synthetic fuels [42]. Marginal gas, considered a type of stranded gas, refers to the production of natural gas from low-productivity well sites, often referred to as marginal well sites. These sites have an average combined oil and gas production of less than 15 barrels of oil equivalent per day [43]. Nevertheless, over 565,000 actively producing marginal well sites in the United States represent 80% of all active oil and gas production sites, and 6.2% and 5.5% of the production of oil and gas, respectively [43].

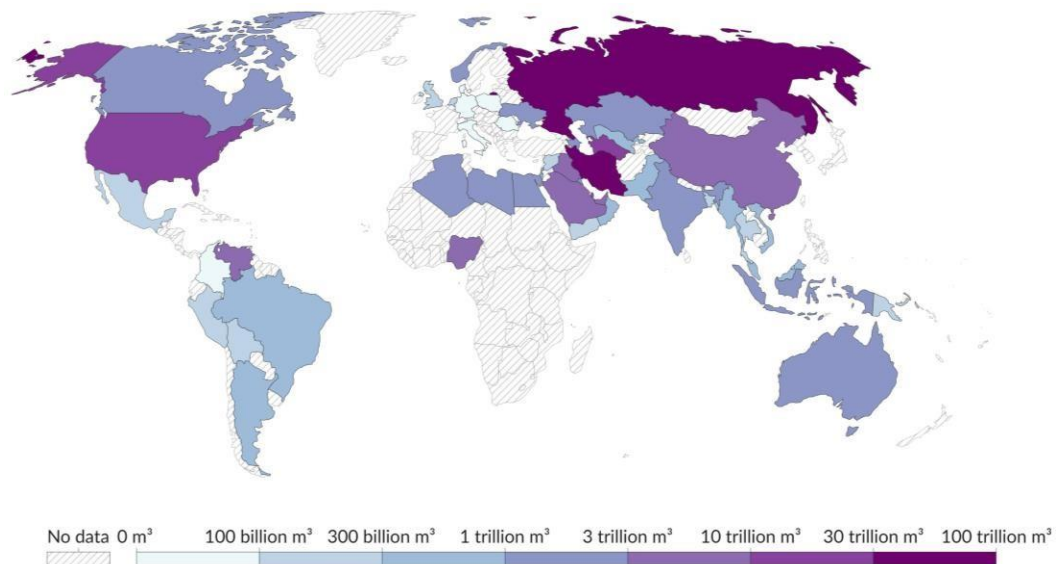


Figure 1.2. Gas reserves, 2020. Proven reserves, measured in cubic meters, are those quantities that can be recovered in the future from known reservoirs under existing economic and operating conditions, according to geological and engineering information [2,3].

On the other hand, natural gas can also be referred to as non-associated when it is found in fields without oil, or produced from coal deposits, shale formations, anaerobic digestion or organic material fermentation. Biogas is produced from the anaerobic digestion or fermentation of organic material including manure, sewage, municipal waste, green waste, and energy crops. Its composition varies but is generally about 50 – 75% methane and 25 – 50% carbon dioxide, with small amounts of nitrogen (2 – 8%), and trace levels of hydrogen sulfide, ammonia, hydrogen, water and various volatile organic compounds [44]. In the petrochemical industry,

biogas can be upgraded to biomethane, by removing impurities like CO₂, hydrogen sulfide and water, resulting in a < 95 % methane content. This makes biomethane more compatible with existing natural gas infrastructure, and more versatile and valuable renewable energy source [45]. Shale gas is a form of natural gas that is found trapped within shale formations, i.e., fine-grained sedimentary rock that is less permeable than sandstone, siltstone, or limestone [46]. Shale gas is trapped in tiny pockets within the shale rocks. To be extracted, hydraulic fracturing, commonly known as fracking, is used to break up the rocks and release the gas. The process involves drilling deep holes into the shale rock, followed by horizontal drilling to access more of the gas, as shale reserves are typically distributed horizontally rather than vertically [47]. Once extracted, the gas is processed to remove impurities and separated into its component parts, which include methane (> 80 %), ethane (3 – 16%), propane (< 4%), carbon dioxide (< 7%), nitrogen (< 3%), and trace amounts of other C₄₊ species [48–51]. However, this practice has several environmental issues such as water contamination, air pollution, methane emissions, seismic activity, habitat disruption and land degradation [47].

1.3 Methane conversion technologies

Methane, being the principal component of natural gas (> 85%) [52], is the most abundant hydrocarbon available worldwide. Methane market forecast predicts natural gas will play a key role in the global energy sector, even overtaking the coal in two decades [53], and being a critical component of the global energy and chemical industries for many years to come. Therefore, developing innovative, less energy-intensive and environmentally friendly processes for methane valorization is crucial for the circular economy for hydrocarbons, as it could help reducing emissions while providing alternative energy and material sources [54]. The challenges facing the adoption of these innovative technologies include kinetic studies, reactor design, simulation, and recycling processes [55,56]. Additionally, the cost of methane valorization technologies must remain competitive with traditional fossil fuel extraction and processing methods. Below, a summary of the conventional processes for methane conversion and the promising alternatives are discussed highlighting the importance of methane as a raw material in the chemical industry and the versatility of methane as a feedstock for the production of a wide range of chemicals and fuels.

1.3.1 Steam and autothermal reforming of methane

Currently, the most used process in the industry for the direct conversion of methane is the highly endothermic Steam Reforming of Methane, SRM [57], see Eq. (1.1), which produces syngas, i.e., carbon monoxide and hydrogen.



SRM, industrialized since 1930s [58], contributes to the 95% of hydrogen production in USA [59] and 50% worldwide [60]. Some advances has been made in the development of technology to increase the efficiency of SRM. In the last decade, an Autothermal Reforming of Methane, ATR, was implemented by TOPSOE [61], combining SRM with the exothermic Partial Oxidation of Methane, POM, see Eq. (1.2), in the same reactor.



The improvements of this technology account for an efficient heat management between the highly endothermic SRM and the exothermic POM, reducing the number of heat exchangers in the process. This process serves as a source of syngas for different chemical processes, such as Fischer-Tropsch to produce liquid hydrocarbons [62] and Haber-Bosch process to ammonia production [63,64]. However, due to the highly endothermic nature of SRM, i.e., temperatures up to 1000 °C required [52], its profitable operation is not economically feasible for smaller or highly remote gas reserves where natural gas is available at low prices, e.g., marginal gas [65,66]. Moreover, despite the direct conversion of methane from natural gas, without going through syngas, has been studied in the last 50 years, an industrial process has not been implemented yet [67]. More details of the alternative technologies are discussed in the next section.

1.3.2 Exploring new frontiers

The direct activation of methane and its conversion to the desired products is a difficult technological challenge, mainly due to the activation of the methane molecule and that downstream products are commonly more reactive than methane [52]. Both endothermic and exothermic alternative reactions to directly convert methane into valuable products have been widely studied in the last five decades. The most promising endothermic proposals are the Dry

Reforming of Methane, DRM, see Eq. (1.3), and the Methane Dehydroaromatization, MDA, see Eq. (1.4).



DRM utilizes the two largest greenhouse gases, i.e., CO₂ and methane, as reactants for the production of syngas, while MDA converts methane into aromatics (mostly benzene) and hydrogen. However, coke formation occurs during DRM due to methane cracking and the Boudouard reaction [68,69], and during MDA due to absence of an oxidant such as water or CO₂, causing the deactivation of the catalyst and, consequently delaying their industrialization [70].

The exothermic alternatives have an advantage over the endothermic reactions because they require lower energy than the conventional endothermic processes, lower energy costs are associated with them. On the one hand, the conversion of methane to methanol, MTM, see Eq. (1.5), is attractive to industry because the potential implementation of methanol as chemical intermediate for the production of hydrocarbons [71].



However, despite that MTM has been researched for over 115 years [72,73], no catalyst has been developed to selectively oxidize methane into methanol, i.e., overoxidation occurs [52,74]. On the other hand, the Oxidative Coupling of Methane, OCM, see Eq. (1.6), widely investigated since the early 80s [75], targets the valorization of methane into C₂ species, particularly targeting ethylene.



Extensive research has been conducted to identify the best suited elements to incorporate in OCM catalysts, covering almost the entire periodic table [76]. Most recent efforts were focused on the understanding of different catalyst combinations, and reactor configurations on the OCM performance [77–82]. Nevertheless, it was concluded that its implementation on the industrial scale has been hindered by the low C₂ yields and no combination of catalyst and operating conditions provides an economically viable single-pass

conversion of methane into ethylene via OCM. [83]. Thus, several process concepts combining OCM have been proposed, e.g., OCM with dry methane reforming [84], OCM with ethane pyrolysis [85,86], and OCM with bioethanol dehydration [87]. Until today, none of them has reached C_2 yields exceeding 35 % mol mol⁻¹, which are considered necessary for commercialization [88,89]. Moreover, due to the resulting gas mixture obtained from the proposed OCM process, e.g., C_2H_4/C_2H_6 molar ratio of 2.5 mol mol⁻¹ and CH_4/C_2H_4 molar ratio between 4 and 8 mol mol⁻¹ [86,90,91], its implementation requires high energy-intensive and expensive separation units to obtain ethylene [92].

Within the CEAP framework mentioned in previous sections, several European projects targeting methane valorization emerged, exploring the coupling of OCM with other potential technologies. For instance, the Oxidative Coupling of Methane followed by Oligomerization to Liquids project (OCMOL) provided an integrated process for the sustainable production of liquid fuels from relatively small natural gas wells [93]. This project integrated the exothermic OCM with the endothermic DRM. However, the separation of the desired products from the downstream process presents an energetic and economic challenge. Additionally, only approximately 10% of the product yields originate from the OCM. Conversely, the Adaptable Reactors for Resource and Energy-Efficient Methane Valorization (ADREM) project focused on developing modular reactors capable of upgrading methane-rich sources to chemicals such as benzene, toluene, xylenes, ethylene, and syngas [80]. Microwave, plasma, and gas-solid vortex reactors were evaluated for methane valorization. Nonetheless, the project concluded that the energy efficiency remains low compared to conventional processes, and the upscale strategy for plasma reactors still presents a challenge.

1.4 The C123 European Horizon 2020 integrated project

The most recent project that overcomes the issues inherently related to OCM is the C123 European Horizon 2020 integrated project [53,94]. The project primarily focuses on the efficient and selective transformation of largely available, unexploited, low-cost methane resources (natural gas and biogas) to C_3 products, i.e., propanal and propanol, see Figure 1.3. C_3 commodities can be easily transported as a liquid prior to further transformation into propylene as a more sustainable feedstock for the growing global markets of polypropylene (anticipated to reach US\$157.8 billion by 2026 [95]), polymethyl methacrylate (projected at

US\$6.3 billion by 2027 [96]), and acrylic acid (forecasted at US\$ 19.2 billion by 2030 [97]). The C123 project proposes an integrated process considering two main reactions, the Oxidative Conversion of Methane (OCoM) and the Hydroformylation of Ethylene (HF). The activities related to methane valorization in this thesis were performed within the framework of the C123 project, with a particular focus on the OCoM process.

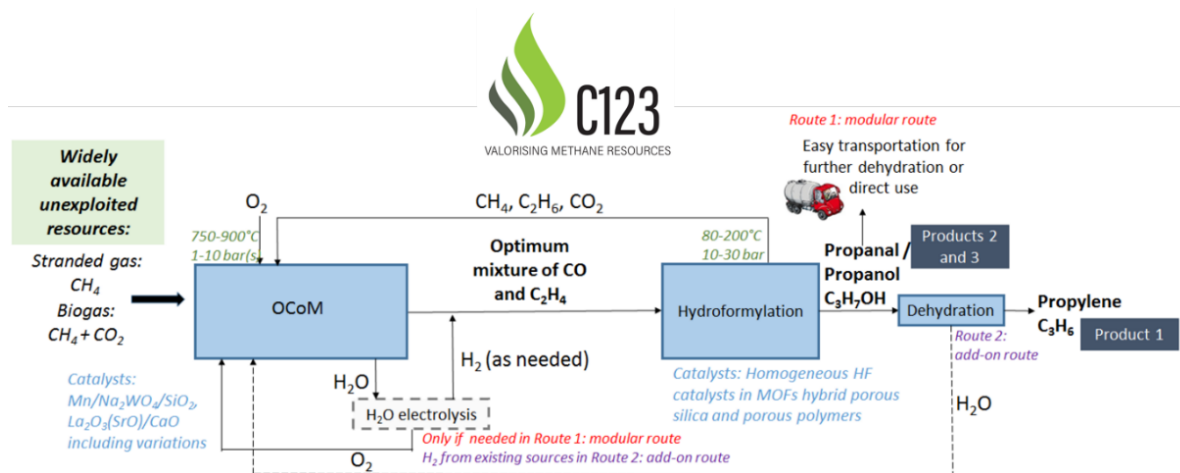


Figure 1.3. C123 project overview, starting from unused methane resources valorization through OCoM. Then, after achieving an optimal CO and C₂H₄ molar mixture, the ethylene hydroformylation produces C₃ species.

1.4.1 Oxidative Conversion of Methane (OCoM)

Among what has been researched to address the issues and limitations related to OCM process concepts, the OCoM from C123 stands out because it does not just target a high methane conversion per pass combined with a maximum C₂ yield, but rather a suitable feedstock for the subsequent downstream process, i.e., ethylene hydroformylation [53,98]. This is achieved by exploiting other methane and ethane conversion reactions such as the SRM and the Thermal Dehydrogenation of Ethane (TDE). This overcomes the challenge of separating the desired products from the gas mixture generated in a single-pass OCM process, while maximizing the yields of ethylene and reaching complete oxygen conversion. The benchmark NaMnW/SiO₂ catalyst has been identified as promising for the OCoM process because of its high temperature performance (800 – 900 °C) without indications of deactivation (> 1000 h) [99] and trade-off between methane conversion (30% mol mol⁻¹) and C₂ selectivity (80% mol mol⁻¹) [100–104].

1.4.2 Hydroformylation of ethylene (HF)

Hydroformylation of ethylene (HF) is a chemical reaction where olefins and syngas react to produce aldehydes containing one more carbon atom than the reactant olefin [98]. Industrially, HF is widely used for the conversion of ethylene to propanal and propanol applying homogeneous catalysts [94,105]. Within the C123 process, OCoM provides an optimized feedstock of ethylene, carbon monoxide and hydrogen for the hydroformylation process, which operates around 100°C and 20–40 bar pressure in the current industrial, homogeneous processes. A suitable heterogeneous catalyst will keep both processes in the gas phase, reduce precious metal losses during operation and address corrosion issues associated with solvent use. In addition to a tuned feedstock for hydroformylation, the reduction of the pressure difference between the two parts of the process (i.e. OCoM and hydroformylation) is targeted. A detailed understanding of the reaction variables for homogeneous ethylene hydroformylation and process development of a heterogeneous version of the reaction and the overall C123 process scheme is discussed elsewhere [98].

1.5 Ethane conversion technologies

Ethane as feedstock took more relevance in industrial chemical processes since the so called “shale gas revolution” [106] increasing the extraction of natural gas from shale rock formations among the other wells, i.e., gas, coalbed and oil wells, see Figure 1.4. This revolution was a significant and transformative change in the energy landscape that began in the United States in the late 1990s characterized by the widespread and economically viable extraction of natural gas from shale rock formations [107]. Inexpensive ethane can be derived from available large reservoirs of shale gas located worldwide, being the largest shale gas reserves found in China, Argentina, Algeria, United States, Canada, Saudi Arabia, and Mexico [108–113]. In the United States, it has been estimated shale gas reserves will last for at least 80 more years [114], while in Saudi Arabia the Jafurah shale gas field project claims to become the third largest gas producer by 2030 [115,116]. The conventional industrial processes that utilize ethane as feedstock and the emerging alternative technologies are presented in the following sections.

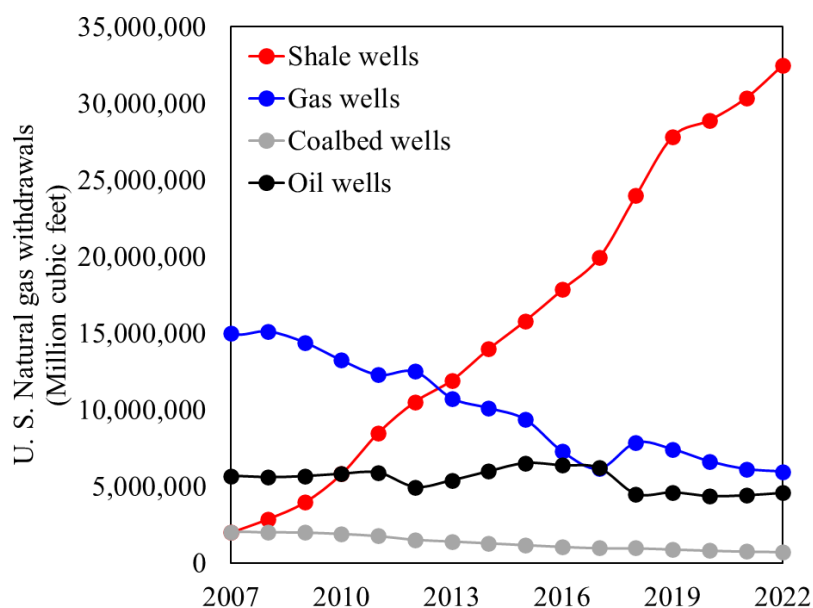


Figure 1.4. Natural gas withdrawals in the U.S. from difference well sources between 2007 – 2022 [4].

1.5.1 Steam cracking of ethane

Before fracking revolutionized the way natural gas was produced in the United States, most steam cracking furnaces used naphtha, i.e., a mixture of hydrocarbons derived from crude oil, as the primary feedstock. The introduction of large supplies of inexpensive and plentiful shale gas rich in ethane [49] into the market resulted in the ethylene industry switching from naphtha to ethane [117]. Moreover, when naphtha is considered as feedstock, products such as propylene, 1,3-butadiene, and aromatic hydrocarbons are also produced [118]. This causes an extra energy-intensive step in the process for the separation of ethylene [92].

At present, steam cracking is the most used process for ethylene production [118], but also the single most energy-consuming process in the chemical industry [66]. This high energy consumption stems from the steam production and the heating of the cracking furnaces. In the steam cracking of ethane, see Eq. (1.7), ethane is mixed with steam to supply the needed heat to reach the reaction temperature needed for the reaction to proceed ($> 800\text{ }^{\circ}\text{C}$).



Then, ethane pyrolysis proceeds through a radical chain mechanism leading to the formation of methane, ethylene, C_3 species and heavier hydrocarbons [118,119]. Nonetheless, coke is also formed during steam cracking of ethane, decreasing the efficiency for ethylene production [120,121], and generating several difficulties on the reactor operation, i.e., pressure

drop and decrease in heat flux [122]. This leads to a periodic decoking of the reactor every 20 – 60 days [121,123].

The issues related to the high endothermicity of the process, which leads to a negative economic and environmental impact, as well as coking issues, led to researchers to investigate and develop alternative technologies, with lower energy consumption for the valorization of ethane. Some of them are discussed here.

1.5.2 Ethane Dehydroaromatization (EDA)

Ethane dehydroaromatization (EDA) is a non-oxidative process that converts ethane into valuable aromatic hydrocarbons. Despite that EDA is an endothermic process, see Eq. (1.8), the reaction temperature (600 °C) is 200 °C lower than steam cracking [118]. Nevertheless, this high temperature results into a rapid catalyst deactivation [124–127], which has been the main reason why EDA has not been industrialized unlike the dehydroaromatization of higher alkanes that occurs at lower temperatures (< 500 °C), i.e., the Cyclar process [128,129].



EDA is a promising alternative for the steam cracking because the gaseous reactants are transformed into liquid products readily available for separation, storage and transportation, but its industrialization seems to be far as no stable catalyst that can operate at higher temperatures (> 600 °C) has been developed yet [118].

1.5.3 Oxidative Dehydrogenation of Ethane (ODH)

The Oxidative Dehydrogenation of Ethane (ODH), studied together with other paraffin oxidations for more than 60 years [130], is an exothermic reaction to produce ethylene, see Eq. (1.9).



Recent developments on catalysts that are highly selective to ethylene (> 90%) and the lower energy demand in comparison with conventional steam cracking makes ODH a promising alternative reaction in the petrochemical industry for ethylene production. In fact, some contributions from our research group have demonstrated that Ni and V-based multi-

metallic materials [131–134] are some of the most promising catalysts because of their high ethane reactivity at relatively low temperatures ($< 500\text{ }^{\circ}\text{C}$), and high selectivity to ethylene ($> 90\%$). Moreover, the oxidative nature of the reaction, makes in situ decoking possible by oxidizing the carbon deposits [135,136]. Nonetheless, despite the several advantages of ODH, the highly exothermic partial and total oxidations, i.e., CO_x formation, are also thermodynamically favored [131–133,135], see Eqs (1.10) – (1.11), respectively, and can therefore not be excluded when considering ODH.



Recently, ODH has been commercialized by Linde with the name of EDHOXTM technology [137]. EDHOXTM converts ethane into ethylene and acetic acid under mild conditions, i.e., $400\text{ }^{\circ}\text{C}$, in a multitubular reactor. The combined selectivity towards ethylene and acetic acid yield is above 93%. Moreover, in 2021 at the Dalian Institute of Chemical Physics (China), ODH technology has been evaluated at pilot plant scale, succeeding the tests, making the ODH process ready for its industrial implementation [138]. These industrial implementations are clear examples that the multitubular ODH reactor is the upcoming alternative technology for ethylene production from unexpensive rich-ethane sources, such as shale gas. However, a reliable pseudo-continuous model for the ODH multitubular packed bed reactor, accurately accounting for all the phenomena occurring during its performance, i.e., intrinsic kinetics and transport phenomena, has not been developed yet [19,132,139–144]. This is crucial for its safe operation and design, control, optimization and intensification.

1.6 Packed bed reactor

Wall-cooled packed bed catalytic reactors with a low tube to particle diameter ratio ($d_t/d_p < 8 \text{ m}_r \text{ m}_s^{-1}$) have been a workhorse in the petrochemical industry for the production of chemical building blocks via the selective oxidation of different hydrocarbons, e.g., o-xylene oxidation [139,145], ethylene oxidation [146,147] and ODH [19,142,148]. Unlike packed bed reactors with a high d_t/d_p ratio ($> 8 \text{ m}_r \text{ m}_s^{-1}$), the low d_t/d_p ratio allows a high contact surface between the packing and the cooling source, as well as the reactor geometrical configuration. This favors the heat transfer dissipation from highly exothermic reactions operated under non-adiabatic and non-isothermal conditions. Although this type of reactor has been studied for

several decades [139,149–153], the main challenge that still needs to be addressed is the minimization of the extent of undesired total oxidation reactions that lead to hot spots and runaway situations. Moreover, there is a high dependency on the operating conditions towards the generation of temperature and concentration gradients [154–156]. It should be mentioned that thermal runaway is defined as a rapid increase in the temperature and pressure due to continuously increasing rate of heat generation. The rate of heat generation increases exponentially with the temperature, contrarily the removed heat increases only linearly with it. The risk of thermal runaway occurs is actually the risk of losing the control of chemical reactions which take place in the system e.g., triggering a runaway reaction. A reaction runaway may have multiple consequences where the worst case is the explosion of reactor. Despite there is not a general agreement on thermal runaway criteria (most criteria are based on the balance between the generated and removed heat), the appearance of an inflection point preceding the temperature maximum in the reactor is considered a key criterion for defining a runaway situation. The inflection point, where the second derivative of the temperature with respect to the reactor length becomes negative, signifies the onset of a positive feedback loop where the temperature and pressure are rapidly increasing in an uncontrolled manner.

Two main crucial aspects are identified for the reliable design of a packed bed reactor with low d_t/d_p ratio ($< 8 m_r m_s^{-1}$): (i) the description of intrinsic kinetics [157] (ii) and transport phenomena, mainly heat transfer and fluid dynamics [19,142,158]. Special attention has been focused on the development, synthesis and understanding of a catalytic material for the ODH in the last decades. In fact, different reliable intrinsic kinetic models have been developed and validated within our research group for promising Ni-based [133,134,148,157,159] and V-based [131,132] materials, as well as in the literature [138,160,161]. Nevertheless, the aspects related to the effect fluid dynamics and heat transfer have on the highly exothermic reaction performance within a packed bed reactor with low d_t/d_p are still not clear.

With the technological advances in the last two decades, Computation Fluid Dynamics (CFD) has become a strong engineering tool to describe two or three dimensional space distribution of the velocity field, temperature and concentration within a packed bed reactor. Research has been focused towards hydrodynamics and heat transfer modeling in absence of reaction [162–175], and their impact under reaction conditions [176–190], i.e., catalytic reactor model. Despite the efforts done so far on CFD, an industrial wall cooled catalytic reactor model, presenting a large tube length ($> 2 m_r$) and a low d_t/d_p , has not been applied. The main issue is the high time consuming an accurate 3D model accounting for industrial operating conditions has, which leads to oversimplifications on the models [178–180,184,191].

This situation demands simplified but effective and reliable solutions to model an industrial packed bed reactor accounting for the role of kinetics and transport phenomena, i.e., hydrodynamics and heat transfer, especially for its conceptual design, control or optimization [139,142].

1.6.1 Fluid Dynamics

Traditionally, fluid dynamics has been neglected when modeling a wall-cooled packed bed reactor [15,19,132,143,147,154,192]. Nevertheless, due to the low d_t/d_p configuration, void fraction profiles within the packed bed are generated, which leads to velocity profiles that affect the convective heat and mass transfer [145,193]. Thus, fluid dynamics plays an essential role on packed bed reactor performances, i.e., prediction of the temperature and concentration profiles [142,158,163,164,194–196].

Fluid dynamics within packed beds with low d_t/d_p ratio have been described by Navier-Stokes-Darcy-Forchheimer (NSDF) [139,158,197–200], Brinkman-Darcy-Forchheimer (BDF) based models [18,194,201], and two-zones based models [142,202]. Moreover, fluid dynamics has been coupled to the heat and mass transfer governing equations to predict the temperature and concentration profiles, respectively, in wall-cooled packed bed reactors [139,142]. Notwithstanding, most of these models are not conservative [19,132,139], which can be attributed to the methodology implemented to determine momentum transfer parameters. For example, the effective viscosity (μ_{eff}), which accounts for the effect of solid surfaces on fluid dynamics near the reactor wall, and the parameters α and β from Ergun's equation, see (1.12), which take the solid–fluid interactions at the core of the reactor into account [5].

$$\frac{\Delta P_z}{L} = \alpha \frac{u_z \mu_f (1 - \varepsilon(r))^2}{d_p^2 \varepsilon(r)^3} + \beta \frac{\rho_f u_z^2 (1 - \varepsilon(r))}{d_p \varepsilon(r)^3} \quad (1.12)$$

1.6.2 Heat transfer

Heat released by highly exothermic reaction within a packed bed reactor generates hot spots which, in turn, induce catalyst deactivation and selectivity losses. Because of the presence of total oxidations, the wall-cooled packed bed reactor, is highly sensitive to operating conditions such as the coolant temperature, inlet gas temperature and reactants concentration [19,203–206]. Research efforts, aiming at improving the performance of the wall-cooled packed bed reactor with low d_t/d_p (< 8), have been focused on developing pseudo-continuous

models to design [18,151,159,207–212], optimize [147,213–217] or simply understand the complex interaction between transport phenomena and reaction kinetics in wall-cooled packed bed reactors. A diversity of one [10,218,219] and two [18,151,152,193,207–212,220,221] dimensional models, such as homogeneous models [18,19,139,151,152,193,203,207–212,220], pseudo-heterogeneous models [19,147,150,192,207] or heterogeneous models [163,197–199,222,223], have been assessed. Some models (~5%) have accounted for fluid dynamics [139,142], while others (~95 %) follow the conventional plug flow approach [19,132,143,147,159,192,218,219,224,225]. So far, there is no pseudo-continuous model, including the methodology to characterize the corresponding kinetic and transport mechanisms, that can accurately describe the performance of a wall-cooled packed bed reactor [19,132,139,142–144]. Even when, for some systems, reaction kinetics and fluid dynamics have been accurately assessed [142], heat transfer characterization remains the main bottleneck when modeling selective oxidations [139,142].

The reliable model-based design of packed bed reactors with low d_t/d_p ratio, which accounts for the complex interactions of transport phenomena and kinetics, requires a proper description of heat transfer in both axial and radial directions [12,158,207]. This is critical for accurately predicting hot spot and runaway situations. Along with a reliable kinetic and fluid dynamic description, the appropriate description of temperature profiles in the wall-cooled packed bed reactor depends on the acquisition of adequate heat transfer parameters: axial effective thermal conductivity, $k_{\text{eff},z}$; radial effective thermal conductivity, $k_{\text{eff},r}$; internal wall heat transfer coefficient, $h_{w,\text{in}}$; external wall heat transfer coefficient, $h_{w,\text{ext}}$; and wall heat transfer coefficient, h_w . Although different methodologies have been proposed for their determination for over 70 years, most of them present several limitations:

- The wall heat transfer coefficient, h_w , lumps the internal heat transfer resistances encountered in the internal heat boundary layer, $\delta_{\text{HT},\text{in}}$, the wall conductivity, k_w , and the heat transfer resistances encountered in the external heat boundary layer, $\delta_{\text{HT},\text{ext}}$ [15,151,210,224,226–230]. Although those mechanisms can be characterized by decoupling the h_w into a $h_{w,\text{in}}$, k_w and $h_{w,\text{ext}}$, respectively, the role of each parameter in the region near the wall of the packed bed reactor, i.e., the heat transfer resistances, is not clear [231].
- The parameters h_w and $k_{\text{eff},r}$ are rarely determined while accounting for fluid dynamics [132,142,151,158,210]. Normally, they are determined considering the plug flow approach [15,207,218,219,224,226–228,230,232–234].

- Experimental observations in absence of reaction and non-weighted regression are used for the estimation of h_w and $k_{eff,r}$, presenting a high statistical correlation [15,132,151,207,230,232,235], making them unreliable for modeling purposes.
- Temperature gradients generated during experiments in absence of reaction for determining the heat transfer parameters are lower than those observed under reaction conditions [11,15,163,207,218,227,236].
- When neglecting the use of h_w , $k_{eff,r}$ is determined but the effect of fluid dynamics on this parameter is neglected [236,237]. Moreover, the effect of the external wall (coolant side) heat transfer resistance on temperature profiles is neglected.
- The impact of $k_{eff,z}$ has been assessed on configurations with high tube-to-particle diameter ratios ($d_t/d_p \gg 8 \text{ m}_r \text{ m}_s^{-1}$) operated at conditions not leading to hot spots, e.g., moderately exothermic reactions [11,13,238].
- Historically, in absence of reaction, the role of axial heat transfer by conduction in a packed bed with a low d_t/d_p ratio under industrial operating conditions, i.e., at high Re_p , (>700) and large L/d_p ratios ($>50 \text{ m}_r \text{ m}_s^{-1}$), has been neglected [151,218,224,230].
- In the best scenario, the effect of $k_{eff,z}$ has been considered but not appropriately addressed, i.e., it has typically been investigated at a low Re_p (< 700) [12,204,239,240].
- Under reaction conditions, the axial conductivity has been disregarded from the reactor model [145,147,154,193,225,241], while in a few studies that have considered it, $k_{eff,z}$ is calculated using literature correlations that were developed under conditions that differ significantly from the industrially relevant ones, i.e., $Re_p < 700$ and $d_t/d_p > 8 \text{ m}_r \text{ m}_s^{-1}$ [19,132,242–246].
- When reactor simulated temperature profiles are compared with experimentally measured ones, typically an overprediction of the hot spot temperature and misprediction of the hot spot location are obtained [247–249]. Thus, although neglecting the effect of $k_{eff,z}$ in the modeling of low d_t/d_p ratio ($< 8 \text{ m}_r \text{ m}_s^{-1}$) industrial-scale packed bed reactors is a common practice, some researchers have claimed that $k_{eff,z}$ should be considered for highly exothermic reactions [250,251].

1.7 Scope and outline of the thesis

The research presented in this thesis encompasses two fundamental processes that attracts significant attention within the framework of the circular economy for hydrocarbons: the Oxidative Conversion of Methane (OCoM) and the Oxidative Dehydrogenation of Ethane

(ODH). The aim is to not only comprehend these processes in-depth but also to contribute valuable insights that can further enhance their efficiency and sustainability.

Chapter 2 explores the OCoM reactor, within the C123 process, accounting for an experimental campaign conducted to examine the performance of the MnNaW/SiO₂ catalyst under relevant industrial operating conditions. The temperature, total pressure, and CH₄/O₂ inlet molar ratio are carefully controlled within the range of 800 – 850 °C, 100 kPa, and 3 to 5 mol mol⁻¹, respectively. The outcomes of this campaign form the basis for the development and validation of a kinetic model, crucial for gaining a deep understanding of OCoM. Subsequently, the viability of the OCoM reactor under different feedstocks is evaluated assessing its potential for methane valorization. Natural gas, shale gas, and biogas, each representing varying compositions and characteristics, are analyzed to understand how they influence the carbon yields in the form of ethylene and CO. This assessment is a critical component of this research, contributing not only to the academic understanding but also to the practical application of OCoM and its potential in a circular economy for hydrocarbons. Furthermore, the C123 process considerations, particularly accounting for the recycling of the effluents, are assessed ensuring the efficient utilization of methane sources, and the sustainable production of C₂ and C₃ species.

The research widens its scope to encompass a groundbreaking approach to heat transfer modeling in wall-cooled packed bed reactors with a low d_i/d_p ratio. **Chapter 3** introduces experimental and theoretical methodologies to determine axial and radial heat transfer parameters that characterize the heat transfer mechanisms for a packed bed reactor with low d_i/d_p . The temperature gradients, a common challenge in industrial-scale reactors, are examined to derive an innovative pseudo-local approach that properly accounts for fluid dynamics on the radial heat transfer mechanisms. This approach overcomes the aforementioned limitations found in conventional methods enhancing the modeling of heat transfer, particularly in zones characterized by high void fractions, including the crucial wall zone. This allows providing insights for a more reliable description of heat transfer, both at the internal and external walls of the packed bed reactor.

Moreover, the impact of axial thermal conductivity is addressed under relevant industrial operating conditions. Axial effective axial thermal conductivities are determined through a proper experimental design in absence of reaction in a bench-scale packed bed operated in adiabatic mode (radial temperature uniformity). Next, the impact of the effective axial thermal conductivity in a non-isothermal bench-scale and industrial-scale packed bed in absence of reaction is assessed by comparison of the experimental temperature profile with the

simulated ones using different correlations for $k_{\text{eff},z}$, i.e., (i) the most widely used one developed by Yagi et al. [11], (ii) the generic one developed by Votruba et al. at Re_p up to 1000 for a packed bed with $4 \text{ m}_r \text{ m}_s^{-1} < d_t/d_p < 56 \text{ m}_r \text{ m}_s^{-1}$ [10], and (iii) the specific one developed in this work.

Chapter 4 addresses the impact of the axial conduction and the novel heat transfer approach developed in Chapter 3, under exothermic reaction conditions setting a high standard for modeling accuracy in packed bed reactors. The ODH reaction over a MoVTeNbO/TiO₂ catalyst serves as a case study, emphasizing the importance of understanding and accurately modeling heat transfer within reactors. The developed pseudo-local approach is compared and evaluated with the conventional heat transfer modeling approaches which are generally applied to describe the performance of highly exothermic reactions in packed bed reactors with a d_t/d_p lower than $8 \text{ m}_r \text{ m}_s^{-1}$. Finally, the impact of the axial conductivity in the ODH packed bed reactor performance, mainly the prediction of hot spots and thermal runaway, is evaluated considering the three different correlations assessed in Chapter 3.

Last, **Chapter 5** provides the general conclusions of this work. Further proposals regarding potential research on OCoM reactor and the ODH packed bed reactor are also provided.

1.8 References

- [1] IEA, Global Methane Tracker 2023, 2023. <https://www.iea.org/reports/global-methane-tracker-2023> (accessed October 31, 2023).
- [2] Our World in Data, Gas reserves, 2020, (n.d.). <https://ourworldindata.org/grapher/natural-gas-proved-reserves> (accessed October 31, 2023).
- [3] BP, Statistical Review of World Energy 2020 | 69th edition, London, 2020. https://www.bp.com/en/global/corporate/energy-economics/statistical-review-of-world-energy.html#tab_sr-2020 (accessed October 31, 2023).
- [4] U.S. Energy Information Administration, Natural Gas Gross Withdrawals and Production, (2023).
- [5] S. Ergun, Fluid flow through packed columns, Chem Eng Prog 48 (1952) 89–94.
- [6] C. Limberg, Computergenerierte Kugelschüttungen in zylindrischen Röhren als Basis für eine differenzierte Modellierung von Festbettreaktoren, Ph. D. thesis, Ph. D. thesis, Technischen Universität Cottbus, 2002.
- [7] A.R. Morcom, Fluid Flow through granular materials, Transactions of Institution of Chemical Engineering 24 (1946) 30–46.
- [8] B. Eisfeld, K. Schnitzlein, The influence of confining walls on the pressure drop in packed beds, Chem Eng Sci 56 (2001) 4321–4329. [https://doi.org/10.1016/S0009-2509\(00\)00533-9](https://doi.org/10.1016/S0009-2509(00)00533-9).

- [9] A. Hernandez-Aguirre, E. Hernandez-Martinez, F. López-Isunza, C.O. Castillo, Framing a novel approach for pseudo continuous modeling using Direct Numerical Simulations (DNS): Fluid dynamics in a packed bed reactor, *Chemical Engineering Journal* 429 (2022). <https://doi.org/10.1016/j.cej.2021.132061>.
- [10] J. Votruba, V. Hlaváček, M. Marek, Packed bed axial thermal conductivity, *Chem Eng Sci* 27 (1972) 1845–1851. [https://doi.org/10.1016/0009-2509\(72\)85046-2](https://doi.org/10.1016/0009-2509(72)85046-2).
- [11] S. Yagi, D. Kunii, N. Wakao, Studies on axial effective thermal conductivities in packed beds, *AIChE Journal* 6 (1960) 543–546. <https://doi.org/10.1002/aic.690060407>.
- [12] M. Elsari, R. Hughes, Axial effective thermal conductivities of packed beds, *Appl Therm Eng* 22 (2002) 1969–1980. [https://doi.org/10.1016/S1359-4311\(02\)00117-5](https://doi.org/10.1016/S1359-4311(02)00117-5).
- [13] D. Vortmeyer, W. Adam, Steady-state measurements and analytical correlations of axial effective thermal conductivities in packed beds at low gas flow rates, *Int J Heat Mass Transf* 27 (1984) 1465–1472. [https://doi.org/10.1016/0017-9310\(84\)90259-X](https://doi.org/10.1016/0017-9310(84)90259-X).
- [14] R.K. Sharma, D.L. Cresswell, E.J. Newson, Kinetics and fixed-bed reactor modeling of butane oxidation to maleic anhydride, *AIChE Journal* 37 (1991) 39–47. <https://doi.org/10.1002/aic.690370103>.
- [15] L.M.D.M. Jorge, R.M.M. Jorge, R. Giudici, Experimental and numerical investigation of dynamic heat transfer parameters in packed bed, *Heat and Mass Transfer/Waerme- Und Stoffuebertragung* 46 (2010) 1355–1365. <https://doi.org/10.1007/s00231-010-0659-6>.
- [16] R. Bauer, E.U. Schlunder, Effective radial thermal conductivity of packings in gas flow, *Int. Chem. Eng.* 18 (1978) 189–204.
- [17] A.G. Dixon, D.L. Cresswell, Theoretical prediction of effective heat transfer parameters in packed beds, *AIChE Journal* 25 (1979) 663–676. <https://doi.org/10.1002/aic.690250413>.
- [18] O. Bey, G. Eigenberger, Gas flow and heat transfer through catalyst filled tubes, *International Journal of Thermal Sciences* 40 (2001) 152–164. [https://doi.org/10.1016/S1290-0729\(00\)01204-7](https://doi.org/10.1016/S1290-0729(00)01204-7).
- [19] G. Che-Galicia, F. López-Isunza, E. Corona-Jiménez, C.O. Castillo-Araiza, The role of kinetics and heat transfer on the performance of an industrial wall-cooled packed-bed reactor: Oxidative dehydrogenation of ethane, *AIChE Journal* 66 (2020). <https://doi.org/10.1002/aic.16900>.
- [20] IEA, Methane Emissions from Oil and Gas Operations, (2022). <https://www.iea.org/reports/methane-emissions-from-oil-and-gas-operations> (accessed June 26, 2023).
- [21] IEA, Methane emissions from the energy sector are 70% higher than official figures, (2022). <https://www.iea.org/news/methane-emissions-from-the-energy-sector-are-70-higher-than-official-figures> (accessed June 26, 2023).
- [22] European Environment Agency, Methane emissions in the EU: the key to immediate action on climate change, (2022). <https://www.eea.europa.eu/publications/methane-emissions-in-the-eu> (accessed June 26, 2023).
- [23] M. Sharma, S. Joshi, M. Prasad, S. Bartwal, Overcoming barriers to circular economy implementation in the oil & gas industry: Environmental and social implications, *J Clean Prod* 391 (2023) 136133. <https://doi.org/10.1016/j.jclepro.2023.136133>.
- [24] A.H. Jagaba, S.R.M. Kutty, I.M. Lawal, A.H. Birniwa, A.C. Affam, N.S.A. Yaro, A.K. Usman, I. Umaru, S. Abubakar, A. Noor, U.B. Soja, A.S. Yakubu, Circular economy potential and contributions of petroleum industry sludge utilization to environmental sustainability through

- engineered processes - A review, *Cleaner and Circular Bioeconomy* 3 (2022) 100029. <https://doi.org/10.1016/j.clcb.2022.100029>.
- [25] EPA, What is a Circular Economy?, (2023). <https://www.epa.gov/circulareconomy/what-circular-economy> (accessed June 26, 2023).
- [26] The White House, Advancing a Circular Economy to Meet Our Climate, Energy, and Economic Goals, (2023). <https://www.whitehouse.gov/ostp/news-updates/2023/07/05/advancing-a-circular-economy-to-meet-our-climate-energy-and-economic-goals/> (accessed October 6, 2023).
- [27] E. Williams, Saudi G20 creates platform for circular carbon economy, (2020). <https://www.arabnews.com/node/1759851> (accessed October 6, 2023).
- [28] M. Al-Surf, SAUDI'S CIRCULAR ECONOMY ROADMAP, (2022). <https://www.linkedin.com/pulse/saudis-circular-economy-roadmap-dr-mohammed-al-surf/> (accessed October 6, 2023).
- [29] European Commission, The European Green Deal, (2019). https://commission.europa.eu/strategy-and-policy/priorities-2019-2024/european-green-deal_en (accessed October 18, 2023).
- [30] European Parliament, REPORT on an EU strategy to reduce methane emissions, (2021). https://www.europarl.europa.eu/doceo/document/A-9-2021-0277_EN.html (accessed June 26, 2023).
- [31] European Commission, Circular economy action plan, (2020). https://environment.ec.europa.eu/strategy/circular-economy-action-plan_en (accessed October 18, 2023).
- [32] EU, Commission presents its evaluation of the 7th Framework Programme for Research, (2016). https://ec.europa.eu/commission/presscorner/detail/de/MEMO_16_146 (accessed June 26, 2023).
- [33] EU, Horizon 2020, (2017). https://www.eeas.europa.eu/eeas/horizon-2020_en (accessed June 26, 2023).
- [34] U.S. Energy Information Administration (EIA), Natural gas explained, (2023). <https://www.eia.gov/energyexplained/natural-gas/use-of-natural-gas.php> (accessed October 9, 2023).
- [35] BP, Statistical Review of World Energy 2021 | 70th edition, London, 2021. <https://www.bp.com/content/dam/bp/business-sites/en/global/corporate/pdfs/energy-economics/statistical-review/bp-stats-review-2021-natural-gas.pdf> (accessed October 10, 2023).
- [36] International Energy Agency, Gas, (2023). <https://www.iea.org/fuels-and-technologies/gas> (accessed June 26, 2023).
- [37] V. Litvinenko, The Role of Hydrocarbons in the Global Energy Agenda: The Focus on Liquefied Natural Gas, *Resources* 9 (2020) 59. <https://doi.org/10.3390/resources9050059>.
- [38] J. Speight, Gas and oil in tight formations, in: *Shale Oil and Gas Production Processes*, Elsevier, 2020: pp. 3–64. <https://doi.org/10.1016/B978-0-12-813315-6.00001-4>.
- [39] U.S. Energy Information Administration (EIA), Glossary, (n.d.). <https://www.eia.gov/tools/glossary/> (accessed October 9, 2023).
- [40] U.S. Department of Energy, National Energy Technology Laboratory, STRANDED NATURAL GAS ROADMAP, 2020. <https://netl.doe.gov/sites/default/files/2020-12/Stranded-Natural-Gas-Roadmap-04142020.pdf> (accessed October 9, 2023).

- [41] V.K. Kudapa, K.A. Suriya Krishna, Heavy oil recovery using gas injection methods and its challenges and opportunities, *Mater Today Proc* (2023). <https://doi.org/10.1016/j.matpr.2023.05.091>.
- [42] L. Dong, S. Wei, S. Tan, H. Zhang, GTL or LNG: which is the best way to monetize “stranded” natural gas?, *Pet Sci* 5 (2008) 388–394. <https://doi.org/10.1007/s12182-008-0063-8>.
- [43] Environmental Defense Fund, By the numbers: Marginal oil and gas wells, 2021. https://www.edf.org/sites/default/files/documents/MarginalWellFactsheet2021_0.pdf (accessed October 9, 2023).
- [44] The Biogas Handbook, Elsevier, 2013. <https://doi.org/10.1533/9780857097415>.
- [45] F. Ardolino, G.F. Cardamone, F. Parrillo, U. Arena, Biogas-to-biomethane upgrading: A comparative review and assessment in a life cycle perspective, *Renewable and Sustainable Energy Reviews* 139 (2021) 110588. <https://doi.org/10.1016/j.rser.2020.110588>.
- [46] S. Zendejboudi, A. Bahadori, Shale Gas, in: *Shale Oil and Gas Handbook*, Elsevier, 2017: pp. 1–26. <https://doi.org/10.1016/B978-0-12-802100-2.00001-0>.
- [47] D. ZHANG, T. YANG, Environmental impacts of hydraulic fracturing in shale gas development in the United States, *Petroleum Exploration and Development* 42 (2015) 876–883. [https://doi.org/10.1016/S1876-3804\(15\)30085-9](https://doi.org/10.1016/S1876-3804(15)30085-9).
- [48] P. V. Snytnikov, D.I. Potemkin, S.I. Uskov, A. V. Kurochkin, V.A. Kirillov, V.A. Sobyenin, Approaches to Utilizing Flare Gases at Oil and Gas Fields: A Review, *Catal Ind* 10 (2018) 202–216. <https://doi.org/10.1134/S207005041803011X>.
- [49] A. Demirbas, N. Cek, S. Acar, Chemical analyses of shale gas and conventional natural gas, *Pet Sci Technol* 36 (2018) 1690–1695. <https://doi.org/10.1080/10916466.2018.1504070>.
- [50] Z.I. S G Adiya, V. Dupont, T. Mahmud, Steam reforming of shale gas in a packed bed reactor with and without chemical looping using nickel based oxygen carrier, *Int J Hydrogen Energy* 43 (2018) 6904–6917. <https://doi.org/10.1016/j.ijhydene.2018.02.083>.
- [51] J. Motte, M. Mahmoud, M. Nieder-Heitmann, H. Vleeming, J.W. Thybaut, J. Poissonnier, R.A.F. Alvarenga, P. Nachtergaele, J. Dewulf, Environmental Performance Assessment of a Novel Process Concept for Propanol Production from Widely Available and Wasted Methane Sources, *Ind Eng Chem Res* 61 (2022) 11071–11079. <https://doi.org/10.1021/acs.iecr.2c00808>.
- [52] R. Franz, E.A. Uslamin, E.A. Pidko, Challenges for the utilization of methane as a chemical feedstock, *Mendeleev Communications* 31 (2021) 584–592. <https://doi.org/10.1016/j.mencom.2021.09.002>.
- [53] A.A. Fonseca, R.H. Heyn, M. Frøseth, J.W. Thybaut, J. Poissonnier, A. Meiswinkel, H.-J. Zander, J. Canivet, A Disruptive Innovation for Upgrading Methane to C3 Commodity Chemicals : Technical challenges faced by the C123 European consortium, *Johnson Matthey Technology Review* 65 (2021) 311–329. <https://doi.org/10.1595/205651321X16051060155762>.
- [54] A. Abánades, Natural Gas Decarbonization as Tool for Greenhouse Gases Emission Control, *Front Energy Res* 6 (2018). <https://doi.org/10.3389/fenrg.2018.00047>.
- [55] H. Song, J. Jarvis, S. Meng, H. Xu, Z. Li, W. Li, Biomass Valorization Under Methane Environment, in: *Methane Activation and Utilization in the Petrochemical and Biofuel Industries*, Springer International Publishing, Cham, 2022: pp. 163–193. https://doi.org/10.1007/978-3-030-88424-6_7.
- [56] R.S. Postma, D.J. Keijsper, B.F. Morsink, E.H. Siegers, M.E.E. Mercimek, L.K. Nieukoop, H. van den Berg, A.G.J. van der Ham, L. Lefferts, Technoeconomic Evaluation of the Industrial

- Implementation of Catalytic Direct Nonoxidative Methane Coupling, *Ind Eng Chem Res* 61 (2022) 566–579. <https://doi.org/10.1021/acs.iecr.1c03572>.
- [57] C. Murkin, J. Brightling, Eighty Years of Steam Reforming, *Johnson Matthey Technology Review* 60 (2016) 263–269. <https://doi.org/10.1595/205651316X692923>.
- [58] J.R. Rostrup-Nielsen, Steam Reforming 1A list of abbreviations/acronyms used in the text is provided at the end of the chapter., in: *Handbook of Heterogeneous Catalysis*, Wiley, 2008: pp. 2882–2905. <https://doi.org/10.1002/9783527610044.hetcat0146>.
- [59] Office of Fossil Energy, *Hydrogen Strategy Enabling A Low-Carbon Economy*, Washington, DC 20585, 2020. https://www.energy.gov/sites/prod/files/2020/07/f76/USDOE_FE_Hydrogen_Strategy_July2020.pdf (accessed October 10, 2023).
- [60] A. Basile, S. Liguori, A. Iulianelli, Membrane reactors for methane steam reforming (MSR), in: *Membrane Reactors for Energy Applications and Basic Chemical Production*, Elsevier, 2015: pp. 31–59. <https://doi.org/10.1016/B978-1-78242-223-5.00002-9>.
- [61] TOPSOE, SynCOR™ - Autothermal Reformer (ATR), (n.d.). <https://www.topsoe.com/our-resources/knowledge/our-products/equipment/syncortm-autothermal-reformer-atr> (accessed October 12, 2023).
- [62] M. Martinelli, M.K. Gnanamani, S. LeViness, G. Jacobs, W.D. Shafer, An overview of Fischer-Tropsch Synthesis: XTL processes, catalysts and reactors, *Appl Catal A Gen* 608 (2020) 117740. <https://doi.org/10.1016/j.apcata.2020.117740>.
- [63] J. Humphreys, R. Lan, S. Tao, Development and Recent Progress on Ammonia Synthesis Catalysts for Haber–Bosch Process, *Advanced Energy and Sustainability Research* 2 (2021). <https://doi.org/10.1002/aesr.202000043>.
- [64] H. Zhang, L. Wang, J. Van herle, F. Maréchal, U. Desideri, Techno-economic comparison of green ammonia production processes, *Appl Energy* 259 (2020) 114135. <https://doi.org/10.1016/j.apenergy.2019.114135>.
- [65] C. Hammond, S. Conrad, I. Hermans, Oxidative Methane Upgrading, *ChemSusChem* 5 (2012) 1668–1686. <https://doi.org/10.1002/cssc.201200299>.
- [66] T. REN, M. PATEL, K. BLOK, Olefins from conventional and heavy feedstocks: Energy use in steam cracking and alternative processes, *Energy* 31 (2006) 425–451. <https://doi.org/10.1016/j.energy.2005.04.001>.
- [67] H. Chen, L. Li, J. Hu, Upgrading of stranded gas via non-oxidative conversion processes, *Catal Today* 310 (2018) 94–97. <https://doi.org/10.1016/j.cattod.2017.05.029>.
- [68] K. Wittich, M. Krämer, N. Bottke, S.A. Schunk, Catalytic Dry Reforming of Methane: Insights from Model Systems, *ChemCatChem* 12 (2020) 2130–2147. <https://doi.org/10.1002/cctc.201902142>.
- [69] N.A.K. Aramouni, J.G. Touma, B.A. Tarboush, J. Zeaiter, M.N. Ahmad, Catalyst design for dry reforming of methane: Analysis review, *Renewable and Sustainable Energy Reviews* 82 (2018) 2570–2585. <https://doi.org/10.1016/j.rser.2017.09.076>.
- [70] C.H.L. Tempelman, E.J.M. Hensen, On the deactivation of Mo/HZSM-5 in the methane dehydroaromatization reaction, *Appl Catal B* 176–177 (2015) 731–739. <https://doi.org/10.1016/j.apcatb.2015.04.052>.
- [71] P. Khirsariya, R.K. Mewada, Single Step Oxidation of Methane to Methanol–Towards Better Understanding, *Procedia Eng* 51 (2013) 409–415. <https://doi.org/10.1016/j.proeng.2013.01.057>.

- [72] D. Lance, H.S. Elworthy, FR Pat., 352687, 1905.
- [73] N.R. Foster, Direct catalytic oxidation of methane to methanol — a review, *Appl Catal* 19 (1985) 1–11. [https://doi.org/10.1016/S0166-9834\(00\)82665-2](https://doi.org/10.1016/S0166-9834(00)82665-2).
- [74] A. Nandy, C. Duan, C. Goffinet, H.J. Kulik, New Strategies for Direct Methane-to-Methanol Conversion from Active Learning Exploration of 16 Million Catalysts, *JACS Au* 2 (2022) 1200–1213. <https://doi.org/10.1021/jacsau.2c00176>.
- [75] G.E. Keller, M.M. Bhasin, Synthesis of ethylene via oxidative coupling of methane. I. Determination of active catalysts, *J Catal* 73 (1982) 9–19. [https://doi.org/10.1016/0021-9517\(82\)90075-6](https://doi.org/10.1016/0021-9517(82)90075-6).
- [76] R. Schmack, A. Friedrich, E. V. Kondratenko, J. Polte, A. Werwatz, R. Kraehnert, A meta-analysis of catalytic literature data reveals property-performance correlations for the OCM reaction, *Nat Commun* 10 (2019). <https://doi.org/10.1038/s41467-019-08325-8>.
- [77] J.W. Thybaut, G.B. Marin, C. Mirodatos, Y. Schuurman, A.C. Van Veen, V.A. Sadykov, H. Pennemann, R. Bellinghausen, L. Mleczko, A novel technology for natural gas conversion by means of integrated oxidative coupling and dry reforming of methane, *Chem Ing Tech* 86 (2014) 1855–1870. <https://doi.org/10.1002/cite.201400068>.
- [78] 7th Framework Programme - Oxidative Coupling of Methane followed by Oligomerization to Liquids, (2009). <https://cordis.europa.eu/project/id/228953>.
- [79] C.E. Bosch, S. Poulston, P. Collier, J.W. Thybaut, G.B. Marin, Exploring microemulsion-prepared lanthanum catalysts for natural gas valorisation, *Johnson Matthey Technology Review* 63 (2019) 265–276. <https://doi.org/10.1595/205651319X15613828987406>.
- [80] E. Korkakaki, S. Walspurger, K. Overwater, H. Nigar, I. Julian, G.D. Stefanidis, S.S. Tharakaraman, D.L. Jurković, Adaptable Reactors for Resource- and Energy-Efficient Methane Valorisation (ADREM), *Johnson Matthey Technology Review* (2020) 298–306. <https://doi.org/10.1595/205651320x15886749783532>.
- [81] P. Bernardo, E. Drioli, Membrane engineering for a sustainable production of ethylene, *Fuel Processing Technology* 212 (2021) 106624. <https://doi.org/10.1016/j.fuproc.2020.106624>.
- [82] European Commission, HORIZON 2020 - MEthane activation via integrated MEMbrane REactors, (2015). <https://cordis.europa.eu/project/id/679933>.
- [83] J.A. Labinger, Oxidative coupling of methane: An inherent limit to selectivity?, *Catal Letters* 1 (1988) 371–375. <https://doi.org/10.1007/BF00766166>.
- [84] H.R. Godini, S. Xiao, S. Jašo, S. Stünkel, D. Salerno, N.X. Son, S. Song, G. Wozny, Techno-economic analysis of integrating the methane oxidative coupling and methane reforming processes, *Fuel Processing Technology* 106 (2013) 684–694. <https://doi.org/10.1016/j.fuproc.2012.10.002>.
- [85] J.H.B.J. Hoebink, H.M. Venderbosch, P.C. van Geem, P.F. Van den Oosterkamp, G.B. Marin, Economics of the oxidative coupling of methane as an add-on unit for naphtha cracking, *Chem Eng Technol* 18 (1995) 12–16. <https://doi.org/10.1002/ceat.270180104>.
- [86] H.R. Godini, M. Azadi, A. Penteado, M. Khadivi, G. Wozny, J.U. Repke, A multi-perspectives analysis of methane oxidative coupling process based on miniplant-scale experimental data, *Chemical Engineering Research and Design* 151 (2019) 56–69. <https://doi.org/10.1016/j.cherd.2019.08.002>.
- [87] X. He, CO<sub>2></sub> Hydrogenation for Ethanol Production: A Thermodynamic Analysis, *International Journal of Oil, Gas and Coal Engineering* 5 (2017) 145. <https://doi.org/10.11648/j.ogce.20170506.14>.

- [88] M.A. Barteau, Is it time to stop searching for better catalysts for oxidative coupling of methane?, *J Catal* 408 (2022) 173–178. <https://doi.org/10.1016/j.jcat.2022.03.006>.
- [89] L. Pirro, P.S.F. Mendes, B.D. Vandegehuchte, G.B. Marin, J.W. Thybaut, Catalyst screening for the oxidative coupling of methane: From isothermal to adiabatic operation: Via microkinetic simulations, *React Chem Eng* 5 (2020) 584–596. <https://doi.org/10.1039/c9re00478e>.
- [90] M. Kim, S. Arndt, M. Yildiz, R. Schomäcker, O. Görke, J.U. Repke, G. Wozny, H.R. Godini, Reaction engineering of oxidative coupling of methane: Experimental observations and analysis of the impacts of operating parameters, *Chemical Engineering Research and Design* 172 (2021) 84–98. <https://doi.org/10.1016/j.cherd.2021.04.029>.
- [91] B. Mokhtarani, J.U. Repke, N.X. Son, G. Wozny, N.M. Yilmaz, K. Senturk, H.R. Godini, Miniplant-Scale Demonstration of Ethylene Adsorption Separation in Downstream of an Oxidative Coupling of Methane Process, *Ind Eng Chem Res* 60 (2021) 11778–11788. <https://doi.org/10.1021/acs.iecr.1c01282>.
- [92] A. Obradović, J.W. Thybaut, G.B. Marin, Oxidative Coupling of Methane: Opportunities for Microkinetic Model-Assisted Process Implementations, *Chem Eng Technol* 39 (2016) 1996–2010. <https://doi.org/10.1002/ceat.201600216>.
- [93] M.W. Erichsen, J.S. Martínez-Espín, Finn. Joensen, U. Olsbye, Chapter 12 Understanding the Mechanisms of Gas to Liquid Processes with the Aid of Quantum Chemistry Tools: Case Studies of the Shilov Reaction and Natural Gas Aromatization, in: *Small-Scale Gas to Liquid Fuel Synthesis*, CRC Press, 2015: pp. 419–444. <https://doi.org/10.1201/b18075-18>.
- [94] J.-L. Dubois, M. Nieder-Heitmann, A. Letoffet, H. Vleeming, C123 - Methane Oxidative Conversion and Hydroformylation to Propylene : Raw material sources and market analyses of the modular route C3 products, *Johnson Matthey Technology Review* 65 (2021) 301–310. <https://doi.org/10.1595/205651321X16051080751506>.
- [95] Business analytiq, Polypropylene price index, (2023). <https://businessanalytiq.com/procurementanalytics/index/polypropylene-price-index/> (accessed November 13, 2023).
- [96] Markets and Markets, Polymethyl Methacrylate (PMMA) Market by Grade, Form, End-Use Industry & Region - Global Forecast to 2027, 2022. <https://www.marketsandmarkets.com/Market-Reports/polymethyl-methacrylate-pmma-market-715.html> (accessed November 13, 2023).
- [97] Markets and Markets, Acrylic Acid Market by Derivative, Acrylic Ester/Polymer Application & Region - Global Forecast 2028, 2023. <https://www.marketsandmarkets.com/Market-Reports/acrylic-acid-market-683.html> (accessed November 13, 2023).
- [98] S. Siradze, J. Poissonnier, M. Frøseth, R.E. Stensrød, R.H. Heyn, J.W. Thybaut, Kinetics Assessment of the Homogeneously Catalyzed Hydroformylation of Ethylene on an Rh Catalyst, *Ind Eng Chem Res* 60 (2021) 16665–16681. <https://doi.org/10.1021/acs.iecr.1c02572>.
- [99] T.P. Tiemersma, M.J. Tuinier, F. Gallucci, J.A.M. Kuipers, M.V.S. Annaland, A kinetics study for the oxidative coupling of methane on a Mn/Na 2WO 4/SiO 2 catalyst, *Appl Catal A Gen* 433–434 (2012) 96–108. <https://doi.org/10.1016/j.apcata.2012.05.002>.
- [100] J.S. Ahari, M.T. Sadeghi, S. Zarrinpashne, Effects of operating parameters on oxidative coupling of methane over Na-W-Mn/SiO₂ catalyst at elevated pressures, *Journal of Natural Gas Chemistry* 20 (2011) 204–213. [https://doi.org/10.1016/S1003-9953\(10\)60167-3](https://doi.org/10.1016/S1003-9953(10)60167-3).
- [101] Y. Gao, L. Neal, D. Ding, W. Wu, C. Baroi, A.M. Gaffney, F. Li, Recent Advances in Intensified Ethylene Production - A Review, *ACS Catal* 9 (2019) 8592–8621. <https://doi.org/10.1021/acscatal.9b02922>.

- [102] S. Arndt, T. Otremba, U. Simon, M. Yildiz, H. Schubert, R. Schomäcker, Mn-Na 2WO₄/SiO₂ as catalyst for the oxidative coupling of methane. What is really known?, *Appl Catal A Gen* 425–426 (2012) 53–61. <https://doi.org/10.1016/j.apcata.2012.02.046>.
- [103] G. Lezcano, V.K. Velisoju, S.R. Kulkarni, A. Ramirez, P. Castaño, Engineering Thermally Resistant Catalytic Particles for Oxidative Coupling of Methane Using Spray-Drying and Incorporating SiC, *Ind Eng Chem Res* 60 (2021) 18770–18780. <https://doi.org/10.1021/acs.iecr.1c02802>.
- [104] G. Lezcano, S.R. Kulkarni, V.K. Velisoju, V.E. Musteata, I. Hita, A. Ramirez, A. Dikhtiarenko, J. Gascon, P. Castaño, Effect of the particle blending-shaping method and silicon carbide crystal phase for Mn-Na-W/SiO₂-SiC catalyst in oxidative coupling of methane, *Molecular Catalysis* 527 (2022). <https://doi.org/10.1016/j.mcat.2022.112399>.
- [105] B.A. Rodriguez, W.J. Tenn, Direct formation of propanol from a dilute ethylene feed via reductive-hydroformylation using homogeneous rhodium catalysts at low feed pressures, *Appl Catal A Gen* 421–422 (2012) 161–163. <https://doi.org/10.1016/j.apcata.2012.02.013>.
- [106] I. Amghizar, L.A. Vandewalle, K.M. Van Geem, G.B. Marin, New Trends in Olefin Production, *Engineering* 3 (2017) 171–178. <https://doi.org/10.1016/J.ENG.2017.02.006>.
- [107] R.S. Middleton, R. Gupta, J.D. Hyman, H.S. Viswanathan, The shale gas revolution: Barriers, sustainability, and emerging opportunities, *Appl Energy* 199 (2017) 88–95. <https://doi.org/10.1016/j.apenergy.2017.04.034>.
- [108] F. Aloulou, Mexico’s shale-rich Burgos Basin opens to private investment for the first time, *Today in Energy - U.S. Energy Information Administration* (2017). <https://www.eia.gov/todayinenergy/detail.php?id=32592> (accessed October 19, 2023).
- [109] Shale oil and shale gas resources are globally abundant, *Today in Energy - U.S. Energy Information Administration* (2013). <https://www.eia.gov/todayinenergy/detail.php?id=11611> (accessed October 19, 2023).
- [110] F. Aloulou, Algeria is reforming its laws to attract foreign investment in hydrocarbons, *Today in Energy - U.S. Energy Information Administration* (2015). <https://www.eia.gov/todayinenergy/detail.php?id=22352> (accessed October 19, 2023).
- [111] F. Aloulou, V. Zaretskaya, Growth in Argentina’s Vaca Muerta shale and tight gas production leads to LNG exports, *Today in Energy - U.S. Energy Information Administration* (2019). <https://www.eia.gov/todayinenergy/detail.php?id=40093> (accessed October 19, 2023).
- [112] V. Zaretskaya, F. Aloulou, China’s natural gas consumption and LNG imports declined in 2022, amid zero-COVID policies, *Today in Energy - U.S. Energy Information Administration* (2023). <https://www.eia.gov/todayinenergy/detail.php?id=56680> (accessed October 19, 2023).
- [113] Saudi Arabia’s \$100bn plan to become largest shale gas producer outside of the US, *Arab News* (2021). <https://www.arabnews.com/node/1978471/business-economy> (accessed October 19, 2023).
- [114] U.S. Energy Information Administration, How much natural gas does the United States have, and how long will it last?, (2023). <https://www.eia.gov/tools/faqs/faq.php?id=58&t=8#:~:text=Assuming%20the%20same%20annual%20rate,gas%20TRR%20in%20future%20years.> (accessed October 17, 2023).
- [115] R. El Gamal, S. Webb, Saudi Aramco launches largest shale gas development outside U.S., *Reuters* (2020). <https://www.reuters.com/article/us-saudi-shale-gas/saudi-aramco-launches-largest-shale-gas-development-outside-u-s-idUSKCN20I29A> (accessed October 17, 2023).

- [116] A. Gray, Jafurah: the jewel of our unconventional gas program, Aramco (2022). <https://www.aramco.com/en/magazine/elements/2022/jafurah-the-jewel-of-our-unconventional-gas-program> (accessed October 17, 2023).
- [117] P. Thiruvenkataswamy, F.T. Eljack, N. Roy, M.S. Mannan, M.M. El-Halwagi, Safety and techno-economic analysis of ethylene technologies, *J Loss Prev Process Ind* 39 (2016) 74–84. <https://doi.org/10.1016/j.jlp.2015.11.019>.
- [118] H. Saito, Y. Sekine, Catalytic conversion of ethane to valuable products through non-oxidative dehydrogenation and dehydroaromatization, *RSC Adv* 10 (2020) 21427–21453. <https://doi.org/10.1039/d0ra03365k>.
- [119] F.O. Rice, K.F. Herzfeld, The thermal decomposition of organic compounds from the standpoint of free radicals. VI. The mechanism of some chain reactions, *J Am Chem Soc* 56 (1934) 284–289.
- [120] G.F. Froment, B.O. Van de Steene, P.S. Van Damme, S. Narayanan, A.G. Goossens, Thermal Cracking of Ethane and Ethane-Propane Mixtures, *Industrial & Engineering Chemistry Process Design and Development* 15 (1976) 495–504.
- [121] K.M. Sundaram, P.S. Van Damme, G.F. Froment, Coke deposition in the thermal cracking of ethane, *AIChE Journal* 27 (1981) 946–951. <https://doi.org/10.1002/aic.690270610>.
- [122] S. Mahamulkar, K. Yin, P.K. Agrawal, R.J. Davis, C.W. Jones, A. Malek, H. Shibata, Formation and Oxidation/Gasification of Carbonaceous Deposits: A Review, *Ind Eng Chem Res* 55 (2016) 9760–9818. <https://doi.org/10.1021/acs.iecr.6b02220>.
- [123] S.H. Symoens, N. Olahova, A.E. Muñoz Gandarillas, H. Karimi, M.R. Djokic, M.-F. Reyniers, G.B. Marin, K.M. Van Geem, State-of-the-art of Coke Formation during Steam Cracking: Anti-Coking Surface Technologies, *Ind Eng Chem Res* 57 (2018) 16117–16136. <https://doi.org/10.1021/acs.iecr.8b03221>.
- [124] Y. Xiang, H. Wang, J. Cheng, J. Matsubu, Progress and prospects in catalytic ethane aromatization, *Catal Sci Technol* 8 (2018) 1500–1516. <https://doi.org/10.1039/C7CY01878A>.
- [125] A. HAGEN, F. ROESSNER, Ethane to Aromatic Hydrocarbons: Past, Present, Future, *Catalysis Reviews* 42 (2000) 403–437. <https://doi.org/10.1081/CR-100101952>.
- [126] M.A. Bañares, Supported metal oxide and other catalysts for ethane conversion: a review, *Catal Today* 51 (1999) 319–348. [https://doi.org/10.1016/S0920-5861\(99\)00053-X](https://doi.org/10.1016/S0920-5861(99)00053-X).
- [127] Y. Ono, Transformation of Lower Alkanes into Aromatic Hydrocarbons over ZSM-5 Zeolites, *Catalysis Reviews* 34 (1992) 179–226. <https://doi.org/10.1080/01614949208020306>.
- [128] J.H. Gregor, C.D. Gosling, H.E. Fullerton, Upgrading Fischer-Tropsch LPG (liquefied petroleum gas) with the Cyclar process, Pittsburgh, PA, and Morgantown, WV (United States), 1989. <https://doi.org/10.2172/7171062>.
- [129] J. Alper, ed., *The Changing Landscape of Hydrocarbon Feedstocks for Chemical Production*, National Academies Press, Washington, D.C., 2016. <https://doi.org/10.17226/23555>.
- [130] P.H. Calderbank, V.P. Hovnanian, F.D.F. Talbot, The autothermic cracking of light hydrocarbons, *Journal of Applied Chemistry* 7 (1957) 425–431. <https://doi.org/10.1002/jctb.5010070802>.
- [131] G. Che-Galicia, R. Quintana-Solórzano, R.S. Ruiz-Martínez, J.S. Valente, C.O. Castillo-Araiza, Kinetic modeling of the oxidative dehydrogenation of ethane to ethylene over a MoVTaNbO catalytic system, *Chemical Engineering Journal* 252 (2014) 75–88. <https://doi.org/10.1016/j.cej.2014.04.042>.

- [132] G. Che-Galicia, R.S. Ruiz-Martínez, F. López-Isunza, C.O. Castillo-Araiza, Modeling of oxidative dehydrogenation of ethane to ethylene on a MoVTeNbO/TiO₂ catalyst in an industrial-scale packed bed catalytic reactor, *Chemical Engineering Journal* 280 (2015) 682–694. <https://doi.org/10.1016/j.cej.2015.05.128>.
- [133] C. Alvarado-Camacho, J. Poissonnier, J.W. Thybaut, C.O. Castillo, Unravelling the redox mechanism and kinetics of a highly active and selective Ni-based material for the oxidative dehydrogenation of ethane, *React Chem Eng* (2022). <https://doi.org/10.1039/d1re00275a>.
- [134] E. Moreno-barrueta, C. Alvarado-camacho, J.F. Dur, A. Morales-p, C.O. Castillo, On the dynamics of the catalytic surface of a bimetallic mixed-oxide formulation during the oxidative dehydrogenation of ethane, *Catal Today* (2021). <https://doi.org/10.1016/j.cattod.2021.07.028>.
- [135] F. Cavani, N. Ballarini, A. Cericola, Oxidative dehydrogenation of ethane and propane: How far from commercial implementation?, *Catal Today* 127 (2007) 113–131. <https://doi.org/10.1016/j.cattod.2007.05.009>.
- [136] S. Najari, S. Saedi, P. Concepcion, D.D. Dionysiou, S.K. Bhargava, A.F. Lee, K. Wilson, Oxidative dehydrogenation of ethane: Catalytic and mechanistic aspects and future trends, *Chem Soc Rev* 50 (2021) 4564–4605. <https://doi.org/10.1039/d0cs01518k>.
- [137] Linde, EDHOX™ technology, (2021). <https://www.linde-engineering.com/en/process-plants/petrochemical-plants/edhox-technology/index.html> (accessed October 16, 2023).
- [138] Y. Chen, B. Yan, Y. Cheng, State-of-the-Art Review of Oxidative Dehydrogenation of Ethane to Ethylene over MoVNbTeO_x Catalysts, *Catalysts* 13 (2023) 204. <https://doi.org/10.3390/catal13010204>.
- [139] C.O. Castillo-Araiza, F. López-Isunza, Modeling the partial oxidation of o-xylene in an industrial packed-bed catalytic reactor: The role of hydrodynamics and catalyst activity in the heat transport, *Ind Eng Chem Res* 49 (2010) 6845–6853. <https://doi.org/10.1021/ie901720z>.
- [140] B. Brooks, *Chemical reactor analysis and design* By G. F. Froment and K. B. Bischoff, 2nd edn., published by Wiley, New York, 1990, 698 pp., price £18.95, paperback, ISBN 0-471-51044-0., *The Chemical Engineering Journal* 47 (1991) 133. [https://doi.org/10.1016/0300-9467\(91\)85016-O](https://doi.org/10.1016/0300-9467(91)85016-O).
- [141] A. Romero-Limones, J. Poissonnier, J.W. Thybaut, C.O. Castillo-Araiza, A pseudo-local heat transfer approach in a low tube to particle diameter ratio packed bed catalytic reactor: Oxidative dehydrogenation of ethane as a case study, *Chemical Engineering Journal* 454 (2023) 140392. <https://doi.org/10.1016/j.cej.2022.140392>.
- [142] G. Aparicio-Mauricio, R.S. Ruiz, F. López-Isunza, C.O. Castillo-Araiza, A simple approach to describe hydrodynamics and its effect on heat and mass transport in an industrial wall-cooled fixed bed catalytic reactor: ODH of ethane on a MoVNbTeO formulation, *Chemical Engineering Journal* 321 (2017) 584–599. <https://doi.org/10.1016/j.cej.2017.03.043>.
- [143] M. Fattahi, M. Kazemeini, F. Khorasheh, A. Darvishi, A.M. Rashidi, Fixed-bed multi-tubular reactors for oxidative dehydrogenation in ethylene process, *Chem Eng Technol* 36 (2013) 1691–1700. <https://doi.org/10.1002/ceat.201300148>.
- [144] M.L. Rodríguez, D.E. Ardissonne, E. López, M.N. Pedernera, D.O. Borio, Reactor designs for ethylene production via ethane oxidative dehydrogenation: Comparison of performance, *Ind Eng Chem Res* 50 (2011) 2690–2697. <https://doi.org/10.1021/ie100738q>.
- [145] H. Delmas, G.F. Froment, A simulation model accounting for structural radial nonuniformities in fixed bed reactors, *Chem Eng Sci* 43 (1988) 2281–2287. [https://doi.org/10.1016/0009-2509\(88\)87116-1](https://doi.org/10.1016/0009-2509(88)87116-1).

- [146] Z. Nawaz, Heterogeneous Reactor Modeling of an Industrial Multitubular Packed-Bed Ethylene Oxide Reactor, *Chem Eng Technol* 39 (2016) 1845–1857. <https://doi.org/10.1002/ceat.201500603>.
- [147] O. Galan, V.G. Gomes, J. Romagnoli, K.F. Ngian, Selective oxidation of ethylene in an industrial packed-bed reactor: Modelling, analysis and optimization, *International Journal of Chemical Reactor Engineering* 7 (2009). <https://doi.org/10.2202/1542-6580.2058>.
- [148] C. Alvarado-Camacho, J. Poissonnier, J.W. Thybaut, C.O. Castillo-Araiza, Toward the Industrial Exploitation of the Oxidative Dehydrogenation of Ethane over a NiO-SnO₂-Based Catalyst: Regime, Parametric Sensitivity, and Optimization Analysis, *Ind Eng Chem Res* 62 (2023) 10342–10357. <https://doi.org/10.1021/acs.iecr.3c00635>.
- [149] C.O. Castillo-Araiza, F. López-Isunza, The role of catalyst activity on the steady state and transient behavior of an industrial-scale fixed bed catalytic reactor for the partial oxidation of o-xylene on V₂O₅/TiO₂ catalysts, *Chemical Engineering Journal* 176–177 (2011) 26–32. <https://doi.org/10.1016/j.cej.2011.06.051>.
- [150] G.J.H. Tasker, The calculation of heat transfer and reaction rate in catalyst beds. Application of theory to phthalic anhydride pilot plant data, *Institution of Chemical Engineers* 24 (1946) 84–89.
- [151] J.J. Lerou, G.F. Froment, Velocity, temperature and conversion profiles in fixed bed catalytic reactors, *Chem Eng Sci* 32 (1977) 853–861. [https://doi.org/10.1016/0009-2509\(77\)80071-7](https://doi.org/10.1016/0009-2509(77)80071-7).
- [152] T. Daszkowski, G. Eigenberger, A reevaluation of fluid flow, heat transfer and chemical reaction in catalyst filled tubes, *Chem Eng Sci* 47 (1992) 2245–2250. [https://doi.org/10.1016/0009-2509\(92\)87042-O](https://doi.org/10.1016/0009-2509(92)87042-O).
- [153] L.E. García-Martínez, C.O. Castillo-Araiza, G. Quijano, S. Huerta-Ochoa, On the modelling and surface response analysis of a non-conventional wall-cooled solid/gas bioreactor with application in esterification, *Chemical Engineering Journal* 437 (2022) 135063. <https://doi.org/10.1016/j.cej.2022.135063>.
- [154] A.I. Anastasov, A study of the influence of the operating parameters on the temperature of the hot spot in a fixed bed reactor, *Chemical Engineering Journal* 86 (2002) 287–297. [https://doi.org/10.1016/S1385-8947\(01\)00178-4](https://doi.org/10.1016/S1385-8947(01)00178-4).
- [155] F. López-Isunza, L.S. Kershenbaum, The role of reversible changes in catalyst activity in the observed multiple steady states during partial oxidation dynamics, *Chem Eng Sci* 47 (1992) 2817–2822. [https://doi.org/10.1016/0009-2509\(92\)87135-D](https://doi.org/10.1016/0009-2509(92)87135-D).
- [156] A.I. Anastasov, An investigation of the kinetic parameters of the o-xylene oxidation process carried out in a fixed bed of high-productive vanadia-titania catalyst, *Chem Eng Sci* 58 (2003) 89–98. [https://doi.org/10.1016/S0009-2509\(02\)00431-1](https://doi.org/10.1016/S0009-2509(02)00431-1).
- [157] J.F. Durán-Pérez, J.G. Rivera de la Cruz, C.O. Castillo-Araiza, Elucidating Selective and Total Oxidation Elementary Reactions over a Ni-Based Catalyst for Sustainable Ethylene Production via Oxidative Dehydrogenation of Ethane: Microkinetic Analysis, *Chemical Engineering Journal* 470 (2023) 143939. <https://doi.org/10.1016/j.cej.2023.143939>.
- [158] C.O. Castillo-Araiza, H. Jiménez-Islas, F. López-Isunza, Heat-transfer studies in packed-bed catalytic reactors of low tube/particle diameter ratio, *Ind Eng Chem Res* 46 (2007) 7426–7435. <https://doi.org/10.1021/ie070097z>.
- [159] G. Che-Galicia, R.S. Ruiz-Martínez, D. Rios-Morales, J.A. Ayala-Romero, C.O. Castillo-Araiza, Kinetic and reactor performance of a Ni-based catalyst during the production of ethene, *Chem Eng Commun* 205 (2018) 372–386. <https://doi.org/10.1080/00986445.2017.1396538>.

- [160] J.S. Valente, R. Quintana-Solórzano, H. Armendáriz-Herrera, G. Barragán-Rodríguez, J.M. López-Nieto, Kinetic study of oxidative dehydrogenation of ethane over MoVTeNb mixed-oxide catalyst, *Ind Eng Chem Res* 53 (2014) 1775–1786. <https://doi.org/10.1021/ie402447h>.
- [161] E. Heracleous, A.A. Lemonidou, Ni-Nb-O mixed oxides as highly active and selective catalysts for ethene production via ethane oxidative dehydrogenation. Part II: Mechanistic aspects and kinetic modeling, *J Catal* 237 (2006) 175–189. <https://doi.org/10.1016/j.jcat.2005.11.003>.
- [162] A.G. Dixon, G. Walls, H. Stanness, M. Nijemeisland, E.H. Stitt, Experimental validation of high Reynolds number CFD simulations of heat transfer in a pilot-scale fixed bed tube, *Chemical Engineering Journal* 200–202 (2012) 344–356. <https://doi.org/10.1016/j.cej.2012.06.065>.
- [163] M. Behnam, A.G. Dixon, M. Nijemeisland, E.H. Stitt, A New Approach to Fixed Bed Radial Heat Transfer Modeling Using Velocity Fields from Computational Fluid Dynamics Simulations, *Ind Eng Chem Res* 52 (2013) 15244–15261. <https://doi.org/10.1021/ie4000568>.
- [164] S.A. Logtenberg, A.G. Dixon, Computational Fluid Dynamics Studies of the Effects of Temperature-Dependent Physical Properties on Fixed-Bed Heat Transfer, *Ind Eng Chem Res* 37 (1998) 739–747. <https://doi.org/10.1021/ie970382q>.
- [165] M. Nijemeisland, A.G. Dixon, Comparison of CFD simulations to experiment for convective heat transfer in a gas-solid fixed bed, *Chemical Engineering Journal* 82 (2001) 231–246. [https://doi.org/10.1016/S1385-8947\(00\)00360-0](https://doi.org/10.1016/S1385-8947(00)00360-0).
- [166] H. Bai, J. Theuerkauf, P.A. Gillis, P.M. Witt, A coupled DEM and CFD simulation of flow field and pressure drop in fixed bed reactor with randomly packed catalyst particles, *Ind Eng Chem Res* 48 (2009) 4060–4074. <https://doi.org/10.1021/ie801548h>.
- [167] G.D. Wehinger, Improving the radial heat transport and heat distribution in catalytic gas-solid reactors, *Chemical Engineering and Processing - Process Intensification* 177 (2022). <https://doi.org/10.1016/j.cep.2022.108996>.
- [168] M. Kutscherauer, P. Reinold, S. Böcklein, G. Mestl, T. Turek, G.D. Wehinger, How Temperature Measurement Impacts Pressure Drop and Heat Transport in Slender Fixed Beds of Raschig Rings, *ACS Engineering Au* 3 (2023) 45–58. <https://doi.org/10.1021/acsengineeringau.2c00039>.
- [169] S. Flaischlen, T. Turek, G.D. Wehinger, Local structure effects on hydrodynamics in slender fixed bed reactors: Spheres and rings, *Chemical Engineering Journal* 475 (2023). <https://doi.org/10.1016/j.cej.2023.146342>.
- [170] G.D. Wehinger, F. Scharf, Thermal radiation effects on heat transfer in slender packed-bed reactors: Particle-resolved CFD simulations and 2D modeling, *Chemical Engineering Research and Design* 184 (2022) 24–38. <https://doi.org/10.1016/j.cherd.2022.05.034>.
- [171] G.R. George, M. Bockelmann, L. Schmalhorst, D. Beton, A. Gerstle, L. Torkuhl, A. Lindermeir, G.D. Wehinger, Workflow for computational fluid dynamics modeling of fixed-bed reactors packed with metal foam pellets: Hydrodynamics, *AIChE Journal* 69 (2023). <https://doi.org/10.1002/aic.17284>.
- [172] G.D. Wehinger, F. Scharf, Supporting Information: Thermal radiation effects on heat transfer in slender packed-bed reactors: Particle-resolved CFD simulations and 2D modeling, n.d.
- [173] G.R. George, M. Bockelmann, L. Schmalhorst, D. Beton, A. Gerstle, A. Lindermeir, G.D. Wehinger, Radial heat transport in a fixed-bed reactor made of metallic foam pellets: Experiment and particle-resolved computational fluid dynamics, *Int J Heat Mass Transf* 197 (2022). <https://doi.org/10.1016/j.ijheatmasstransfer.2022.123376>.

- [174] Y. Dong, B. Sosna, O. Korup, F. Rosowski, R. Horn, Investigation of radial heat transfer in a fixed-bed reactor: CFD simulations and profile measurements, *Chemical Engineering Journal* 317 (2017) 204–214. <https://doi.org/10.1016/j.cej.2017.02.063>.
- [175] M. Müller, M. Kutscherauer, S. Böcklein, G.D. Wehinger, T. Turek, G. Mestl, Modeling the selective oxidation of n-butane to maleic anhydride: From active site to industrial reactor, *Catal Today* 387 (2022) 82–106. <https://doi.org/10.1016/j.cattod.2021.04.009>.
- [176] G.D. Wehinger, T. Eppinger, M. Kraume, Detailed numerical simulations of catalytic fixed-bed reactors: Heterogeneous dry reforming of methane, *Chem Eng Sci* 122 (2015) 197–209. <https://doi.org/10.1016/j.ces.2014.09.007>.
- [177] G.D. Wehinger, F. Klippel, M. Kraume, Modeling pore processes for particle-resolved CFD simulations of catalytic fixed-bed reactors, *Comput Chem Eng* 101 (2017) 11–22. <https://doi.org/10.1016/j.compchemeng.2017.02.029>.
- [178] E.A. Daymo, M. Hettel, O. Deutschmann, G.D. Wehinger, Accelerating particle-resolved CFD simulations of catalytic fixed-bed reactors with DUO, *Chem Eng Sci* 250 (2022). <https://doi.org/10.1016/j.ces.2021.117408>.
- [179] G.D. Wehinger, H. Heitmann, M. Kraume, An artificial structure modeler for 3D CFD simulations of catalytic foams, *Chemical Engineering Journal* 284 (2016) 543–556. <https://doi.org/10.1016/j.cej.2015.09.014>.
- [180] W. Peng, M. Xu, X. Huai, Z. Liu, 3D CFD simulations of acetone hydrogenation in randomly packed beds for an isopropanol-acetone-hydrogen chemical heat pump, *Appl Therm Eng* 94 (2016) 238–248. <https://doi.org/10.1016/j.applthermaleng.2015.10.130>.
- [181] X. Guo, Z. Zhu, CFD based modeling on chemical looping combustion in a packed bed reactor, *Chem Eng Sci* 138 (2015) 303–314. <https://doi.org/10.1016/j.ces.2015.08.006>.
- [182] M. Kuroki, S. Ookawara, K. Ogawa, A High-Fidelity CFD Model of Methane Steam Reforming in a Packed Bed Reactor, 2009.
- [183] T. Maffei, G. Gentile, S. Rebughini, M. Bracconi, F. Manelli, S. Lipp, A. Cuoci, M. Maestri, A multiregion operator-splitting CFD approach for coupling microkinetic modeling with internal porous transport in heterogeneous catalytic reactors, *Chemical Engineering Journal* 283 (2016) 1392–1404. <https://doi.org/10.1016/j.cej.2015.08.080>.
- [184] M. Maestri, A. Cuoci, Coupling CFD with detailed microkinetic modeling in heterogeneous catalysis, *Chem Eng Sci* 96 (2013) 106–117. <https://doi.org/10.1016/j.ces.2013.03.048>.
- [185] X. Zhou, Y. Duan, X. Huai, X. Li, 3D CFD modeling of acetone hydrogenation in fixed bed reactor with spherical particles, *Particuology* 11 (2013) 715–722. <https://doi.org/10.1016/j.partic.2012.10.009>.
- [186] B. Partopour, A.G. Dixon, Computationally efficient incorporation of microkinetics into resolved-particle CFD simulations of fixed-bed reactors, *Comput Chem Eng* 88 (2016) 126–134. <https://doi.org/10.1016/j.compchemeng.2016.02.015>.
- [187] G.D. Wehinger, M. Kraume, V. Berg, O. Korup, K. Mette, R. Schlögl, M. Behrens, R. Horn, Investigating dry reforming of methane with spatial reactor profiles and particle-resolved CFD simulations, *AIChE Journal* 62 (2016) 4436–4452. <https://doi.org/10.1002/aic.15520>.
- [188] G.M. Karthik, V. V. Buwa, Effect of particle shape on fluid flow and heat transfer for methane steam reforming reactions in a packed bed, *AIChE Journal* 63 (2017) 366–377. <https://doi.org/10.1002/aic.15542>.
- [189] B. Partopour, A.G. Dixon, Resolved-particle fixed bed CFD with microkinetics for ethylene oxidation, *AIChE Journal* 63 (2017) 87–94. <https://doi.org/10.1002/aic.15422>.

- [190] M. Behnam, A.G. Dixon, P.M. Wright, M. Nijemeisland, E.H. Stitt, Comparison of CFD simulations to experiment under methane steam reforming reacting conditions, *Chemical Engineering Journal* 207–208 (2012) 690–700. <https://doi.org/10.1016/j.cej.2012.07.038>.
- [191] N. Jurtz, M. Kraume, G.D. Wehinger, Advances in fixed-bed reactor modeling using particle-resolved computational fluid dynamics (CFD), *Reviews in Chemical Engineering* 35 (2019) 139–190. <https://doi.org/10.1515/revce-2017-0059>.
- [192] A.I. Anastasov, The behaviour of a low-productive non-pretreated V2O5–TiO2 (anatase) catalyst for oxidation of o-xylene to phthalic anhydride, *Chemical Engineering Journal* 109 (2005) 57–66. <https://doi.org/10.1016/j.cej.2005.03.010>.
- [193] J.N. Papageorgiou, G.F. Froment, Simulation models accounting for radial voidage profiles in fixed-bed reactors, *Chem Eng Sci* 50 (1995) 3043–3056. [https://doi.org/10.1016/0009-2509\(95\)00138-U](https://doi.org/10.1016/0009-2509(95)00138-U).
- [194] C.O. Castillo-araiza, F. Lopez-isunza, Hydrodynamic Models for Packed Beds with Low Tube-to-Particle Diameter Ratio Hydro, *International Journal of Chemical Reactor Engineering* 6 (2008) 1–14. <https://doi.org/https://doi.org/10.2202/1542-6580.1550>.
- [195] S.A. Logtenberg, A.G. Dixon, Computational fluid dynamics studies of fixed bed heat transfer, *Chemical Engineering and Processing: Process Intensification* 37 (1998) 7–21. [https://doi.org/10.1016/S0255-2701\(97\)00032-9](https://doi.org/10.1016/S0255-2701(97)00032-9).
- [196] S.A. Logtenberg, M. Nijemeisland, A.G. Dixon, Computational fluid dynamics simulations of fluid flow and heat transfer at the wall-particle contact points in a fixed-bed reactor, *Chem Eng Sci* 54 (1999) 2433–2439. [https://doi.org/10.1016/S0009-2509\(98\)00445-X](https://doi.org/10.1016/S0009-2509(98)00445-X).
- [197] P.E.C. Burström, V. Frishfelds, A.L. Ljung, T.S. Lundström, B.D. Marjavaara, Modelling heat transfer during flow through a random packed bed of spheres, *Heat and Mass Transfer/Waerme- Und Stoffuebertragung* 54 (2018) 1225–1245. <https://doi.org/10.1007/s00231-017-2192-3>.
- [198] B. Hou, R. Ye, Y. Huang, X. Wang, T. Zhang, A CFD model for predicting the heat transfer in the industrial scale packed bed, *Chin J Chem Eng* 26 (2018) 228–237. <https://doi.org/10.1016/j.cjche.2017.07.008>.
- [199] S. Wang, C. Xu, W. Liu, Z. Liu, Numerical study on heat transfer performance in packed bed, *Energies (Basel)* 12 (2019). <https://doi.org/10.3390/en12030414>.
- [200] X. Guo, Y. Sun, R. Li, F. Yang, Experimental investigations on temperature variation and inhomogeneity in a packed bed CLC reactor of large particles and low aspect ratio, *Chem Eng Sci* 107 (2014) 266–276. <https://doi.org/10.1016/j.ces.2013.12.032>.
- [201] M. Giese, K. Rottschäfer, D. Vortmeyer, Measured and Modeled Superficial Flow Profiles in Packed Beds with Liquid Flow, *AIChE Journal* 44 (1998) 484–490. <https://doi.org/10.1002/aic.690440225>.
- [202] G.A. Gómez-Ramos, C.O. Castillo-Araiza, S. Huerta-Ochoa, M. Couder-García, A. Prado-Barragán, Assessment of hydrodynamics in a novel bench-scale wall-cooled packed bioreactor under abiotic conditions, *Chemical Engineering Journal* 375 (2019) 121945. <https://doi.org/10.1016/j.cej.2019.121945>.
- [203] H.F. López-Isunza, Steady state and dynamic behaviour of an industrial scale fixed bed catalytic reactor, Ph. D. thesis, Ph.D. thesis, University of London, 1983.
- [204] W.R. Paterson, J.J. Carberry, Fixed bed catalytic reactor modelling. The heat transfer problem, *Chem Eng Sci* 38 (1983) 175–180. [https://doi.org/10.1016/0009-2509\(83\)80149-3](https://doi.org/10.1016/0009-2509(83)80149-3).

- [205] G. Emig, H. Hofmann, U. Hoffmann, U. Fiand, Experimental studies on runaway of catalytic fixed-bed reactors (vinyl-acetate-synthesis), *Chem Eng Sci* 35 (1980) 249–257. [https://doi.org/10.1016/0009-2509\(80\)80094-7](https://doi.org/10.1016/0009-2509(80)80094-7).
- [206] R. Shinnar, F.J. Doyle, H.M. Budman, M. Morari, Design considerations for tubular reactors with highly exothermic reactions, *AIChE Journal* 38 (1992) 1729–1743. <https://doi.org/10.1002/aic.690381106>.
- [207] D. Wen, Y. Ding, Heat transfer of gas flow through a packed bed, *Chem Eng Sci* 61 (2006) 3532–3542. <https://doi.org/10.1016/j.ces.2005.12.027>.
- [208] O.R. Derkx, A.G. Dixon, Effect of the wall Nusselt number on the simulation of catalytic fixed bed reactors, *Catal Today* 35 (1997) 435–442. [https://doi.org/10.1016/S0920-5861\(96\)00210-6](https://doi.org/10.1016/S0920-5861(96)00210-6).
- [209] J. Skrzypek, M. Grzesik, M. Galantowicz, J. Soliński, Kinetics of the catalytic air oxidation of o-xylene over a commercial V₂O₅-TiO₂ catalyst, *Chem Eng Sci* 40 (1985) 611–620. [https://doi.org/10.1016/0009-2509\(85\)80005-1](https://doi.org/10.1016/0009-2509(85)80005-1).
- [210] C. McGreavy, E.A. Foumeny, K.H. Javed, Characterization of transport properties for fixed bed in terms of local bed structure and flow distribution, *Chem Eng Sci* 41 (1986) 787–797. [https://doi.org/10.1016/0009-2509\(86\)87159-7](https://doi.org/10.1016/0009-2509(86)87159-7).
- [211] P.H. Calderbank, K. Chandrasekharan, C. Fumagalli, The prediction of the performance of packed-bed catalytic reactors in the air-oxidation of o-xylene, *Chem Eng Sci* 32 (1977) 1435–1443. [https://doi.org/10.1016/0009-2509\(77\)80240-6](https://doi.org/10.1016/0009-2509(77)80240-6).
- [212] E. Tsotsas, E.U. Schlünder, Heat transfer in packed beds with fluid flow: remarks on the meaning and the calculation of a heat transfer coefficient at the wall, *Chem Eng Sci* 45 (1990) 819–837. [https://doi.org/10.1016/0009-2509\(90\)85005-X](https://doi.org/10.1016/0009-2509(90)85005-X).
- [213] I.M. Gerzeliev, A.M. Gyul'Maliev, A.Y. Popov, S.N. Khadzhiev, Thermodynamic and quantum-chemical study of the oxidative dehydrogenation of ethane to ethylene, *Petroleum Chemistry* 55 (2015) 146–153. <https://doi.org/10.1134/S0965544115020097>.
- [214] M. Xie, H. Freund, Optimal reactor design and operation taking catalyst deactivation into account, *Chem Eng Sci* 175 (2018) 405–415. <https://doi.org/10.1016/j.ces.2017.10.010>.
- [215] A. Vandervoort, J. Thibault, Y.P. Gupta, Multi-Objective Optimization of an Ethylene Oxide Reactor, *International Journal of Chemical Reactor Engineering* 9 (2012). <https://doi.org/10.1515/1542-6580.2548>.
- [216] Z. Till, T. Varga, J. Réti, T. Chován, Optimization Strategies in a Fixed-Bed Reactor for HCl Oxidation, *Ind Eng Chem Res* 56 (2017) 5352–5359. <https://doi.org/10.1021/acs.iecr.7b00750>.
- [217] Y. Nie, P.M. Witt, A. Agarwal, L.T. Biegler, Optimal active catalyst and inert distribution in catalytic packed bed reactors: Ortho-xylene oxidation, *Ind Eng Chem Res* 52 (2013) 15311–15320. <https://doi.org/10.1021/ie4005699>.
- [218] A.P. De Wasch, G.F. Froment, Heat transfer in packed beds, *Chem Eng Sci* 27 (1972) 567–576. [https://doi.org/10.1016/0009-2509\(72\)87012-X](https://doi.org/10.1016/0009-2509(72)87012-X).
- [219] S. Ströhle, A. Haselbacher, Z.R. Jovanovic, A. Steinfeld, Transient discrete-granule packed-bed reactor model for thermochemical energy storage, *Chem Eng Sci* 117 (2014) 465–478. <https://doi.org/10.1016/j.ces.2014.07.009>.
- [220] W. Kwapinski, Combined wall and thermal effects during non-isothermal packed bed adsorption, *Chemical Engineering Journal* 152 (2009) 271–276. <https://doi.org/10.1016/j.cej.2009.05.023>.

- [221] W. Kwapinski, M. Winterberg, E. Tsotsas, D. Mewes, Modeling of the Wall Effect in Packed Bed Adsorption, *Chem Eng Technol* 27 (2004) 1179–1186. <https://doi.org/10.1002/ceat.200407001>.
- [222] E.M. Moghaddam, E.A. Foumeny, A.I. Stankiewicz, J.T. Padding, Multiscale modelling of wall-to-bed heat transfer in fixed beds with non-spherical pellets: From particle-resolved CFD to pseudo-homogenous models, *Chem Eng Sci* 236 (2021) 116532. <https://doi.org/10.1016/j.ces.2021.116532>.
- [223] E.M. Moghaddam, E.A. Foumeny, A.I. Stankiewicz, J.T. Padding, Heat transfer from wall to dense packing structures of spheres, cylinders and Raschig rings, *Chemical Engineering Journal* 407 (2021) 127994. <https://doi.org/10.1016/j.cej.2020.127994>.
- [224] G.F. Froment, FIXED BED CATALYTIC REACTORS—CURRENT DESIGN STATUS, *Ind Eng Chem* 59 (1967) 18–27. <https://doi.org/10.1021/ie50686a006>.
- [225] V.A. Nikolov, A.I. Anastasov, Influence of the inlet temperature on the performance of a fixed-bed reactor for oxidation of o-xylene into phthalic anhydride, *Chem Eng Sci* 47 (1992) 1291–1298. [https://doi.org/10.1016/0009-2509\(92\)80249-C](https://doi.org/10.1016/0009-2509(92)80249-C).
- [226] S. Yagi, D. Kunii, Studies on heat transfer near wall surface in packed beds, *AIChE Journal* 6 (1960) 97–104. <https://doi.org/10.1002/aic.690060119>.
- [227] S. Yagi, N. Wakao, Heat and mass transfer from wall to fluid in packed beds, *AIChE Journal* 5 (1959) 79–85. <https://doi.org/10.1002/aic.690050118>.
- [228] T.H. Tsang, T.F. Edgar, J.O. Hougen, Estimation of heat transfer parameters in a packed bed, *The Chemical Engineering Journal* 11 (1976) 57–66. [https://doi.org/10.1016/0300-9467\(76\)80006-8](https://doi.org/10.1016/0300-9467(76)80006-8).
- [229] S. Ströhle, A. Haselbacher, Z.R. Jovanovic, A. Steinfeld, The effect of the gas-solid contacting pattern in a high-temperature thermochemical energy storage on the performance of a concentrated solar power plant, *Energy Environ Sci* 9 (2016) 1375–1389. <https://doi.org/10.1039/c5ee03204k>.
- [230] Z. Wan, J. Jiang, H. Ma, Y. Li, Y. Lu, F. Cao, A study of the heat transfer characteristics of novel Ni-foam structured catalysts, *Canadian Journal of Chemical Engineering* 94 (2016) 2225–2234. <https://doi.org/10.1002/cjce.22587>.
- [231] D.A. Asensio, M.T. Zambon, G.D. Mazza, G.F. Barreto, Heterogeneous two-region model for low-aspect-ratio fixed-bed catalytic reactors. Analysis of fluid-convective contributions, *Ind Eng Chem Res* 53 (2014) 3587–3605. <https://doi.org/10.1021/ie403219q>.
- [232] S. Yagi, D. Kunii, Studies on effective thermal conductivities in packed beds, *AIChE Journal* 3 (1957) 373–381. <https://doi.org/10.1002/aic.690030317>.
- [233] J.R. Fernández, J.M. Alarcón, J.C. Abanades, Investigation of a Fixed-Bed Reactor for the Calcination of CaCO₃ by the Simultaneous Reduction of CuO with a Fuel Gas, *Ind Eng Chem Res* 55 (2016) 5128–5132. <https://doi.org/10.1021/acs.iecr.5b04073>.
- [234] N. Wakao, S. Kaguei, T. Funazkri, Effect of fluid dispersion coefficients on particle-to-fluid heat transfer coefficients in packed beds. Correlation of nusselt numbers, *Chem Eng Sci* 34 (1979) 325–336. [https://doi.org/10.1016/0009-2509\(79\)85064-2](https://doi.org/10.1016/0009-2509(79)85064-2).
- [235] D.J. Gunn, M. Khalid, Thermal dispersion and wall heat transfer in packed beds, *Chem Eng Sci* 30 (1975) 261–267. [https://doi.org/10.1016/0009-2509\(75\)80014-5](https://doi.org/10.1016/0009-2509(75)80014-5).
- [236] M. Winterberg, E. Tsotsas, A. Krischke, D. Vortmeyer, A simple and coherent set of coefficients for modelling of heat and mass transport with and without chemical reaction in

- tubes filled with spheres, *Chem Eng Sci* 55 (2000) 967–979. [https://doi.org/10.1016/S0009-2509\(99\)00379-6](https://doi.org/10.1016/S0009-2509(99)00379-6).
- [237] E.A. Foumeny, J. Ma, Non-Darcian non-isothermal compressible flow and heat transfer in cylindrical packed beds, *Chem Eng Technol* 17 (1994) 50–60. <https://doi.org/10.1002/ceat.270170109>.
- [238] B. Sosna, Y. Dong, L. Chromow, O. Korup, R. Horn, Effective Axial Thermal Conductivity in Catalyst Packings from High Resolution Temperature Profiles, *Chem Ing Tech* 88 (2016) 1676–1683. <https://doi.org/10.1002/cite.201600062>.
- [239] B. Legawiec, D. Ziółkowski, Axial thermal effective conductivity in packed-bed catalytic tubular reactors, *Chem Eng Sci* 52 (1997) 1875–1882. [https://doi.org/10.1016/S0009-2509\(97\)00016-X](https://doi.org/10.1016/S0009-2509(97)00016-X).
- [240] V. Specchia, G. Baldi, S. Sicardi, Heat transfer in packed bed reactors with one phase flow, *Chem Eng Commun* 4 (1980) 361–380. <https://doi.org/10.1080/00986448008935916>.
- [241] T. Mongkhonsi, L.S. Kershenbaum, The Effect of Deactivation of a V2O5/TiO2 (anatase) Industrial Catalyst on Reactor Behaviour During the Partial Oxidation of o-Xylene to Phthalic Anhydride, *Appl Catal A Gen* 170 (1998) 33.
- [242] W.M. Brandstädter, B. Kraushaar-Czarnetzki, Maleic anhydride from mixtures of n-butenes and n-butane: Simulation of a production-scale nonisothermal fixed-bed reactor, *Ind Eng Chem Res* 46 (2007) 1475–1484. <https://doi.org/10.1021/ie061142q>.
- [243] Y. Dong, F.J. Keil, O. Korup, F. Rosowski, R. Horn, Effect of the catalyst pore structure on fixed-bed reactor performance of partial oxidation of n-butane: A simulation study, *Chem Eng Sci* 142 (2016) 299–309. <https://doi.org/10.1016/j.ces.2015.12.004>.
- [244] A.G. Dixon, Local transport and reaction rates in a fixed bed reactor tube: Exothermic partial oxidation of ethylene, *Chem Eng Sci* 231 (2021) 116305. <https://doi.org/10.1016/j.ces.2020.116305>.
- [245] R. Henda, A. Machac, B. Nilsson, Heat and mass transport in a nonlinear fixed-bed catalytic reactor: Hot spots and thermal runaway, *Chemical Engineering Journal* 143 (2008) 195–200. <https://doi.org/10.1016/j.ces.2008.04.015>.
- [246] V. Spallina, B. Marinello, F. Gallucci, M.C. Romano, M.V.S. Annaland, Chemical looping reforming in packed-bed reactors : Modelling , experimental validation and large-scale reactor design, 156 (2017) 156–170.
- [247] S. Purwono, H. Budman, R.R. Hudgins, P.L. Silveston, Yu.Sh. Matros, Runaway in packed bed reactors operating with periodic flow reversal, *Chem Eng Sci* 49 (1994) 5473–5487. [https://doi.org/10.1016/0009-2509\(94\)00386-6](https://doi.org/10.1016/0009-2509(94)00386-6).
- [248] G. Tauer, C. Kern, A. Jess, Transient Effects during Dynamic Operation of a Wall-Cooled Fixed-Bed Reactor for CO 2 Methanation, *Chem Eng Technol* 42 (2019) 2401–2409. <https://doi.org/10.1002/ceat.201900367>.
- [249] J. Ducamp, A. Bengaouer, P. Baurens, Modelling and Experimental Validation of a CO 2 Methanation Annular Cooled Fixed-Bed Reactor Exchanger, *Can J Chem Eng* 9999 (2016) 1–12. <https://doi.org/https://doi.org/10.1002/cjce.22706>.
- [250] L.A. Vandewalle, R. Van de Vijver, K.M. Van Geem, G.B. Marin, The role of mass and heat transfer in the design of novel reactors for oxidative coupling of methane, *Chem Eng Sci* 198 (2019) 268–289. <https://doi.org/10.1016/j.ces.2018.09.022>.

- [251] V. Hlaváček, P. van Rompay, Current problems of multiplicity, stability and sensitivity of states in chemically reacting systems, *Chem Eng Sci* 36 (1981) 1587–1597.
[https://doi.org/10.1016/0009-2509\(81\)80002-4](https://doi.org/10.1016/0009-2509(81)80002-4).

Chapter 2 – Oxidative Conversion of Methane (OCoM)

This Chapter presents the investigation of the Oxidative Conversion of Methane (OCoM) within the framework of the C123 European Horizon 2020 integrated project. Section 2.1 provides a brief introduction on the methane valorization and the main features of OCoM. Section 2.2 introduces the procedures followed on the kinetic experimentation, the definitions of carbon conversion, selectivity and yields, the reactor model and the contribution analysis. Section 2.3 gives details on the kinetic model construction based on both what has been reported in literature and experimental observations obtained within the group. Moreover, the validation of the OCoM kinetic model is presented. Section 2.4 outlines the C123 process, particularly the role of OCoM within it. An analysis of the impact of the operating conditions on OCoM is given. The evaluation of real feedstock in the OCoM reactor is made, and further C123 process considerations are provided. Last, Section 2.5 presents the conclusion of the research done regarding OCoM.

The results of this chapter are published as:

Romero-Limones A., Poissonnier J., Cheng Y., Mahmoud M., Castillo-Araiza, C. O., and Thybaut J. W., (2024). Oxidative Conversion of Methane: maximizing the carbon yield in natural gas valorization via the C123 process. *Chemical Engineering and Processing-Process Intensification*. DOI: 10.1016/j.cep.2024.109857

2.1 Introduction

The chemical composition of natural gas depends on the location where it is extracted and on the processing treatment it receives to remove impurities, even reaching a composition of ~100% of methane. Different kinds of natural gas, e.g. shale gas and biogas, exhibit high potential for use as feedstock in the petrochemical industry [1–4]. Shale gas, commonly containing over 84 % of methane, and 3 – 16% of ethane [5–7], has gained importance in industrial chemical processes since the so called “shale gas revolution” [8,9] increasing the extraction of natural gas from shale rock formations among the other wells, i.e., gas, coalbed and oil wells [8,9]. Biogas has been a topic of recent research efforts because of its potential as renewable energy source [10], rather than its valorization into chemicals. To better exploit these resources, while reducing the carbon footprint of natural gas from the petrochemical industry [11,12], and to transition to a less energy-intensive methane conversion technology than methane reforming [13], it is imperative to find novel approaches to convert methane into higher value products [14–16].

In this Chapter, a detailed study of the proposed Oxidative Conversion of Methane (OCoM), as part of the C123 European Horizon 2020 integrated project [14,16], is done targeting the valorization of methane (C_1) into C_2 species as a feedstock for the further C_3 species production, mainly propanal, via ethylene hydroformylation.

2.2 Procedures

2.2.1 Experimental

The OCoM experiments were performed over a MnNaW/SiO₂ catalyst in a lab-scale fixed-bed reactor operated isothermally in the plug-flow regime, i.e., overcoming heat and mass transfer limitations and pressure drop through the catalyst bed [17]. This catalyst is selected for OCoM because of its good stability (> 90h), high temperature performance (850 °C) without indications of deactivation [18] and trade-off between methane conversion (30% mol mol⁻¹) and C_2 selectivity (80% mol mol⁻¹) [19–23]. The catalyst was kindly provided by Johnson-Matthey and shared within the C123 project [14]. Experimental data were collected by means of a calibrated gas chromatograph (μ -GC, Agilent Industries 3000A). The operating conditions of the experiments are presented in Table 2.1. The catalyst loading was set to 50 mg. The kinetic experiments were performed at temperatures below 850 °C to ensure long-

term catalyst stability [21]. More details concerning the setup utilized have been reported previously by our group [24].

Table 2.1. Operating conditions of the OCoM experiments

Variable	Range	Units
Temperature	800 – 850	°C
Total pressure	100	kPa
Space time	2 – 2.5	kg _{cat} s mol ⁻¹
CH ₄ /O ₂ inlet molar ratio	3 – 5	mol mol ⁻¹
CO ₂ inlet molar fraction	0 – 20	%
He dilution molar fraction	50	%

2.2.2 Definitions

Because the reactions investigated in this work involve several carbon-containing components, the carbon conversion, X_C , the selectivity towards carbon species products, S_i , and the yield of the carbon species products, Y_i , were determined as follows:

$$X_C = \frac{F_{C,in} - F_{C,out}}{F_{C,in}} \times 100 = \frac{\text{Moles of carbon reacted}}{\text{Moles of carbon fed as reactant}} \quad [\text{mol mol}^{-1}] \quad (2.1)$$

$$S_i = \frac{N_{C,i}(F_{i,out} - F_{i,in})}{F_{C,in} - F_{C,out}} \times 100 = \frac{\text{Moles of carbon of species } i \text{ produced}}{\text{Moles of carbon reacted}} \quad [\text{mol mol}^{-1}] \quad (2.2)$$

$$Y_i = \frac{N_{C,i}(F_{i,out} - F_{i,in})}{F_{C,in}} \times 100 = \frac{\text{Moles of carbon of species } i \text{ produced}}{\text{Moles of carbon fed as reactant}} \quad [\text{mol mol}^{-1}] \quad (2.3)$$

In addition, a relevant carbon yield taking into account the cumulative yield of ethylene and CO is considered.

2.2.3 Reactor model

The (outlet) molar flow rate of component i is calculated by solving the set of ordinary differential equations (ODEs) given by Eq. (2.4), that describes the mass balance for each component i in an infinitesimal element of fixed bed reactor considering plug flow.

$$\frac{dF_i}{dW_{cat}} = R_i \quad (2.4)$$

This equation describes an isobaric, isothermal, one-dimensional pseudo-homogeneous continuous integral fixed-bed reactor model. As the experiments were performed at intrinsic

kinetics conditions, terms corresponding to intra and inter-particle transport limitations were omitted from Eq. (2.4). The net formation rate of the component i , R_i , is obtained by the summation of the specific reaction rates:

$$R_i = \sum_{j=1}^N \nu_{i,j} r_j \quad (2.5)$$

The specific reaction rates, r_j , are determined from rate expressions shown in Eqs. (2.9) – (2.11), see Section 2.3.4.

The resulting set of ordinary differential equations is solved using a fourth-order Runge-Kutta-Fehlberg method [25]. The kinetic parameter estimation is done using a weighted regression [26] according to the Levenberg-Marquardt algorithm [27], as available in ODRPACK [28], by the minimization of the sum of squares of the weighted residuals between the experimental molar flow rates and the model calculated ones:

$$RSS(\varphi) = \sum_{i=1}^N W_i \sum_{k=1}^M (F_{k,i} - \hat{F}_{k,i})^2 \rightarrow \min_{\varphi_1, \varphi_2, \dots, \varphi_p} \quad (2.6)$$

The dependence of the Residual Sum of Squares (RSS) on various responses is adjusted by weights W_i assigned to the i^{th} response, allowing for accurate estimates of all adjustable parameters. Statistical tests are conducted to assess the performance of the kinetic model. The individual significance of each model parameter is determined by verifying that their 95% confidence interval does not include zero. Moreover, a correlation matrix shows the binary correlations between all model parameters, ranging from -1 to 1. When the absolute value of the binary correlation coefficient two parameters is below 0.95, it is considered that these parameters are statistically uncorrelated. The F test is used to determine the global significance of the regression, with an F value exceeding the tabulated one indicating that the regression sum of squares significantly exceeds the residual sum of squares divided by the corresponding degrees of freedom. The overall model behavior is also visually assessed using parity diagrams and performance plots of the carbon species selectivity as a function of the methane conversion. Both visual tools allow for a comparison between the experimental and simulated data.

2.2.4 Contribution analysis

A contribution analysis was conducted on the various reactions included in the model, following the methodology outlined in the existing literature [29]. This approach proves highly valuable for quantifying the relative significance of different reactions within a kinetic model, as it incorporates both kinetic and concentration effects by relying on reaction rates.

Specifically, the integral contribution factor (φ_j) associated with reaction j in a given experiment is defined as the ratio of the rate of the reaction j to the sum of all the reaction rates at a specific location within the reactor.

$$\varphi_j = \frac{r_j}{\sum_j r_j} \quad (2.7)$$

Integral contribution factors are established through the integration of rates throughout the reactor, i.e., the catalyst bed, see Eq. (2.8), employing the trapezoid formula.

$$r_{int,j} = \int_0^{W_{cat}} r_j dW \quad (2.8)$$

For brevity, in the following sections, reaction rates refer to the integral reaction rates instead of reaction rates at the outlet of the reactor, unless explicitly mentioned otherwise.

2.3 Kinetic model construction

2.3.1 Reaction network

As a first step in the construction of the kinetic model, twelve global reactions are proposed taking as reference different reaction networks reported in literature [18,30,31], see Figure 2.1.

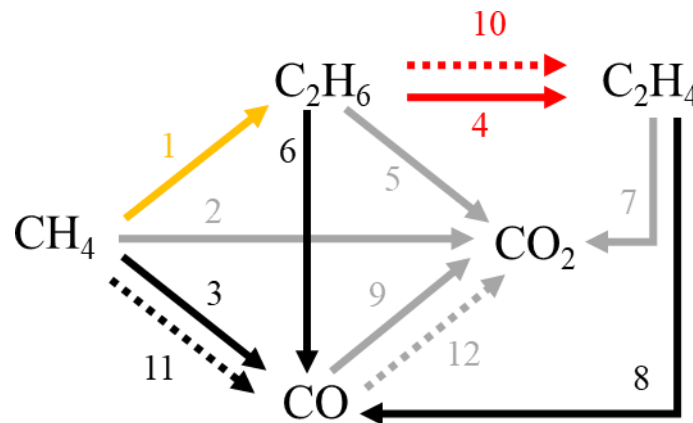


Figure 2.1. Simplified reaction network describing OCoM focusing on the carbon containing components.

The primary steps are the oxidation of methane in three parallel reactions: (1) Oxidative Coupling of Methane (OCM), producing ethane; (2) Total Oxidation of Methane (TOM), producing CO_2 ; and (3) Partial Oxidation of Methane (POM), producing CO. Subsequently, the produced ethane from the OCM is oxidized in three different reactions: (4)

the Oxidative Dehydrogenation of Ethane (ODH), producing ethylene; (5) the Total Oxidation of Ethane (TOE), producing CO₂; and (6) the Partial Oxidation of Ethane (POE), producing CO. Ethylene is oxidized via (7) the Total Oxidation of Ethylene (TOEt), producing CO₂, and (8) the Partial Oxidation of Ethylene (POEt), producing CO. All these oxidation reactions also produce water. As last oxidation, the (9) Total Oxidation of CO (TOCO), producing CO₂, is considered. Due to the high temperatures (> 800 °C) and total oxygen conversion, the non-oxidative (10) Thermal Dehydrogenation of Ethane (TDE) is also considered. Furthermore, the presence of water has led to the inclusion of the (11) Steam Methane Reforming (SMR), and the (12) Water Gas Shift Reaction (WGSR) in the kinetic model. In addition to the simplified representation of the reaction network in Figure 2.1, a comprehensive version of the network is given in Table 2.2.

Table 2.2. Reactions considered for the kinetic model

Acronym	Steps	Reaction steps
OCM	1	$\text{CH}_4 + \frac{1}{4}\text{O}_2 \rightarrow \frac{1}{2}\text{C}_2\text{H}_6 + \frac{1}{2}\text{H}_2\text{O}$
TOM	2	$\text{CH}_4 + 2\text{O}_2 \rightarrow \text{CO}_2 + 2\text{H}_2\text{O}$
POM	3	$\text{CH}_4 + \frac{3}{2}\text{O}_2 \rightarrow \text{CO} + 2\text{H}_2\text{O}$
ODH	4	$\text{C}_2\text{H}_6 + \frac{1}{2}\text{O}_2 \rightarrow \text{C}_2\text{H}_4 + \text{H}_2\text{O}$
TOE	5	$\text{C}_2\text{H}_6 + \frac{7}{2}\text{O}_2 \rightarrow 2\text{CO}_2 + 3\text{H}_2\text{O}$
POE	6	$\text{C}_2\text{H}_6 + \frac{5}{2}\text{O}_2 \rightarrow 2\text{CO} + 3\text{H}_2\text{O}$
TOEt	7	$\text{C}_2\text{H}_4 + 3\text{O}_2 \rightarrow 2\text{CO}_2 + 2\text{H}_2\text{O}$
POEt	8	$\text{C}_2\text{H}_4 + 2\text{O}_2 \rightarrow 2\text{CO} + 2\text{H}_2\text{O}$
TOCO	9	$\text{CO} + \frac{1}{2}\text{O}_2 \rightarrow \text{CO}_2$
TDE	10	$\text{C}_2\text{H}_6 \rightarrow \text{C}_2\text{H}_4 + \text{H}_2$
SRM	11	$\text{CH}_4 + \text{H}_2\text{O} \rightarrow \text{CO} + 3\text{H}_2$



2.3.2 Catalyst testing experiments - effect of the methane to oxygen inlet molar ratio

The operating condition effects on the methane and oxygen conversion, the selectivity towards CO, CO₂, ethane, ethylene and C₂ species (C₂ = C₂H₆ + C₂H₄), and the water and H₂ outlet molar flow rates are assessed in this section. In addition, it should be mentioned that no significant effect of co-feeding CO₂ was observed when the MnNaW/SiO₂ catalyst was tested. For the sake of brevity, these experimental observations are presented in Appendix 2A.

Figure 2.2a depicts the effect of the CH₄/O₂ inlet molar ratio on the selectivities towards the different carbon species. Four clear trends can be discerned with increasing CH₄/O₂ inlet molar ratio from 3 to 5 mol mol⁻¹, which was achieved by decreasing the amount of oxygen in the feedstock while keeping the amount of methane fixed. The methane conversion and CO selectivity decrease from 16% to 12% mol mol⁻¹ and 26% to 21% mol mol⁻¹, respectively, while the oxygen conversion and ethane selectivity increase from 25% to 36% mol mol⁻¹ and 30% to 38% mol mol⁻¹, respectively. The trade-off between methane conversion and ethane selectivity is consistent with what has been reported in literature [32], confirming that at these operating conditions OCM effectively takes place. The CO selectivity exceeds the CO₂ selectivity in the range of CH₄/O₂ inlet molar ratio from 3 to 5 mol mol⁻¹, indicating that the partial oxidations, i.e., POE, POEt, and POM, are favored over the total oxidations, i.e., TOM, TOE, and TOEt. Both the CO and CO₂ selectivity decrease with increasing methane to oxygen ratio, but also get closer to each other, suggesting the potential occurrence of the Total Oxidation of CO (TOCO) at high methane to oxygen ratios.

As the CH₄/O₂ inlet molar ratio increases from 3 to 4 mol mol⁻¹, there is a slight decrease in selectivity towards ethylene and CO, from 26% to 22% mol mol⁻¹ and 27% to 25% mol mol⁻¹, respectively, while the overall C₂ selectivity remains the same. This suggests a contribution of Oxidative Dehydrogenation of Ethane (ODH) to ethylene, mainly at CH₄/O₂ inlet molar ratio of 3 mol mol⁻¹. With a further increase in the CH₄/O₂ inlet molar ratio from 4 to 5 mol mol⁻¹, both ethylene and ethane selectivities increase from 22% to 24% mol mol⁻¹, and from 33% to 38% mol mol⁻¹, respectively. Conversely, the selectivity towards CO and CO₂ decreases from 25% to 21% mol mol⁻¹ and 19% to 17% mol mol⁻¹, respectively. This indicates

that the contribution of the Total Oxidation of Ethane (TOE), the Partial Oxidation of Ethylene (POEt), the TOEt, and the POE, is reduced as the oxygen content decreases. Moreover, the methane conversion and CO₂ selectivity slightly decrease in the same way, showing that the extent of the Total Oxidation of Methane (TOM) is limited.

Figure 2.2b illustrates the effect of the CH₄/O₂ inlet molar ratio on the H₂ and water molar flow rates. As the CH₄/O₂ inlet molar ratio increases from 3 to 5 mol mol⁻¹ the molar flow rate of H₂ decreases from 57 to 27 mmol s⁻¹ kg_{cat}⁻¹. The molar flow rate of water increases from 26 to 37 mmol s⁻¹ kg_{cat}⁻¹ when the CH₄/O₂ inlet molar ratio increases from 3 to 4 mol mol⁻¹, and decreases from 37 to 30 mmol s⁻¹ kg_{cat}⁻¹ when the CH₄/O₂ inlet molar ratio further increases from 4 to 5 mol mol⁻¹. Indeed, the increase of water with the CH₄/O₂ inlet molar ratio from 3 to 4 mol mol⁻¹ confirms that partial and total oxidations are taking place, while the decrease of water when the CH₄/O₂ inlet molar ratio increases from 4 to 5 mol mol⁻¹ suggests that water is reacting with methane, e.g., via the steam reforming of methane (SRM). Moreover, as the CO selectivity also decreases at these conditions, the Water Gas Shift Reaction (WGSR) can also take place. As H₂ is not produced directly from partial or total oxidations, it is most likely produced from the SRM and WGSR.

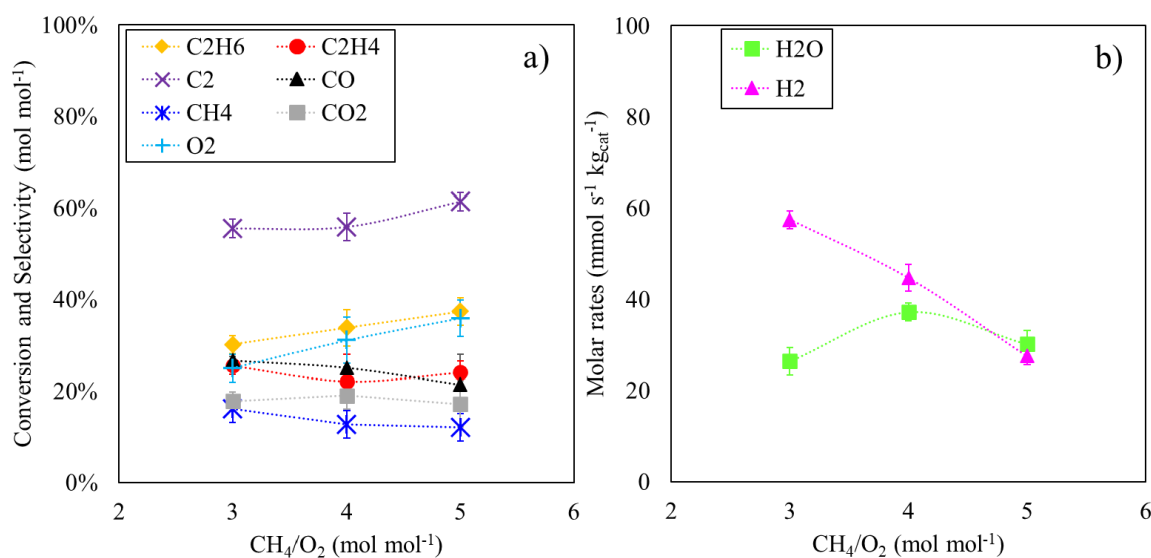


Figure 2.2. (a) Methane and oxygen conversion and selectivities towards ethane, ethylene, C₂, CO and CO₂ as a function of the CH₄/O₂ inlet molar flow ratio. (b) Molar flow rates of H₂ and water as a function of the CH₄/O₂ inlet molar flow ratio. T = 800 °C, p_{tot} = 100 kPa, W_{cat}/F_{CH₄,in} = 2.50 kg_{cat} s mol⁻¹. Lines are added to guide the eye.

2.3.3 Catalyst testing experiments – effect of temperature

Figure 2.3a illustrates the temperature effect on the methane and oxygen conversion and the selectivities towards the different carbon species. With increasing temperature, the methane conversion, oxygen conversion and ethylene selectivity increase, while the ethane selectivity decreases. This is consistent with what is generally proposed in the literature [18,30,33], i.e. ethane is produced from methane and ethylene is consecutively formed from ethane. The C₂ selectivity decreases from 65% mol mol⁻¹ at 800 °C to 58% mol mol⁻¹ at 825 °C and remains constant when further increasing the temperature from 825 °C to 850 °C. This indicates that, due to the high temperatures (850 °C) and the possibility to operate under both oxygen rich and oxygen-lean conditions, the production of ethylene can occur via both Thermal Dehydrogenation of Ethane (TDE) and ODH. Two opposite trends can be seen in the selectivity towards carbon oxides with increasing temperature. From 800 °C to 825 °C, the selectivity towards CO₂ decreases from 20% to 15% mol mol⁻¹, while the selectivity to CO increases from 15% to 28% mol mol⁻¹, and from 825 °C to 850 °C, both selectivities remain constant. From 800 °C to 825 °C, the partial oxidations, i.e., production of CO, are more likely to occur than the total oxidations, i.e., production of CO₂. As mentioned in the previous section, the partial oxidation of C₂ species as well as of methane are taking place. Moreover, the CO₂ selectivity decreases as the methane conversion increases, suggesting that the TOM is hindered. When further increasing the temperature from 825 °C to 850 °C, the selectivity towards CO, CO₂ and C₂ remains essentially the same.

Figure 2.3b illustrates the effect of the temperature on the H₂ and water molar flow rates. The production of both compounds increases with the temperature. The increasing water molar flow rate, i.e., from 35 mmol s⁻¹ kg_{cat}⁻¹ at 800 °C to 98 mmol s⁻¹ kg_{cat}⁻¹ at 850 °C, is more pronounced than that of the H₂ molar flow rate, i.e., from 27 mmol s⁻¹ kg_{cat}⁻¹ at 800 °C to 45 mmol s⁻¹ kg_{cat}⁻¹ at 850 °C. This is in line with the increasing trend of oxygen conversion, i.e., partial and total oxidations that produce water. The H₂ molar flow rate increases smoothly with the temperature, indicating that, as long as oxygen is not totally consumed, the non-oxidative reactions are less favored as the temperature increases compared to the oxidative reactions.

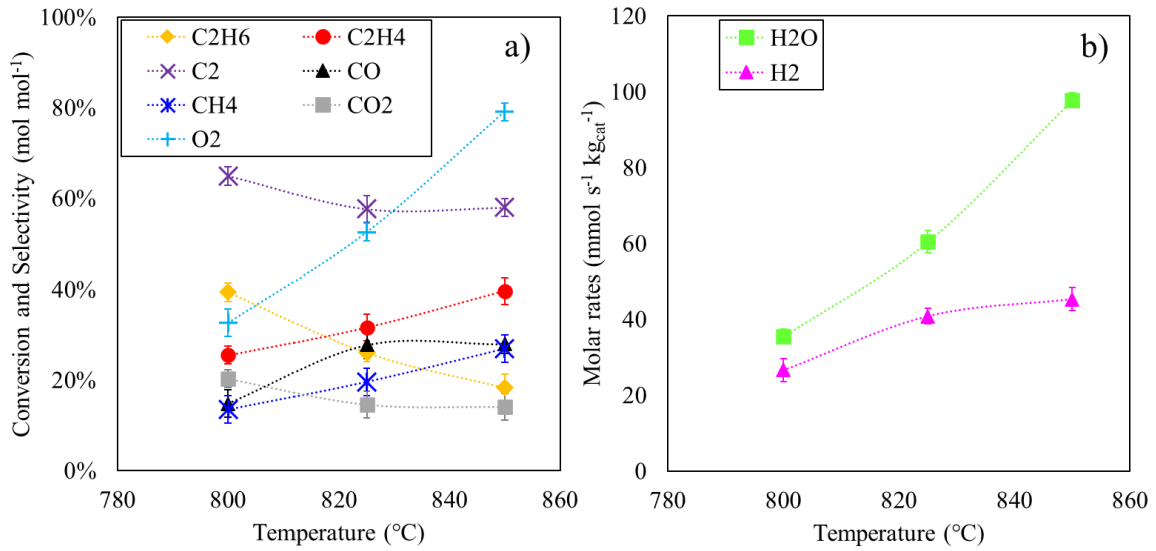


Figure 2.3. (a) Methane and oxygen conversion and selectivities towards ethane, ethylene, C₂, CO and CO₂ as a function of the temperature. (b) Molar flow rates of H₂ and water as a function of the temperature. CH₄/O₂ = 4 mol mol⁻¹, p_{tot} = 100 kPa, W_{cat}/F_{CH₄,in} = 2.50 kg_{cat} s mol⁻¹. Lines are added to guide the eye.

2.3.4 Rate equations

The rate equations of the twelve reaction steps, see Table 2.2, are presented as follows:

$$r_j = k_{0,j} e^{-E_{a_j}/RT} p_{C,i} p_{O_2} \quad j = 1 - 9 \quad (2.9)$$

$$r_{10} = k_{0,10} e^{-E_{a_{10}}/RT} p_{C_2H_6} \quad (2.10)$$

$$r_j = k_{0,j} e^{-E_{a_j}/RT} p_{C,i} p_{H_2O} \quad j = 11 - 12 \quad (2.11)$$

Eq. (2.9) indicates the nine oxidative reactions, while the subscript C specifies the carbon species considered in the reaction *j*, i.e., methane, ethane, ethylene, or CO, Eq. (2.10) describes the non-oxidative TDE, and Eq. (2.11) describes those reactions where water reacts with the carbon species. The calculation of the reaction rates, *r_j*, requires the corresponding pre-exponential factor, *k_{0,j}*, activation energy, *E_{aj}*, and partial pressure of the reactants *i*, *p_i*, for the reaction.

2.3.5 Model performance

The parameter estimates, along with their corresponding confidence intervals, obtained after regression of the kinetic model to the experimental data are presented in Table 2.3.

Table 2.3. Parameter estimates and corresponding 95% confidence intervals from the OCoM kinetic model over the MnNaW/SiO₂ catalyst.

Acronym	k_0 [mmol s ⁻¹ kg _{cat} ⁻¹ Pa ⁻²]	E _a [kJ mol ⁻¹]
OCM	$1.95 \times 10^4 \pm 1.11 \times 10^3$	227 ± 6
TOM	3.07×10^{-1b}	210^b
POM	$6.90 \times 10^{-2} \pm 4.08 \times 10^{-3}$	129 ± 14
ODH	$2.86 \times 10^2 \pm 8.25 \times 10$	176 ± 79
TOE	$1.47 \times 10^{-1} \pm 5.95 \times 10^{-2}$	107 ± 39
POE	4.65×10^b	224^b
TOEt	9.53×10^{-2b}	136^b
POEt	$2.64 \times 10^5 \pm 6.51 \times 10^4$	242 ± 60
TOCO	$5.99 \times 10^2 \pm 2.18 \times 10^2$	204 ± 39
TDE	$2.45 \times 10^8 \pm 8.71 \times 10^{7a}$	220 ± 11
SRM	$7.88 \times 10^4 \pm 2.01 \times 10^4$	262 ± 3
WGSR	2.84×10^b	161^b

^a units [mmol s⁻¹ kg_{cat}⁻¹ Pa⁻¹]. ^b No statistically significant values determined

The initial guesses for the activation energies and pre-exponential factors were chosen from physically realistic values reported in literature [30,31,33,34]. No statistically significant values were obtained for the parameters corresponding to TOM, POE, TOEt, and WGSR. After an analysis of the reaction rates, see Appendix 2B, these four reactions were omitted from the kinetic model because their reaction rates are one or more orders of magnitude lower than those of the other reactions. It is noteworthy that the reactions were removed one by one starting with POE, then TOM, TOEt, and lastly WGSR.

The model comprising the remaining eight global reactions is globally significant with an F value of 636, exceeding the tabulated one of 3 by two orders of magnitude. The estimated pre-exponential factors and activation energies are within the range of those reported in literature [13,33–35], and the highest absolute value determined for the binary correlation coefficients amounts to 0.85, indicating that the parameters are statistically uncorrelated.

Figure 2.4 highlights the correspondence between model simulations and experimental observations in a parity plot. The kinetic model exhibits a good fit to the observations over the range of the experimental conditions presented in Table 2.1 and no evidence of any systematic deviations can be observed. Moreover, Figure 2.5 compares the experimentally observed and model simulated evolution of carbon species selectivity as a function of methane conversion at the operating conditions. At low methane conversion, the ethane selectivity is the highest among the carbon species. From the primary step reactions, i.e., OCM and POM, the OCM pre-exponential factor is six orders of magnitude higher than the one of POM. This significant difference results in a higher simulated production of ethane than of CO. From the ethane oxidations, the ODH pre-exponential factor is three orders of magnitude higher than the one from TOE, resulting in the simulation of more ethylene than CO₂. This stems from ethane being converted more to ethylene at higher methane conversion. The pre-exponential factor of the TDE cannot be directly compared with the pre-exponential factor of the other reactions as it is a monomolecular rather than a bimolecular one. Nevertheless, the analysis of the reaction rates presented in Appendix 2B shows that the TDE rate has the same order of magnitude as the one of ODH at 800 °C and is one order of magnitude higher than the ODH rate at 850 °C. Thus, at high temperature (850 °C) ethylene tends to be produced more from the non-oxidative TDE than from ODH. From the bimolecular reactions proposed in the kinetic model, POEt and SRM have the highest pre-exponential factor, both producing CO. This explains why CO has the second highest selectivity among the carbon species at high methane conversions. Furthermore, reactions such as SRM, POEt, OCM, and TDE have activation energies equal to or exceeding 220 kJ mol⁻¹, hence, indicating that these reactions are more sensitive to the temperature, which is in line with literature [30,33,36] and with what has been shown in Figure 2.5. If, at high temperatures (~850 °C), the ethane produced from OCM is totally consumed by the TDE, no more ethylene can be formed and the production of CO is favored, mainly through the POEt and SRM.

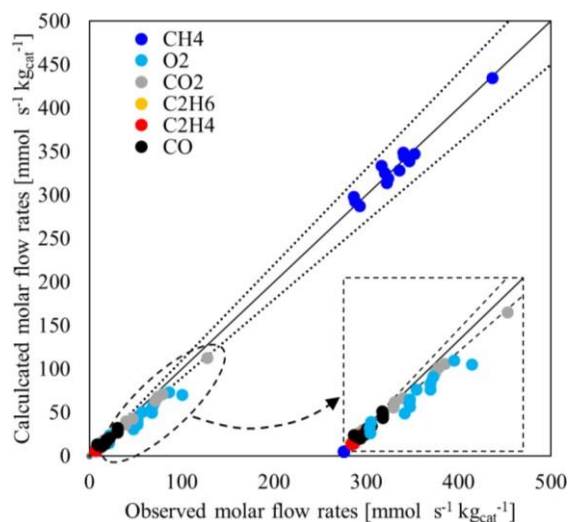


Figure 2.4. Parity diagram of the observed and calculated molar flow rates for the 8-steps kinetic model. Full line is the first bisector and dashed lines represent the 10% deviation.

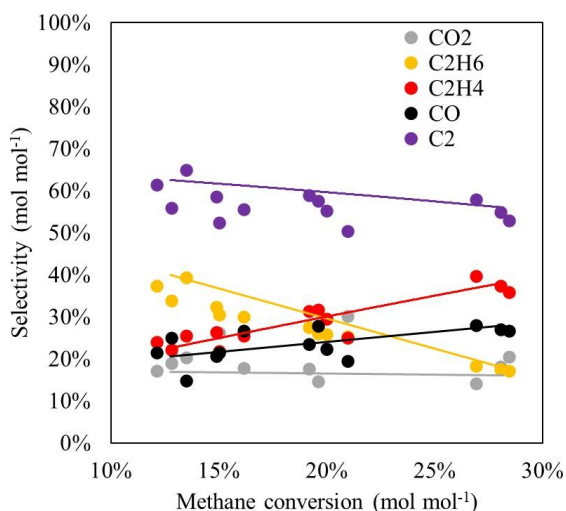


Figure 2.5. Carbon species selectivity as a function of the methane conversion. Symbols represent the experimental data and full lines the simulations from the kinetic model.

2.4 The C123 process

2.4.1 General concept

The proposed C123 process configuration, see Figure 2.6, considers as feedstock a methane-rich source, e.g., natural gas, shale gas, or biogas, which is mixed with oxygen. Please note that a third stream can be fed to the mixer accounting for the recycling of one of the separation unit outlet streams set downstream. Then, this mixture of gases is fed into the OCoM

reactor, from which the effluent is sent to the subsequent hydroformylation reactor to produce propanal from ethylene, CO and hydrogen [14,28]. The HF reactor outlet stream is sent to a separation unit that separates the liquid species, i.e., propanal and water, from the unreacted gases, i.e., CH₄ and CO₂, assuming total conversion of ethylene, H₂ and CO. The separation unit outlet stream containing the gases is led towards the mixer at the beginning of the C123 process.

In contrast to what is typically pursued in the OCM literature, OCoM not specifically targets a high methane conversion and C₂ yield per pass, but rather the production of a suitable feedstock for subsequent hydroformylation of ethylene (HF) to propanal, i.e., C₂H₄/CO/H₂ molar ratio of 1/1/1 and total conversion of oxygen. This can be achieved by exploiting the other than OCM reactions and, equally importantly, allows overcoming the challenges related to the desired products separation from the single-pass OCM outlet gas mixture. Simultaneously, it avoids the presence of oxygen in the outlet stream which can trigger undesired performance of HF reactor. The OCoM reactor is the core of the C123 process and its performance is assessed making use of the kinetic model developed in the previous section.

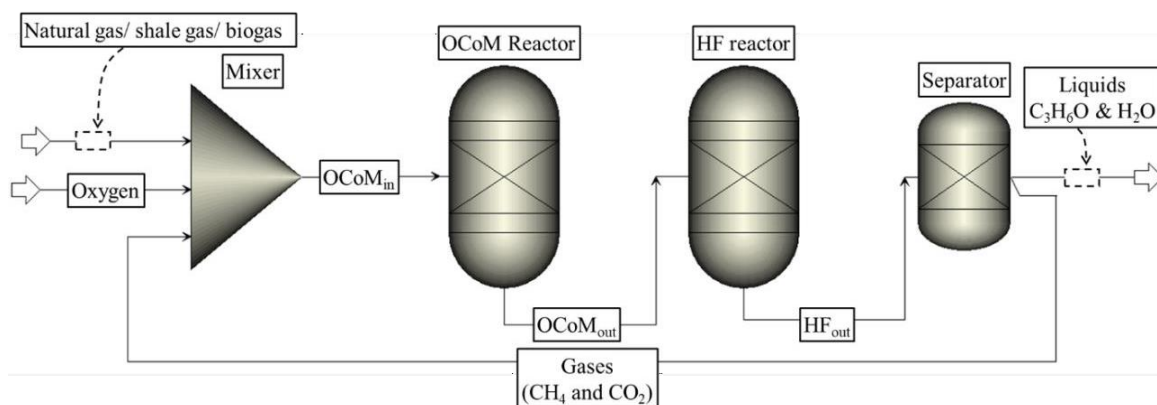


Figure 2.6. Representation of unit-operations in the C123 process. Depending of the methane source, natural gas, shale gas or biogas is considered. The C123 process consists of a mixer unit, an Oxidative Conversion of Methane (OCoM) reactor, the Hydroformylation of Ethylene reactor (HF), and a separation unit. The separation unit separates the C₃ liquid species (propanal) and the gas species from the HF outlet stream. Gas species are recycled towards the mixer.

2.4.2 OCoM reactor - temperature assessment

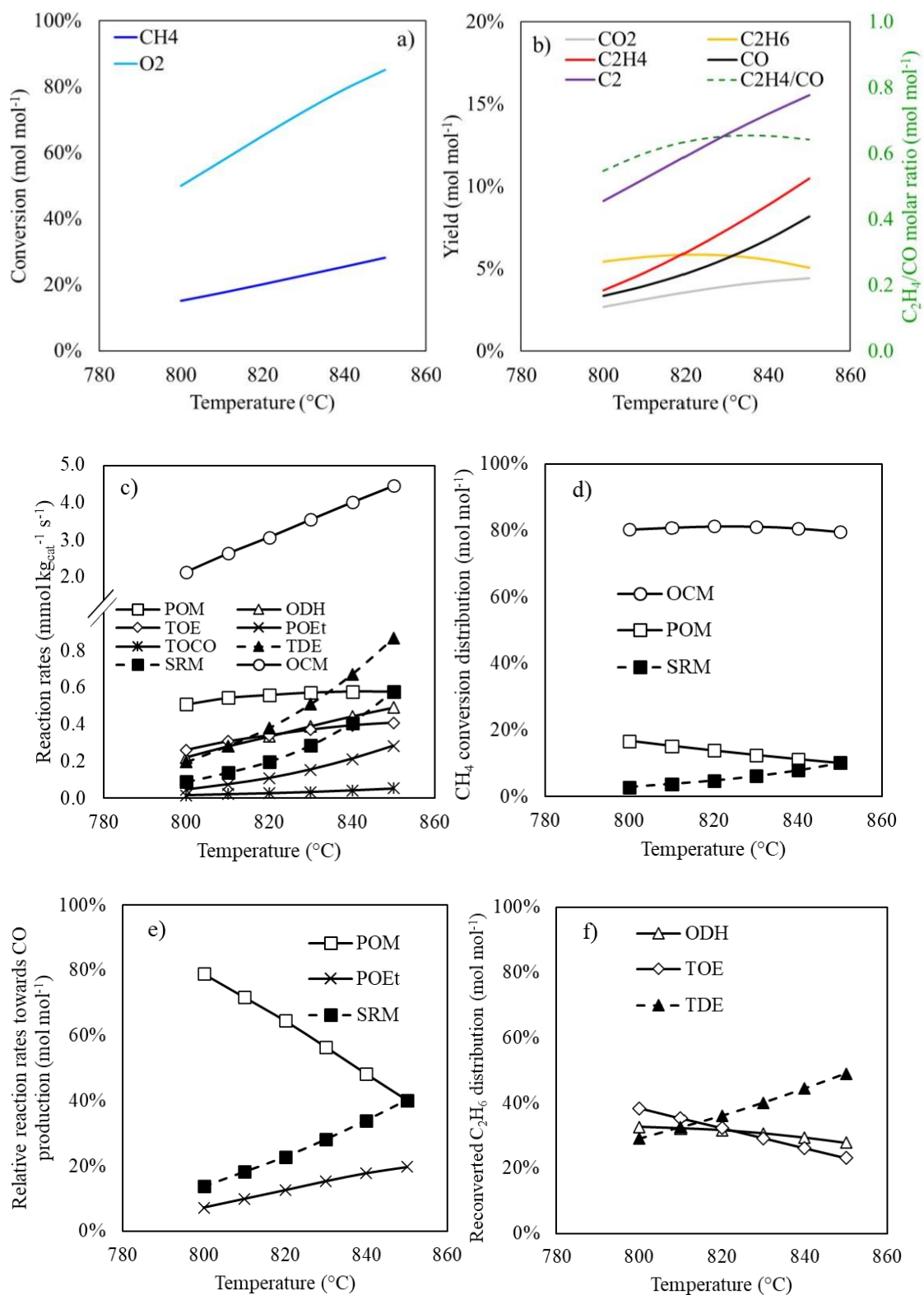
The effect of the temperature on OCoM is illustrated in Figure 2.7. The CH₄/O₂ inlet molar ratio and the $W_{\text{cat}}/F_{\text{CH}_4,\text{in}}$ are set at 4 mol mol⁻¹ and 2.5 kg_{cat} s mol⁻¹, respectively. The methane and oxygen conversion increase with the temperature, see Figure 2.7a, amounting to

maximally 28% and 85% mol mol⁻¹, respectively, at 850 °C, meaning that the desired total oxygen conversion for OCoM is not reached yet. At low temperatures (800 °C), i.e., where the methane conversion remains as low as 15% mol mol⁻¹, ethane has the highest yield (5% mol mol⁻¹) among the other carbon species, see Figure 2.7b. However, as the temperature increases, the yields of the C₂ species, ethylene, CO and CO₂ increase, while the ethane yield slightly decreases. Because the ethylene and CO yield exhibit a similar increase as the temperature increases, the C₂H₄/CO molar ratio slightly increases from 0.5 to 0.65 mol mol⁻¹ with temperature from 800 °C to 830 °C, and then its value remains constant from 830 °C to 850 °C. The yield trends can be interpreted in terms of the simulated reaction rates shown in Figure 2.7c and the contribution factors displayed in Figure 2.7d – g. OCM has the highest reaction rate among the eight kinetically relevant reactions, which is in line with the fact that ethane is formed in one of the primary reaction steps. At 800 °C, POM exhibits the second highest rate (0.58 mmol kg_{cat}⁻¹ s⁻¹) between the other reaction rates. Nevertheless, as the temperature increases from 800 °C to 850 °C, the SRM rate approximates that of the POM. This change in the reaction rates explains the distribution of the methane conversion depicted in Figure 2.7d and e. Methane conversion occurs mainly (80% mol mol⁻¹) via OCM. At 800 °C, 3% mol mol⁻¹ of methane conversion occurs via SRM, representing the 14% mol mol⁻¹ of CO production, while 17% mol mol⁻¹ of methane conversion proceeds via POM, amounting to 79% mol mol⁻¹ of CO production. As the temperature increases to 850 °C, both SRM and POM contribute equally, each responsible of 10% mol mol⁻¹ of methane conversion and 40% mol mol⁻¹ of CO production. The relevance of SRM is enhanced due to the production of water during the hydrocarbon oxidative reactions, i.e., producing CO from methane and water.

On the other hand, as the temperature increases from 800 °C to 850 °C, the TOE, ODH and TDE rates exhibit an increase from 0.26 mmol kg_{cat}⁻¹ s⁻¹ to 0.41 mmol kg_{cat}⁻¹ s⁻¹, 0.22 mmol kg_{cat}⁻¹ s⁻¹ to 0.49 mmol kg_{cat}⁻¹ s⁻¹, and 0.20 mmol kg_{cat}⁻¹ s⁻¹ to 0.87 mmol kg_{cat}⁻¹ s⁻¹, respectively. These increasing trends indicate that ethane is further converted into ethylene and CO₂, being the reason why ethane yield does not increase as the temperature rises. At 800 °C ethane is further converted as follows: 29%, 33% and 38% mol mol⁻¹ via TOE, ODH and TDE, respectively, see Figure 2.7f. While at 850 °C, ethane further conversion occurs through TOE and ODH decreases to 23% and 28% mol mol⁻¹, respectively and for TDE increases to 49% mol mol⁻¹. This because at 850 °C the TDE rate becomes the second highest reaction rate among all reaction rates, contributing to 60% mol mol⁻¹ of ethylene production, see Figure 2.7g.

Chapter 2 – Oxidative Conversion of Methane (OCoM)

The analysis made of the temperature impact on OCoM indicates that, to reach total conversion of oxygen, the maximum temperature possible should be considered in the operating conditions. Thus, 850 °C is set for the further operating condition assessment.



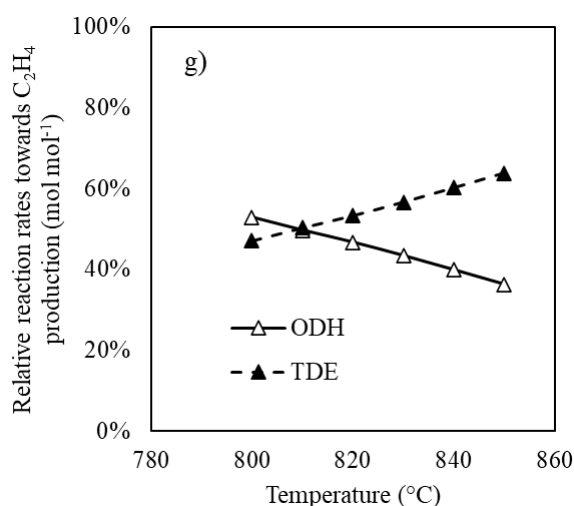


Figure 2.7. Temperature effect on: (a) Methane and oxygen conversion, (b) carbon species yields, (c) reaction rates, (d) CH₄ conversion distribution, (e) relative reaction rates towards CO production, (f) reconverted ethane distribution, and (g) relative reaction rates towards ethylene production. CH₄/O₂ inlet molar ratio of 4 mol mol⁻¹ and W_{cat}/F_{CH₄,in} of 2.5 kg_{cat} s mol⁻¹. Symbols are added to distinguish between the reactions.

2.4.3 OCoM reactor – space time assessment

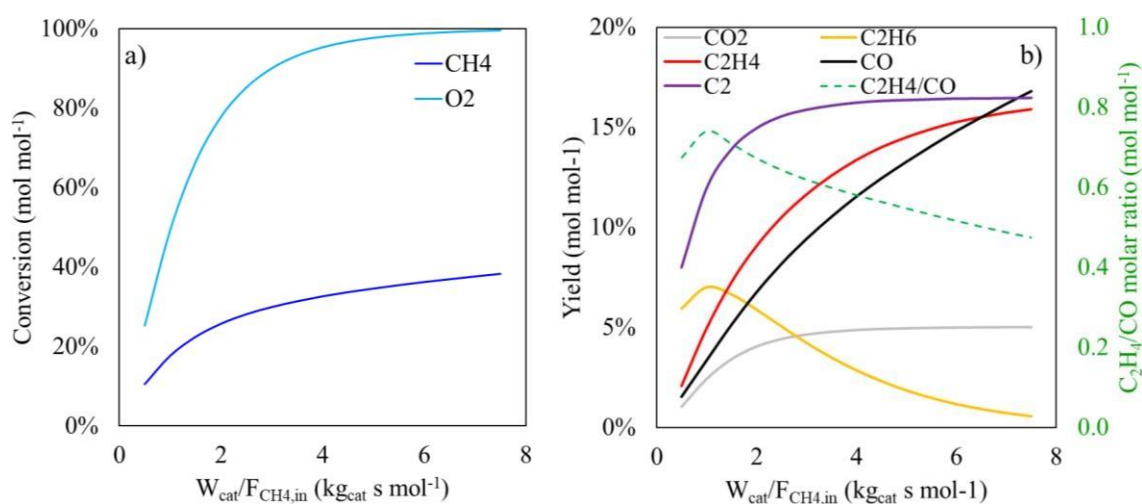
The effect of increasing the $W_{\text{cat}}/F_{\text{CH}_4,\text{in}}$ from 0.5 to 7.5 kg_{cat} s mol⁻¹, by decreasing the amount of methane in feedstock while keeping the catalyst mass fixed, on OCoM is illustrated in Figure 2.8. The CH₄/O₂ inlet molar ratio and temperature are fixed at 4 mol mol⁻¹, and 850 °C, respectively. The methane and oxygen conversion increase with the $W_{\text{cat}}/F_{\text{CH}_4,\text{in}}$, see Figure 2.8a. Total oxygen conversion is reached at $W_{\text{cat}}/F_{\text{CH}_4,\text{in}}$ of 6.5 kg_{cat} s mol⁻¹, with the methane conversion amounting to 36% mol mol⁻¹. Three different trends can be discerned with respect to the yield of the different carbon species as the $W_{\text{cat}}/F_{\text{CH}_4,\text{in}}$ increases, see Figure 2.8b. The yields of ethylene and CO increase, the yields towards CO₂ and C₂ increase up to $W_{\text{cat}}/F_{\text{CH}_4,\text{in}}$ of 3 kg_{cat} s mol⁻¹, after which they remain constant, and the ethane yield increases slightly from 0.5 to 1 kg_{cat} s mol⁻¹ and subsequently decreases. Furthermore, the C₂H₄/CO molar ratio trend follows the same trend as the ethane yield. This is not desired for OCoM, because the C₂H₄/CO molar ratio decreases.

The reaction rates indicate that OCM has the highest contribution among all the reactions, as aforementioned, because ethane is formed in one of the primary reaction steps, see Figure 2.8c. From 0.5 kg_{cat} s mol⁻¹ to 2.5 kg_{cat} s mol⁻¹, the oxidative reaction rates, i.e., ODH, POM, ODH, TOE, POEt and TOCO, significantly increase, and from 2.5 kg_{cat} s mol⁻¹ to 6.5 kg_{cat} s mol⁻¹ their rates further slightly increase until reaching a maximum rate due to the

total conversion of oxygen. In contrast, the non-oxidative reactions, i.e., TDE and SRM, continue to increase from $0.5 \text{ kg}_{\text{cat}} \text{ s mol}^{-1}$ to above $6.5 \text{ kg}_{\text{cat}} \text{ s mol}^{-1}$.

The effect of having different reaction rate trends for the oxidative and non-oxidative can be seen in the conversion distribution of methane, see Figure 2.8d. At $0.5 \text{ kg}_{\text{cat}} \text{ s mol}^{-1}$, 87% mol mol^{-1} of the methane conversion is attributed to OCM, 11% mol mol^{-1} to POM and 2% mol mol^{-1} to SRM. However, at $7.5 \text{ kg}_{\text{cat}} \text{ s mol}^{-1}$, methane conversion via OCM amounts to 65% mol mol^{-1} , 8% mol mol^{-1} via POM and 26% mol mol^{-1} through SRM. Moreover, the increasing contribution of SRM with the $W_{\text{cat}}/F_{\text{CH}_4,\text{in}}$ is also reflected in the CO production, see Figure 2.8e. At $0.5 \text{ kg}_{\text{cat}} \text{ s mol}^{-1}$, CO is mainly produced from POM (81% mol mol^{-1}), and, to a lower extent, via POEt (7% mol mol^{-1}) and SRM (12% mol mol^{-1}). Nevertheless, at $7.5 \text{ kg}_{\text{cat}} \text{ s mol}^{-1}$, CO is produced mostly by SRM (65% mol mol^{-1}), while the rest is produced by POM (21% mol mol^{-1}) and POEt (14% mol mol^{-1}).

Conversely, the further conversion of ethane at $0.5 \text{ kg}_{\text{cat}} \text{ s mol}^{-1}$ approximately equally occurs through ODH, TOE, and TDE ($\sim 33\% \text{ mol mol}^{-1}$), see Figure 2.8f. Nevertheless, at $7.5 \text{ kg}_{\text{cat}} \text{ s mol}^{-1}$, the further conversion of ethane is largely attributed to TDE (60% mol mol^{-1}), while the rest occurs via ODH (22% mol mol^{-1}) and TOE (18% mol mol^{-1}). In terms of ethylene production, see Figure 2.8g, the difference between the ethylene produced by TDE and ODH becomes more pronounced as the $W_{\text{cat}}/F_{\text{CH}_4,\text{in}}$ increases, being 73% and 27% mol mol^{-1} of ethylene produced via TDE and ODH, respectively, at $7.5 \text{ kg}_{\text{cat}} \text{ s mol}^{-1}$.



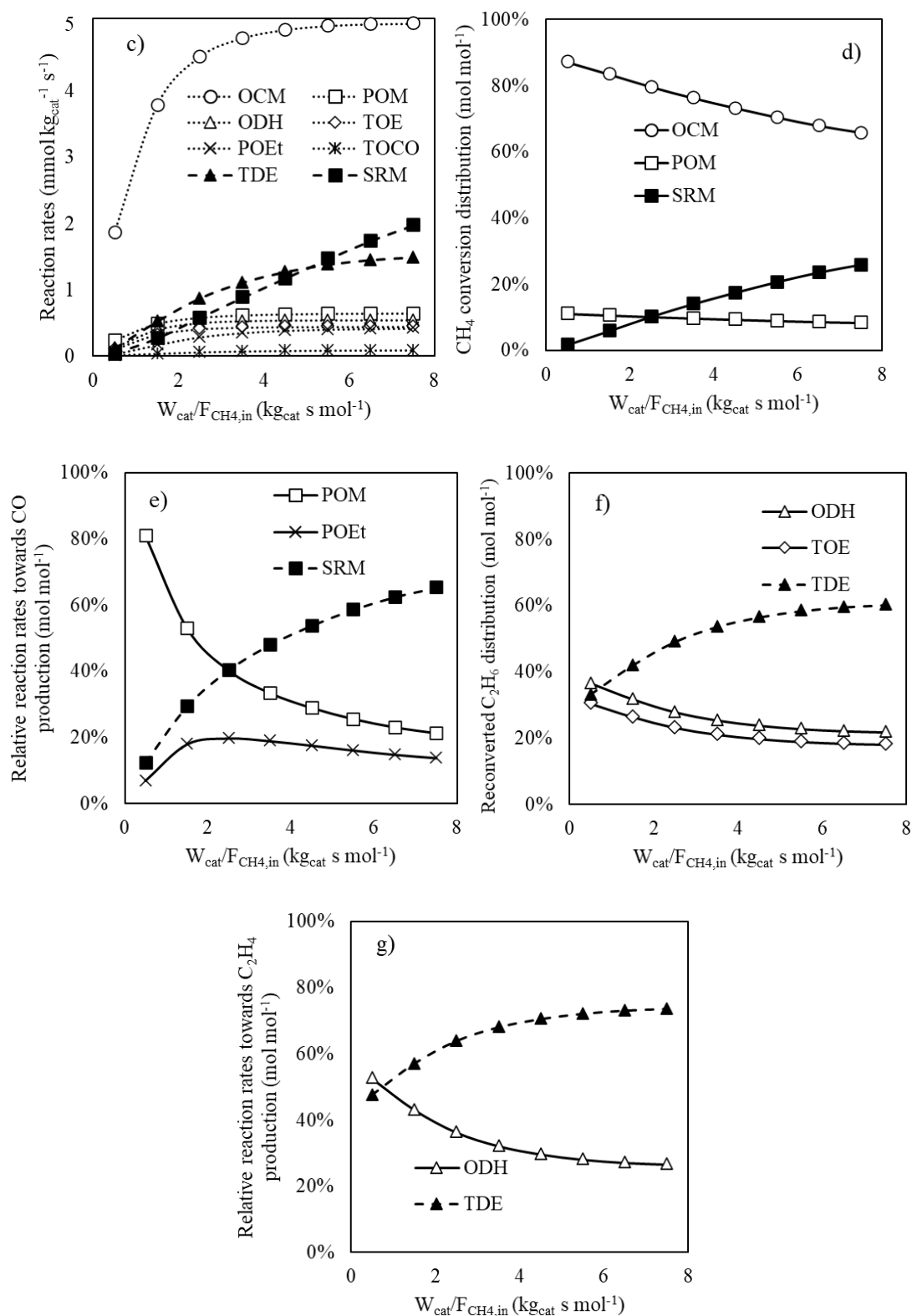


Figure 2.8. $W_{cat}/F_{CH_4,in}$ effect on: (a) Methane and oxygen conversion, (b) carbon species yields, (c) reaction rates, (d) CH_4 conversion distribution, (e) relative reaction rates towards CO production, (f) reconverted ethane distribution, and (g) relative reaction rates towards ethylene production. CH_4/O_2 inlet molar ratio of 4 mol mol⁻¹ and temperature of 850 °C. Symbols are added to distinguish between the reactions.

The results indicate that the desired total conversion of oxygen is reached at $6.5 \text{ kg}_{\text{cat}} \text{ s mol}^{-1}$. Moreover, a higher $W_{\text{cat}}/F_{\text{CH}_4,\text{in}}$ leads to higher CO yields than ethylene yields, decreasing the $\text{C}_2\text{H}_4/\text{CO}$ molar ratio, which is not desired for OCoM purposes. Based on this, the $W_{\text{cat}}/F_{\text{CH}_4,\text{in}}$ of $6.5 \text{ kg}_{\text{cat}} \text{ s mol}^{-1}$ is selected for the further operating condition analysis and optimization.

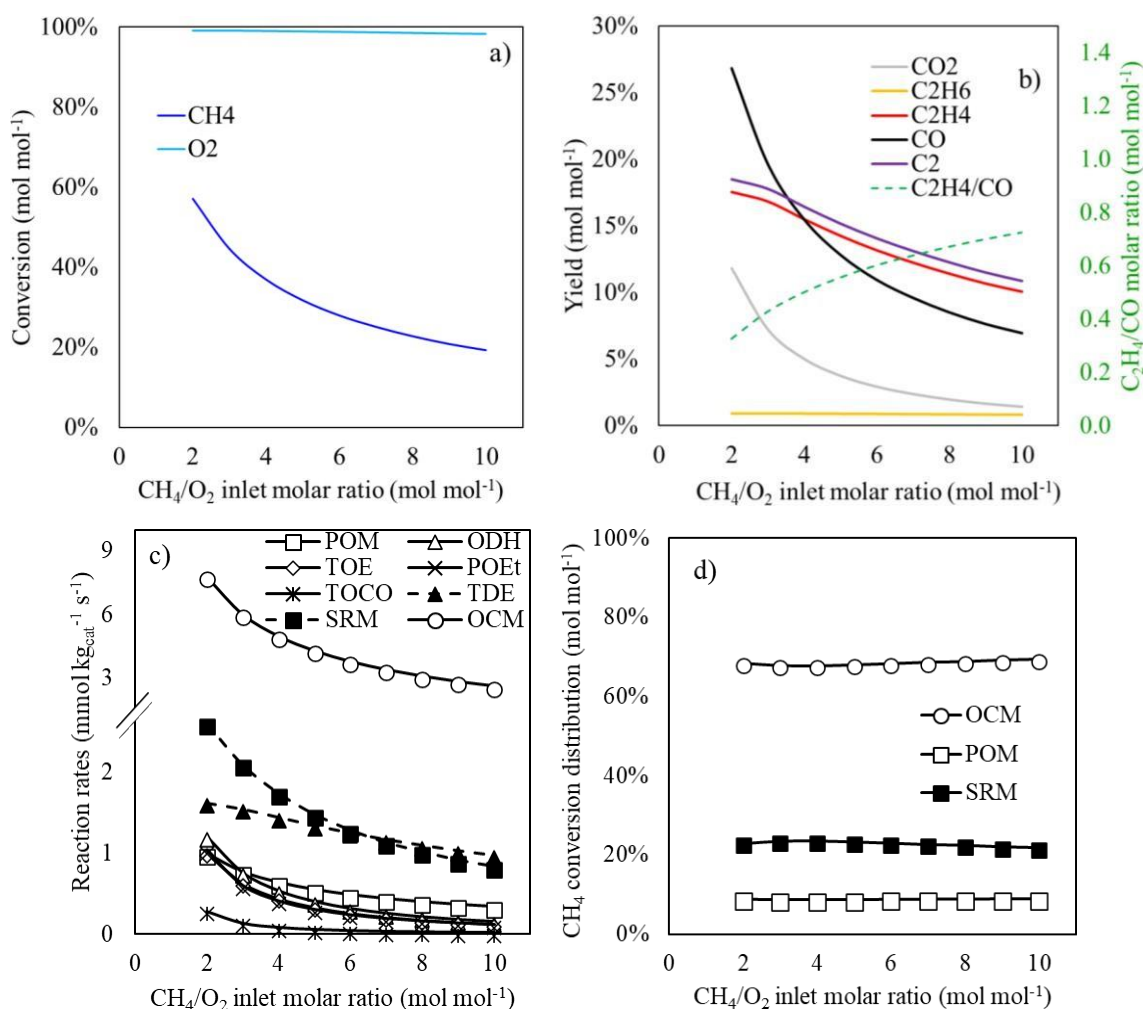
2.4.4 OCoM reactor - methane to oxygen inlet molar ratio assessment

The CH_4/O_2 inlet molar ratio is varied from 2 to 10 mol mol^{-1} by decreasing the amount of oxygen in feedstock while keeping the amount of methane fixed. The corresponding effect on the OCoM behavior is illustrated in Figure 2.9. The $W_{\text{cat}}/F_{\text{CH}_4,\text{in}}$ and temperature are set at $6.5 \text{ kg}_{\text{cat}} \text{ s mol}^{-1}$, and $850 \text{ }^\circ\text{C}$, respectively. The methane conversion decreases from 57% to 19% mol mol^{-1} as the CH_4/O_2 inlet molar ratio increases from 2 to 10 mol mol^{-1} , while the oxygen conversion essentially remains complete, see Figure 2.9a. Being already below 1% mol mol^{-1} , the ethane yield is not significantly impacted, while the other carbon species yields decrease with increasing CH_4/O_2 inlet molar ratio, see Figure 2.9b. Furthermore, the decrease of the CO and CO_2 yields is more pronounced than that of the ethylene yield. This trend is also seen in the reaction rates, see Figure 2.9c, where the TDE rate decreases linearly, while the other reaction rates exhibit an exponential decrease. At low CH_4/O_2 inlet molar ratio (2 mol mol^{-1}), i.e., more oxygen in the feedstock, the production of CO is higher compared to ethylene. While, at high CH_4/O_2 inlet molar ratio (10 mol mol^{-1}), CO production is lower than ethylene, i.e., TDE rate is more pronounced than SRM, leading to an increase in the $\text{C}_2\text{H}_4/\text{CO}$ outlet molar ratio. In terms of methane conversion distribution, the simulation results show that there is no significant effect of the CH_4/O_2 inlet molar ratio, see Figure 2.9d. Because OCM has the highest reaction rate among all the reactions, methane conversion occurs for 69% mol mol^{-1} through it. Furthermore, POM and SRM contribute for 9% and 22% mol mol^{-1} to the methane conversion, respectively. This indicates that CO is mainly produced through SRM (56% – 65% mol mol^{-1}), while the rest is produced through POM (21% – 26% mol mol^{-1}), and POEt (22% – 9% mol mol^{-1}), see Figure 2.9e.

On other hand, with a CH_4/O_2 inlet molar ratio of 2 mol mol^{-1} , the distribution of ethane further conversion occurs as follows: 32% mol mol^{-1} through ODH, 26% mol mol^{-1} via TOE, and 42% mol mol^{-1} through TDE, see Figure 2.9f. Moreover, as the CH_4/O_2 inlet molar ratio increases up to 10 mol mol^{-1} , the reconverted ethane distribution mainly takes place via

Chapter 2 – Oxidative Conversion of Methane (OCoM)

TDE (78% mol mol⁻¹). This is because the TDE rate linearly decreases while ODH and TOE rates exhibit a steeper decrease. Regarding the ethylene production, a similar trend is observed, see Figure 2.9g. At CH₄/O₂ inlet molar ratio of 2 mol mol⁻¹, 57% mol mol⁻¹ of ethylene is produced via TDE and 43% mol mol⁻¹ through ODH. However, at CH₄/O₂ inlet molar ratio of 10 mol mol⁻¹, 86% mol mol⁻¹ of ethylene is produced from TDE and 14% mol mol⁻¹ from ODH. Based on the results presented in this section, for OCoM purposes, i.e., high ethylene yield and C₂H₄/CO outlet molar ratio, a high CH₄/O₂ inlet molar ratio is preferable.



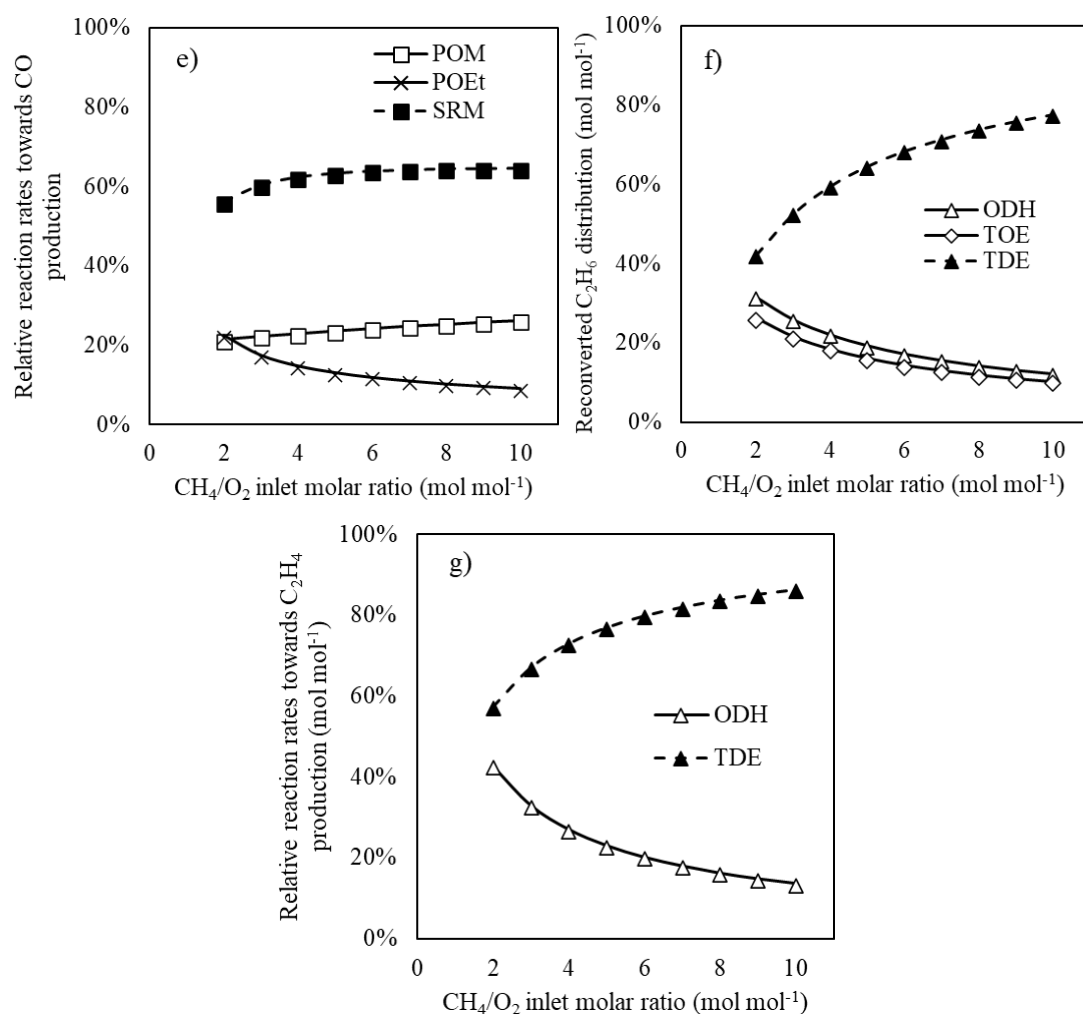
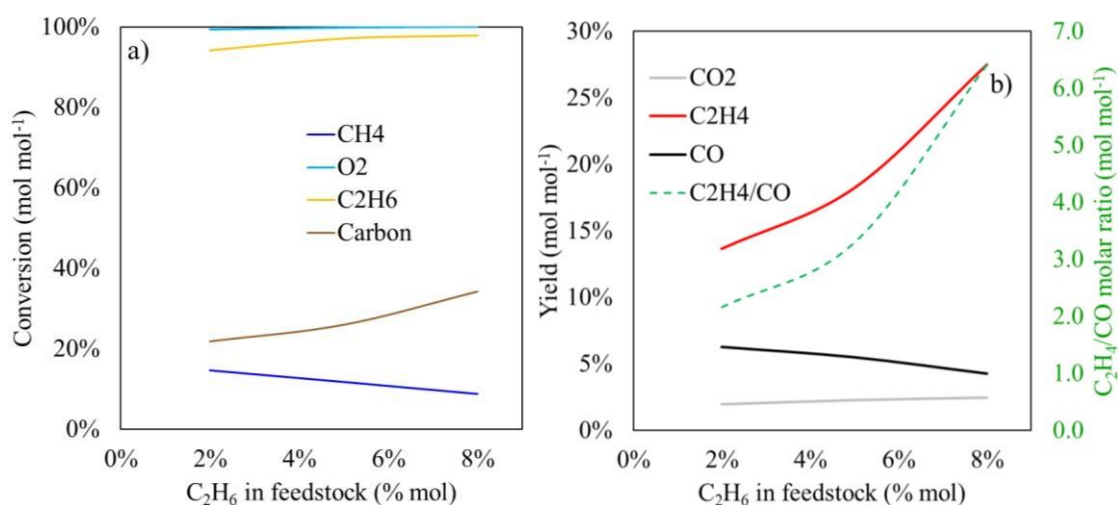


Figure 2.9. CH_4/O_2 inlet molar ratio effect on: (a) Methane and oxygen conversion, (b) carbon species yields, (c) reaction rates, (d) CH_4 conversion distribution, (e) relative reaction rates towards CO production, (f) reconverted ethane distribution, and (g) relative reaction rates towards ethylene production. $W_{\text{cat}}/F_{\text{CH}_4,\text{in}}$ of 2.5 kg_{cat} s mol⁻¹ and temperature of 850 °C. Symbols are added to distinguish between the reactions.

2.4.5 OCoM reactor - co-feeding ethane assessment

Depending of the source, shale gas might contain a significant amount of ethane, i.e., up to 13% [11]. Hence, the effect of co-feeding ethane on OCoM and, more particularly, the carbon conversion, carbon species yields and reaction rates, is analyzed in this section. The ethane content in the feedstock is varied from 2 to 8 %, by increasing the amount of ethane while keeping the amount of methane and oxygen fixed. The amount of inert was adjusted to maintain an identical total molar flow rate in all simulations. The CH_4/O_2 inlet molar ratio, $W_{\text{cat}}/F_{\text{CH}_4,\text{in}}$, and temperature are set at 10 mol mol⁻¹, 6.5 kg_{cat} s mol⁻¹ and 850 °C, respectively. Because there is more than one carbon species reacting, the carbon conversion, see Eq. (2.1),

is plotted along with the methane, ethane, and the oxygen conversion in Figure 2.10a. With an increasing amount of ethane in the feedstock, the methane conversion decreases, while the ethane conversion, which consistently exceeds 90% mol mol⁻¹, even slightly increases further. This stems from ethane being more reactive than methane [37] and, hence, less oxygen remains for ‘activating’ methane. As the amount of ethane in the feedstock increases from 2% to 8% mol mol⁻¹, the ethylene yield increases from 14% to 28% mol mol⁻¹, see Figure 2.10b. Conversely, the CO yield decreases from 6% to 4% mol mol⁻¹. Thus the C₂H₄/CO molar ratio in the effluent increases with the amount of ethane in the feedstock. These trends are further assessed making use of the reaction rates and the contribution factors presented in Figure 2.10c – g. The methane oxidation reaction rates, i.e., OCM and POM, decrease as the amount of ethane increases in the feedstock, while the ethane consumption rates increase, i.e., ODH, TOE, and TDE, see Figure 2.10c, TDE exhibiting the highest rate when the feedstock contains 8% of ethane. It is noteworthy that the SRM rate remains constant with the variation of ethane in the feedstock. Considering 2% of ethane in the feedstock, the methane conversion occurs as follows: 63% mol mol⁻¹ via OCM, 8% mol mol⁻¹ via POM and 29% mol mol⁻¹ through SRM, Figure 2.10d. Nevertheless, because SRM rate remains constant with the amount of ethane, but OCM and POM rates decrease, when 8% of ethane is considered in the feedstock, the conversion of methane mostly occurs via SRM (50% mol mol⁻¹) in that case. CO is, hence, mainly produced via SRM (69% – 80% mol mol⁻¹), see Figure 2.10e. In terms of ethane further conversion, from the moment oxygen reaches total conversion, most of ethane further conversion takes place through TDE (76% – 83 % mol mol⁻¹), see Figure 2.10f. In the same way, most of the production of ethylene proceeds via TDE (85% – 90 % mol mol⁻¹), as indicated in Figure 2.10g.



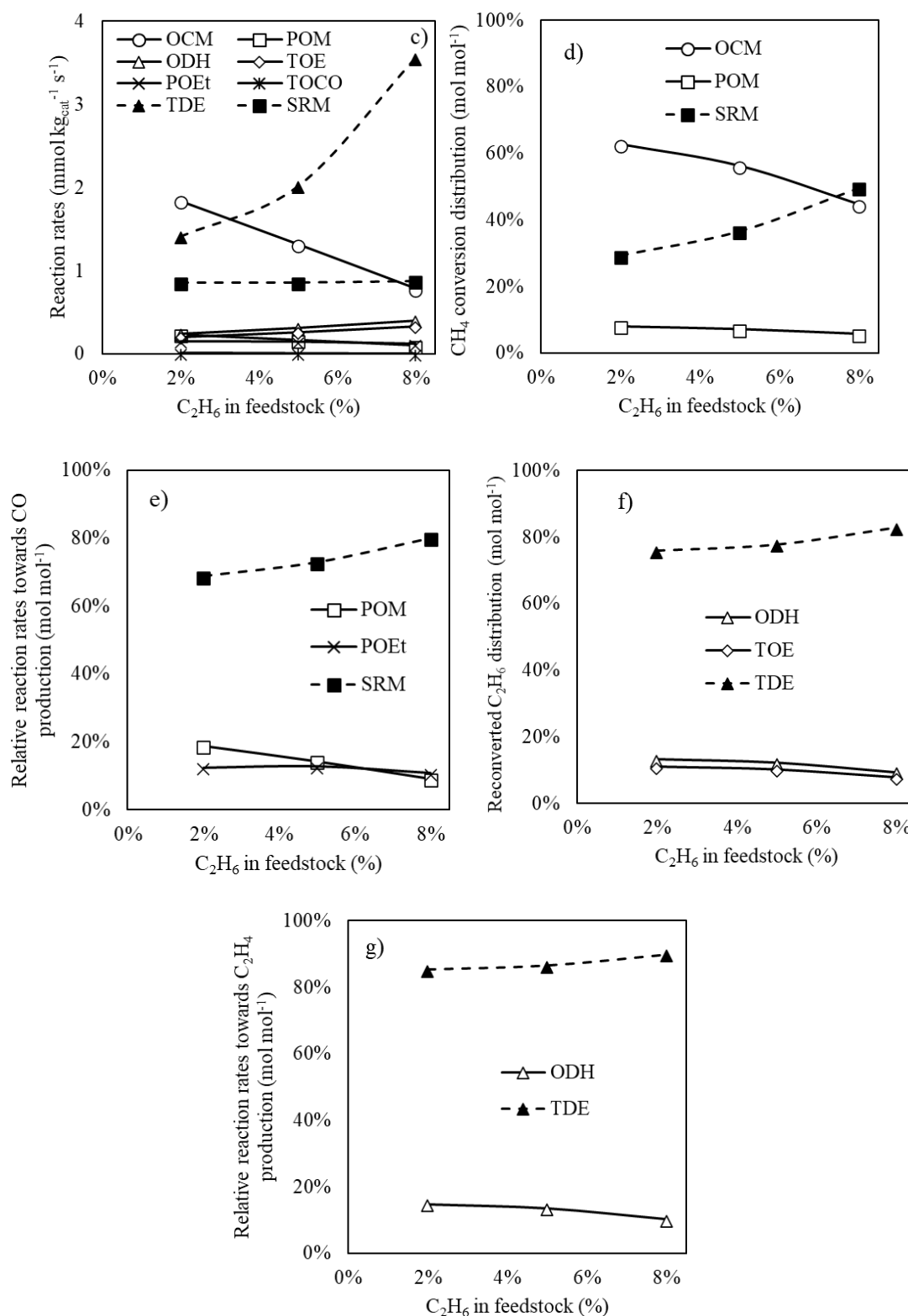


Figure 2.10. Effect of co-feeding ethane on: (a) Methane and oxygen conversion, (b) carbon species yields, (c) reaction rates, (d) CH₄ conversion distribution, (e) relative reaction rates towards CO production, (f) reconverted ethane distribution, and (g) relative reaction rates towards ethylene production. $W_{\text{cat}}/F_{\text{CH}_4,\text{in}}$ of 6.5 kg_{cat} s mol⁻¹, CH₄/O₂ inlet molar ratio of 10 mol mol⁻¹, and temperature of 850 °C. Symbols are added to distinguish between the reactions.

2.4.6 Realistic feedstocks assessment

The (once-through) OCoM reactor and the C123 process performance are evaluated considering three different feedstocks: natural gas containing only methane (NG), shale gas containing methane, CO₂ and ethane (SG), and biogas (BG), a mixture of methane and CO₂. The composition of each feedstock is listed in Table 2.4. It should be mentioned that the results discussed in Sections 2.4.2 – 2.4.4 correspond to the NG feedstock.

Table 2.4. Molar composition of the three different feedstocks considered for OCoM

Component	Composition (mol%)		
	Natural gas (NG)	Shale gas (SG)	Biogas (BG)
Methane	100	85	64
Ethane	0	8	0
CO ₂	0	7	36

2.4.7 (Once-through) OCoM reactor performance

Based on the analysis made in the previous sections, the selected operating conditions are: temperature of 850 °C, $W_{\text{cat}}/F_{\text{CH}_4,\text{in}}$ of 6.5 kg_{cat} s mol⁻¹ and CH₄/O₂ inlet molar ratio of 10 mol mol⁻¹. The calculated oxygen conversion, carbon species conversion, carbon species yields, and C₂H₄/CO molar ratio for the three OCoM feedstocks are depicted in Figure 2.11. Total conversion of oxygen is reached for each of the feedstocks (not shown). Moreover, the calculated carbon conversion when NG, SG, and BG, are considered as feedstocks amount to 27%, 31%, and 23% mol mol⁻¹, respectively, see Figure 2.11a. For SG, the methane and ethane conversion are visualized by showing them separately. Half of the carbon yield stems from methane conversion, while the other half stems from ethane conversion. In comparison with the other feedstocks, SG exhibits a higher carbon conversion (31% mol mol⁻¹), higher yield towards ethylene (19% mol mol⁻¹), and an ethylene to CO molar ratio closer to one (0.9 mol mol⁻¹), see Figure 2.11b. This is because the ethane contained in SG is totally converted, which

increases the amount of carbon converted with a factor two compared to methane conversion only, particularly via TDE and ODH. Moreover, the $C_2H_4:CO:H_2$ molar ratio (not shown in the Figure) for SG is 1/1.1/3.7, while this ratio for NG and BG amounts to 1/2.7/7.8 and 1/2/5.4, respectively. These results show that SG offers more potential than the other feedstocks for OCoM, thanks to the ethane content. Additionally, the carbon products obtained are primarily ethylene and CO. This reduces the costs associated with the separation process of the desired products from the outlet gas mixture.

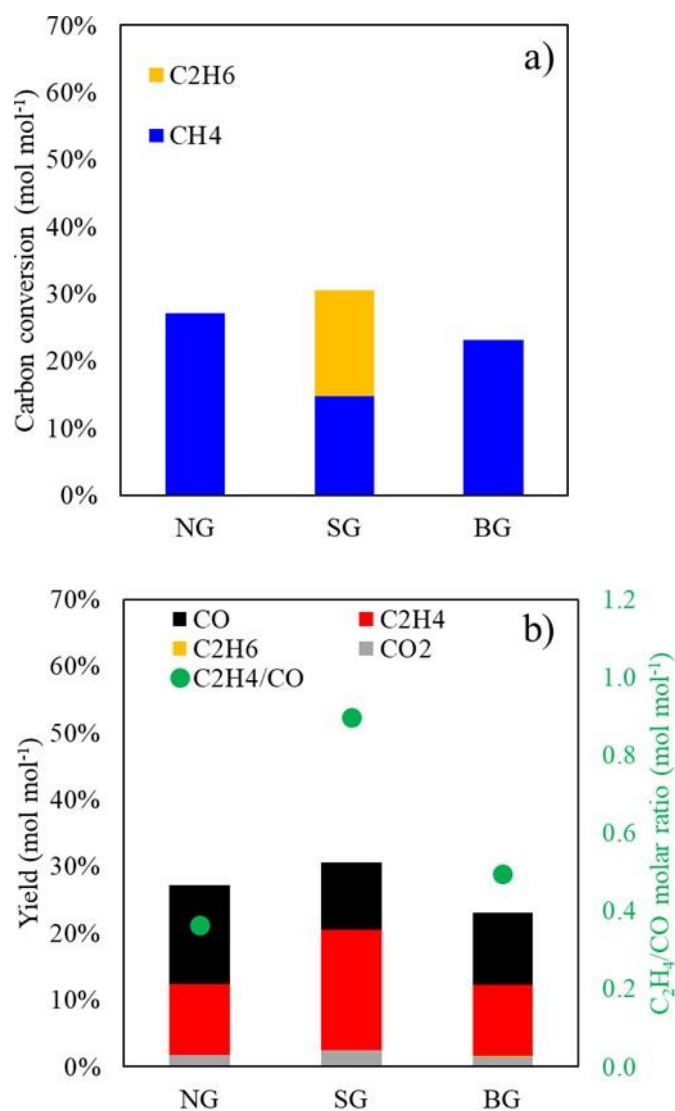


Figure 2.11. (a) Carbon conversion, and (b) carbon species yields at different OCoM feedstock compositions. Operating conditions of the (once-through) OCoM reactor: $CH_4/O_2 = 10 \text{ mol mol}^{-1}$, $W_{cat}/F_{CH_4,in} = 6.5 \text{ kg}_{cat} \text{ s mol}^{-1}$, and $T = 850 \text{ }^\circ\text{C}$.

2.4.8 Process considerations

In addition to the conversion of methane through OCoM, the C123 process also entails the production of C3 species from the OCoM effluent via hydroformylation, see Figure 2.6.

As demonstrated in Section 2.4.7, the OCoM reactor achieves its highest performance when working with SG as feedstock and with full ethane conversion. Apart from the desired components for hydroformylation, i.e., ethylene, CO and H₂, the OCoM reactor effluent also contains unreacted methane, the methane conversion amounts to 15% mol mol⁻¹, and, unavoidably, CO₂. As the CO₂ yield during OCoM only amounts to 2% mol mol⁻¹, the CO₂ mostly originates from the feedstock. It is assumed that methane and CO₂ are inert compounds in the HF reactor. To avoid significant methane emissions from the C123 process, this methane and CO₂ are recycled to the feed mixer unit.

To preserve the validity of the (once-through) OCoM reactor calculations presented in Section 2.4.7, i.e., a carbon conversion amounting to 31% mol mol⁻¹ and an ethylene yield of 19% mol mol⁻¹, the corresponding C123 process feedstock should be back-calculated. It should contain less of the recycled compounds (CH₄/CO₂) and more of the unrecycled ones (C₂H₆) such that the (once-through) OCoM reactor feedstock used in Section 2.4.7, i.e., a CH₄/C₂H₆/CO₂ inlet molar ratio of 85/8/7 and CH₄/O₂ inlet molar ratio of 10 mol mol⁻¹, remains valid after mixing the C123 process feedstock with the recycle stream. As CO₂ is produced but further considered inert in the OCoM reactor (and in the HF reactor, see above), a purge is required to prevent CO₂ from infinite accumulation and maintain the desired OCoM reactor feedstock composition. By considering shale gas with a higher content of ethane, i.e., up to 16% [7], as the C123 process feedstock, a composition, after mixing with the recycle stream containing methane and CO₂, of the OCoM reactor feedstock close to the one presented in Section 2.4.7 is envisaged. Consequently, this leads to an OCoM reactor product composition similar to that presented for the (once-through) OCoM reactor. In this way methane removal is limited to a minor amount together with the unavoidable CO₂ purging. Moreover, ca. twice the amount of oxygen considered for the (once-through) OCoM reactor calculations should be fed to maintain the CH₄/O₂ inlet molar ratio of 10 mol mol⁻¹ in the C123 process.

Although we consider the HF reactor to selectively produce C₃ species, it should be noted that ethane can be formed as a by-product in the HF reactor via ethylene hydrogenation

[38]. Recycling this ethane alongside methane and CO₂ will have a beneficial effect on the OCoM reactor performance, as explained above.

Furthermore, as the targeted equimolar mixture between ethylene and CO is not obtained, the C₂H₄/CO ratio amounted to 0.9 mol mol⁻¹ in the (once-through) OCoM reactor calculations, only 90% mol mol⁻¹ conversion of CO can be reached in the HF reactor. Thus, in a detailed design, the remainder CO needs to be considered in the recycling stream. The fate of CO in the OCoM reactor has not been explicitly considered, but it is most likely to be subject to total oxidation (TOCO). Thus, the amount of CO from the recycling stream is most likely to be converted into CO₂ in the OCoM reactor and, hence, should be kept as limited as possible.

The total inlet molar flow for the C123 process, before mixing with the recycle stream, is adjusted such that after mixing the composition corresponds to the one computed for the (once-through) OCoM simulations. The performance validation of the C123 process is thus ensured and, consequently the calculations performed for the (once-through) OCoM reactor can be considered valid during the C123 process operation.

2.5 Conclusions

The Oxidative Conversion of Methane (OCoM) has been proposed as a promising concept to valorize methane into ethylene and CO serving as an optimal feedstock towards ethylene hydroformylation for C₃ production, relevant for the growing polypropylene market. An OCoM kinetic model, trained and validated against experimental data acquired on a MnNaW/SiO₂ catalyst, was employed for assessing the potential OCoM behavior as a function of the operating conditions, more particularly, pursuing total oxygen conversion, maximal ethylene yield and an as close to equimolar C₂H₄/CO ratio as possible. The optimal operating conditions determined are a temperature of 850 °C, W_{cat}/F_{CH₄,in} of 6.5 kg_{cat} s mol⁻¹ and CH₄/O₂ inlet molar ratio of 10 mol mol⁻¹. At these conditions, the reaction rates of the Oxidative Coupling of Methane (OCM), the Steam Reforming of Methane (SRM) and the non-oxidative Thermal Dehydrogenation of Ethane (TDE) are the highest. Three different real feedstocks were assessed in OCoM reactor simulations, leading to the conclusion that shale gas is the most promising feedstock for OCoM, i.e., high carbon conversion (31% mol mol⁻¹), high ethylene yield (19% mol mol⁻¹) and C₂H₄/CO/H₂ molar ratio of 1/1.1/3.7. This leads to a more suitable OCoM outlet stream for further ethylene hydroformylation. Additionally, the high yields towards ethylene and CO from OCoM allow minimizing the energetic and economic

challenges of desired products separation from the downstream process. Last, details of the C123 process performance are given by providing some considerations to adjust the C123 process feedstock composition, considering the recycling stream within the process, such as that obtained for the (once-through) OCoM reactor calculations. This validates the C123 process viability through those calculations computed for the (once-through) OCoM reactor.

The findings of this lab-scale study offer insights for future investigations focused on process optimization, intensification, and strategies to maximize carbon yields from natural gas valorization. Within the framework of the circular economy for hydrocarbons, particularly on the assessment of potential highly exothermic reaction to industrialize as alternative of the conventional processes, an analysis of the fundamentals of a multitubular Oxidative Dehydrogenation of Ethane packed bed reactor is given in the next chapters.

2.6 References

- [1] D. Saha, H.A. Grappe, A. Chakraborty, G. Orkoulas, Postextraction Separation, On-Board Storage, and Catalytic Conversion of Methane in Natural Gas: A Review, *Chem Rev* 116 (2016) 11436–11499. <https://doi.org/10.1021/acs.chemrev.5b00745>.
- [2] B. Bharathiraja, T. Sudharsana, J. Jayamuthunagai, R. Praveenkumar, S. Chozhavendhan, J. Iyyappan, Biogas production – A review on composition, fuel properties, feed stock and principles of anaerobic digestion, *Renewable and Sustainable Energy Reviews* 90 (2018) 570–582. <https://doi.org/10.1016/j.rser.2018.03.093>.
- [3] J. Motte, P. Nachtergaele, M. Mahmoud, H. Vleeming, J.W. Thybaut, J. Poissonnier, J. Dewulf, Developing circularity, renewability and efficiency indicators for sustainable resource management: Propanol production as a showcase, *J Clean Prod* 379 (2022) 134843. <https://doi.org/10.1016/j.jclepro.2022.134843>.
- [4] J. Motte, M. Mahmoud, M. Nieder-Heitmann, H. Vleeming, J.W. Thybaut, J. Poissonnier, R.A.F. Alvarenga, P. Nachtergaele, J. Dewulf, Environmental Performance Assessment of a Novel Process Concept for Propanol Production from Widely Available and Wasted Methane Sources, *Ind Eng Chem Res* 61 (2022) 11071–11079. <https://doi.org/10.1021/acs.iecr.2c00808>.
- [5] P. V. Snytnikov, D.I. Potemkin, S.I. Uskov, A. V. Kurochkin, V.A. Kirillov, V.A. Sobyenin, Approaches to Utilizing Flare Gases at Oil and Gas Fields: A Review, *Catal Ind* 10 (2018) 202–216. <https://doi.org/10.1134/S207005041803011X>.
- [6] A. Demirbas, N. Cek, S. Acar, Chemical analyses of shale gas and conventional natural gas, *Pet Sci Technol* 36 (2018) 1690–1695. <https://doi.org/10.1080/10916466.2018.1504070>.
- [7] Z.I. S G Adiya, V. Dupont, T. Mahmud, Steam reforming of shale gas in a packed bed reactor with and without chemical looping using nickel based oxygen carrier, *Int J Hydrogen Energy* 43 (2018) 6904–6917. <https://doi.org/10.1016/j.ijhydene.2018.02.083>.
- [8] I. Amghizar, L.A. Vandewalle, K.M. Van Geem, G.B. Marin, New Trends in Olefin Production, *Engineering* 3 (2017) 171–178. <https://doi.org/10.1016/J.ENG.2017.02.006>.
- [9] R.S. Middleton, R. Gupta, J.D. Hyman, H.S. Viswanathan, The shale gas revolution: Barriers, sustainability, and emerging opportunities, *Appl Energy* 199 (2017) 88–95. <https://doi.org/10.1016/j.apenergy.2017.04.034>.
- [10] M.R. Atelge, H. Senol, D. Mohammed, T.A. Hansu, D. Krisa, A. Atabani, C. Eskicioglu, H. Muratçobanoğlu, S. Unalan, K. Slimane, N. Azbar, H.D. Kıvrak, A critical overview of the state-

- of-the-art methods for biogas purification and utilization processes, *Sustainability* (Switzerland) 13 (2021). <https://doi.org/10.3390/su132011515>.
- [11] R. Mansoor, M. Tahir, Recent Developments in Natural Gas Flaring Reduction and Reformation to Energy-Efficient Fuels: A Review, *Energy and Fuels* 35 (2021) 3675–3714. <https://doi.org/10.1021/acs.energyfuels.0c04269>.
- [12] M. Qi, Y. Liu, T. He, L. Yin, C.M. Shu, I. Moon, System perspective on cleaner technologies for renewable methane production and utilisation towards carbon neutrality: Principles, techno-economics, and carbon footprints, *Fuel* 327 (2022) 125130. <https://doi.org/10.1016/j.fuel.2022.125130>.
- [13] Y. Xu, A.C. Lausche, S. Wang, T.S. Khan, F. Abild-Pedersen, F. Studt, J.K. Nørskov, T. Bligaard, In silico search for novel methane steam reforming catalysts, *New J Phys* 15 (2013). <https://doi.org/10.1088/1367-2630/15/12/125021>.
- [14] A.A. Fonseca, R.H. Heyn, M. Frøseth, J.W. Thybaut, J. Poissonnier, A. Meiswinkel, H.-J. Zander, J. Canivet, A Disruptive Innovation for Upgrading Methane to C3 Commodity Chemicals: Technical challenges faced by the C123 European consortium, *Johnson Matthey Technology Review* 65 (2021) 311–329. <https://doi.org/10.1595/205651321X16051060155762>.
- [15] V.G. Yadav, G.D. Yadav, S.C. Patankar, The production of fuels and chemicals in the new world: critical analysis of the choice between crude oil and biomass vis-à-vis sustainability and the environment, *Clean Technol Environ Policy* 22 (2020) 1757–1774. <https://doi.org/10.1007/s10098-020-01945-5>.
- [16] J.-L. Dubois, M. Nieder-Heitmann, A. Letoffet, H. Vleeming, C123 - Methane Oxidative Conversion and Hydroformylation to Propylene: Raw material sources and market analyses of the modular route C3 products, *Johnson Matthey Technology Review* 65 (2021) 301–310. <https://doi.org/10.1595/205651321X16051080751506>.
- [17] J.W. Thybaut, G.B. Marin, Kinetics of Catalyzed Reactions—Heterogeneous, in: *Encyclopedia of Catalysis*, Wiley, 2010. <https://doi.org/10.1002/0471227617.eoc128.pub2>.
- [18] T.P. Tiemersma, M.J. Tuinier, F. Gallucci, J.A.M. Kuipers, M.V.S. Annaland, A kinetics study for the oxidative coupling of methane on a Mn/Na 2WO₄/SiO₂ catalyst, *Appl Catal A Gen* 433–434 (2012) 96–108. <https://doi.org/10.1016/j.apcata.2012.05.002>.
- [19] J.S. Ahari, M.T. Sadeghi, S. Zarrinpashne, Effects of operating parameters on oxidative coupling of methane over Na-W-Mn/SiO₂ catalyst at elevated pressures, *Journal of Natural Gas Chemistry* 20 (2011) 204–213. [https://doi.org/10.1016/S1003-9953\(10\)60167-3](https://doi.org/10.1016/S1003-9953(10)60167-3).
- [20] Y. Gao, L. Neal, D. Ding, W. Wu, C. Baroi, A.M. Gaffney, F. Li, Recent Advances in Intensified Ethylene Production - A Review, *ACS Catal* 9 (2019) 8592–8621. <https://doi.org/10.1021/acscatal.9b02922>.
- [21] S. Arndt, T. Otremba, U. Simon, M. Yildiz, H. Schubert, R. Schomäcker, Mn-Na 2WO₄/SiO₂ as catalyst for the oxidative coupling of methane. What is really known?, *Appl Catal A Gen* 425–426 (2012) 53–61. <https://doi.org/10.1016/j.apcata.2012.02.046>.
- [22] G. Lezcano, S.R. Kulkarni, V.K. Velisoju, V.E. Musteata, I. Hita, A. Ramirez, A. Dikhtiarenko, J. Gascon, P. Castaño, Effect of the particle blending-shaping method and silicon carbide crystal phase for Mn-Na-W/SiO₂-SiC catalyst in oxidative coupling of methane, *Molecular Catalysis* 527 (2022). <https://doi.org/10.1016/j.mcat.2022.112399>.
- [23] G. Lezcano, V.K. Velisoju, S.R. Kulkarni, A. Ramirez, P. Castaño, Engineering Thermally Resistant Catalytic Particles for Oxidative Coupling of Methane Using Spray-Drying and Incorporating SiC, *Ind Eng Chem Res* 60 (2021) 18770–18780. <https://doi.org/10.1021/acs.iecr.1c02802>.
- [24] S.S. Tharakaraman, M. Nunez Manzano, S.R. Kulkarni, P. Yazdani, Y. De Vos, T. Verspeelt, G. Heynderickx, K.M. Van Geem, G.B. Marin, M. Saeys, Development of an Active and Mechanically Stable Catalyst for the Oxidative Coupling of Methane in a Gas-Solid Vortex Reactor, *Ind Eng Chem Res* 61 (2022) 7748–7759. <https://doi.org/10.1021/acs.iecr.1c02121>.

- [25] L. Lapidus, J.H. Seinfeld, Numerical solution of ordinary differential equations, Academic Press, New York, 1971.
- [26] P.T. Boggs, J.R. Donaldson, R.H. Byrd, R.B. Schnabel, Algorithm 676: ODRPACK: software for weighted orthogonal distance regression, *ACM Transactions on Mathematical Software* 15 (1989) 348–364. <https://doi.org/10.1145/76909.76913>.
- [27] D.W. Marquardt, An algorithm for least-squares estimation of nonlinear parameters, *Journal of the Society for Industrial and Applied Mathematics* 11 (1963) 431–441. <https://doi.org/https://doi.org/10.1137/0111030>.
- [28] S. Siradze, J. Poissonnier, M. Frøseth, R.E. Stensrød, R.H. Heyn, J.W. Thybaut, Kinetics Assessment of the Homogeneously Catalyzed Hydroformylation of Ethylene on an Rh Catalyst, *Ind Eng Chem Res* 60 (2021) 16665–16681. <https://doi.org/10.1021/acs.iecr.1c02572>.
- [29] R. Quintana-Solórzano, A. Rodríguez-Hernández, R. García-de-León, Study of the Performance of Catalysts for Catalytic Cracking by Applying a Lump-Based Kinetic Model, *Ind Eng Chem Res* 48 (2009) 1163–1171. <https://doi.org/10.1021/ie800570z>.
- [30] M. Daneshpayeh, A. Khodadadi, N. Mostoufi, Y. Mortazavi, R. Sotudeh-Gharebagh, A. Talebizadeh, Kinetic modeling of oxidative coupling of methane over Mn/Na₂WO₄/SiO₂ catalyst, *Fuel Processing Technology* 90 (2009) 403–410. <https://doi.org/10.1016/j.fuproc.2008.11.001>.
- [31] Z. Stansch, L. Mleczko M, Baerns, Comprehensive Kinetics of Oxidative Coupling of Methane over the La₂O₃/CaO Catalyst, *Ind Eng Chem Res* 36 (1997) 2568–2579. <https://doi.org/10.1021/ie960562k>.
- [32] L. Pirro, A. Obradović, B.D. Vandegheuchte, G.B. Marin, J.W. Thybaut, Model-Based Catalyst Selection for the Oxidative Coupling of Methane in an Adiabatic Fixed-Bed Reactor, *Ind Eng Chem Res* 57 (2018) 16295–16307. <https://doi.org/10.1021/acs.iecr.8b04242>.
- [33] A. Vatani, E. Jabbari, M. Askarieh, M.A. Torangi, Kinetic modeling of oxidative coupling of methane over Li/MgO catalyst by genetic algorithm, *J Nat Gas Sci Eng* 20 (2014) 347–356. <https://doi.org/10.1016/j.jngse.2014.07.005>.
- [34] G. Che-Galicia, R.S. Ruiz-Martínez, F. López-Isunza, C.O. Castillo-Araiza, Modeling of oxidative dehydrogenation of ethane to ethylene on a MoVTenbO/TiO₂ catalyst in an industrial-scale packed bed catalytic reactor, *Chemical Engineering Journal* 280 (2015) 682–694. <https://doi.org/10.1016/j.cej.2015.05.128>.
- [35] M. Daneshpayeh, A. Khodadadi, N. Mostoufi, Y. Mortazavi, R. Sotudeh-Gharebagh, A. Talebizadeh, Kinetic modeling of oxidative coupling of methane over Mn/Na₂WO₄/SiO₂ catalyst, *Fuel Processing Technology* 90 (2009) 403–410. <https://doi.org/10.1016/j.fuproc.2008.11.001>.
- [36] L. Mleczko, M. Baerns, Catalytic oxidative coupling of methane-reaction engineering aspects and process schemes, *Fuel Processing Technology* 42 (1995) 217–248. [https://doi.org/10.1016/0378-3820\(94\)00121-9](https://doi.org/10.1016/0378-3820(94)00121-9).
- [37] M. Lin, T.E. Hogan, A. Sen, Catalytic Carbon–Carbon and Carbon–Hydrogen Bond Cleavage in Lower Alkanes. Low-Temperature Hydroxylations and Hydroxycarbonylations with Dioxide as the Oxidant, *J Am Chem Soc* 118 (1996) 4574–4580. <https://doi.org/10.1021/ja953670r>.
- [38] S. Siradze, J. Poissonnier, M. Frøseth, R.E. Stensrød, R.H. Heyn, J.W. Thybaut, Kinetics Assessment of the Homogeneously Catalyzed Hydroformylation of Ethylene on an Rh Catalyst, *Ind Eng Chem Res* 60 (2021) 16665–16681. <https://doi.org/10.1021/acs.iecr.1c02572>.
- [39] A. V. Milkov, M. Faiz, G. Etiope, Geochemistry of shale gases from around the world: Composition, origins, isotope reversals and rollovers, and implications for the exploration of shale plays, *Org Geochem* 143 (2020) 103997. <https://doi.org/10.1016/j.orggeochem.2020.103997>.
- [40] B. Bharathiraja, T. Sudharsana, J. Jayamuthunagai, R. Praveenkumar, S. Chozhavendhan, J. Iyyappan, Biogas production – A review on composition, fuel properties, feed stock and principles of anaerobic digestion, *Renewable and Sustainable Energy Reviews* 90 (2018) 570–582. <https://doi.org/10.1016/j.rser.2018.03.093>.

Appendices

Appendix 2A Effect of CO₂ in the feedstock

CO₂ is a significant component found in both natural gas and biogas, with concentrations reaching up to 7% and 60%, respectively [39,40]. Because of this, an experimental campaign was conducted to analyze its influence on methane and oxygen conversion, and carbon species selectivities. The experimental results are illustrated in Figure 2A.1, indicating that the presence of CO₂ during co-feeding did not result in any significant changes in the performance of the MnNaW/SiO₂ catalyst, i.e., methane and oxygen conversion remain constant. Based on these results, no CO₂ reactions, e.g., the Reverse Water Gas Shift reaction (RWGSR) or Dry Reforming of Methane (DRM), are considered in the kinetic model.

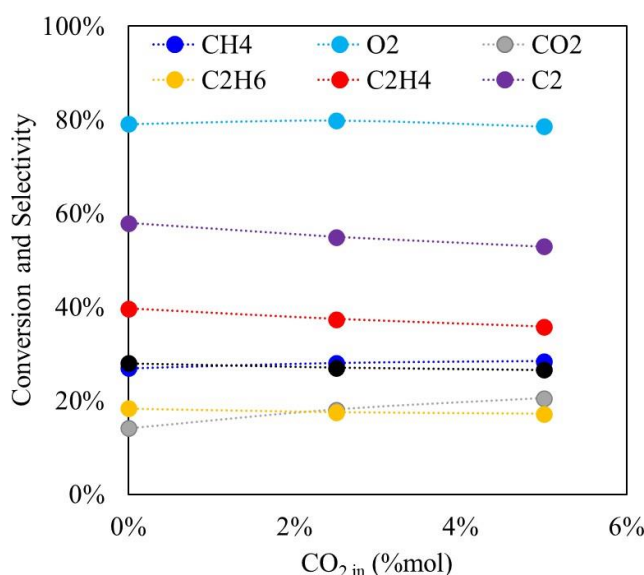


Figure 2A.1. Conversion and selectivity as a function of the CO₂ content in feedstock. CH₄/O₂ = 4 mol_{CH₄,in} mol_{O₂,in}⁻¹, p_{tot} = 1 bar, W_{cat}/F_{CH₄,in} = 2.50 kg s mol_{CH₄,in}⁻¹. Lines are added to show experimental trends.

Appendix 2B Reaction rates analysis

A reaction rates analysis was conducted for the reactions proposed in Section 2.3.1 at different operating conditions to assess the significance and reliability of each reaction in the kinetic model. The effect of the CH₄/O₂ inlet molar ratio, by decreasing the amount of oxygen in feedstock while keeping the amount of methane fixed, on OCoM is depicted in Figure 2B.1a.

As discussed in Section 2.3.5, the kinetic parameters associated with the TOM, WGSR, POE and TOEt showed no statistically significant values. These reactions exhibited computed reaction rates one or more magnitude orders lower than the TOCO, which demonstrated statistically significant values. Moreover, Figure 2B.1b illustrates the effect of the temperature on the OCoM reaction rates, reaffirming that the reaction rates of the TOM, WGSR, POE and TOEt were one or more magnitude orders lower than TOCO. Based on these results, these four reactions are excluded from the kinetic model. It is noteworthy that the reactions were removed one by one starting with POE, then TOM, TOEt, and lastly WGSR.

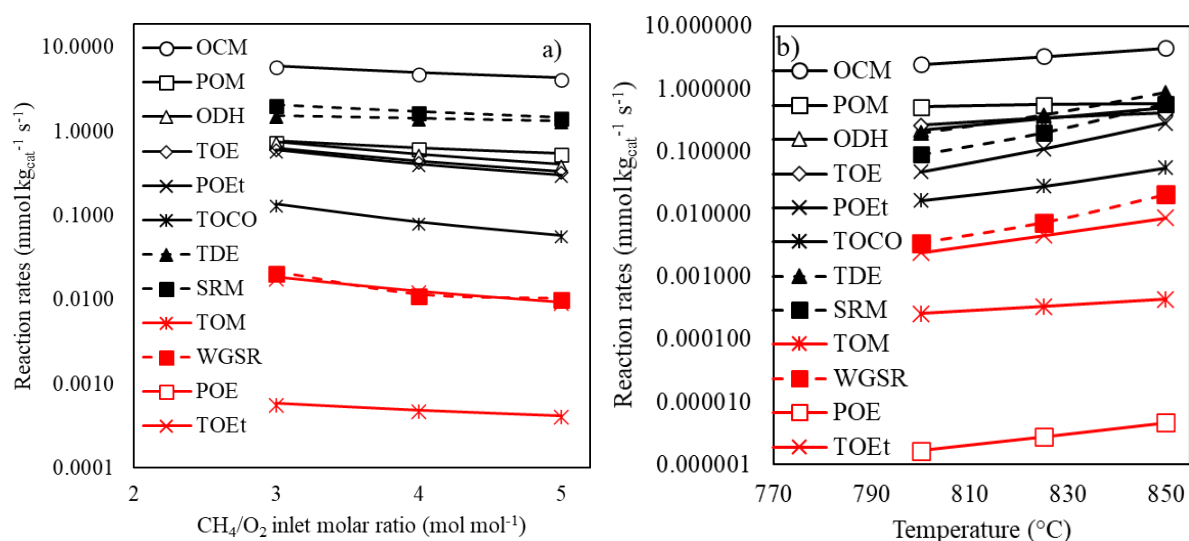


Figure 2B.1. Computed reaction rates from the OCoM kinetic model as function of the (a) CH_4/O_2 inlet molar ratio with a fixed temperature of 800 °C and $W_{\text{cat}}/F_{\text{CH}_4, \text{in}}$ of 2.5 kg s mol_{CH₄,in}⁻¹, and as a function of the (b) temperature with a fixed CH_4/O_2 inlet molar ratio of 4 mol_{CH₄,in} mol_{O₂,in}⁻¹ and $W_{\text{cat}}/F_{\text{CH}_4, \text{in}}$ of 2.5 kg s mol_{CH₄,in}⁻¹. Symbols are added to distinguish between the reactions.

Chapter 3 – Transport phenomena within a packed bed reactor with low d_t/d_p

This Chapter elaborates on the procedures adopted in this thesis to characterize the phenomena transport mechanism within a bench-scale and an industrial-scale single-tube packed bed with a tube-to-particle diameter ratio of $\sim 3 \text{ m}_r \text{ m}_s^{-1}$. Section 3.1 provides a brief introduction of the problem statement, i.e., the reliable characterization and understanding of transport phenomena within a packed bed with low d_t/d_p ($< 8 \text{ m}_r \text{ m}_s^{-1}$). Section 3.2 introduces the experimental set-ups and the operating conditions at which both the pressure drop, and temperature gradient experiments are performed. Section 3.3 provides a detailed approach for computing fluid dynamics, i.e., axial velocity profiles. Solid-fluid interactions at the center of the bed characterized by the apparent permeability constants (K and K_z), and solid-fluid and fluid-fluid interactions close to the wall quantified by the effective viscosity (μ_{eff}) are elucidated. Section 3.4 outlines the experimental and theoretical methodology to characterize the axial and radial heat transfer mechanisms within the packed beds. Details of the main heat transfer mechanisms within the packed beds are provided. A non-reactive adiabatic scenario with radial temperature uniformity is used to estimate $k_{\text{eff},z}$ via regression and to develop a corresponding correlation. Then, the pseudo-local approach developed in this work, accounting for the pseudo-local radial effective conductivity ($k_{\text{eff},r,\text{PLA}}$) as a function of the radial void fraction and fluid dynamics, is introduced. Additionally, based on the adequate internal heat transfer characterization, the external wall heat transfer coefficient ($h_{w,\text{ext}}$) is characterized. The temperature profiles computed, accounting for the $k_{\text{eff},z}$ and the pseudo-local approach, are compared with profiles obtained based on conventional approaches from literature. Once $k_{\text{eff},r,\text{PLA}}$ and $h_{w,\text{ext}}$ are determined, an analysis of the heat transfer resistances effect is presented. Last, Section 3.5 presents the conclusion of research done regarding the transport phenomena characterization.

Part of the results of this chapter are published as:

Romero-Limones A., Poissonnier J., Thybaut J. W., and Castillo-Araiza C. O., (2023). A pseudo-local heat transfer approach in a low tube to particle diameter ratio packed bed catalytic reactor: Oxidative Dehydrogenation of ethane as a case study. *Chemical Engineering Journal*. DOI: 10.1016/j.cej.2022.140392

Romero-Limones A., Poissonnier J., Castillo-Araiza C. O., and Thybaut J. W., (2023). Avoiding false runaway prediction by properly describing axial conductive heat transfer in a low d_t/d_p industrial-scale packed bed reactor. *Chemical Engineering Journal*. DOI: 10.1016/j.cej.2023.146167

3.1 Introduction

Within the framework of the circular economy for hydrocarbons, a lab-scale perspective to valorize methane from three different natural gas feedstocks has been presented through the assessment of the novel OCoM was presented in Chapter 2. Now, an industrial perspective analysis for the Oxidative Dehydrogenation of Ethane (ODH) is carried out.

Wall-cooled packed bed catalytic reactors with a low tube-to-particle diameter ratio ($d_t/d_p < 8 m_r m_s^{-1}$), have been extensively employed in the petrochemical industry for highly exothermic reactions, such as the selective oxidation of o-xylene, ethylene, among others hydrocarbons [1–4]. In fact, it has been reported that the first commercialization of the ODH has been done in a multitubular packed bed reactor [5]. The recent industrialization of the ODH, as well as the upcoming implementations coming worldwide [6], demand for effective and reliable reactor models accounting for the role of ODH kinetics and transport phenomena, primarily heat transfer and fluid dynamics, for conceptual design, control, and optimization. This is because, despite decades of study, the main challenge that still needs to be addressed is the minimization of the extent of undesired total oxidation reactions leading to hot spots and runaway scenarios, which occurs due to the high sensitivity on the operating conditions, e.g., inlet temperature, cooling temperature, feedstock composition.

The assessment of an ODH packed bed reactor is split in two Chapters. The analysis and characterization of transport phenomena, particularly fluid dynamics and heat transfer, within a bench-scale and industrial-scale packed bed with a $d_t/d_p \sim 3 m_r m_s^{-1}$ under non-reactive conditions is presented in this Chapter. While the integration of transport phenomena and intrinsic kinetics into the ODH reactor model is given in Chapter 4.

3.2 Experimental systems (bench-scale and industrial-scale)

A schematic diagram, representative for both the bench and the industrial-scale packed bed reactor, is shown in Figure 3.1. The different ways in which the packed bed set-up can be operated, depending on which information is pursued, i.e., pressure-drop, axial temperature gradients or axial and radial temperature-gradients, are depicted. The bench-scale packed bed is a tube, with a length of $0.5060 m_r$ and a diameter of $0.0254 m_r$, packed with ca. 300 g (400 pellets) and 1.73 kg (2260 pellets) for the bench- and industrial-scale packed bed reactor, respectively. The pellets are spherical catalyst particles with a diameter of $0.0082 m_s$. These

particles are composed of a V-based active phase externally deposited on a non-porous TiO₂ (anatase) core. The non-porous TiO₂ pellets have been chosen because its non-porosity avoids the energy accumulation, i.e., internal heat transfer resistances, favoring the removal of the heat generated out from an exothermic reaction [2,7,8]. Pressure drop along both packed beds is measured by two manometers positioned at both the inlet and outlet. For axial temperature gradients considering radial isothermicity, the bench-scale packed bed is heated with a 250 W infra-red lamp from the top, while a thermal insulation jacket of fiberglass is wrapped around the stainless steel tube in the axial direction to ensure adiabatic conditions [9,10]. To generate significant temperature gradients in the axial direction, air is fed at room temperature from the bottom of the packed at Re_p between 210 and 1260, while nine 0.1mm outside diameter K-type thermocouples (not shown so as not to overload Figure 3.1) are used to measure the temperature at different axial positions in the center of the bed.

For the generation of both radial and axial temperature gradients, the bench-scale packed bed is surrounded by an electric resistance (the heat source). The temperature is measured with nine 0.1 mm outside diameter K-type thermocouples set up at different axial positions in the packed bed, through thermowells from the side, such that each thermocouple can be moved over the entire diameter of the packed bed. At each axial position the temperature is measured at twelve radial positions. One thermocouple is positioned at mid-height of the reactor at the tube wall as a control set point to generate the required temperature gradients. This configuration allows the measurement of radial and axial temperature gradients. Inlet air flow rates corresponding to a Re_p between 210 and 1260 at normal conditions are used during heat transfer experimentation.

For the industrial-scale packed bed, a tube with a length of $2.6 m_r$ and a diameter of $0.025m_r$ surrounded by a molten salt bath is utilized. This industrial-scale packed bed has the same geometrical configuration as the packed bed used in the bench-scale set-up, i.e., same d_t/d_p ratio. Platinum resistance thermometers and 1.5 mm outside diameter chromel-alumel sheathed thermocouples are used to measure the temperature from the wall to the center of the packed bed at different axial positions [11]. In this packed bed system, the coolant temperature, i.e., molten salt bath, is set at 400 °C and it is monitored during the experimentation. Moreover, air is fed at Re_p between 700 and 1400. The observed temperature gradients are then used to estimate the parameters from the radial heat transfer mechanisms.

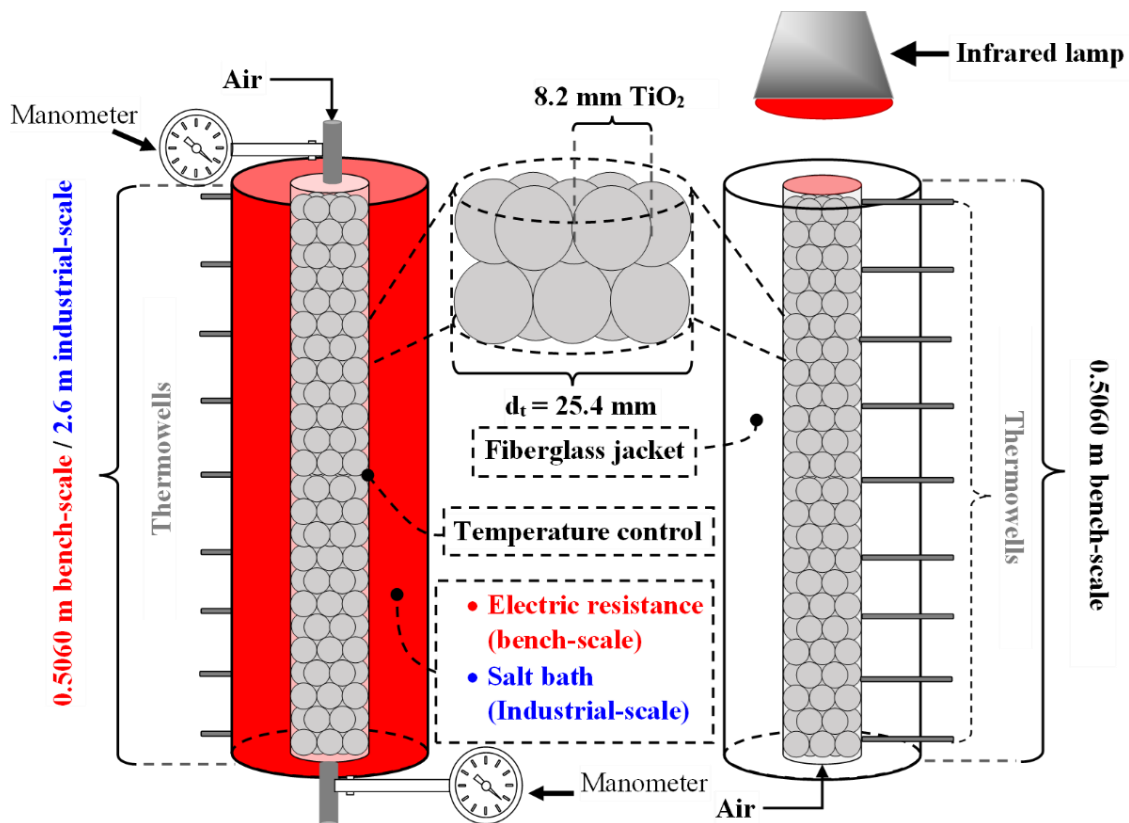


Figure 3.1. Schematic diagram of the packed bed showing the different kind of operations depending on the targeted parameters. Left, industrial-scale and bench-scale non-adiabatic operation (bed length in blue and red letters, respectively). Right, bench-scale adiabatic operation.

3.3 Fluid dynamics

3.3.1 Pressure drop

Pressure drop experiments consisted of measuring the pressure at normal conditions at the inlet and outlet of the bench-scale and industrial-scaled packed bed for a particle Reynolds number (Re_p) between 210 and 1680, and between 750 and 1750 [11], respectively. The pressure drop in packed beds is caused by frictional energy losses due to both viscous and inertial frictional resistances. The viscous frictional resistances occurs particularly at low flow rates having a linear relationship with the flow velocity (Blake-Kozeny equation [12]), while the inertial frictional resistances have a quadratic relationship with the flow velocity (Burke-Plummer equation [13]). Ergun [14] demonstrated that the summation of the expressions for the low and high-velocity ranges provides an expression for the entire range of volumetric flow rate. This leads to Ergun's equation where the pressure drop along the axial coordinate ($\Delta p_z/L$)

can be seen for the studied bed as the z-component of the solid-fluid resistance vector [15], $\mathbf{D}(\mathbf{r})$:

$$\frac{\Delta p_z}{L} = D(r)_z = \alpha \frac{u_z \mu_f (1 - \varepsilon(r))^4}{d_p^2 \varepsilon(r)^3} + \beta \frac{\rho_f u_z^2 (1 - \varepsilon(r))}{d_p \varepsilon(r)^3} \quad (3.1)$$

or, expressed in function of the apparent permeability:

$$D(r)_z = \mu_f H(r)_{zz}^{-1} u_z \quad (3.2)$$

where u_z is the axial superficial velocity, μ_f is the fluid viscosity, ε is the radial void fraction averaged at the axial and tangential axis, $H(r)_{zz}^{-1}$ is the axial component of the apparent permeability tensor ($\mathbf{H}(\mathbf{r})$), and α and β are two constants related to the viscous and inertial terms, respectively. Because these contributions are different for each system, i.e., the geometrical configuration attributed to the shape and size of the packings and the d_t/d_p ratio, α and β are re-estimated based on the experimentally measured pressure drop. Figure 3.2 depicts the pressure drop observations and the simulation results using Eq. (3.1) with the parameters, α and β , estimated in this work as well as determined using some of the well-accepted correlations from literature [14,16–18].

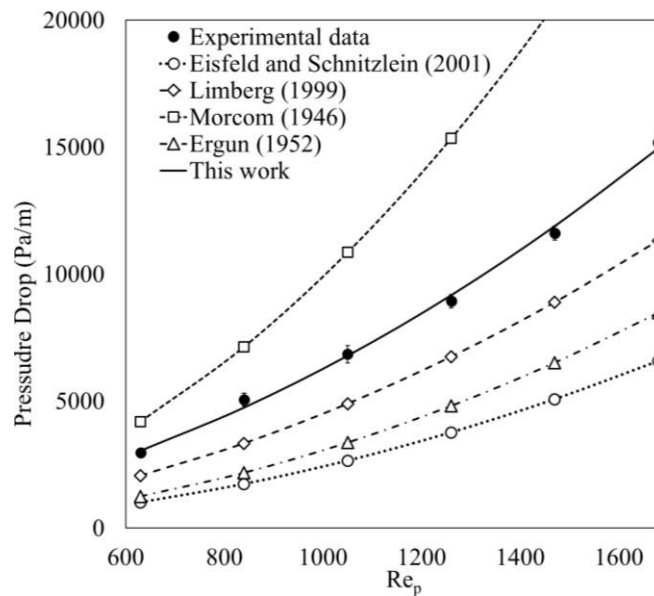


Figure 3.2. Pressure drop within the packed bed. A comparison between the experimental data (full symbols) and simulations with, the parameters estimated in this work (continuous line), Ergun’s parameters [14] ($\alpha = 150$ and $\beta = 1.75$), Limberg’s parameters [16] ($\alpha = 260$ and $\beta = 0.9$), Morcom’s parameters [17] ($\alpha = 245$ and $\beta = 2.4$), and Einfeld’s correlation [18].

Estimates for α and β and their confidence intervals are 2480 ± 447 and 2.31 ± 0.19 , respectively. Simulations considering literature reported values for α and β are not able to describe the experimental data acquired in the studied bed properly. This shows the importance of obtaining both parameters for a packed bed with low d_t/d_p . Moreover, the estimated value of α and β are higher than the values reported in the literature. Regarding β , i.e., related to inertial forces which dominate at high flow rates, for the current case study, the inertial energy losses have a higher influence on the pressure drop than the viscous energy losses.

3.3.2 Viscous and inertial frictional forces

The geometrical configuration of packed beds with low d_t/d_p ratio (< 8) generates significant radial void fraction profiles which have a significant effect on velocity profiles, mainly in those areas with high void fraction [1,19]. The empirical correlation developed by De Klerk, see Eqs. (3.3) – (3.5) [20], accounting for spherical pellets, has been well accepted within the scientific community because its well description of the void fraction at relatively wide range of d_t/d_p ratios, i.e., 1.7 – 20 [21–23]. This correlation considers two regions along the tube radius, i.e., near the wall and at the core of the bed. In this work, the void fraction is calculated using this correlation. In this work, the void fraction is calculated utilizing the correlation reported by De Klerk.

$$\varepsilon(\kappa) = 2.14\kappa^2 - 2.53\kappa + 1 \text{ for } \kappa < 0.637 \quad (3.3)$$

$$\varepsilon(\kappa) = 0.36 + (0.29 e^{-0.6m} \cos(2.3\pi(\kappa - 0.16))) + 0.15e^{-0.9m} \text{ for } \kappa < 0.637 \quad (3.4)$$

where:

$$\kappa = \frac{R_t - r}{d_p} \quad (3.5)$$

Considering the permeability as the ability of the packed bed to allow the fluid flows through it, the calculation of the radial void fraction profile, and the re-estimation of α and β , presented in Section 3.3.1, allow the calculation of the Darcy and Forchheimer permeability, see Eqs. (3.6) – (3.7), respectively.

$$K = \frac{\varepsilon(r)^3 d_p^2}{\alpha(1 - \varepsilon_0)^2} \quad (3.6)$$

$$K_z = \frac{\varepsilon(r)^3 d_p}{\beta(1 - \varepsilon(r))} \quad (3.7)$$

and thus the dimensionless numbers Da and Fo, see (3.8) – (3.9), respectively.

$$Da = \frac{K}{R_t^2} \quad (3.8)$$

$$Fo = \frac{K_z}{R_t} \quad (3.9)$$

Da provides information of the influence of the viscous term due to frictional energy losses from fluid-fluid and solid-fluid interactions, while Fo gives details of the inertial resistances within the packed bed [22,24–26]. Figure 3.3a illustrates the Da and Fo numbers obtained in this work and a comparison with two works from literature [9,14]. Moreover, the void fraction within the bed for the bench-scale packed bed is also added to indicate its impact on the Da and Fo. The void fraction profile shows two zones with higher void fraction, i.e., near the wall and after one pellet-distance from the wall, where interstitial velocities are expected to be higher than the rest of the packed bed. The Da and Fo radial profiles present a similar trend to the void fraction profile. Da and Fo vary from 10^{-5} up to 10^1 and 10^{-5} up to 10^1 , respectively. The close values between both terms indicates that the inertial term and the Brinkman term should be considered in the fluid dynamic model. Otherwise, the impact of frictional energy losses on the fluid-fluid and solid-fluid interaction, i.e., non-Darcyan behavior, could not be properly accounted for. Furthermore, Figure 3.3b depicts the apparent permeability within the packed bed calculated in this work, exhibiting a similar trend as the one reported in the literature from particle resolved simulations (PRS) [15] for the same packed bed. However, a steeper increase in the wall zone and decrease in the center of the bed are identified. This is attributed to the methodology used to determine the apparent permeability, which in this work is calculated by using macroscopic pressure drop data through the estimation of α and β , while in PRS it is obtained by using local information. The agreement between the apparent permeability obtained here and the one reported in the literature, and the adequate prediction of the pressure drop observations provide confidence in the values of α and β estimated for quantifying the solid-fluid resistances at the core of the bed.

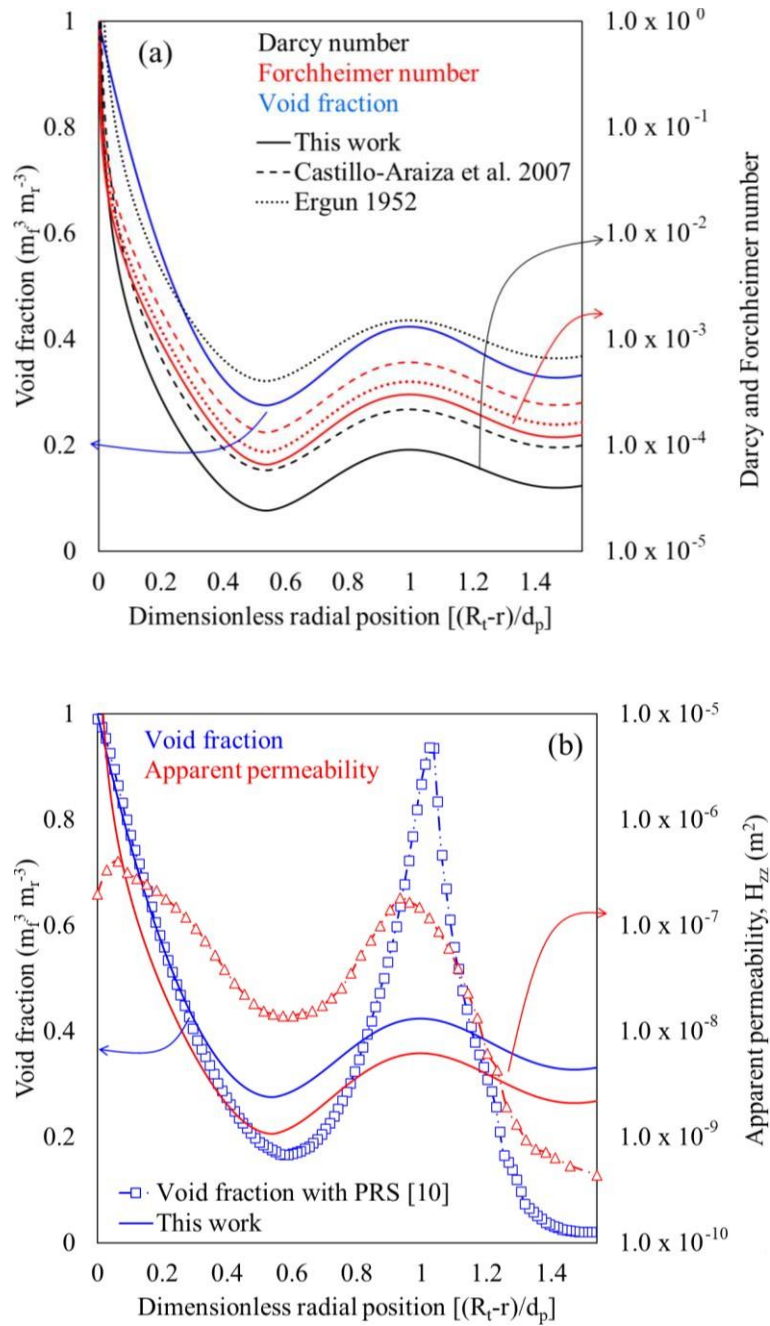


Figure 3.3. (a) Void fraction, Darcy and Forchheimer number for the bench and industrial-scale packed bed; and (b) Void fraction and apparent permeability in the packed bed obtained in this work and reported in the literature from a particle resolved simulation (PRS) [15].

3.3.3 Axial velocity profiles within a packed bed

The governing equations to model momentum transfer within the packed bed with low tube-to-particle diameter ratio are given by the continuity equation, see Eq. (3.10), and the Navier-Stokes-Darcy-Forchheimer equation following Brinkman's approach (BDF) where an effective viscosity (μ_{eff}) is introduced to characterize solid-fluid interactions close to the wall [27], see Eqs. (3.11) – (3.16).

Continuity equation

$$\frac{\partial v_z}{\partial z} = 0 \quad (3.10)$$

Momentum equation:

$$\begin{aligned} \rho_f \left[\frac{\partial v_z}{\partial t} + \varepsilon(r) v_z \frac{\partial v_z}{\partial z} \right] \\ = -\varepsilon(r) \frac{\partial p_z}{\partial z} + \mu_{\text{eff}} \nabla^2 \varepsilon(r) v_z - \left(\frac{\mu_f}{K} \varepsilon(r) v_z + \frac{\rho_f}{K_z} \varepsilon(r)^2 v_z^2 \right) + \varepsilon \rho_f g_z \end{aligned} \quad (3.11)$$

The initial and boundary conditions are:

$$t = 0 \quad v_z = v_{z,ss} \quad (3.12)$$

$$r = 0 \quad \frac{\partial v_z}{\partial r} = 0 \quad (3.13)$$

$$r = R_t \quad v_z = 0 \quad (3.14)$$

$$z = 0 \quad v_z = u_{z,0} \quad (3.15)$$

$$z = L \quad \frac{\partial v_z}{\partial z} = 0 \quad (3.16)$$

The left side of Eq. (3.11) describes the inertial forces due to fluid-fluid interactions. On the right side, the first term accounts for the pressure drop within the bed (pressure forces), the second term describes the radial viscous dissipation, including the use of an effective viscosity (μ_{eff}), proposed by Brinkman [27], to account for the impact of solid surfaces, associated with the wall and the packing on fluid dynamics in the region near the wall of the bed. The third term contains the Darcy and Forchheimer contributions. These terms describe the viscous and inertial solid-fluid interactions in the packed bed, respectively. The last term captures the gravitational forces. The void fraction profile within the bed is obtained by

following the correlation developed by De Klerk [20] for packed beds with $d_t/d_p < 8$ containing spheres.

Since the pressure drop and the void fraction were determined with high certainty, an accurate description of velocity profiles in a packed bed with low tube-to-particle diameter ratio depends on determining three parameters, the so-called fluid dynamic descriptors, i.e., μ_{eff} , α and β . The parameters α and β were estimated from pressure drop data for the further determination of K and K_z , while determining μ_{eff} is more challenging. Although a continuity equation is stated when presenting the fluid dynamic model, in the literature approaches [24,28–30] mass conservation is not accomplished, i.e., the mass flux at any axial position in the bed can deviate from the mass flux at the inlet of the system. To overcome this shortcoming, a conservative methodology aimed at determining μ_{eff} is proposed here to describe the fluid dynamics within packed beds with a tube-to-particle diameter ratio smaller than $8 \text{ m}_r \text{ m}_s^{-1}$ by forcing the momentum equation to meet the continuity equation by fitting the mass flux with the observed one at the bed inlet. Firstly, the superficial velocity (u_z) at any axial position in the packed bed is obtained by determining the interstitial velocity (v_z) and multiplying it with the void fraction within the bed (ε_i), see Eq. (3.17).

$$u_z = v_z \varepsilon_i \quad (3.17)$$

Then, the average superficial velocity, i.e., the result of dividing the volumetric flow by the cross-sectional area where the fluid flows, is calculated as follows:

$$\langle u_z \rangle = \frac{\int_0^{2\pi} \int_{r=0}^{r=R_t} v_z r \, dr \, d\theta}{\int_0^{2\pi} \int_{r=0}^{r=R_t} r \, dr \, d\theta} \quad (3.18)$$

Eq. (3.18) can be solved using weighted orthogonal collocation, resulting in Eq. (3.19) for the superficial velocity:

$$\langle u_z \rangle = \sum_{i=1}^N W_i \varepsilon_i v_{z,i} \quad (3.19)$$

where W_i is the weight factor assigned to the i -th collocation point, $v_{z,i}$ is the interstitial velocity, ε_i is the void fraction and N is the number of radial collocation points. Once the average superficial velocity is calculated, the mass flux at any axial position within the bed can be calculated as follows:

$$G = \rho_f \langle u_z \rangle \tag{3.20}$$

μ_{eff} is, then, ultimately determined via regression, while ensuring mass conservation along the bed. It is worth mentioning that this approach allows the determining the μ_{eff} without the need for interstitial velocity measurements.

Figure 3.4 shows a comparison between the axial velocities at different particle Reynolds numbers considering the fluid dynamic models developed in this work accounting for the mass conservation criteria, i.e., μ_{eff} was determined, and the ones which do not account it, i.e., μ_f is considered [8,31]. An overprediction of the velocity when μ_f is used is clearly observed near the wall, because $\mu_f < \mu_{\text{eff}}$ at high Re_p . Considering μ_f leads to lower fluid resistances than when μ_{eff} is used, leading to the increment in velocity, which have an impact on the convective heat transfer mechanisms. Table 3.1 lists the estimated values of μ_{eff} along with the confidence intervals. The μ_{eff} exceeds μ_f because the former captures the effect of the wall and packing surfaces on fluid dynamics along the radial direction of the bed. Moreover, μ_{eff} increases with the particle Reynolds number, in agreement with the literature [22,28,32].

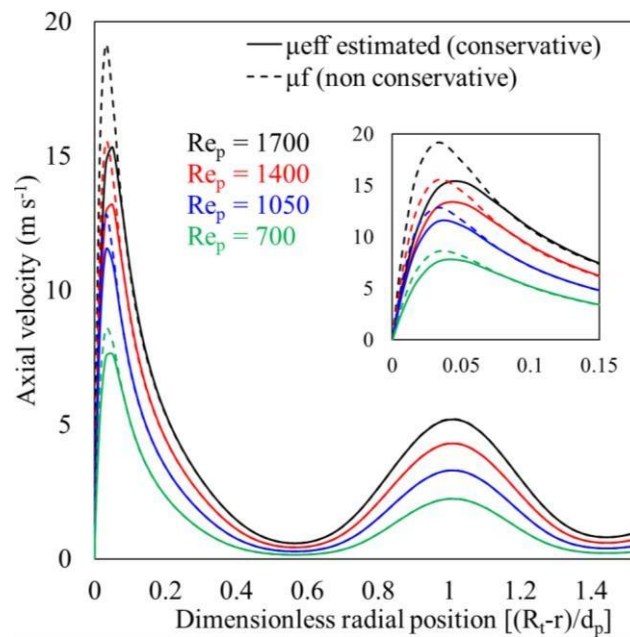


Figure 3.4. Axial velocity profiles within the packed bed. Re_p ranging from 700 to 1700.

Table 3.1. Estimated μ_{eff} values with their 95% probability confidence intervals and the μ_{eff}/μ_f ratio. Note that μ_f equals $222 \text{ kg}_f \text{ m}_r^{-2} \text{ s}^{-1}$.

Re_p	$\mu_{\text{eff}} [\text{kg}_f \text{ m}_r^{-2} \text{ s}^{-1}]$	μ_{eff}/μ_f
210	222 ± 2.1	1.00
420	233 ± 2.4	1.05
630	246 ± 3.3	1.11
700	251 ± 3.6	1.13
1050	289 ± 5.4	1.30
1260	340 ± 5.0	1.53
1400	402 ± 5.6	1.81
1750	524 ± 6.8	2.36

3.4 Heat transfer (no reaction)

3.4.1 Qualitative description of the axial and radial temperature gradients

A common operation of an exothermic reaction carried out in a multitubular wall-cooled packed bed reactor considers a feedstock, i.e., reactants, with a lower temperature than the control temperature of the reactor, i.e., coolant [2,11,33–35]. Regardless the significant radial temperature gradient between the coolant, the tube surface, and the center of the packed bed, these operating conditions generate a considerable axial temperature gradient, particularly in the first lengths of the reactor, see Figure 3.5. Although it has been widely stated that the $k_{\text{eff},z}$ can be neglected when these reactors are modeled, the reasons behind this statement relies on its negligible effect on the outlet temperature prediction and due to the high flow utilized at industrial operating conditions, i.e., convective mechanisms dominate on the conductive ones [36–39]. Nevertheless, there is no clear assessment of the $k_{\text{eff},z}$ impact in those areas of high sensitivity where hot spots and runaway situations take place. For the sake of brevity, the heat transfer mechanisms capture by the effective thermal conductivity are detailed in Appendix 3A.

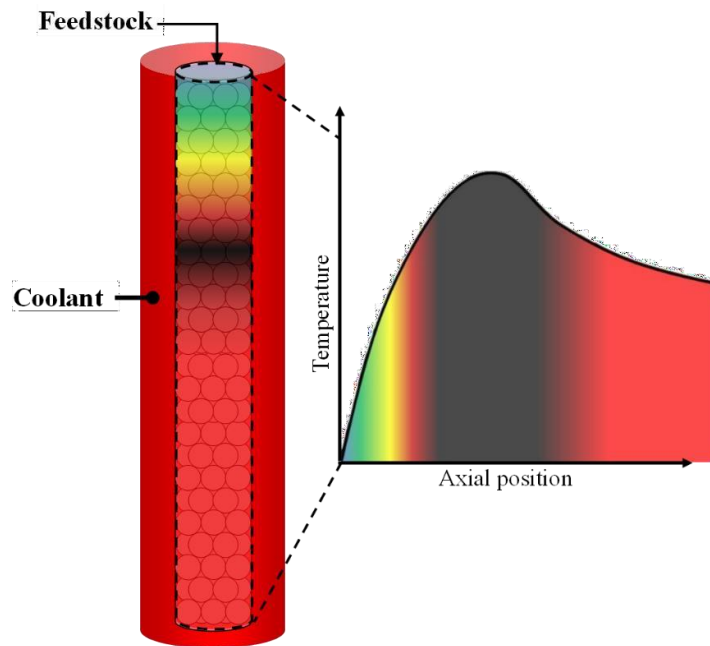


Figure 3.5. Schematic diagram of the qualitative axial temperature distribution within a packed bed reactor with low d_t/d_p ratio ($< 8 \text{ m}_r \text{ m}_s^{-1}$) when a highly exothermic reaction is considered.

Regarding the radial heat transfer mechanisms, these are described according to four different radial heat transfer zones of the packed bed reactor illustrated in Figure 3.6. Each of these zones relates to an effective heat transfer parameter, such that each zone presents a characteristic temperature gradient which can be associated with a corresponding heat transfer mechanism. The core zone (blue) spans from the center of the bed to the heat boundary layer near the internal tube wall. In this region, the radial heat transfer mechanisms are captured by the radial effective conductivity, $k_{\text{eff},r}$, commonly considered as a constant parameter, i.e., it does not vary radially. In the internal wall zone (green), an internal heat pseudo-boundary layer, $\delta_{\text{HT,int}}$, generates a significant heat transfer resistance increasing the temperature gradient, i.e., the temperature difference between T_δ and $T_{w,\text{in}}$. In this heat pseudo-boundary layer, the heat transfer is described by the internal wall heat transfer coefficient, $h_{w,\text{int}}$. In the external wall zone (yellow), an external heat pseudo-boundary layer, $\delta_{\text{HT,ext}}$, generates another temperature gradient at the external surface of the reactor tube. In this zone, the external wall heat transfer coefficient, $h_{w,\text{ext}}$, quantifies the temperature gradient between $T_{w,\text{in}}$ and T_b . It is noteworthy that in the literature no distinction is made between the internal and external heat pseudo-boundary layer, and h_w is modeled as a single parameter that captures the heat transfer mechanisms in both zones, i.e., internal and external wall zones. Lastly, the coolant zone (red) represents the zone where the heat source/sink for the packed bed is situated and it can be assumed that there are no significant temperature gradients in this zone because of the mixing

in it [2,11]. It should be remarked that the tube thickness, represented by a black line between the internal and external wall zone, has no significant effect on the radial heat transfer resistances because of the sufficiently high thermal conductivity of the tube material, e.g., stainless steel.

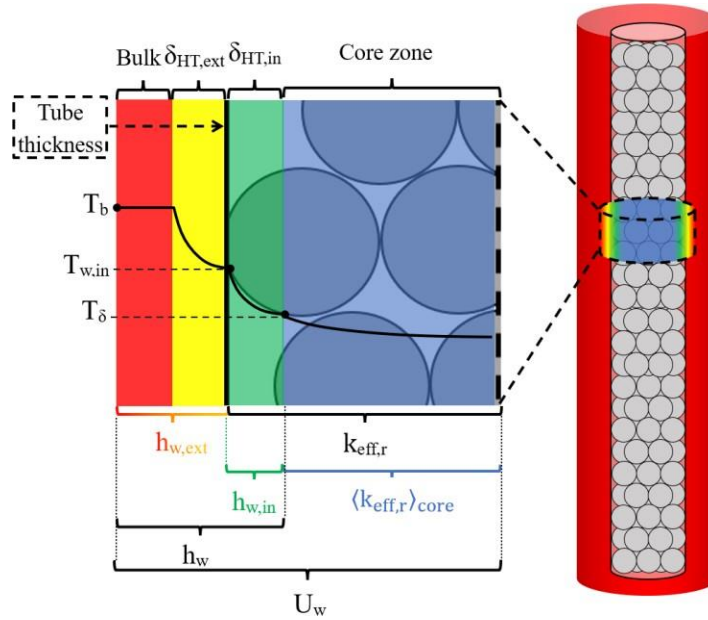


Figure 3.6. Schematic diagram of the relevant radial zones in a packed bed: core zone (blue), internal wall zone (green), external wall zone (yellow) and heat transfer medium (red).

3.4.2 Determination of $k_{eff,z}$ at adiabatic conditions (radial isothermicity)

A one-dimensional pseudo-homogeneous heat transfer model, see Eqs. (3.21) – (3.24), is used to describe the axial temperature profiles within the bench-scale packed bed.

$$(\rho_s C_p s + \rho_f C_p f) \frac{\partial T}{\partial t} + \rho_f C_p f \epsilon v_z \frac{\partial T}{\partial z} = k_{eff,z} \frac{\partial^2 T}{\partial z^2} \quad (3.21)$$

$$t = 0 \quad T(0, z) = T_{ss} \quad (3.22)$$

$$z = 0 \quad u_{z,0} \rho_f C_p f T_0 = \epsilon v_{z,0} \rho_f C_p f T - k_{eff,z} \frac{\partial T}{\partial z} \quad (3.23)$$

$$z = L \quad k_{eff,z} \frac{\partial T}{\partial z} = q_0 \quad (3.24)$$

The assumptions considered in this model are: (i) no significant radial temperature gradients within the bed, (ii) thermal equilibrium between the solid and fluid phase at the steady state, and (iii) Newtonian and incompressible fluid within the packed bed. This model is discretized using orthogonal collocation (15 axial points), employing shifted Legendre polynomials [40]. The resulting set of ordinary differential equations is solved using a fourth-order Runge-Kutta-Fehlberg method [41]. The experimental measurements from the heat transfer experiments performed at adiabatic conditions are used for the estimation of $k_{eff,z}$. The $k_{eff,z}$ is estimated using a combination of weighted orthogonal distance regression [42] and the Levenberg-Marquardt algorithm [43] by the minimization of the sum of squares of the weighted residuals between the experimental temperature and the model calculated ones, see Eq. (3.25).

$$RSS(\varphi) = \sum_{i=1}^{N} W_i \sum_{k=1}^M (F_{k,i} - \hat{F}_{k,i})^2 \rightarrow \min \quad (3.25)$$

Based on the determined $k_{eff,z}$ at different Re_p in the present work, a modified correlation is proposed as follows:

$$\frac{k_{eff,z}}{k_f} = \frac{k_{eff,z}^v}{k_f} + \delta_1 PrRe_p^{\delta_2} \quad (3.26)$$

where two empirical parameters δ_1 and δ_2 are employed to capture the evolution of the dynamic contribution to the value of $k_{eff,z}$. The estimated values for δ_1 and δ_2 amount to 0.6133 ± 0.2202 and 1.3259 ± 0.0517 , respectively.

Figure 3.7a compares the evolution of $k_{eff,z}$ as a function of Re_p for the correlation developed in this work with the selected correlations from the literature. Notably, as Re_p increases, the difference between the $k_{eff,z}$ determined in this work and the one obtained from the most used correlation in the literature [44–51], i.e., the one from Yagi et al., becomes more significant, particularly at Re_p relevant for industrial-scale packed bed reactor operation. On the other hand, the evolution of the $k_{eff,z}$ determined in this work as function of Re_p is similar to that obtained by Votruba et al. Thus, for comparison purposes, the developed correlation in this work and the two aforementioned selected from literature, i.e., Yagi et al. and Votruba et al., are used to calculate $k_{eff,z}$ and determine its impact on the temperature profile predictions. Details of these correlations are described in Appendix 3B.

Figure 3.7b displays a comparison of the axial temperature profiles within the bench-scale packed bed operating under adiabatic conditions, considering different values of $k_{eff,z}$ as obtained via the correlations proposed by Yagi et al. and Votruba et al., as well as the one determined in this work.

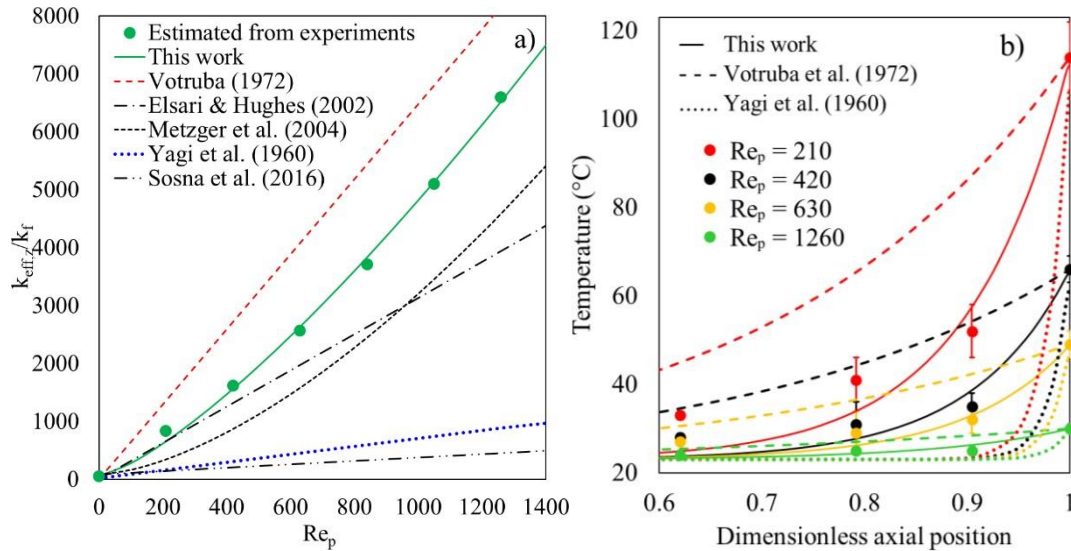


Figure 3.7. (a) $k_{eff,z}$ variation with the Re_p . Symbols represent the $k_{eff,z}$ obtained in this work, the green continuous line represents the correlation developed in this work, the red dashed line shows Votruba et al. correlation [52], the blue dotted line shows Yagi et al. [10], and the non-continuous black lines show the $k_{eff,z}$ obtained by different correlations from the literature [53–55]. (b) Axial temperature profiles for the bench-scale packed bed obtained in absence of flow and at Re_p between 210 and 1260 in absence of reaction. Dotted lines show the simulations considering the $k_{eff,z}$ from Yagi et al., full lines represent the $k_{eff,z}$ estimated in this work, and the dashed lines show the $k_{eff,z}$ from Votruba et al.

It should be noted that the axial temperature gradients are most pronounced in the upper part of the packed bed due to the positioning of the heat source, as illustrated in Figure 3.1. Therefore, the lower part of the packed bed exhibited no significant axial temperature gradients. The simulations using $k_{eff,z}$ from the correlation in this work provide an accurate description of the experimental data. However, simulations that consider $k_{eff,z}$ from the two correlations associated with Yagi et al. and Votruba et al. deviate from the experimental data at lower Re_p . The $k_{eff,z}$ from Yagi et al. has lower values than those determined in this work, resulting in a large temperature gradient at the top of the bed instead of a prolonged temperature profile through the packed bed. In contrast, the $k_{eff,z}$ from Votruba et al. has higher values than those estimated in this work, leading to the opposite effect. These findings offer initial observations on the contributing factors to the axial heat conduction in a packed bed with low d_i/d_p when a large temperature gradient is present.

3.4.3 Pseudo-local heat transfer approach

Through the development of a pseudo-continuous model for a packed bed, the use of a pseudo-local approach accounting for the role of the velocity profile on radial heat transfer has led to a better understanding and characterization of the radial heat transfer mechanisms, mainly in the wall zone [1,19,29,30,56]. Nevertheless, the pseudo-locality itself has not been adequately assessed such that fluid dynamics has not been properly considered during the determination of a pseudo local $k_{\text{eff},r}$ (hereafter called $k_{\text{eff},r,PLA}$). Typically, a plug flow approach has been considered in the literature [3,22,31,33,36,37,57–61]. When fluid dynamics is included, $k_{\text{eff},r,PLA}$ remains constant in the core zone, where the lowest temperature gradients occur, while in the internal wall zone the $k_{\text{eff},r,PLA}$ starts to decrease linearly. Additionally, the estimation of the pseudo-local parameters has been performed at adiabatic conditions [56], or considering an uniform static thermal conductivity, $k_{\text{eff},r}^0$ in the core zone and the fluid thermal conductivity as the $k_{\text{eff},r}$ in the wall zone [29]. To this end, the approach developed in this work not only allows the characterization of the internal heat transfer mechanisms by determining a pseudo-local $k_{\text{eff},r,PLA}$, but also the heat transfer mechanisms at the external surface of the tube by determining the $h_{w,\text{ext}}$.

Firstly, the pseudo-homogeneous heat transfer model used to describe the radial temperature profiles within the packed bed is presented as follows:

$$(\rho_s C_{p_s} + \rho_f C_{p_f}) \frac{\partial T}{\partial t} + \rho_f C_{p_f} \epsilon v_z \frac{\partial T}{\partial z} = \frac{1}{r} \frac{\partial}{\partial r} \left[k_{\text{eff},r,PLA}(r) r \frac{\partial T}{\partial r} \right] + k_{\text{eff},z} \frac{\partial^2 T}{\partial z^2} \quad (3.27)$$

$$t = 0 \quad T(0, r, z) = T_{ss} \quad (3.28)$$

$$z = 0 \quad v_z \rho_f C_{p_f} (T_0 - T) = -k_{\text{eff},z} \frac{\partial T}{\partial z} \quad (3.29)$$

$$z = L \quad \frac{\partial T}{\partial z} = 0 \quad (3.30)$$

$$r = 0 \quad \frac{\partial T}{\partial r} = 0 \quad (3.31)$$

$$r = R_t \quad T = T_{w,\text{in}}(z) \quad (3.32)$$

The first term on the left-hand side of Eq. (3.27) is the accumulation term while the second is the convective one where fluid dynamics plays a significant role. The term on the

right-hand side is the radial conductive term where the pseudo-local $k_{\text{eff},r,\text{PLA}}$ captures the static and dynamic internal radial heat transfer mechanisms. The assumptions considered in this model are: (i) a pseudo-local thermal equilibrium between solid and fluid phases, (ii) Newtonian and incompressible fluid within the packed bed, and (iii) constant physical properties of the fluid. The boundary condition from Eq. (3.32), referred to as the known wall-temperature boundary condition (KWT-BC), allows the characterization of the internal heat transfer mechanisms in the packed bed. Following the mathematical equations proposed by the group of Vortmeyer [56,62], see Eqs. (3.33) – (3.34), the pseudo-local radial effective conductivity, $k_{\text{eff},r,\text{PLA}}$, can be determined accounting for fluid dynamics.

$$k_{\text{eff},r,\text{PLA}}(r) = k_{\text{eff},r}^0 + \frac{1}{k_{1,h}} \text{PrRe}_p \left[\frac{f(R_t - r)}{k_f} \right] \quad (3.33)$$

$$f(R_t - r) = \begin{cases} \frac{R_t - r}{k_{2,h} d_p} & \text{for } 0 < R_t - r \leq k_{2,h} d_p \\ 1 & \text{for } k_{2,h} d_p < R_t - r \leq R_t \end{cases} \quad (3.34)$$

Here $k_{\text{eff},r}^0$ is the static radial effective conductivity, i.e., when the Re_p approaches 0, $k_{1,h}$ is the constant impacting on the dynamic contribution of the $k_{\text{eff},r,\text{PLA}}$, $k_{2,h}$ is the damping parameter that determines where the pseudo-local $k_{\text{eff},r,\text{PLA}}$ decreases due to the effect of the internal heat pseudo-boundary layer, $\delta_{\text{HT},\text{in}}$, and k_f is the fluid thermal conductivity. Hereafter, this approach is referred as the Pseudo-local Internal Heat Transfer Approach (PL-IHTA).

Additionally, the reproduction of the temperature profiles in absence of reaction from the PL-IHTA are compared with the conventional state-of-the-art approach, i.e., Boundary Layer Approach considering the KWT-BC, here referred as the KWT-BLA. For the sake of brevity, the details of KWT-BLA are given in Appendix 3C. Since the pseudo-local $k_{\text{eff},r,\text{PLA}}$ can be determined from the PL-IHTA, the following boundary condition is proposed for the estimation of the $h_{\text{w},\text{ext}}$:

$$r = R_t \quad - k_{\text{eff},r,\text{PLA}}(r) \frac{\partial T}{\partial r} = h_{\text{w},\text{ext}}(T_{\text{w},\text{in}} - T_b) \quad (3.35)$$

This model, Eqs. (3.27) – (3.35), is discretized using orthogonal collocation (40 radial and 15 axial points), employing shifted Legendre polynomials [40]. The resulting set of ordinary differential equations is solved using a fourth-order Runge-Kutta-Fehlberg method [41]. The experimental measurements from the non-isothermal and non-adiabatic heat transfer experiments are used for the estimation of $k_{\text{eff},r,\text{PLA}}$ and $h_{\text{w},\text{ext}}$. These parameters are estimated

using a combination of weighted orthogonal distance regression [42] and the Levenberg-Marquardt algorithm [43] by the minimization of the sum of squares of the weighted residuals between the experimental temperature and the model calculated ones, see Eq. (3.25).

In the following, this approach is referred to as the Pseudo-Local Approach (PLA). PLA helps to understand the role of the heat transfer mechanisms in the high void fraction zones and provides quantitative information of the internal heat boundary layer. For the sake of comparison between PLA and the conventional approaches utilized in literature, i.e., Classic Approach (CA) and the Boundary Layer Approach (BLA), more details of these approaches are given in Appendix 3D. Moreover, it is noteworthy that PLA avoids the historical cross-correlation issue between $k_{eff,r}$ and h_w , from the conventional approaches, because the pseudo-local $k_{eff,r,PLA}$ is obtained separately from $h_{w,ext}$. With the pseudo-local $k_{eff,r,PLA}$ and $h_{w,ext}$ estimated, a resistance analysis for the different zones is developed as follows [63]:

$$\frac{1}{U_w} = \frac{1}{h_{w,ext}} + \frac{R_t}{4k_{eff,r,PLA}} \quad (3.36)$$

where U_w is the overall heat transfer coefficient, the internal heat transfer resistances are characterized by the pseudo-local $k_{eff,r,PLA}$, and the external heat transfer resistances are characterized by $h_{w,ext}$. Moreover, for comparison sake, a conventional 1-D pseudo-homogeneous model is utilized for the estimation of U_w , see Appendix 3E.

3.4.4 Determining the radial effective thermal conductivity

The experimental methodology presented in Section 3.1, by heating the bench-scale and industrial-scale packed bed with an electric resistance and a salt bath around the external surface of the tube, targets at determining temperature gradients similar to those observed in industrial-scale wall-cooled packed-bed reactors. These observations are used to estimate the radial heat transfer parameters. The estimation of the heat transfer parameters is performed using weighted regression focusing on the temperature gradients at the core of the bed and near the wall. The estimates of $k_{eff,r,PLA}$ from PL-IHTA are presented in Table 3.2. The impact of considering and neglecting the $k_{eff,z}$ obtained in Section 3.4.2 is addressed on these estimations. For both scenarios, when $k_{eff,z}$ is considered or not, the parameters $k_{1,h}$ and $k_{2,h}$, from $k_{eff,r,PLA}$, follow the same trend for both the bench and industrial-scale packed bed. This is because the operating conditions, the d_i/d_p , and the packing geometrical configuration within both packed beds are the same. These results demonstrate what is well known in the literature, an

appropriate experimental design in a bench-scale packed bed allows an adequate internal heat transfer characterization which can be used for an accurate scale-up of the industrial-scale packed bed [2,11,35]. Figure 3.8 illustrates the pseudo-local variation of $k_{\text{eff},r,\text{PLA}}$, neglecting and accounting for $k_{\text{eff},z}$, within the bench and industrial-scale bed for Re_p between 210 and 1400 with the void fraction profile as a reference.

Table 3.2. Heat transfer parameter estimates and their corresponding 95% confidence intervals for the PL-IHTA (see Eqs. (3.33) – (3.34)).

Case	Re_p	$k_{1,h}$ without $k_{\text{eff},z}$	$k_{2,h}$ without $k_{\text{eff},z}$	$k_{1,h}$ with $k_{\text{eff},z}$	$k_{2,h}$ with $k_{\text{eff},z}$
PL-IHTA (Bench-scale)	210	0.56 ± 0.05	1.36 ± 0.12	0.82 ± 0.07	1.21 ± 0.11
	420	0.69 ± 0.05	1.20 ± 0.09	0.84 ± 0.09	1.10 ± 0.07
	630	0.96 ± 0.04	1.06 ± 0.10	0.97 ± 0.08	1.02 ± 0.08
	1260	5.34 ± 0.05	0.59 ± 0.04	4.90 ± 0.07	0.64 ± 0.04
PL-IHTA (Industrial-scale)	700	1.23 ± 0.08	1.10 ± 0.09	1.20 ± 0.08	0.95 ± 0.09
	1050	3.40 ± 0.07	0.71 ± 0.01	3.04 ± 0.04	0.75 ± 0.05
	1400	7.05 ± 0.05	0.52 ± 0.03	7.81 ± 0.04	0.42 ± 0.01

At all Re_p the trend is the same, there is a small decrease of the effective conductivity at the center of the bed, then a sudden rise in the high void fraction in the core zone, followed by a decrease after the high void fraction in the core zone and finally the effect of the $\delta_{\text{HT},\text{in}}$ decreasing the $k_{\text{eff},r,\text{PLA}}$ value until the static contribution value at the tube wall. The $k_{\text{eff},r,\text{PLA}}$ captures heat transfer mechanisms when there is no flow, i.e., the static contribution, and when there is flow, i.e., the dynamic contribution [64–66]. In the static contribution, $k_{\text{eff},r,\text{PLA}}$ captures the thermal conduction through solids and the contact surface of the pellets, while in the dynamic contribution $k_{\text{eff},r,\text{PLA}}$ captures the thermal conduction through the heat boundary layer near the pellets, heat transfer by convection between solid particles and by lateral mixing of the fluid. The results suggest that the dynamic heat transfer mechanisms are favored up to a Re_p of 630 in the core zone, after which a limit is reached such that the dynamic heat transfer mechanisms start to be affected, i.e., $k_{\text{eff},r,\text{PLA}}$ decreases as Re_p is increased up to 1400. This unexpected decrease of $k_{\text{eff},r,\text{PLA}}$ at high Re_p can be attributed to the synergy between the heat and fluid dynamics along the radial axis and axial convective mechanisms. Furthermore, the results show that difference between the profiles neglecting and considering $k_{\text{eff},z}$ at different Re_p can be neglected while estimating $k_{\text{eff},r,\text{PLA}}$. For a proper comparison between the axial and radial temperature profile descriptions considering the pseudo-local approach (PL-IHTA) and

the state-of-the-art conventional approaches, (KWT-BLA and KWT-CA), $k_{eff,r}$ is estimated. For the sake of brevity, more details of these approaches are given in Appendix 3C.

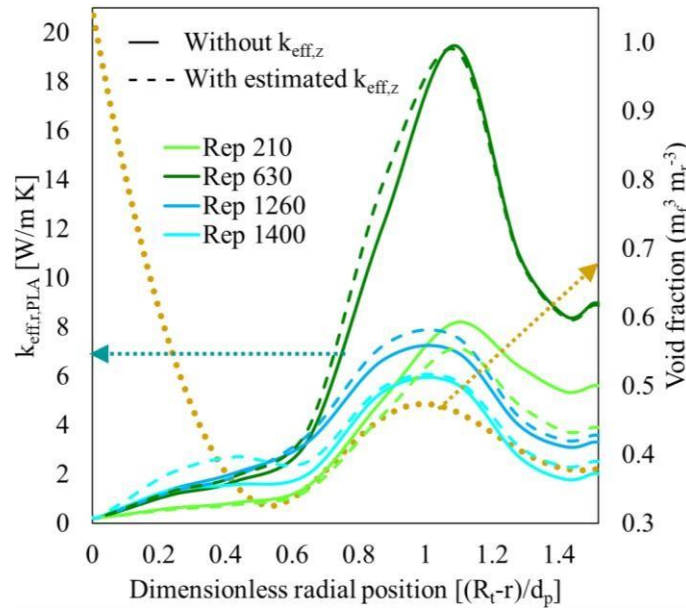
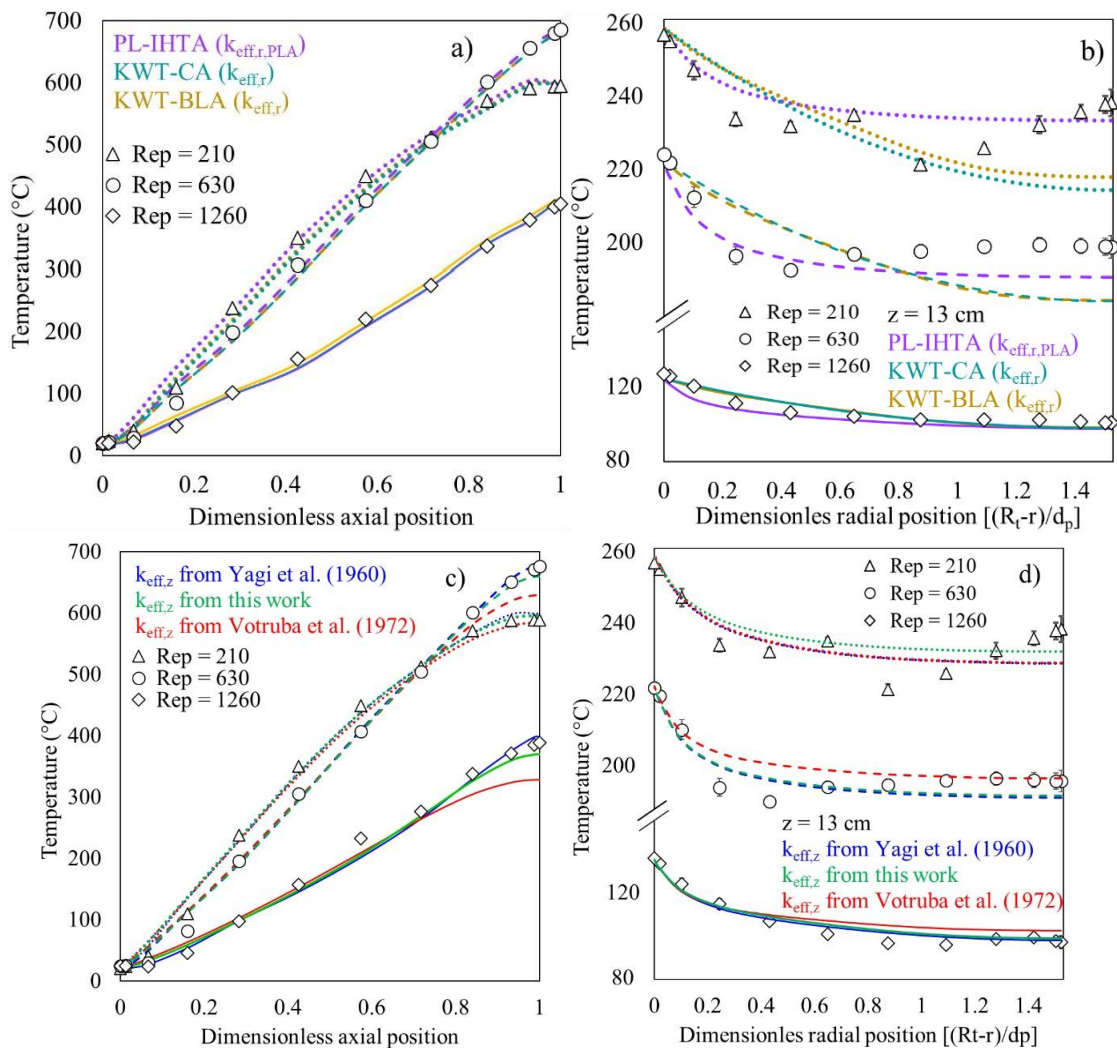


Figure 3.8. Pseudo-local $k_{eff,r,PLA}$ within the packed bed at Re_p from 210 to 1400. Estimations considering and neglecting $k_{eff,z}$ are presented as continuous lines and dashed lines, respectively. Void fraction is shown as reference with a yellow dotted line.

The capability of PL-IHTA, KWT-CA and KWT-BLA for describing radial and axial temperature profiles within the bench-scale packed bed at several Re_p , as well as the effect of $k_{eff,z}$ on the PL-IHTA, is illustrated in Figure 3.9. It should be noted that the temperatures at Re_p of 1260 are lower due to limitation of power on the electric resistance at this high flow. From the axial temperature profile descriptions at Re_p of 210, 630 and 1260, no significant difference is seen between the three approaches, see Figure 3.9a. Nevertheless, the radial temperature profile descriptions show PL-IHTA fit better to the experimental data than KWT-CA and KWT-BLA, particularly in the wall zone, see Figure 3.9b. This is because the radial heat transfer resistances are captured better by the pseudo-locality of the $k_{eff,r,PLA}$, as depicted in Figure 3.8, than when utilizing a constant $k_{eff,r}$. Moreover, since fluid dynamics significantly impacts the magnitude of the radial heat transfer mechanisms, its modelling is essential to accurately determine the pseudo-local $k_{eff,r,PLA}$. Regarding the impact of considering $k_{eff,z}$ on the temperature profile descriptions, three different correlations are considered for $k_{eff,z}$ on the PL-IHTA: (i) the one from Yagi et al. [10], (ii) that from Votruba et al. [52], and (iii) the one developed in this work. The axial temperature profiles show that at the entrance of the packed bed, there is no significant effect between considering $k_{eff,z}$ from the three correlations at any Re_p , see Figure 3.9c. This is remarked with the radial temperature profiles presented at 0.13 m_r

from the inlet, see Figure 3.9d. However, close to the outlet of the bed, the axial temperature gradients simulated using the $k_{eff,z}$ from Votruba et al. are less pronounced than the experimentally observed ones and those simulated with the $k_{eff,z}$ determined from the correlation developed in our present work and the one calculated from Yagi et al. correlation. The radial temperature gradients near at 0.43 m_r from the inlet indicate that the simulations considering the $k_{eff,z}$ from Votruba et al. underpredict the radial temperature gradient by 40 °C and 30 °C, for a Re_p of 1260 and 630, respectively. Considering the $k_{eff,z}$ calculated from Yagi et al. correlation or the one determined in this work leads to an adequate description of the radial temperature gradients. This is due to the $k_{eff,z}$ from Votruba et al. is higher than the one from Yagi et al., and the one estimated in this work. In other words, a high $k_{eff,z}$ leads to a less pronounced axial temperature gradient than those computed with a low $k_{eff,z}$. Because of the heating strategy considered, i.e., temperature control set at the center of the packed bed length, and the resulting development of a significant wall temperature profile along the bed, these results show that the impact of $k_{eff,z}$ is more significant at the outlet of the bed.



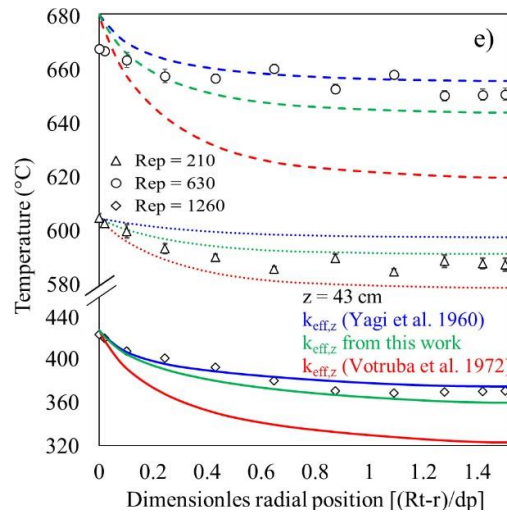
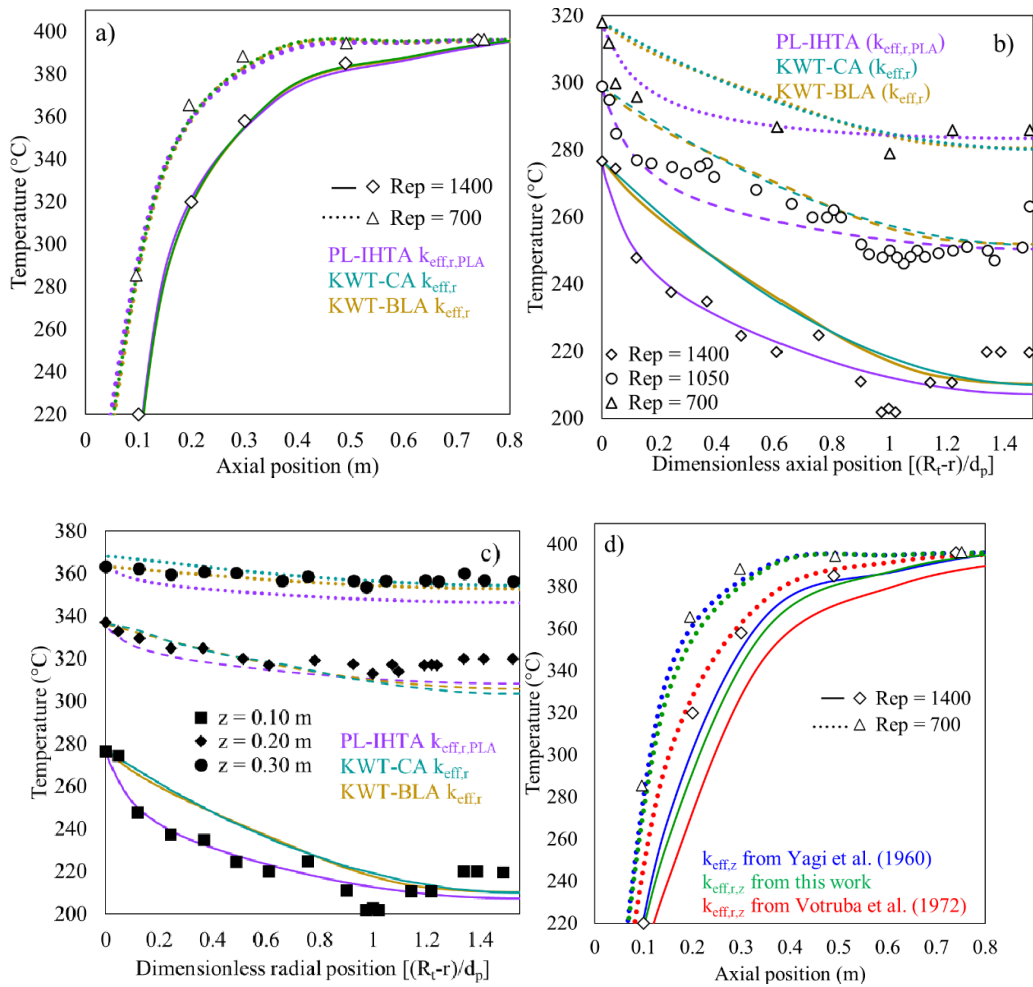


Figure 3.9. Temperature profiles within the bench-scale packed bed. a) Axial temperature profiles at the center of the bed assessing the pseudo-local $k_{eff,r}$. b) Radial temperature profiles at 13 cm from the inlet assessing the pseudo-local $k_{eff,r}$. c) Axial temperature profiles at the center of the bed assessing the $k_{eff,z}$. d) Radial temperature profiles at 13 cm from the inlet assessing the $k_{eff,z}$. e) Radial temperature profiles at 43 cm from the inlet assessing the $k_{eff,z}$.

On the other hand, Figure 3.10 depicts the simulated industrial-scale packed bed temperature profiles without $k_{eff,z}$ using the PL-IHTA, KWT-CA and KWT-BLA, and assessing the impact of $k_{eff,z}$ utilizing PL-IHTA. The operating conditions are a coolant temperature of 400 °C and Re_p between 700 and 1400. From the axial temperature profile descriptions at Re_p of 700 and 1400, no significant difference is seen between the three approaches, see Figure 3.10a. It should be noted that the main axial temperature gradients are from the entrance of the packed bed until 0.8 m_r , then isothermal conditions can be considered, i.e., constant temperature of 400 °C (not shown in Figure). The radial temperature profile descriptions at Re_p of 700, 1050 and 1400, at 0.10 m_r , show that PL-IHTA has a better description of the experimental measurements than the KWT-CA and KWT-BLA, particularly in the wall zone, see Figure 3.10b. This adequate description of the radial temperature gradients is also seen at different axial positions for a Re_p of 1400, see Figure 3.10c. Regarding the impact of $k_{eff,z}$, the simulations considering the $k_{eff,z}$ from Votruba et al. are those with the largest misprediction of the axial temperature data in the first 0.80 m_r of the industrial-scale packed bed, Figure 3.10d. However, at lengths larger than 0.80 m_r , the temperature profiles converge towards those calculated considering the $k_{eff,z}$ from Yagi et al. and the one determined in this work. The radial temperature profile descriptions at Re_p of 700, 1050 and 1400, at 0.10 m_r , show that there is not significant difference between considering the $k_{eff,z}$ from any correlation, see Figure 3.10e. Nonetheless, at different axial positions with a Re_p of 1400, the radial

temperature description considering the $k_{eff,z}$ from Votruba et al. correlation has a higher deviation than those simulations considering the $k_{eff,z}$ calculated with Yagi et al. correlation and the one developed in this work, see Figure 3.10f. It is noteworthy that the heating strategy in the industrial packed bed considers a constant temperature from the heat source, i.e., salt bath, at the wall as generally industrial wall-cooled packed bed reactors operate. Hence, due to the design of the heat transfer experiment, i.e., temperature difference between the salt bath and inlet air flow of 200 °C, the largest radial temperature gradients occur at the inlet of the packed bed, i.e., the first 0.80 m_r. This result shows that $k_{eff,z}$ has an impact on the temperature profile simulations particularly in the inlet of the packed bed, i.e., where hot spots are commonly identified (and where temperature gradients are most pronounced).



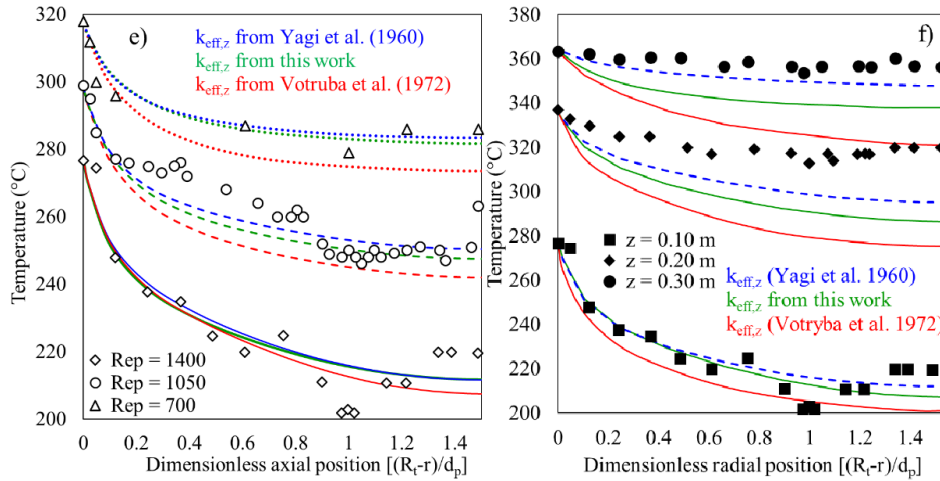


Figure 3.10. Temperature profiles within the industrial-scale packed bed. a) Axial temperature profiles at the center of the bed assessing the pseudo-local $k_{eff,r}$. b) Radial temperature profiles at 10 cm from the inlet with a Re_p of 700, 1050 and 1400 assessing the pseudo-local $k_{eff,r}$. c) Radial temperature profiles at 10, 20, and 30 cm from the inlet with a Re_p of 1400 assessing the pseudo-local $k_{eff,r}$. d) Axial temperature profiles at the center of the bed assessing the $k_{eff,z}$. e) Radial temperature profiles at 10 cm from the inlet with a Re_p of 700, 1050 and 1400 assessing the $k_{eff,z}$. f) Radial temperature profiles at 10, 20, and 30 cm from the inlet with a Re_p of 1400 assessing $k_{eff,z}$.

3.4.5 Determination of the wall heat transfer coefficient

Since the pseudo-local $k_{eff,r,PLA}$ has been determined from PL-IHTA, the estimation of the $h_{w,ext}$ is conducted considering the Pseudo-local approach (PLA), as indicated in Eq. (3.35). Additionally, for the sake of comparison with the conventional approaches utilized in literature, the estimation of h_w is done following the Classic Approach (CA) and the Boundary Layer Approach (BLA) detailed in Appendix 3D. The estimates of $h_{w,ext}$ are presented in Table 3.3.

It is worth noting that the wall heat transfer coefficient, h_w , obtained from CA and BLA, captures the radial heat transfer resistances of a “negligible” heat boundary layer, as was shown in Figure 3.6. Because the boundary condition is set at the tube wall, $k_{eff,r}$ captures the radial heat transfer mechanisms from the center of the bed to the “negligible” heat boundary layer [29,32,61,67–75]. In contrast, the use of the pseudo-local $k_{eff,r,PLA}$ allows properly characterizing the radial heat transfer resistances, such that the wall heat transfer coefficient, $h_{w,ext}$, is the only parameter estimated with the PLA. Thus, $h_{w,ext}$ captures the heat transfer mechanisms at the external side of the packed bed, i.e., the external heat pseudo-boundary layer. Moreover, in contrast to the high cross-correlation between $k_{eff,r}$ and h_w , normally higher than 0.85 [22,38,39,61,66–68], when both parameters are estimated following the conventional state-of-the-art approaches, i.e., CA and BLA, the cross-correlation obtained in this work was

between 0.41 and 0.75 for the considered operating conditions, i.e., Re_p 700 – 1400. This is because the regression method applied in this work considers the effect of weights along the radial zone of the bed, which allows a proper description of the most pronounced temperature gradients, including those observed near the wall.

Table 3.3. External heat wall transfer coefficient estimates and their corresponding 95% confidence intervals.

Case	Re_p	$h_{w,ext}$ ($W\ m^{-2}\ K^{-1}$)
PLA	700	55 ± 0.2
	1050	61 ± 0.3
	1400	71 ± 0.7

Figure 3.11 illustrates the temperature profiles predicted for the PLA and BLA, as well as the effect of $k_{eff,z}$ on the PLA, within the industrial-scale packed bed, with a coolant temperature of 400 °C and Re_p between 700 and 1400. It is worth noting that PLA and BLA are the only approaches that can be used during the heat transfer modeling of an industrial-scale reactor, in comparison with the PL-IHTA or KWT-BLA. This is because PLA and BLA contain the effect of the coolant source, i.e., coolant or bath temperature, T_b . For modeling highly exothermic packed bed reactors in the literature [2,3,18,22,57], BLA is the state-of-the-art for characterizing radial heat transfer mechanisms. The computed axial temperature profiles show that there is no significant difference between PLA and BLA, see Figure 3.11a. Nevertheless, when the effect of $k_{eff,z}$ is considered on PLA, similar trends as those presented in Figure 3.10d are seen, i.e., the simulations considering the $k_{eff,z}$ from Votruba et al. are those with the largest misprediction of the axial temperature data in the first 0.80 m_r . The radial temperature profile descriptions with a Re_p of 700 and 1400, at 0.10 m_r , indicate that BLA, accounting for h_w , does not predict properly the radial temperature gradient observed in the wall zone in comparison to PLA, which accounts for $h_{w,ext}$, see Figure 3.11b. This same trend is seen at different axial positions with a Re_p of 1400, see Figure 3.11c. When $k_{eff,z}$ is considered on PLA, the simulations accounting for the $k_{eff,z}$ calculated from Votruba et al. correlation underpredict the experimental data, while considering $k_{eff,z}$ from this work describes more adequately the observations, and $k_{eff,z}$ from Yagi et al. overpredicts them.

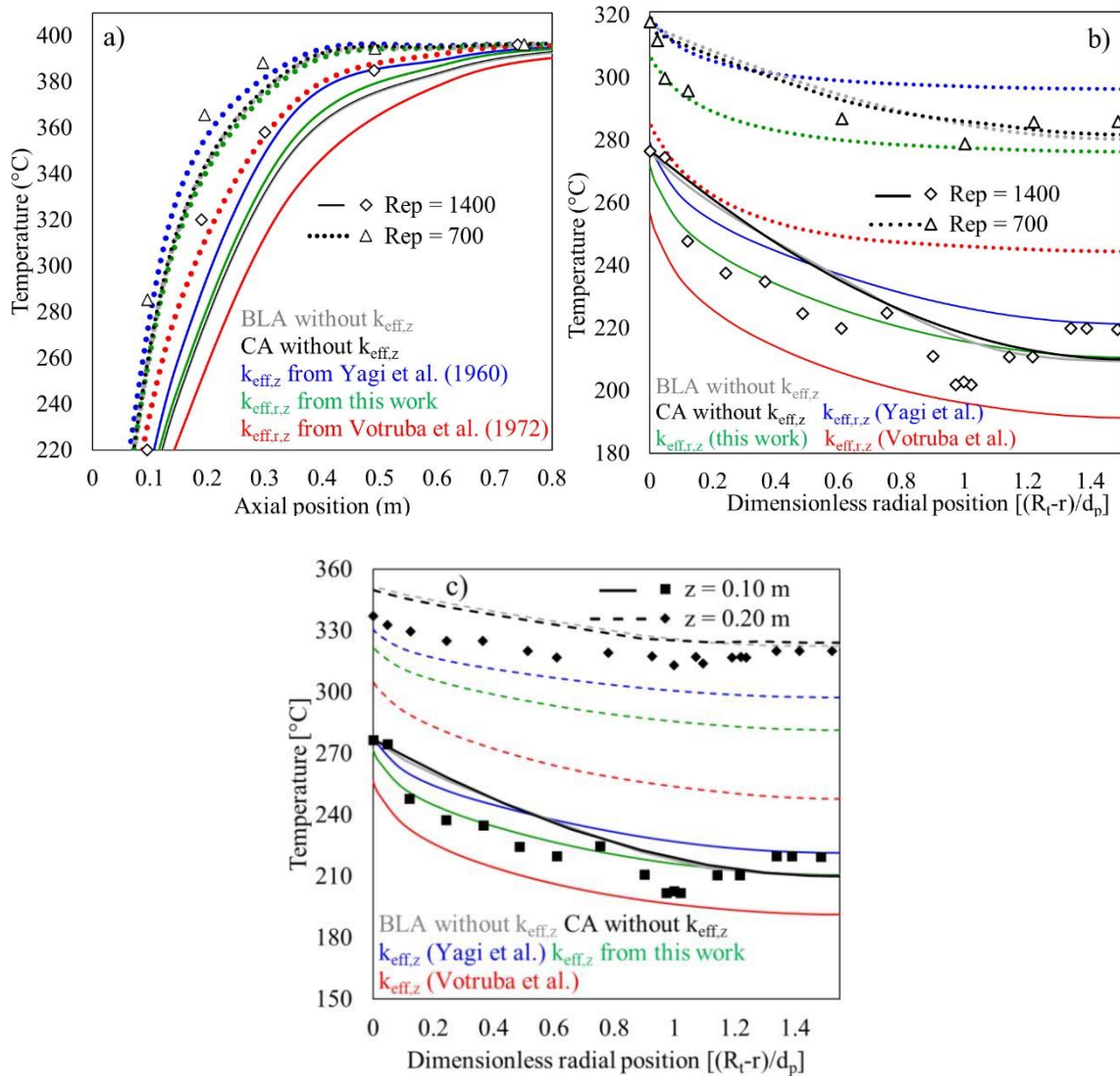


Figure 3.11. Temperature profiles within the industrial-scale packed bed. Axial temperature profiles at the center of the bed. Radial temperature profiles at 10 from the inlet with a Re_p of 700, 1050 and 1400. c) Radial temperature profiles at 10, 20, and 30 cm from the inlet with a Re_p of 1400.

3.4.6 Heat transfer resistance analysis

With the heat transfer parameters estimated out of PLA, i.e., $h_{w,ext}$, and the pseudo-local $k_{eff,r,PLA}$, a heat transfer resistance analysis is made following Eq. (3.36). Furthermore, for the sake of comparison, U_w is estimated from Eqs. (E1) – (E4), for the industrial-scale packed bed are calculated. The results of the internal and external resistances indicate that the external and internal heat transfer resistances are ca. 70% and 30 %, respectively, see Table 3.4. Moreover, regarding the 30% referred to the internal heat transfer resistances, these are lower than 1% in most of the packed bed except in the wall zone, see Figure 3.12. This indicates that the heat transfer resistances due to the $\delta_{HT,in}$ or shear stresses on the fluid by solid surfaces start to have

impact at ca. one pellet distance from the wall. Furthermore, between 0.7 pellets from the wall, the heat transfer resistances increase considerably from 1% up to 10%, which is in line with the pseudo-local $k_{eff,r,PLA}$ variation showed in Figure 3.8.

Table 3.4. Internal and external heat transfer resistances.

Re_p	Internal Resistances [W ⁻¹ K]	External Resistances [W ⁻¹ K]	Internal resistances (%)	External resistances (%)	Estimated U_w [W m ⁻² K ⁻¹]
700	0.00763	0.01822	29.58	70.42	75 ± 3.72
1050	0.00702	0.01634	30.07	69.93	81 ± 4.86
1400	0.00666	0.01400	32.29	67.71	78 ± 4.61

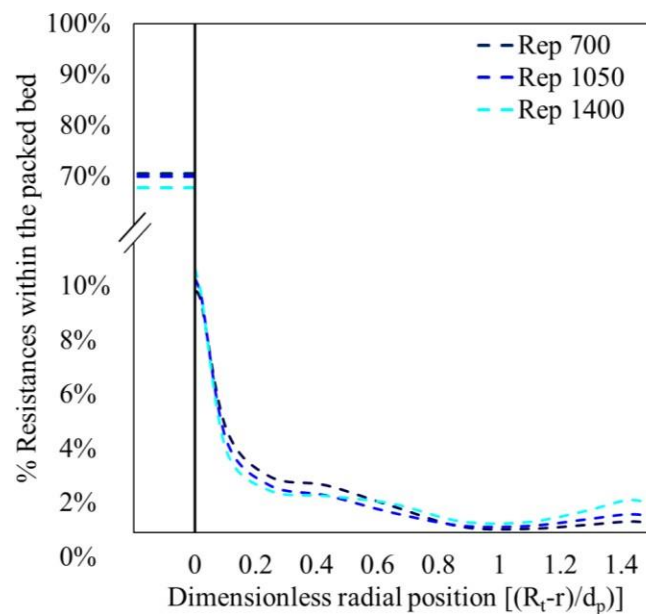


Figure 3.12. Percentage of external and internal heat transfer resistances within the industrial-scale packed bed at Re_p from 210 to 1400 Re_p

3.5 Conclusions

A novel developed methodology to reliably describe the temperature gradients within a packed bed with low tube to particle diameter ratio ($d_t/d_p < 8 \text{ m}_r \text{ m}_s^{-1}$) has demonstrated the

need to account for both fluid dynamics and pseudo local radial effective thermal conductivity, $k_{\text{eff},r,\text{PLA}}$.

The fluid dynamics within the packed bed was determined, using pressure drop experiments within a packed bed reactor, while ensuring the mass conservation criterion is met during the estimation of the effective viscosity, μ_{eff} . It was demonstrated that the velocity profiles, mainly in the wall zone, obtained from the non-conservative approaches overpredict the maximum velocity profile compared to the fluid dynamic model used in this work, particularly close to the wall.

A specifically determined $k_{\text{eff},z}$ from experiments at ‘adiabatic’ conditions, i.e., radially uniform temperatures, allows more accurately reproducing the experimentally measured axial temperature profile than when using more generic literature correlations, also at non-adiabatic and non-isothermal conditions, i.e., in the presence of radial temperature gradients. For industrial-scale packed beds, operated in the absence of reaction, the $k_{\text{eff},z}$ as determined in our work performs overall slightly less than the mostly used correlation from literature.

The radial temperature predictions obtained via the PLA greatly improves the lack of temperature description along the radial axis, including the zone near to the wall using the conventional approaches. At ca. one-pellet distance from the wall the pseudo-local $k_{\text{eff},r,\text{PLA}}$ has the highest value, because fluid velocity favors the dynamic heat transfer contribution. In the wall zone, $k_{\text{eff},r,\text{PLA}}$ decreases as a result of the synergy between fluid dynamics and the heat boundary layers in the wall. Moreover, the pseudo-local parameters, i.e., $k_{1,h}$ and $k_{2,h}$, are in good agreement with those obtained at bench-scale and industrial-scale. This is mainly thanks to the operating conditions, the geometrical configuration and the packing that can be considered the same at both scales. Thus, an accurate scale-up can be ensured thanks to the use of the pseudo-local $k_{\text{eff},r,\text{PLA}}$ considering that the internal heat transfer mechanisms are very similar between both scales. Considering a pseudo-local $k_{\text{eff},r,\text{PLA}}$, when describing radial temperature observations, results in a major enhancement of the description of the temperature data along the radial axis, particularly in the wall zone. This improvement in the temperature description demonstrates the limitations of the conventional heat transfer approaches that consider $k_{\text{eff},r}$.

Moreover, the pseudo-local approach allows a reliable analysis to determine heat transfer resistances at the coolant side by estimating the external wall heat transfer coefficient, $h_{w,\text{ext}}$. The proper characterization of the external heat transfer resistances encountered in the

$\delta_{HT,ext}$ via the $h_{w,ext}$ demonstrated that the internal and external heat transfer resistances are ca. 30% and 70% of the total heat transfer resistances, respectively.

One of the goals from this thesis is to assess the impact of the pseudo-local approach and the axial heat transfer by conduction on the simulated temperature profiles within packed bed reactors in which highly exothermic reactions occur, particularly at lengths around 0.5 m, where hot spots occur during reactor performance [31,76–78]. In the next Chapter, this is addressed by evaluating the system under ODH reaction conditions.

3.6 References

- [1] H. Delmas, G.F. Froment, A simulation model accounting for structural radial nonuniformities in fixed bed reactors, *Chem Eng Sci* 43 (1988) 2281–2287. [https://doi.org/10.1016/0009-2509\(88\)87116-1](https://doi.org/10.1016/0009-2509(88)87116-1).
- [2] C.O. Castillo-Araiza, F. López-Isunza, Modeling the partial oxidation of o-xylene in an industrial packed-bed catalytic reactor: The role of hydrodynamics and catalyst activity in the heat transport, *Ind Eng Chem Res* 49 (2010) 6845–6853. <https://doi.org/10.1021/ie901720z>.
- [3] O. Galan, V.G. Gomes, J. Romagnoli, K.F. Ngian, Selective oxidation of ethylene in an industrial packed-bed reactor: Modelling, analysis and optimization, *International Journal of Chemical Reactor Engineering* 7 (2009). <https://doi.org/10.2202/1542-6580.2058>.
- [4] Z. Nawaz, Heterogeneous Reactor Modeling of an Industrial Multitubular Packed-Bed Ethylene Oxide Reactor, *Chem Eng Technol* 39 (2016) 1845–1857. <https://doi.org/10.1002/ceat.201500603>.
- [5] Linde, EDHOX™ technology, (2021). <https://www.linde-engineering.com/en/process-plants/petrochemical-plants/edhox-technology/index.html> (accessed October 16, 2023).
- [6] Y. Chen, B. Yan, Y. Cheng, State-of-the-Art Review of Oxidative Dehydrogenation of Ethane to Ethylene over MoVNbTeOx Catalysts, *Catalysts* 13 (2023) 204. <https://doi.org/10.3390/catal13010204>.
- [7] C.O. Castillo-Araiza, F. López-Isunza, The role of catalyst activity on the steady state and transient behavior of an industrial-scale fixed bed catalytic reactor for the partial oxidation of o-xylene on V2O5/TiO2 catalysts, *Chemical Engineering Journal* 176–177 (2011) 26–32. <https://doi.org/10.1016/j.cej.2011.06.051>.
- [8] G. Che-Galicia, R.S. Ruiz-Martínez, F. López-Isunza, C.O. Castillo-Araiza, Modeling of oxidative dehydrogenation of ethane to ethylene on a MoVTenbO/TiO2 catalyst in an industrial-scale packed bed catalytic reactor, *Chemical Engineering Journal* 280 (2015) 682–694. <https://doi.org/10.1016/j.cej.2015.05.128>.
- [9] C.O. Castillo-Araiza, H. Jiménez-Islas, F. López-Isunza, Heat-transfer studies in packed-bed catalytic reactors of low tube/particle diameter ratio, *Ind Eng Chem Res* 46 (2007) 7426–7435. <https://doi.org/10.1021/ie070097z>.
- [10] S. Yagi, D. Kunii, N. Wakao, Studies on axial effective thermal conductivities in packed beds, *AIChE Journal* 6 (1960) 543–546. <https://doi.org/10.1002/aic.690060407>.
- [11] H.F. López-Isunza, Steady state and dynamic behaviour of an industrial scale fixed bed catalytic reactor, Ph. D. thesis, Ph.D. thesis, University of London, 1983.

- [12] F.C. Blake, The Resistance of packing to fluid flow, Transactions of the American Institute of Chemical Engineers 14 (1922) 415–421.
- [13] S.P. Burke, W.B. Plummer, Gas Flow through Packed Columns, Ind Eng Chem 20 (1928) 1196–1200.
- [14] S. Ergun, Fluid flow through packed columns, Chem Eng Prog 48 (1952) 89–94.
- [15] A. Hernandez-Aguirre, E. Hernandez-Martinez, F. López-Isunza, C.O. Castillo, Framing a novel approach for pseudo continuous modeling using Direct Numerical Simulations (DNS): Fluid dynamics in a packed bed reactor, Chemical Engineering Journal 429 (2022). <https://doi.org/10.1016/j.cej.2021.132061>.
- [16] C. Limberg, Computergenerierte Kugelschüttungen in zylindrischen Rohren als Basis für eine differenzierte Modellierung von Festbettreaktoren, Ph. D. thesis, Ph. D. thesis, Technischen Universität Cottbus, 2002.
- [17] A.R. Morcom, Fluid Flow through granular materials, Transactions of Institution of Chemical Engineering 24 (1946) 30–46.
- [18] B. Eisfeld, K. Schnitzlein, The influence of confining walls on the pressure drop in packed beds, Chem Eng Sci 56 (2001) 4321–4329. [https://doi.org/10.1016/S0009-2509\(00\)00533-9](https://doi.org/10.1016/S0009-2509(00)00533-9).
- [19] J.N. Papageorgiou, G.F. Froment, Simulation models accounting for radial voidage profiles in fixed-bed reactors, Chem Eng Sci 50 (1995) 3043–3056. [https://doi.org/10.1016/0009-2509\(95\)00138-U](https://doi.org/10.1016/0009-2509(95)00138-U).
- [20] A. De Klerk, Voidage variation in packed beds at small column to particle diameter ratio, AIChE Journal 49 (2003) 2022–2029. <https://doi.org/10.1002/aic.690490812>.
- [21] P. Kumar, S.K. Saha, A. Sharma, Experimental and CFD-DEM study on local packing distribution and thermofluidic analysis of binary packed bed, Chem Eng Sci 282 (2023) 119372. <https://doi.org/10.1016/j.ces.2023.119372>.
- [22] G. Aparicio-Mauricio, R.S. Ruiz, F. López-Isunza, C.O. Castillo-Araiza, A simple approach to describe hydrodynamics and its effect on heat and mass transport in an industrial wall-cooled fixed bed catalytic reactor: ODH of ethane on a MoVNbTeO formulation, Chemical Engineering Journal 321 (2017) 584–599. <https://doi.org/10.1016/j.cej.2017.03.043>.
- [23] C. Li, J. Xu, T. Qiu, Z. Sun, H. Zhang, W. Ge, Trans-level multi-scale simulation of porous catalytic systems: Bridging reaction kinetics and reactor performance, Chemical Engineering Journal 455 (2023) 140745. <https://doi.org/10.1016/j.cej.2022.140745>.
- [24] C.O. Castillo-araiza, F. Lopez-isunza, Hydrodynamic Models for Packed Beds with Low Tube-to-Particle Diameter Ratio Hydro, International Journal of Chemical Reactor Engineering 6 (2008) 1–14. <https://doi.org/https://doi.org/10.2202/1542-6580.1550>.
- [25] H. Darcy, Les Fontaines Publiques de la Ville de Dijon, Dalmon, Paris, 1856.
- [26] P. Forchheimer, Tratado de Hidráulica, Ed. Labor, Barcelona, 1935.
- [27] H.C. Brinkman, A calculation of the viscous force exerted by a flowing fluid on a dense swarm of particles, Flow Turbul Combust 1 (1949) 27. <https://doi.org/10.1007/BF02120313>.
- [28] M. Giese, K. Rottschäfer, D. Vortmeyer, Measured and Modeled Superficial Flow Profiles in Packed Beds with Liquid Flow, AIChE Journal 44 (1998) 484–490. <https://doi.org/10.1002/aic.690440225>.
- [29] O. Bey, G. Eigenberger, Fluid flow through catalyst filled tubes, Chem Eng Sci 52 (1997) 1365–1376. [https://doi.org/10.1016/S0009-2509\(96\)00509-X](https://doi.org/10.1016/S0009-2509(96)00509-X).

- [30] M. Winterberg, E. Tsotsas, Impact of tube-to-particle-diameter ratio on pressure drop in packed beds, *AIChE Journal* 46 (2000) 1084–1088. <https://doi.org/10.1002/aic.690460519>.
- [31] G. Che-Galicia, F. López-Isunza, E. Corona-Jiménez, C.O. Castillo-Araiza, The role of kinetics and heat transfer on the performance of an industrial wall-cooled packed-bed reactor: Oxidative dehydrogenation of ethane, *AIChE Journal* 66 (2020). <https://doi.org/10.1002/aic.16900>.
- [32] O. Bey, G. Eigenberger, Gas flow and heat transfer through catalyst filled tubes, *International Journal of Thermal Sciences* 40 (2001) 152–164. [https://doi.org/10.1016/S1290-0729\(00\)01204-7](https://doi.org/10.1016/S1290-0729(00)01204-7).
- [33] A.I. Anastasov, The behaviour of a low-productive non-pretreated V₂O₅–TiO₂ (anatase) catalyst for oxidation of o-xylene to phthalic anhydride, *Chemical Engineering Journal* 109 (2005) 57–66. <https://doi.org/10.1016/j.cej.2005.03.010>.
- [34] A.I. Anastasov, A study of the influence of the operating parameters on the temperature of the hot spot in a fixed bed reactor, *Chemical Engineering Journal* 86 (2002) 287–297. [https://doi.org/10.1016/S1385-8947\(01\)00178-4](https://doi.org/10.1016/S1385-8947(01)00178-4).
- [35] L.S. Kershenbaum, F. Lopez-Isunza, Dynamic Behavior of an Industrial Scale Fixed-Bed Catalytic Reactor., *ACS Symposium Series* (1982) 109–120. <https://doi.org/10.1021/bk-1982-0196.ch010>.
- [36] G.F. Froment, FIXED BED CATALYTIC REACTORS—CURRENT DESIGN STATUS, *Ind Eng Chem* 59 (1967) 18–27. <https://doi.org/10.1021/ie50686a006>.
- [37] A.P. De Wasch, G.F. Froment, Heat transfer in packed beds, *Chem Eng Sci* 27 (1972) 567–576. [https://doi.org/10.1016/0009-2509\(72\)87012-X](https://doi.org/10.1016/0009-2509(72)87012-X).
- [38] J.J. Lerou, G.F. Froment, Velocity, temperature and conversion profiles in fixed bed catalytic reactors, *Chem Eng Sci* 32 (1977) 853–861. [https://doi.org/10.1016/0009-2509\(77\)80071-7](https://doi.org/10.1016/0009-2509(77)80071-7).
- [39] Z. Wan, J. Jiang, H. Ma, Y. Li, Y. Lu, F. Cao, A study of the heat transfer characteristics of novel Ni-foam structured catalysts, *Canadian Journal of Chemical Engineering* 94 (2016) 2225–2234. <https://doi.org/10.1002/cjce.22587>.
- [40] B.A. Finlayson, *Nonlinear Analysis in Chemical Engineering*, McGraw-Hill, New York, 2003.
- [41] L. Lapidus, J.H. Seinfeld, *Numerical solution of ordinary differential equations*, Academic Press, New York, 1971.
- [42] P.T. Boggs, J.R. Donaldson, R.H. Byrd, R.B. Schnabel, Algorithm 676: ODRPACK: software for weighted orthogonal distance regression, *ACM Transactions on Mathematical Software* 15 (1989) 348–364. <https://doi.org/10.1145/76909.76913>.
- [43] D.W. Marquardt, An algorithm for least-squares estimation of nonlinear parameters, *Journal of the Society for Industrial and Applied Mathematics* 11 (1963) 431–441. <https://doi.org/https://doi.org/10.1137/0111030>.
- [44] B. Sosna, Y. Dong, L. Chromow, O. Korup, R. Horn, Effective Axial Thermal Conductivity in Catalyst Packings from High Resolution Temperature Profiles, *Chem Ing Tech* 88 (2016) 1676–1683. <https://doi.org/10.1002/cite.201600062>.
- [45] F. Maqbool, S.Z. Abbas, S. Ramirez-Solis, V. Dupont, T. Mahmud, Modelling of one-dimensional heterogeneous catalytic steam methane reforming over various catalysts in an adiabatic packed bed reactor, *Int J Hydrogen Energy* 46 (2021) 5112–5130. <https://doi.org/10.1016/j.ijhydene.2020.11.071>.
- [46] R. Tariq, F. Maqbool, S.Z. Abbas, Small-scale production of hydrogen via auto-thermal reforming in an adiabatic packed bed reactor: Parametric study and reactor's optimization

- through response surface methodology, *Comput Chem Eng* 145 (2021) 107192. <https://doi.org/10.1016/j.compchemeng.2020.107192>.
- [47] K.N. Son, J.A. Weibel, J.C. Knox, S. V. Garimella, Limitations of the Axially Dispersed Plug-Flow Model in Predicting Breakthrough in Confined Geometries, *Ind Eng Chem Res* 58 (2019) 3853–3866. <https://doi.org/10.1021/acs.iecr.8b05925>.
- [48] G. Pantoleontos, E.S. Kikkinides, M.C. Georgiadis, A heterogeneous dynamic model for the simulation and optimisation of the steam methane reforming reactor, *Int J Hydrogen Energy* 37 (2012) 16346–16358. <https://doi.org/10.1016/j.ijhydene.2012.02.125>.
- [49] M. Parhoudeh, F. Farshchi Tabrizi, M.R. Rahimpour, Auto-Thermal Chemical Looping Reforming Process in a Network of Catalytic Packed-Bed Reactors for Large-Scale Syngas Production: A Comprehensive Dynamic Modeling and Multi-Objective Optimization, *Top Catal* (2022). <https://doi.org/10.1007/s11244-021-01522-0>.
- [50] E. V. Ovchinnikova, N. V. Vernikovskaya, A.G. Gribovskii, V.A. Chumachenko, Multichannel microreactors for highly exothermic catalytic process: The influence of thermal conductivity of reactor material and of transport phenomena inside the channels on the process efficiency, *Chemical Engineering Journal* 409 (2021) 128046. <https://doi.org/10.1016/j.cej.2020.128046>.
- [51] T. Metzger, S. Didierjean, D. Maillet, Optimal experimental estimation of thermal dispersion coefficients in porous media, *Int J Heat Mass Transf* 47 (2004) 3341–3353. <https://doi.org/10.1016/j.ijheatmasstransfer.2004.02.024>.
- [52] J. Votruba, V. Hlaváček, M. Marek, Packed bed axial thermal conductivity, *Chem Eng Sci* 27 (1972) 1845–1851. [https://doi.org/10.1016/0009-2509\(72\)85046-2](https://doi.org/10.1016/0009-2509(72)85046-2).
- [53] M. Elsari, R. Hughes, Axial effective thermal conductivities of packed beds, *Appl Therm Eng* 22 (2002) 1969–1980. [https://doi.org/10.1016/S1359-4311\(02\)00117-5](https://doi.org/10.1016/S1359-4311(02)00117-5).
- [54] D. Vortmeyer, W. Adam, Steady-state measurements and analytical correlations of axial effective thermal conductivities in packed beds at low gas flow rates, *Int J Heat Mass Transf* 27 (1984) 1465–1472. [https://doi.org/10.1016/0017-9310\(84\)90259-X](https://doi.org/10.1016/0017-9310(84)90259-X).
- [55] R.K. Sharma, D.L. Cresswell, E.J. Newson, Kinetics and fixed-bed reactor modeling of butane oxidation to maleic anhydride, *AIChE Journal* 37 (1991) 39–47. <https://doi.org/10.1002/aic.690370103>.
- [56] M. Winterberg, E. Tsotsas, A. Krischke, D. Vortmeyer, A simple and coherent set of coefficients for modelling of heat and mass transport with and without chemical reaction in tubes filled with spheres, *Chem Eng Sci* 55 (2000) 967–979. [https://doi.org/10.1016/S0009-2509\(99\)00379-6](https://doi.org/10.1016/S0009-2509(99)00379-6).
- [57] G. Che-Galicia, R.S. Ruiz-Martínez, D. Rios-Morales, J.A. Ayala-Romero, C.O. Castillo-Araiza, Kinetic and reactor performance of a Ni-based catalyst during the production of ethene, *Chem Eng Commun* 205 (2018) 372–386. <https://doi.org/10.1080/00986445.2017.1396538>.
- [58] L.M.D.M. Jorge, R.M.M. Jorge, R. Giudici, Experimental and numerical investigation of dynamic heat transfer parameters in packed bed, *Heat and Mass Transfer/Waerme- Und Stoffuebertragung* 46 (2010) 1355–1365. <https://doi.org/10.1007/s00231-010-0659-6>.
- [59] S. Ströhle, A. Haselbacher, Z.R. Jovanovic, A. Steinfeld, Transient discrete-granule packed-bed reactor model for thermochemical energy storage, *Chem Eng Sci* 117 (2014) 465–478. <https://doi.org/10.1016/j.ces.2014.07.009>.
- [60] M. Fattahi, M. Kazemini, F. Khorasheh, A. Darvishi, A.M. Rashidi, Fixed-bed multi-tubular reactors for oxidative dehydrogenation in ethylene process, *Chem Eng Technol* 36 (2013) 1691–1700. <https://doi.org/10.1002/ceat.201300148>.

- [61] V.A. Nikolov, A.I. Anastasov, Influence of the inlet temperature on the performance of a fixed-bed reactor for oxidation of o-xylene into phthalic anhydride, *Chem Eng Sci* 47 (1992) 1291–1298. [https://doi.org/10.1016/0009-2509\(92\)80249-C](https://doi.org/10.1016/0009-2509(92)80249-C).
- [62] D. Vortmeyer, E. Haidegger, Discrimination of three approaches to evaluate heat fluxes for wall-cooled fixed bed chemical reactors, *Chem Eng Sci* 46 (1991) 2651–2660. [https://doi.org/10.1016/0009-2509\(91\)80058-7](https://doi.org/10.1016/0009-2509(91)80058-7).
- [63] E.I. Smirnov, A. V. Muzykantov, V.A. Kuzmin, A.E. Kronberg, I.A. Zolotarskii, Radial heat transfer in packed beds of spheres, cylinders and Rashig rings Verification of model with a linear variation of λ_{er} in the vicinity of the wall, *Chemical Engineering Journal* 91 (2003) 243–248. [https://doi.org/10.1016/S1385-8947\(02\)00160-2](https://doi.org/10.1016/S1385-8947(02)00160-2).
- [64] S. Yagi, N. Wakao, Heat and mass transfer from wall to fluid in packed beds, *AIChE Journal* 5 (1959) 79–85. <https://doi.org/10.1002/aic.690050118>.
- [65] J.R. Fernández, J.M. Alarcón, J.C. Abanades, Investigation of a Fixed-Bed Reactor for the Calcination of CaCO_3 by the Simultaneous Reduction of CuO with a Fuel Gas, *Ind Eng Chem Res* 55 (2016) 5128–5132. <https://doi.org/10.1021/acs.iecr.5b04073>.
- [66] N. Wakao, S. Kaguei, T. Funazkri, Effect of fluid dispersion coefficients on particle-to-fluid heat transfer coefficients in packed beds. Correlation of nusselt numbers, *Chem Eng Sci* 34 (1979) 325–336. [https://doi.org/10.1016/0009-2509\(79\)85064-2](https://doi.org/10.1016/0009-2509(79)85064-2).
- [67] D. Wen, Y. Ding, Heat transfer of gas flow through a packed bed, *Chem Eng Sci* 61 (2006) 3532–3542. <https://doi.org/10.1016/j.ces.2005.12.027>.
- [68] D.J. Gunn, M. Khalid, Thermal dispersion and wall heat transfer in packed beds, *Chem Eng Sci* 30 (1975) 261–267. [https://doi.org/10.1016/0009-2509\(75\)80014-5](https://doi.org/10.1016/0009-2509(75)80014-5).
- [69] G.F. Froment, Design of fixed-bed catalytic reactors based on effective transport models, *Chem Eng Sci* 17 (1962) 849–859. [https://doi.org/10.1016/0009-2509\(62\)87017-1](https://doi.org/10.1016/0009-2509(62)87017-1).
- [70] E.M. Moghaddam, E.A. Foumeny, A.I. Stankiewicz, J.T. Padding, Multiscale modelling of wall-to-bed heat transfer in fixed beds with non-spherical pellets: From particle-resolved CFD to pseudo-homogenous models, *Chem Eng Sci* 236 (2021) 116532. <https://doi.org/10.1016/j.ces.2021.116532>.
- [71] A.G. Dixon, D.L. Cresswell, Comments on “Estimation of heat transfer parameters in packed beds from radial temperature profiles” by J. J. Lerou and G. F. Froment, *The Chemical Engineering Journal* 17 (1979) 247–248. [https://doi.org/10.1016/0300-9467\(79\)85020-0](https://doi.org/10.1016/0300-9467(79)85020-0).
- [72] A.G. Dixon, J.H. Van Dongeren, The influence of the tube and particle diameters at constant ratio on heat transfer in packed beds, *Chemical Engineering and Processing: Process Intensification* 37 (1998) 23–32. [https://doi.org/10.1016/S0255-2701\(97\)00033-0](https://doi.org/10.1016/S0255-2701(97)00033-0).
- [73] R.A. Dekhtyar', D.P. Sikovsky, A. V. Gorine, V.A. Mukhin, Heat transfer in a packed bed at moderate values of the Reynolds number, *High Temperature* 40 (2002) 693–700. <https://doi.org/10.1023/A:1020432619305>.
- [74] E.I. Smirnov, V.A. Kuzmin, I.A. Zolotarskii, Radial thermal conductivity in cylindrical beds packed by shaped particles, *Chemical Engineering Research and Design* 82 (2004) 293–296. <https://doi.org/10.1205/026387604772992891>.
- [75] J.C. Thoméo, J.T. Freire, Heat transfer in fixed bed: a model non-linearity approach, *Chem Eng Sci* 55 (2000) 2329–2338. [https://doi.org/10.1016/S0009-2509\(99\)00465-0](https://doi.org/10.1016/S0009-2509(99)00465-0).
- [76] T. Daszkowski, G. Eigenberger, A reevaluation of fluid flow, heat transfer and chemical reaction in catalyst filled tubes, *Chem Eng Sci* 47 (1992) 2245–2250. [https://doi.org/10.1016/0009-2509\(92\)87042-O](https://doi.org/10.1016/0009-2509(92)87042-O).

- [77] E. Tsotsas, E.U. Schlünder, Heat transfer in packed beds with fluid flow: remarks on the meaning and the calculation of a heat transfer coefficient at the wall, *Chem Eng Sci* 45 (1990) 819–837. [https://doi.org/10.1016/0009-2509\(90\)85005-X](https://doi.org/10.1016/0009-2509(90)85005-X).
- [78] S. Wang, C. Xu, W. Liu, Z. Liu, Numerical study on heat transfer performance in packed bed, *Energies (Basel)* 12 (2019). <https://doi.org/10.3390/en12030414>.
- [79] O.R. Derkx, A.G. Dixon, Effect of the wall Nusselt number on the simulation of catalytic fixed bed reactors, *Catal Today* 35 (1997) 435–442. [https://doi.org/10.1016/S0920-5861\(96\)00210-6](https://doi.org/10.1016/S0920-5861(96)00210-6).
- [80] J. Skrzypek, M. Grzesik, M. Galantowicz, J. Soliński, Kinetics of the catalytic air oxidation of o-xylene over a commercial V₂O₅-TiO₂ catalyst, *Chem Eng Sci* 40 (1985) 611–620. [https://doi.org/10.1016/0009-2509\(85\)80005-1](https://doi.org/10.1016/0009-2509(85)80005-1).
- [81] C. McGreavy, E.A. Foumeny, K.H. Javed, Characterization of transport properties for fixed bed in terms of local bed structure and flow distribution, *Chem Eng Sci* 41 (1986) 787–797. [https://doi.org/10.1016/0009-2509\(86\)87159-7](https://doi.org/10.1016/0009-2509(86)87159-7).
- [82] P.H. Calderbank, K. Chandrasekharan, C. Fumagalli, The prediction of the performance of packed-bed catalytic reactors in the air-oxidation of o-xylene, *Chem Eng Sci* 32 (1977) 1435–1443. [https://doi.org/10.1016/0009-2509\(77\)80240-6](https://doi.org/10.1016/0009-2509(77)80240-6).
- [83] W. Kwapinski, Combined wall and thermal effects during non-isothermal packed bed adsorption, *Chemical Engineering Journal* 152 (2009) 271–276. <https://doi.org/10.1016/j.cej.2009.05.023>.
- [84] W. Kwapinski, M. Winterberg, E. Tsotsas, D. Mewes, Modeling of the Wall Effect in Packed Bed Adsorption, *Chem Eng Technol* 27 (2004) 1179–1186. <https://doi.org/10.1002/ceat.200407001>.
- [85] S. Yagi, D. Kunii, Studies on effective thermal conductivities in packed beds, *AIChE Journal* 3 (1957) 373–381. <https://doi.org/10.1002/aic.690030317>.
- [86] R. Bauer, E.U. Schlünder, Effective radial thermal conductivity of packings in gas flow, *Int. Chem. Eng.* 18 (1978) 189–204.
- [87] A.G. Dixon, D.L. Cresswell, Theoretical prediction of effective heat transfer parameters in packed beds, *AIChE Journal* 25 (1979) 663–676. <https://doi.org/10.1002/aic.690250413>.

Appendices

Appendix 3A Heat transfer mechanisms captured by the effective thermal conductivity

Due to the complexity on describing the heat transfer mechanisms between solids and the fluid phase within a packed bed reactor with low d_t/d_p ($< 8 m_r m_s^{-1}$), 2-D pseudo-continuous models employing an effective thermal conductivity (k_{eff}) and a wall heat transfer coefficient (h_w), have been widely utilized [19,32,38,67,76,77,79–84]. The k_{eff} encompasses nine different heat transfer mechanisms [85], see Figure 3A.1, divided by those at static (no fluid flow) and dynamic (fluid flowing) conditions. At static conditions, heat transfer occurs by the conduction through motionless fluid, conduction through pellet contact, the radiation between void fraction, the radiation between solid surfaces, and the conduction through the pellet. While at dynamic conditions, heat transfer occurs by the convection in the fluid flow, conduction in the boundary layer between pellets, heat transfer by mixing, and heat transfer by convection solid-fluid-solid. Generally, k_{eff} is considered an anisotropic parameter, being referred to the axial and radial coordinate as the axial effective thermal conductivity ($k_{eff,z}$) and radial effective thermal conductivity ($k_{eff,r}$), respectively.

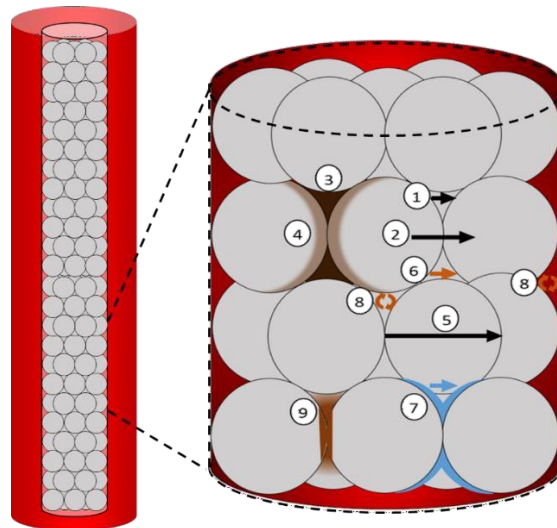


Figure 3A.1. Schematic diagram of the heat transfer mechanisms captured by the effective thermal conductivity. Independent of fluid flow: (1) Conduction through motionless fluid, (2) Conduction through pellet contact, (3) Radiation between void fraction, (4) Radiation between solid surfaces, (5) Conduction through the pellet. Dependent on fluid flow: (6) Convection in the fluid flow direction, (7) Conduction in the boundary layer between pellets, (8) Heat transfer by mixing, and (9) Heat transfer by convection solid-fluid-solid.

Appendix 3B Literature correlations for the calculation of $k_{eff,z}$

For comparison sake, two literature correlations are utilized to calculate $k_{eff,z}$ and evaluate its impact in Eqs. (3.21) – (3.24). The first one is the correlation from Yagi et al. [10], see Eq. (3B.1).

$$\frac{k_{eff,z}}{k_f} = \frac{k_{eff,z}^0}{k_f} + \delta \frac{Re Pr}{p} \quad (3B.1)$$

In which $k_{eff,z}^0$ represents the axial effective conductivity in absence of flow, i.e., the static contribution, k_f the fluid thermal conductivity, and δ an empirical parameter related to the dynamic contribution. The latter has values between 0.7 and 0.8 depending on the material used as packing. Characteristic for Yagi et al. [10] correlation is that it has been developed based on experiments at $Re_p < 100$. The second correlation is that developed by the group of Votruba [52], see Eq. (3B.2), for spherical particles.

$$\frac{k_{eff,z}}{k_f} = C_1 \varepsilon + \frac{C_2 Re_p Pr}{1 + \left(\frac{C_3}{Re_p Pr} \right)} \quad (3B.2)$$

This correlation has been developed at Re_p up to 1000 in an adiabatic packed bed with a $3.85 < d_i/d_p < 55.77$, and considers three empirical parameters: C_1 for the static contribution, and C_2 and C_3 for the dynamic contribution. Moreover, the parameter values depend on the materials employed, the d_i/d_p ratio, and the fluid used. The range for the parameters are 4.5 – 228 for C_1 , 1.92 – 22.41 for C_2 , and 0 – 70.8 for C_3 . For this work, the following values, obtained for glass spheres, are selected: $C_1 = 8.3$, $C_2 = 7.93$, and $C_3 = 2.9$. This, because the calculated $k_{eff,z}$ is the largest for spherical particles when using this correlation.

Appendix 3C Estimated $k_{eff,r}$ from KWT-BC

The Known Wall Temperature Boundary Condition (KWT-BC) is commonly utilized in literature for the $k_{eff,r}$ estimation without the h_w . The Classic Approach considering the KWT-BC, here referred as KWT-CA, neglects the fluid dynamics, i.e., plug flow is considered. On the other hand, the Boundary Layer Approach considering the KWT-BC, here referred as the KWT-BLA, takes into account the effect of fluid dynamics.

Generally, a pseudo-homogeneous heat transfer model is used to describe the radial temperature profiles within the packed bed as follows:

$$(\rho_s C_{p_s} + \rho_f C_{p_f}) \frac{\partial T}{\partial t} + \rho_f C_{p_f} \epsilon V_z \frac{\partial T}{\partial z} = k_{\text{eff},r} \frac{1}{r} \frac{\partial}{\partial r} \left[r \frac{\partial T}{\partial r} \right] \quad (3C.1)$$

$$t = 0 \quad T(0, r, z) = T_{ss} \quad (3C.2)$$

$$z = 0 \quad T_0 = T \quad (3C.3)$$

$$z = L \quad \frac{\partial T}{\partial z} = 0 \quad (3C.4)$$

$$r = 0 \quad \frac{\partial T}{\partial r} = 0 \quad (3C.5)$$

$$r = R_t \quad T = T_{w,\text{in}}(z) \quad (3C.6)$$

As can be seen in Eqs. (3C.1) – (3C.6), the main difference between the PL-IHTA and the conventional approaches, i.e., KWT-CA and KWT-BLA, is that the latter uses a constant $k_{\text{eff},r}$ rather than the pseudo-local $k_{\text{eff},r,\text{PLA}}$. It is noteworthy that once $k_{\text{eff},r}$ is estimated, it is used as initial guess to re-estimate $k_{\text{eff},r}$ for those models that consider the heat wall transfer coefficient, h_w . More details regarding this are given in Appendix 3D. The estimates of $k_{\text{eff},r}$ are listed in Table 3C.1. These values are compared with those reported in literature for different correlations having a similar range and magnitude order, see Figure 3C.1.

Table 3C.1. $k_{\text{eff},r}$ estimates and their corresponding 95% confidence intervals for KWT-CA and KWT-BLA

Packed bed	Re_p	KWT-BLA	KWT-CA
Bench-scale	210	0.98 ± 0.07	0.65 ± 0.06
	420	1.94 ± 0.19	1.47 ± 0.17
	630	2.44 ± 0.23	1.90 ± 0.20
	1260	2.81 ± 0.20	2.23 ± 0.16
Industrial-scale	700	2.31 ± 0.10	2.02 ± 0.11
	1050	2.74 ± 0.09	2.34 ± 0.07
	1400	2.66 ± 0.13	1.88 ± 0.10

Note: $k_{\text{eff},r}$ [=] $\text{W m}^{-1} \text{K}^{-1}$

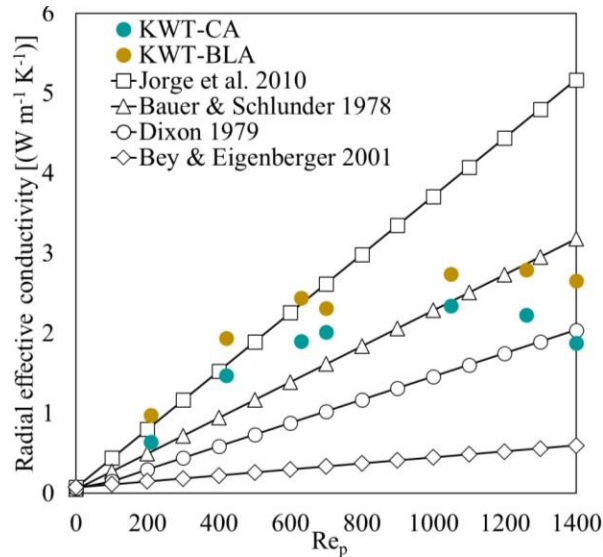


Figure 3C.1. Radial effective conductivity estimated for the bench and industrial-scale packed bed and determined from literature correlations [32,58,86,87].

Appendix 3D Conventional heat transfer approaches for wall-cooled packed beds

Generally, the conventional approaches used in the literature describes the radial and axial temperature profiles within the packed bed by using the two-dimensional heat transfer pseudo-homogeneous model given by Eqs. (3.27) – (3.32), but with the difference that the $k_{\text{eff},r}$ is considered constant and the wall heat transfer coefficient h_w captures the heat transfer resistances inside and outside of the packed-bed wall [2–7]. The corresponding boundary condition at the tube wall is:

$$r = R_t \quad -k_{\text{eff},r} \frac{\partial T}{\partial r} = h_w(T - T_b) \quad (3D.1)$$

The two conventional approaches assessed in this work are: (i) the Classical Approach (CA) [3–7] which considers plug flow instead of fluid dynamics; and (ii) the Boundary Layer Approach (BLA) [1,2,8,9] where fluid dynamics is accounted for. Both approaches are used to describe the performance of packed bed reactors [2,8] because the boundary condition used captures the radial heat transfer mechanisms from the coolant source, e.g., bath temperature, to the tube wall of the bed. Parameters $k_{\text{eff},r}$ and h_w are estimated considering temperature observations generated in a bench and industrial-scale packed bed in absence of reaction. For the latter, the experiments are performed using a coolant fluid to determine h_w and not only $k_{\text{eff},r}$. Nevertheless, as aforementioned, CA and BLA present a cross-correlation issue between

the $k_{\text{eff},r}$ and h_w , since both are estimated from the same set of observations without considering radial weighting during the regression. The KWT-CA and KWT-BLA approaches described in Appendix 3C are used as initial guess for $k_{\text{eff},r}$ to minimize the cross-correlation between $k_{\text{eff},r}$ and h_w . Table 3D.1 lists the estimates for h_w for the CA and BLA approaches, while Figure 3D.1 depicts h_w obtained for CA and BLA, along with parameter values calculated using correlations from the literature. All parameter estimates are within the order of magnitude reported in the literature.

Table 3D.1. Heat wall transfer coefficient estimates and their corresponding 95% confidence intervals for CA and BLA.

Case	Re_p	h_w ($W\ m^{-2}\ K^{-1}$)
CA	700	105 ± 1.2
	1050	126 ± 1.1
	1400	127 ± 0.9
BLA	700	166 ± 1.4
	1050	204 ± 1.5
	1400	256 ± 1.5

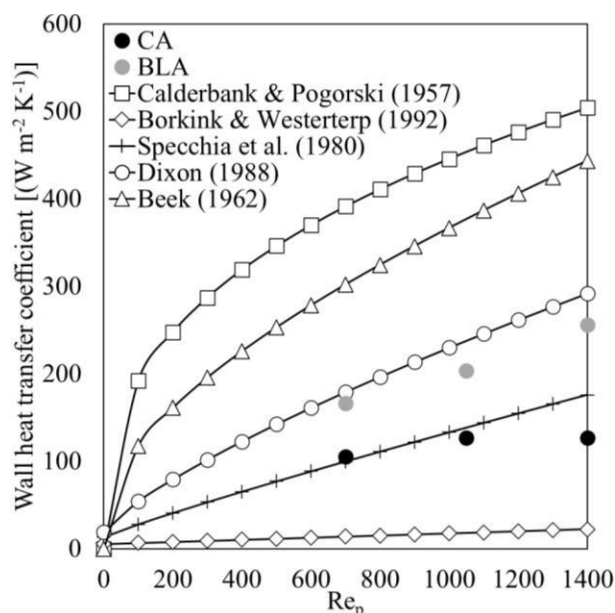


Figure 3D.1. Heat transfer parameters estimated for the bench and industrial-scale packed bed and determined from correlations from the literature [15,45,100,103–108].

Appendix 3E 1-D Pseudo-homogeneous heat transfer model

The following model is considered in order to estimate the U_w and compare it with the calculated from Eq. (27):

$$(\rho_s C_{p_s} + \rho_f C_{p_f}) \frac{\partial T}{\partial t} + \rho_f C_{p_f} \epsilon v_z \frac{\partial T}{\partial z} = \frac{4U_w}{d_t} (T - T_w) \quad (3E.1)$$

$$t = 0 \quad T(0, z) = T_{ss} \quad (3E.2)$$

$$z = 0 \quad T_0 = T \quad (3E.3)$$

$$z = L \quad \frac{\partial T}{\partial z} = 0 \quad (3E.4)$$

Chapter 4 – Oxidative dehydrogenation of ethane packed bed reactor

This Chapter focuses on the evaluation of the pseudo-local approach, assessed under non-reactive conditions in Chapter 3, and the axial heat transfer by conduction on the simulated temperature profiles within a wall-cooled industrial-scale packed bed reactor. The Oxidative Dehydrogenation of Ethane (ODH) over a V-based multi-metallic catalyst is considered as the case study because of the exothermicity of the involved reactions, i.e., the partial and total oxidation of ethane. Section 4.1 describes the reactor model for the ODH over a V-based multi-metallic catalyst. Section 4.2 provides the results obtained from the reactor simulations targeting the elucidation of the advantages of the pseudo-local approach in comparison with the conventional approximations. Section 4.3 presents the evaluation of the impact of the axial heat transfer conduction on the ODH reactor performance, mainly in the zones where a hot spot is commonly expected. The axial heat transfer conduction is evaluated by three different correlations for $k_{eff,z}$: (i) the most widely used one developed by Yagi et al. [12], (ii) the generic one developed by Votruba et al. at Re_p up to 1000 for a packed bed with $3.85 < d_t/d_p < 55.77$ [17], and (iii) the specific one developed in this work.

Part of the results of this chapter are published as:

Romero-Limones A., Poissonnier J., Thybaut J. W., and Castillo-Araiza C. O., (2023). A pseudo-local heat transfer approach in a low tube to particle diameter ratio packed bed catalytic reactor: Oxidative Dehydrogenation of ethane as a case study. *Chemical Engineering Journal*. DOI: 10.1016/j.cej.2022.140392

Romero-Limones A., Poissonnier J., Castillo-Araiza C. O., and Thybaut J. W., (2023). Avoiding false runaway prediction by properly describing axial conductive heat transfer in a low d_t/d_p industrial-scale packed bed reactor. *Chemical Engineering Journal*. DOI: 10.1016/j.cej.2023.146167

4.1 Reactor model

The characterization of transport phenomena within a packed bed reactor with low d_t/d_p ($< 8 \text{ m}_r \text{ m}_s^{-1}$) was done in Chapter 3. In this Chapter, the development of a reactor model, coupling an intrinsic ODH kinetic model with transport phenomena, is presented.

The performance of a multitubular wall-cooled packed bed reactor is normally predicted by assuming that a single tube operates the same as the rest of the tubes [1–3]. Thus, the performance of an industrial-scale single tube wall-cooled packed bed reactor operating in a non-isothermal and non-adiabatic mode is simulated here. Since the industrialization of the ODH [4], it is imperative to have a reliable reactor model that describes the complex kinetics and transport phenomena interactions, and the effect of the operating conditions within an industrial wall-cooled packed bed reactor. Thus, ODH is considered as the case study for the reactor simulations. The intrinsic ODH kinetics have been described previously in our research group [5,6] for a multi-metallic V-based catalyst supported on TiO_2 following an Eley-Rideal mechanism. For the sake of brevity, the details of the kinetics are given in Appendix 4A.

The reactor model is constructed while accounting for fluid dynamics, because of its effect on the heat transfer mechanisms within the bed, including its effect on the pseudo-local effective heat transfer parameters. To this end, heat and mass transfer mechanisms are accounted for in a pseudo-heterogeneous two-dimensional model, based on averaged general conservation relations, yet, by considering effective transport parameters:

Gas phase

$$\varepsilon \frac{\partial C_i}{\partial t} + \varepsilon v_z \frac{\partial C_i}{\partial z} = \varepsilon D_{\text{eff},z} \frac{\partial^2 C_i}{\partial z^2} + \varepsilon D_{\text{eff},r} \left[\frac{\partial^2 C_i}{\partial r^2} + \frac{1}{r} \frac{\partial C_i}{\partial r} \right] + (1 - \varepsilon) k_g a_s (C_{i,s} - C_i) \quad (4.1)$$

$$\begin{aligned} \varepsilon \rho_f C_{p,f} \frac{\partial T}{\partial t} + \varepsilon v_z \rho_f C_{p,f} \frac{\partial T}{\partial z} \\ = k_{\text{eff},z} \frac{\partial^2 T}{\partial z^2} + \frac{1}{r} \frac{\partial}{\partial r} \left[k_{\text{eff},r,PLA}(r) r \frac{\partial T}{\partial r} \right] + (1 - \varepsilon) h_g a_s (T_s - T) \end{aligned} \quad (4.2)$$

Solid phase

$$(1 - \varepsilon) \frac{\partial C_{i,s}}{\partial t} = (1 - \varepsilon) k_g a_s (C_i - C_{i,s}) + \rho_b \sum_{i=1}^5 v_{i,j} r_j \quad (4.3)$$

$$\rho_b C_{p,s} \frac{\partial T_s}{\partial t} = (1 - \varepsilon) h_g a_s (T - T_s) + \rho_b \sum_{j=1}^5 (-\Delta H_j) r_j \quad (4.4)$$

where C_i and $C_{i,s}$ are the molar concentration of the component i in the gas and solid phase, respectively, v_z is the interstitial axial velocity within the bed, $u_{z,0}$ is the inlet superficial axial velocity of the bed, T and T_s are the temperature in the gas and solid phase, respectively, $k_{\text{eff},z}$ is the axial thermal conductivity and $k_{\text{eff},r,\text{PLA}}$ is the pseudo-local radial thermal conductivity.

The corresponding initial and boundary conditions are:

$$t = 0; C_i = C_{i,\text{ss}} \text{ and } C_{i,s} = C_{i,s,\text{ss}} \quad (4.5)$$

$$t = 0; T = T_{\text{ss}} \text{ and } T_s = T_{\text{ss}} \quad (4.6)$$

$$z = 0; u_{z,0}C_{i,0} = \varepsilon v_z C_i - \varepsilon D_{\text{eff},z} \frac{\partial C_i}{\partial z} \quad (4.7)$$

$$u_{z,0}\rho_f C_{p,f} T_0 = \varepsilon v_z \rho_f C_{p,f} T - k_{\text{eff},z} \frac{\partial T}{\partial z} \quad (4.8)$$

$$z = L; \frac{\partial C_i}{\partial z} = 0 \text{ and } \frac{\partial T}{\partial z} = 0 \quad (4.9)$$

$$r = 0; \frac{\partial C_i}{\partial r} = 0 \text{ and } \frac{\partial T}{\partial r} = 0 \quad (4.10)$$

$$r = R; \frac{\partial C_i}{\partial r} = 0 \quad \text{and} \quad k_{\text{eff},r,\text{PLA}}(r) \frac{\partial T}{\partial r} = h_{\text{w,ext}} (T - T_b) \quad (4.11)$$

The reactor model, following the PLA is compared with the conventional state-of-the-art approaches, i.e., Classical Approach (CA) and Boundary Layer Approach (BLA) aiming at the elucidation of their limitations and providing the most reliable reactor model. For the sake of brevity, the details of CA and BLA are given in Appendix 3D. Moreover, the impact of the axial heat transfer by conduction on the axial temperature profile predictions, particularly in the zones where the hot spot are commonly detected, is target by considering $k_{\text{eff},z}$. Both reactor and catalyst dimensions, operating conditions and parameters used for the packed bed reactor simulations are listed in Table 4.1. This model, Eqs. (4.1) – (4.11), is discretized using orthogonal collocation (40 radial and 15 axial points), employing shifted Legendre polynomials [7]. The resulting set of ordinary differential equations is solved using a fourth-order Runge-Kutta-Fehlberg method [8].

Table 4.1. Reactor and catalyst dimensions, operating conditions, and transport phenomena parameters used in the reactor model.

	Value	Reference
Reactor and catalyst dimensions		
L [m _r]	2.6	[9]
d _t [m _r]	0.025	[9]
d _p [m _s]	0.0082	[9]
ε [m _f ³ m _r ⁻³]	0.48	[9]
ρ _b [kg _{cat} m _r ⁻³]	75	[10]
Operating conditions		
p _{tot} [atm]	1	[9]
T _b [°C]	440 – 480	[9]
T ₀ [°C]	200	[9]
Re _p	700 – 1400	[9]
Flow rate [Nm ³ h ⁻¹]	2 – 4	[9]
Ethane feed concentration [% mol]	9	[9]
Oxygen feed concentration [% mol]	7	[10]
Transport parameters		
D _{eff,r} [m _r ² h ⁻¹]	32	[9]
D _{eff,z} [m _r ² h ⁻¹]	53	[9]
k _g [m _r ² h ⁻¹]	576	[9]
h _g [m _r ² h ⁻¹]	928.8	[9]

4.2 The role of PLA on the description of the ODH reactor

Targeting the elucidation of properly account for the radial heat transfer and the uncertainties related to it when modeling an industrial reactor, the PLA is evaluated under reaction conditions for the ODH.

Figure 4.1 shows the comparison between the axial temperature profiles within the packed bed reactor simulated for both solid and fluid phase by applying PLA and the conventional approaches, i.e., CA and BLA, at Re_p of 1400 and T_b of 440 °C. It should be noted that the simulations referred to the conventional approaches do not account for the effect of $k_{eff,z}$. The simulations regarding CA and BLA consider the parameters estimated in this work, i.e., $k_{eff,r}$ and h_w , and those reported in literature [6]. The differences between the estimated values obtained here and those determined in literature for the classic approaches are due to in this work fluid dynamics considers the mass conservation, and the parameters are estimated following a weighted regression method.

The simulations reported in the literature exhibit significant differences in simulated temperature profiles compared to the ones obtained with the PLA developed in this work. So far, there is a difference up to ca. 1 m_r and ca. 7 °C between the conventional approaches from literature and the PLA reported in this work in the simulation of the hot spot position and magnitude, respectively. When fluid dynamics is neglected, i.e., CA, larger hot spot temperatures and larger displacements of the hot spot towards the reactor outlet are simulated. Moreover, fluid dynamics also impacts on the prediction of the broadness of the hot spot, i.e., the hot spot is wider when fluid dynamics is not accounted for. The inclusion of the velocity profile impacts on the convective transfer mechanisms, especially, at those zones of high void fraction, which in turn improves the heat transfer rates. These results show the sensitivity of the reaction kinetics to fluid dynamics and radial heat transfer impacting on both the microscopic and macroscopic performance of the of the reactor. Additionally, for all simulations, the temperature difference between the solid and fluid phase is the highest at the hot spot position, albeit that also there it remains below 5 °C.

When PLA is utilized, a similar hot spot temperature is predicted as when using BLA. Using the former approach, the hot spot is simulated to occur at 0.52 m_r while with the latter it is simulated to occur already at 0.40 m_r from the reactor inlet. Similarities in the simulations

can be related to the methodology implemented for the BLA. Heat transfer parameters are determined accounting for fluid dynamics such that they account for its impact on heat transfer once applied to the modeling of the industrial-scale reactor. PLA is developed accounting for capturing properly the heat transfer mechanisms inside the packed bed as well as the fluid dynamics effect on them. Moreover, $h_{w,ext}$ properly captures properly the external heat transfer mechanisms and it is estimated independently.

Figure 4.2 illustrates the axial temperature profiles from the ODH packed bed reactor simulations accounting for PLA at different bath temperatures. The results show a hot spot appearing at ca. 0.5 m from the reactor inlet for all the bath temperatures. However, as the bath temperature is increased, the hot spot is moved closer to the reactor inlet. Moreover, for the bath temperature of 480 °C, a hot spot temperature of ca. 820 °C is predicted (not shown in the Figure). This runaway situation is in line with results reported in literature when an Eley-Rideal kinetic model is coupled with the BLA, i.e., a hot spot temperature of 717 °C [6] is predicted.

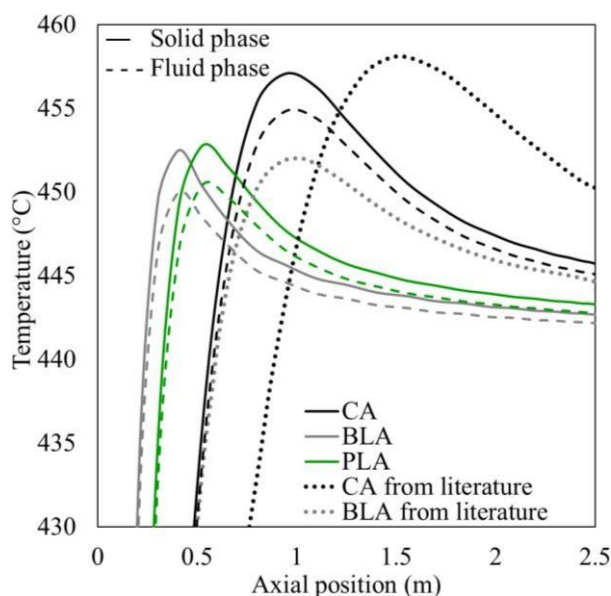


Figure 4.1. Axial temperature profiles predicted from PLA, CLA and BLA for the industrial-scale packed bed reactor at a Re of 1400, $T_b = 440$ °C and inlet $C_2H_6/O_2/N_2 = 9/7/84$. The parameters h_w [$W\ m^{-2}\ K^{-1}$] and $k_{eff,r}$ [$W\ m^{-1}\ K^{-1}$] from literature [6] are 91.5 and 1.17, respectively, for the CA, while for the BLA they are 155 and 1.65, respectively.

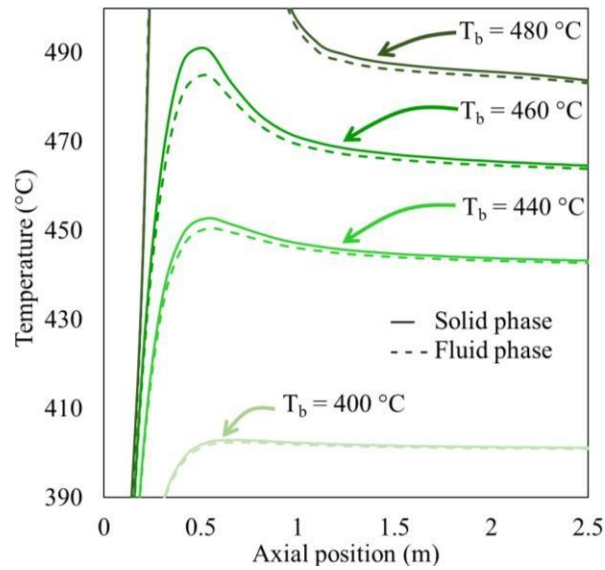


Figure 4.2. Axial temperature profiles predicted from PLA for the industrial-scale packed bed reactor at a Re_p of 1400 and inlet $C_2H_6/O_2/N_2 = 9/7/84$. The bath temperature ranges from 400 – 480 °C. Dashed lines describes fluid temperature and continuous lines the solid temperature.

4.3 The impact of $k_{eff,z}$ on the description of the ODH reactor

Figure 4.3a and b display the axial temperature profiles with bath temperatures, T_b , of 440 °C and 480 °C, respectively, at Re_p of 700 and 1400, an inlet molar ratio $C_2H_6/O_2/N_2$ of 9/7/84 and an inlet temperature, T_0 , of 200 °C. Although in Chapter 3 the heat transfer simulations without reaction exhibited similar simulated temperature profiles when using the $k_{eff,z}$ estimated in this work, and those calculated from Yagi et al. correlation, the impact of considering either one is significant under reaction conditions. Particularly in regions of parametric sensitivity, such discrepancies have been reported before [11–13].

The simulations conducted at a T_b of 440 °C (see Figure 4.3a) show that the temperature difference between the simulated hot spots is less than 10 °C for the reactor model using $k_{eff,z}$ as determined from this work, $k_{eff,z}$ from Yagi et al., or $k_{eff,z}$ from Votruba et al. at these specific “mild” conditions, the predicted temperature profiles are consistent with those reported in the literature when Yagi et al. $k_{eff,z}$ is considered [6]. Apart from the hot spot temperature, the axial position of the hot spot at Re_p of 700 varies between 0.2 m_r and 0.5 m_r , and at Re_p of 1400 between 0.4 m_r and 0.8 m_r . To this end, the hot spots predicted using the $k_{eff,z}$ from Yagi et al. are closer to the reactor inlet compared to those predicted using the $k_{eff,z}$ estimated in this work or from Votruba et al.

At harsher conditions, when the T_b amounts to 480 °C, simulations with the $k_{eff,z}$ from Yagi et al. predict runaway. Moreover, simulations without $k_{eff,z}$ also yield similar results to those obtained with the $k_{eff,z}$ from Yagi et al. correlation, but they are not shown in Figure 4.3 for brevity. On the other hand, simulations with the $k_{eff,z}$ as determined in our work and the one from Votruba et al. do not predict runaway. This indicates that neglecting the impact of $k_{eff,z}$ can lead to predicting hot spots that result in runaway for highly exothermic reactions as the flow increases or as the bath temperature increases, whereas properly describing the $k_{eff,z}$ overcomes this overprediction. Indeed, although discrepancies between the prediction of both hot spots magnitude and location and the experimental observations have been associated with neglecting the axial heat transfer by conduction within reactor models for highly exothermic reactions [9,14], the issue was not addressed before for low d_t/d_p packed bed reactors [6,10,15]. Simulated axial temperature gradients based on the $k_{eff,z}$ as determined in our work are more pronounced than those considering the $k_{eff,z}$ from Votruba et al., reaching 520 °C and 510 °C at Re_p of 1400 and 700, respectively. This demonstrates that an accurate determination of $k_{eff,z}$ not only prevents the misprediction of a runaway situation, but also ensures correct hot spot temperatures and location in the packed bed reactor.

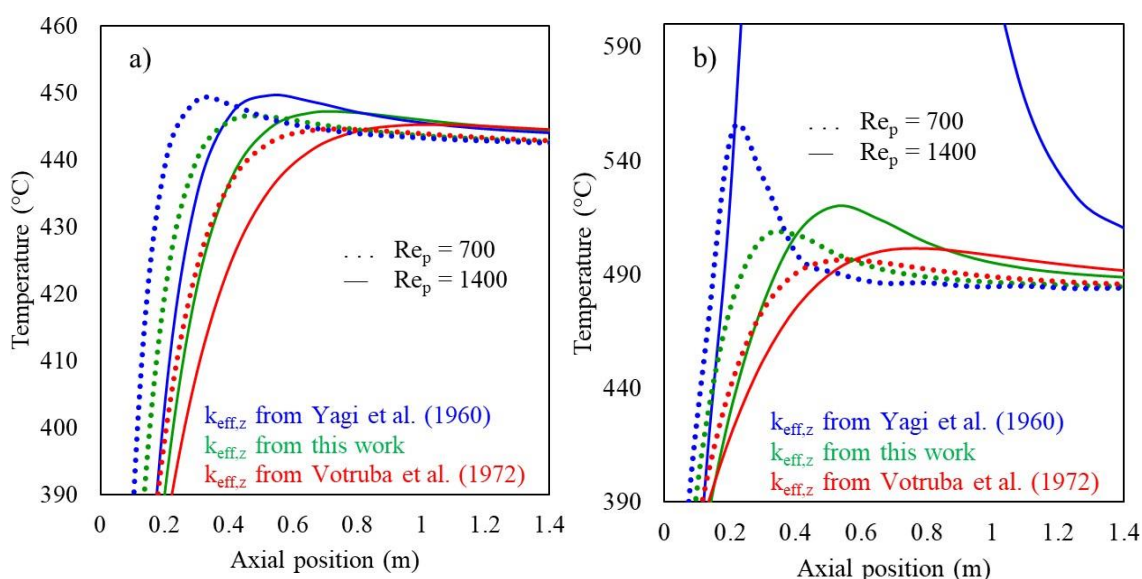


Figure 4.3. Axial temperature profiles predicted for the industrial-scale packed bed reactor, inlet molar ratio $C_2H_6/O_2/N_2 = 9/7/84$, $T_0 = 200$ °C. (a) At $T_b = 440$ °C. (b) At $T_b = 480$ °C. Dotted lines refer to $Re_p = 700$, and continuous lines refer to $Re_p = 1400$. Blue lines refer to considering $k_{eff,z}$ from Yagi et al. [16], green lines refer to the $k_{eff,z}$ estimated in this work, and red lines to $k_{eff,z}$ from Votruba et al. [17].

Figure 4.4a and b depict the axial temperature profiles with T_b of 440 °C and 480 °C, respectively, T_0 of 200 °C, Re_p of 1400, and an inlet molar ratio $C_2H_6/O_2/N_2$ of 9/7/84 and

13/3/84. The computed results with a T_b of 440 °C (see Figure 4.4a) show that the temperature difference between the simulated hot spots is less than 5 °C for the reactor model considering $k_{eff,z}$ determined from this work, from Yagi et al., or from Votruba et al. Additionally, no significant difference between considering an inlet molar ratio $C_2H_6/O_2/N_2$ of 9/7/84 and 13/3/84 was seen in the axial temperature profiles when a T_b of 440 °C is utilized. On the other hand, with a T_b of 480 °C, the simulations considering an inlet molar ratio $C_2H_6/O_2/N_2$ of 9/7/84 predict a higher temperature in the hot spot, than those with an inlet molar ratio $C_2H_6/O_2/N_2$ of 13/3/84. This is because a high content of oxygen, i.e., $C_2H_6/O_2/N_2$ of 9/7/84, favors the high exothermic total oxidation reactions, increasing the temperature in the hot spot. This temperature increment was not seen with a T_b of 440 °C, indicating that the sensitivity toward triggering a runaway situation becomes higher as the T_b increases. Moreover, considering a $k_{eff,z}$ from Yagi et al. leads to a runaway situation when the inlet molar ratio $C_2H_6/O_2/N_2$ is 9/7/84 but to a hot spot of 545 °C when the inlet molar ratio $C_2H_6/O_2/N_2$ is 13/3/84. Even with an inlet molar ratio $C_2H_6/O_2/N_2$ of 13/3/84, which decreases the exothermicity of the reaction, the hot spot value predicted considering the $k_{eff,z}$ from Yagi et al. is 35 °C higher than the hot spot predicted when the $k_{eff,z}$ from this work is considered. This not only demonstrates the sensitivity that the oxygen content has on the hot spot predictions for highly exothermic reactions, but remarks the importance that the accurate $k_{eff,z}$ determination has in the avoiding of the runaway situation misprediction.

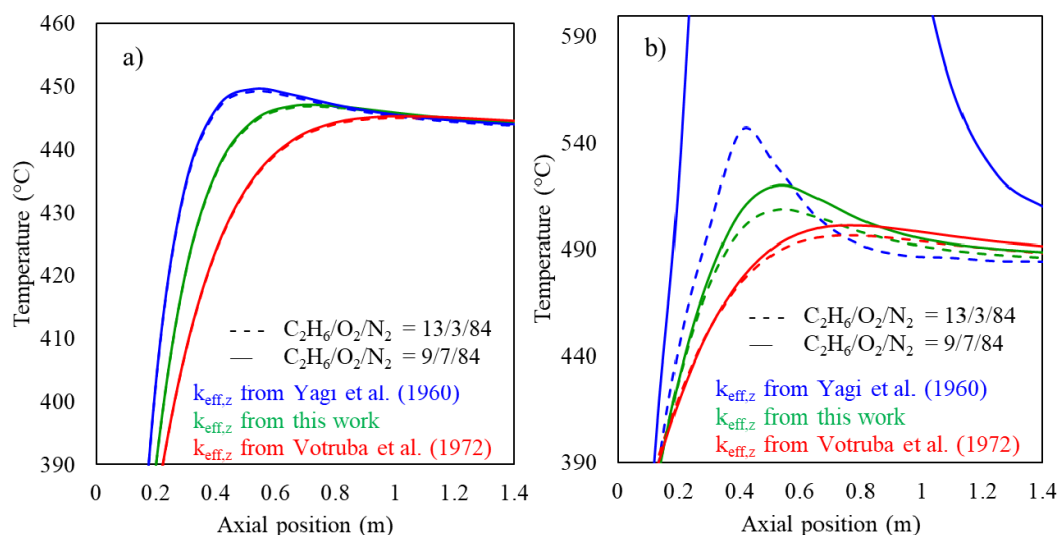


Figure 4.4. Axial temperature profiles predicted for the industrial-scale packed bed reactor, $T_0 = 200$ °C, $Re_p = 1400$. (a) At $T_b = 440$ °C. (b) At $T_b = 480$ °C. Dashed lines refer to an inlet molar ratio $C_2H_6/O_2/N_2 = 13/3/84$, and continuous lines refer to inlet molar ratio $C_2H_6/O_2/N_2 = 9/7/84$. Blue lines refer to considering $k_{eff,z}$ from Yagi et al. [16], green lines refer to the $k_{eff,z}$ estimated in this work, and red lines to $k_{eff,z}$ from Votruba et al. [17].

Figure 4.5a and b illustrate the axial temperature profiles with a T_b of 440 °C and 480 °C, respectively, an inlet molar ratio $C_2H_6/O_2/N_2$ of 9/7/84, at Re_p of 1400, and T_0 of 200 °C and 300 °C. The results obtained with both T_b show that considering a T_0 of 300 °C predicts the same hot spot temperature but closer to the packed bed reactor entrance than considering a T_0 of 200 °C. For example, with a T_b of 440 °C (see Figure 4.5a), when the $k_{eff,z}$ from Yagi et al. is considered, the hot spot predictions with a T_0 of 300 °C is at 0.4 m_r , while with a T_0 of 200 °C is at 0.5 m_r , both with a temperature of 450 °C. This is because the inlet gas mixture is hotter at T_0 of 300 °C than at 200 °C, leading to an earlier hot spot formation. Moreover, the results obtained with a T_b of 480 °C (see Figure 4.5b) indicate that, at the operating condition tested, the inlet temperature has not significant sensitivity on the predicted temperature of the hot spot but in its predicted location.

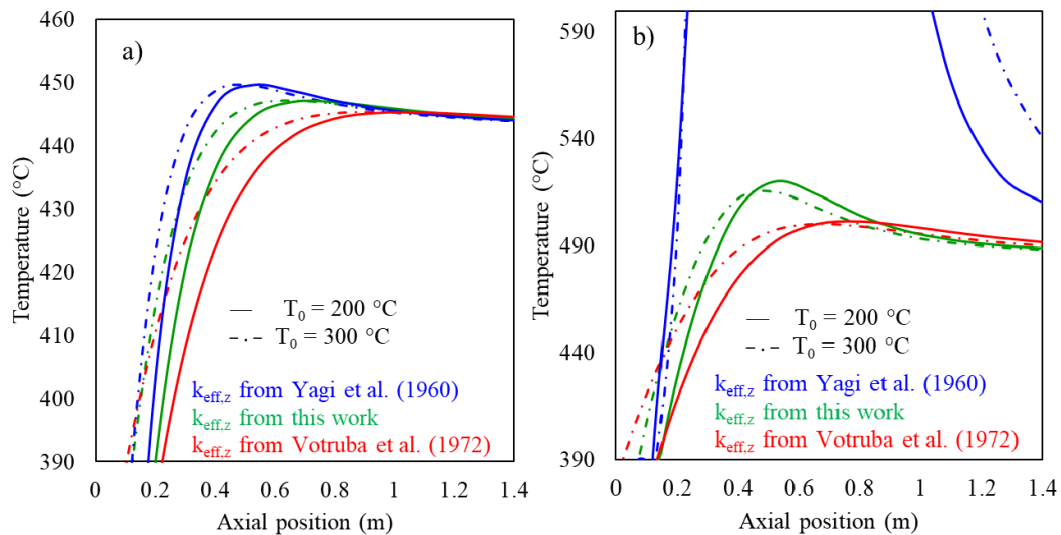


Figure 4.5. Axial temperature profiles predicted for the industrial-scale packed bed reactor, inlet molar ratio $C_2H_6/O_2/N_2 = 9/7/84$, $Re_p = 1400$. (a) At $T_b = 440$ °C. (b) At $T_b = 480$ °C. Continuous lines refer to $T_0 = 200$ °C, and non-continuous lines refer to $T_0 = 300$ °C. Blue lines refer to considering $k_{eff,z}$ from Yagi et al. [16], green lines refer to the $k_{eff,z}$ estimated in this work, and red lines to $k_{eff,z}$ from Votruba et al. [17].

4.4 Conclusions

The Pseudo-Local Approach (PLA), developed in Chapter 3 was assessed on an industrial ODH reactor accounting for the impact of the $k_{eff,z}$. The predictions showed significant differences related to the hot spot within the packed bed reactor, i.e., width of the hot spot and the position in the reactor where the hot spot is located, in comparison with the

Classic Approach (CA). On the other hand, PLA predictions versus the Boundary Layer Approach (BLA) were similar, agreeing with the literature.

Concerning the impact of $k_{\text{eff},z}$, the results showed that axial conduction is an important phenomenon to account for, especially at operating conditions where so-called ‘parametric sensitivity’ occurs, i.e., the development of hot spots and even runaway. Particularly for packed bed reactors with a $d_t/d_p < 8 \text{ m}_r \text{ m}_s^{-1}$, the use of generic correlations for the effective axial conductivity, either developed for packed bed reactors with a $d_t/d_p > 8 \text{ m}_r \text{ m}_s^{-1}$ or $d_t/d_p < 8 \text{ m}_r \text{ m}_s^{-1}$, led to mispredictions, either in the occurrence of runaway or not or in the development of radial gradients. Hence, particularly for highly exothermic reactions, a $k_{\text{eff},z}$ specific to the relevant reactor configuration, e.g., particle materials, shape, operating conditions, d_t/d_p ratio, should be considered.

When simulating the industrial packed bed reactor under harsh conditions, i.e., T_b of 480 °C, using the mostly employed literature correlation for $k_{\text{eff},z}$, thermal runaway is predicted where it was not been reported. Simulations completely neglecting $k_{\text{eff},z}$ exhibited the same behavior indicating that the mostly used literature correlation for $k_{\text{eff},z}$ results in a too low value. In contrast, considering the $k_{\text{eff},z}$ determined in our work led to hot spot predictions up to 520 °C, after which the temperature smoothly decreased until the cooling temperature. The higher $k_{\text{eff},z}$ as obtained from the correlation developed in this work avoids the accumulation of energy in the hot spot and the simulation of thermal runaway due to highly exothermic reactions. On the other hand, when $k_{\text{eff},z}$ exceeds the one obtained from the correlation developed in our work, the simulated axial temperature profile increases smoothly, without significant hot spot, which is not in line either with literature reported behavior.

The adequate characterization and prediction of both axial and radial heat transfer is crucial in the simulation of the reactor performance for highly exothermic reactions in a packed bed with low $d_t/d_p (< 8 \text{ m}_r \text{ m}_s^{-1})$, mainly near the reactor inlet, where hot spots/runaway typically develops. The reactor model developed in this thesis can be considered as one of the most consistent and generalized approximations to model heat transfer in the industrial-scale wall cooled packed bed reactor with a low tube-to-particle ratio. It overcomes historical limitations on the characterization of radial heat transfer, including the methodology applied to account for the effect of fluid dynamics on the PLA which properly captures the heat transfer mechanisms inside the packed bed reactor, mainly in those high void fraction zones. Moreover, PLA paves the way for suitable process concept design, optimization, and intensification in

future works, where highly exothermic reactions take place, e.g., partial oxidation of o-xylene to phthalic anhydride [18–20], oxidative dehydrogenation of ethane [6,21,22], oxidative coupling of methane [23,24], partial oxidation of methane to synthesis gas [25], hydrogenation of benzene [26], ethylene oxidation [27], among others. However, it should be mentioned that the use of a complex reactor model as the one developed in this thesis would be impractical for optimization and control purposes. Other methodologies can be considered to simplify this model, without losing its robustness, such as the surface response method [28,29].

4.5 References

- [1] A. Stankiewicz, Advances in modelling and design of multitubular fixed- bed reactors, *Chem Eng Technol* 12 (1989) 113–130. <https://doi.org/10.1002/ceat.270120117>.
- [2] A. Jess, C. Kern, Modeling of Multi-Tubular Reactors for Fischer-Tropsch Synthesis, *Chem Eng Technol* 32 (2009) 1164–1175. <https://doi.org/10.1002/ceat.200900131>.
- [3] J. Chen, P. Bollini, V. Balakotaiah, Oxidative dehydrogenation of ethane over mixed metal oxide catalysts: Autothermal or cooled tubular reactor design?, *AIChE Journal* 67 (2021). <https://doi.org/10.1002/aic.17168>.
- [4] Linde, EDHOXTM technology, (2021). <https://www.linde-engineering.com/en/process-plants/petrochemical-plants/edhox-technology/index.html> (accessed October 16, 2023).
- [5] G. Che-Galicia, R. Quintana-Solórzano, R.S. Ruiz-Martínez, J.S. Valente, C.O. Castillo-Araiza, Kinetic modeling of the oxidative dehydrogenation of ethane to ethylene over a MoVTeNbO catalytic system, *Chemical Engineering Journal* 252 (2014) 75–88. <https://doi.org/10.1016/j.cej.2014.04.042>.
- [6] G. Che-Galicia, F. López-Isunza, E. Corona-Jiménez, C.O. Castillo-Araiza, The role of kinetics and heat transfer on the performance of an industrial wall-cooled packed-bed reactor: Oxidative dehydrogenation of ethane, *AIChE Journal* 66 (2020). <https://doi.org/10.1002/aic.16900>.
- [7] B.A. Finlayson, *Nonlinear Analysis in Chemical Engineering*, McGraw-Hill, New York, 2003.
- [8] L. Lapidus, J.H. Seinfeld, *Numerical solution of ordinary differential equations*, Academic Press, New York, 1971.
- [9] H.F. López-Isunza, *Steady state and dynamic behaviour of an industrial scale fixed bed catalytic reactor*, Ph. D. thesis, Ph.D. thesis, University of London, 1983.
- [10] G. Che-Galicia, R.S. Ruiz-Martínez, F. López-Isunza, C.O. Castillo-Araiza, Modeling of oxidative dehydrogenation of ethane to ethylene on a MoVTeNbO/TiO₂ catalyst in an industrial-scale packed bed catalytic reactor, *Chemical Engineering Journal* 280 (2015) 682–694. <https://doi.org/10.1016/j.cej.2015.05.128>.
- [11] S. Purwono, H. Budman, R.R. Hudgins, P.L. Silveston, Yu.Sh. Matros, Runaway in packed bed reactors operating with periodic flow reversal, *Chem Eng Sci* 49 (1994) 5473–5487. [https://doi.org/10.1016/0009-2509\(94\)00386-6](https://doi.org/10.1016/0009-2509(94)00386-6).
- [12] J. Ducamp, A. Bengaouer, P. Baurens, Modelling and Experimental Validation of a CO₂ Methanation Annular Cooled Fixed-Bed Reactor Exchanger, *Can J Chem Eng* 9999 (2016) 1–12. <https://doi.org/https://doi.org/10.1002/cjce.22706>.
- [13] R.K. Sharma, D.L. Cresswell, E.J. Newson, Kinetics and fixed-bed reactor modeling of butane oxidation to maleic anhydride, *AIChE Journal* 37 (1991) 39–47. <https://doi.org/10.1002/aic.690370103>.
- [14] V. Hlaváček, P. van Rompay, Current problems of multiplicity, stability and sensitivity of states in chemically reacting systems, *Chem Eng Sci* 36 (1981) 1587–1597. [https://doi.org/10.1016/0009-2509\(81\)80002-4](https://doi.org/10.1016/0009-2509(81)80002-4).
- [15] G. Aparicio-Mauricio, R.S. Ruiz, F. López-Isunza, C.O. Castillo-Araiza, A simple approach to describe hydrodynamics and its effect on heat and mass transport in an industrial wall-cooled fixed bed catalytic

- reactor: ODH of ethane on a MoVNbTeO formulation, *Chemical Engineering Journal* 321 (2017) 584–599. <https://doi.org/10.1016/j.cej.2017.03.043>.
- [16] S. Yagi, D. Kunii, N. Wakao, Studies on axial effective thermal conductivities in packed beds, *AIChE Journal* 6 (1960) 543–546. <https://doi.org/10.1002/aic.690060407>.
- [17] J. Votruba, V. Hlaváček, M. Marek, Packed bed axial thermal conductivity, *Chem Eng Sci* 27 (1972) 1845–1851. [https://doi.org/10.1016/0009-2509\(72\)85046-2](https://doi.org/10.1016/0009-2509(72)85046-2).
- [18] C.O. Castillo-Araiza, F. López-Isunza, Modeling the partial oxidation of o-xylene in an industrial packed-bed catalytic reactor: The role of hydrodynamics and catalyst activity in the heat transport, *Ind Eng Chem Res* 49 (2010) 6845–6853. <https://doi.org/10.1021/ie901720z>.
- [19] P.H. Calderbank, K. Chandrasekharan, C. Fumagalli, The prediction of the performance of packed-bed catalytic reactors in the air-oxidation of o-xylene, *Chem Eng Sci* 32 (1977) 1435–1443. [https://doi.org/10.1016/0009-2509\(77\)80240-6](https://doi.org/10.1016/0009-2509(77)80240-6).
- [20] J.N. Papageorgiou, M.C. Abello, G.F. Froment, Kinetic modeling of the catalytic oxidation of o-xylene over an industrial V₂O₅-TiO₂ (anatase) catalyst, *Appl Catal A Gen* 120 (1994) 17–43. [https://doi.org/10.1016/0926-860X\(94\)80331-5](https://doi.org/10.1016/0926-860X(94)80331-5).
- [21] C. Alvarado-Camacho, J. Poissonnier, J.W. Thybaut, C.O. Castillo, Unravelling the redox mechanism and kinetics of a highly active and selective Ni-based material for the oxidative dehydrogenation of ethane, *React Chem Eng* (2022). <https://doi.org/10.1039/d1re00275a>.
- [22] E. Moreno-barrueta, C. Alvarado-camacho, J.F. Dur, A. Morales-p, C.O. Castillo, On the dynamics of the catalytic surface of a bimetallic mixed-oxide formulation during the oxidative dehydrogenation of ethane, *Catal Today* (2021). <https://doi.org/10.1016/j.cattod.2021.07.028>.
- [23] S. Arndt, T. Otremba, U. Simon, M. Yildiz, H. Schubert, R. Schomäcker, Mn-Na 2WO₄/SiO₂ as catalyst for the oxidative coupling of methane. What is really known?, *Appl Catal A Gen* 425–426 (2012) 53–61. <https://doi.org/10.1016/j.apcata.2012.02.046>.
- [24] L. Pirro, A. Obradović, B.D. Vandegehuchte, G.B. Marin, J.W. Thybaut, Model-Based Catalyst Selection for the Oxidative Coupling of Methane in an Adiabatic Fixed-Bed Reactor, *Ind Eng Chem Res* 57 (2018) 16295–16307. <https://doi.org/10.1021/acs.iecr.8b04242>.
- [25] C.R.H. de Smet, M.H.J.M. de Croon, R.J. Berger, G.B. Marin, J.C. Schouten, Design of adiabatic fixed-bed reactors for the partial oxidation of methane to synthesis gas. Application to production of methanol and hydrogen-for-fuel-cells, *Chem Eng Sci* 56 (2001) 4849–4861. [https://doi.org/10.1016/S0009-2509\(01\)00130-0](https://doi.org/10.1016/S0009-2509(01)00130-0).
- [26] M.H. Karimi Darvanjooghi, M. Malakootikhah, S. Magdoui, S.K. Brar, Ethylene and cyclohexane co-production in the fixed-bed catalytic membrane reactor: Experimental study and modeling optimization, *J Memb Sci* 643 (2022) 120044. <https://doi.org/10.1016/j.memsci.2021.120044>.
- [27] Z. Nawaz, Heterogeneous Reactor Modeling of an Industrial Multitubular Packed-Bed Ethylene Oxide Reactor, *Chem Eng Technol* 39 (2016) 1845–1857. <https://doi.org/10.1002/ceat.201500603>.
- [28] L.E. García-Martínez, C.O. Castillo-Araiza, G. Quijano, S. Huerta-Ochoa, On the modelling and surface response analysis of a non-conventional wall-cooled solid/gas bioreactor with application in esterification, *Chemical Engineering Journal* 437 (2022) 135063. <https://doi.org/10.1016/j.cej.2022.135063>.
- [29] C. Alvarado-Camacho, J. Poissonnier, J.W. Thybaut, C.O. Castillo-Araiza, Toward the Industrial Exploitation of the Oxidative Dehydrogenation of Ethane over a NiO-SnO₂-Based Catalyst: Regime, Parametric Sensitivity, and Optimization Analysis, *Ind Eng Chem Res* 62 (2023) 10342–10357. <https://doi.org/10.1021/acs.iecr.3c00635>.

Appendices

Appendix 4A ODH kinetic model

The kinetic model used during the reactor simulations has been developed in our research group [10] for a multi-metallic V-based catalyst supported on TiO₂. The reaction rate equations, following an Eley-Rideal mechanism, written as a function of the partial pressures of the gas phase components, are given in Eqs. (4A.1) – (4A.5):

$$r_1 = k_1 p_{C_2H_6} \theta_O \quad (4A.1)$$

$$r_2 = k_2 p_{C_2H_6} \theta_O^{0.922} \quad (4A.2)$$

$$r_3 = k_3 p_{C_2H_6} \theta_O^{0.906} \quad (4A.3)$$

$$r_4 = k_4 p_{C_2H_4} \theta_O^{1.23} \quad (4A.4)$$

$$r_5 = k_5 p_{C_2H_4} \theta_O^{0.905} \quad (4A.5)$$

where k_j is the rate coefficient of the j -reaction, and K_i and p_i are the adsorption equilibrium coefficient and partial pressure for the i -component, respectively. Assuming that the total number of active sites on the catalytic surface does not change over time, the total site balance and the coverage fraction of each oxygen and water are defined as:

$$\theta_* + \theta_O + \theta_{H_2O} = 1 \quad (4A.6)$$

$$\theta_O = (K_O p_O)^{\frac{1}{2}} \theta_* \quad (4A.7)$$

$$\theta_{H_2O} = K_{H_2O} p_{H_2O} \theta_* \quad (4A.8)$$

where θ_* , θ_O , and θ_{H_2O} are the free site, the oxygen coverage and the water coverage fraction, respectively. This kinetic model is coupled to the reactor model accounting for fluid dynamics, on the heat transfer mechanisms.

Chapter 5 – Conclusions and perspectives

5.1 Conclusions

Two fundamental processes, within the framework of the circular economy for hydrocarbons, have been assessed: the Oxidative Conversion of Methane (OCoM) and the Oxidative Dehydrogenation of Ethane (ODH).

In Chapter 2, OCoM has been proposed as a promising concept to valorize methane into ethylene and CO serving as an optimal feedstock towards ethylene hydroformylation for C₃ production, relevant for the growing polypropylene market. An OCoM kinetic model, trained and validated against experimental data acquired on a MnNaW/SiO₂ catalyst, was employed for assessing the potential OCoM behavior as a function of the operating conditions, more particularly, pursuing total oxygen conversion, maximal ethylene yield and an as close to equimolar C₂H₄/CO ratio as possible. The optimal operating conditions determined are a temperature of 850 °C, $W_{\text{cat}}/F_{\text{CH}_4,\text{in}}$ of 6.5 kg_{cat} s mol⁻¹ and CH₄/O₂ inlet molar ratio of 10 mol mol⁻¹. At these conditions, the reaction rates of the Oxidative Coupling of Methane (OCM), the Steam Reforming of Methane (SRM) and the non-oxidative Thermal Dehydrogenation of Ethane (TDE) are the highest. Three different real feedstocks were assessed in OCoM reactor simulations, leading to the conclusion that shale gas is the most promising feedstock for OCoM, i.e., high carbon conversion (31% mol mol⁻¹), high ethylene yield (19% mol mol⁻¹) and C₂H₄/CO/H₂ molar ratio of 1/1.1/3.7. This leads to a more suitable OCoM outlet stream for further ethylene hydroformylation. Additionally, the high yields towards ethylene and CO from OCoM allow minimizing the energetic and economic challenges of desired products separation from the downstream process. Last, the C123 process considerations are given in view of ensuring the efficient utilization of shale gas, and the sustainable production C₂ and C₃ species.

On the other hand, fundamentals for the adequate modeling of a multitubular packed bed reactor for the ODH has been assessed in Chapter 3 and 4. In Chapter 3, a novel developed methodology to reliably describe the temperature gradients within a packed bed (in absence of reaction) with low tube to particle diameter ratio ($d_t/d_p < 8 \text{ m}_r \text{ m}_s^{-1}$) has demonstrated the need to account for both fluid dynamics and pseudo local radial effective thermal conductivity, $k_{\text{eff},r,\text{PLA}}$. The fluid dynamics within the packed bed was determined, using pressure drop experiments within a packed bed reactor, while ensuring the mass conservation criterion is met

during the estimation of the effective viscosity, μ_{eff} . It was demonstrated that the velocity profiles, mainly in the wall zone, obtained from the non-conservative approaches overpredict the maximum velocity profile compared to the fluid dynamic model used in this work, particularly close to the wall. Axial heat transfer conduction was specifically determined via $k_{\text{eff},z}$ from experiments in a bench-scale packed bed at ‘adiabatic’ conditions, i.e., radially uniform temperatures, allowing more accurately reproducing the experimentally measured axial temperature profile than when using more generic literature correlations, also at non-adiabatic and non-isothermal conditions, i.e., in the presence of radial temperature gradients. The radial temperature predictions obtained via the developed Pseudo Local Approach (PLA) greatly improves the lack of temperature description along the radial axis, including the zone near to the wall using the conventional approaches. This improvement in the temperature description demonstrates the limitations of the conventional heat transfer approaches that consider $k_{\text{eff},r}$. At ca. one-pellet distance from the wall the pseudo-local $k_{\text{eff},r,\text{PLA}}$ has the highest value, because fluid velocity favors the dynamic heat transfer contribution. In the wall zone, $k_{\text{eff},r,\text{PLA}}$ decreases as a result of the synergy between fluid dynamics and the heat boundary layers in the wall. Moreover, the pseudo-local parameters, i.e., $k_{1,h}$ and $k_{2,h}$, are in good agreement with those obtained at bench-scale and industrial-scale. This is mainly thanks to the operating conditions, the geometrical configuration and the packing that can be considered the same at both scales. Thus, an accurate scale-up can be ensured thanks to the use of the pseudo-local $k_{\text{eff},r,\text{PLA}}$ considering that the internal heat transfer mechanisms are very similar between both scales. Moreover, the pseudo-local approach allows a reliable analysis to determine heat transfer resistances at the coolant side by estimating the external wall heat transfer coefficient, $h_{w,\text{ext}}$. The proper characterization of the external heat transfer resistances encountered in the $\delta_{\text{HT},\text{ext}}$ via the $h_{w,\text{ext}}$ demonstrated that the internal and external heat transfer resistances are ca. 30% and 70% of the total heat transfer resistances, respectively. Additionally, for industrial-scale packed beds operated in the absence of reaction, the $k_{\text{eff},z}$ as determined in this work performs overall slightly less than the mostly used correlation from literature.

In Chapter 4, the Pseudo-Local Approach (PLA), developed in Chapter 3 was assessed on an industrial ODH reactor accounting for the impact of the $k_{\text{eff},z}$. The predictions showed significant differences related to the hot spot within the packed bed reactor, i.e., width of the hot spot and the position in the reactor where the hot spot is located, in comparison with the Classic Approach (CA). On the other hand, PLA predictions versus the Boundary Layer Approach (BLA) were similar, agreeing with the literature. Concerning the impact of $k_{\text{eff},z}$, the

results showed that axial conduction is an important phenomenon to account for, especially at operating conditions where so-called ‘parametric sensitivity’ occurs, i.e., the development of hot spots and even runaway. Particularly for packed bed reactors with a $d_t/d_p < 8 m_r m_s^{-1}$, the use of generic correlations for the effective axial conductivity, either developed for packed bed reactors with a $d_t/d_p > 8 m_r m_s^{-1}$ or $d_t/d_p < 8 m_r m_s^{-1}$, led to mispredictions, either in the occurrence of runaway or not or in the development of radial gradients. Hence, particularly for highly exothermic reactions, a $k_{eff,z}$ specific to the relevant reactor configuration, e.g., particle materials, shape, operating conditions, d_t/d_p ratio, should be considered. When simulating the industrial packed bed reactor under harsh conditions, i.e., T_b of 480 °C, using the mostly employed literature correlation for $k_{eff,z}$, thermal runaway is predicted where it was not been reported. Simulations completely neglecting $k_{eff,z}$ exhibited the same behavior indicating that the mostly used literature correlation for $k_{eff,z}$ results in a too low value. In contrast, considering the $k_{eff,z}$ determined in our work led to hot spot predictions up to 520 °C, after which the temperature smoothly decreased until the cooling temperature. The higher $k_{eff,z}$ as obtained from the correlation developed in this work avoids the accumulation of energy in the hot spot and the simulation of thermal runaway due to highly exothermic reactions. On the other hand, when $k_{eff,z}$ exceeds the one obtained from the correlation developed in our work, the simulated axial temperature profile increases smoothly, without significant hot spot, which is not in line either with literature reported behavior.

5.2 Perspectives

The findings of the OCoM analysis demonstrate its efficiency to convert methane into a suitable feedstock for the Hydroformylation of Ethylene (HF), representing an innovative step forward in the efficient and sustainable use of methane resources. Further research and development should be encouraged to keep optimizing the OCoM reactions, such an extensive analysis concerning process configurations, optimization and intensification, scaling-up, reactor modeling, and strategies to maximize carbon yields from natural gas valorization.

Moreover, despite the promising potential of OCoM, the effective utilization of CO₂ (biogas) is not possible due to catalytic materials appear to present severe challenges in processing sufficient amounts of CO₂. This analysis uncovers potential directions for future investigation that include considering reactions like the hydrogenation of CO₂ for methanol synthesis, and dry reforming of methane (DRM). The former has the potential to convert excess atmospheric CO₂, a potent greenhouse gas, into fuels and value-added chemicals, establishing

a cycle of reuse for this otherwise harmful human-generated byproduct. Currently, various catalysts, including transition metals, metal oxide-based catalysts for CO₂ to methanol conversion, and zeolite catalysts for subsequent methanol to hydrocarbons conversion, are being explored [1]. This creates additional pathways for converting greenhouse gases into beneficial materials [2]. On the other hand, DRM is a process that can convert methane and carbon dioxide into synthesis gas, which can be further refined into chemicals and fuels. While Despite the utilization of biomass for DRM is an emerging field with enormous potential to diminish the carbon footprint of the petrochemical industry and amplify the use of renewable resources [3], several challenges need to be addressed. For example, improving the catalytic activity and stability of catalysts used in DRM to increase the synthesis gas yield and reduce greenhouse gas emissions [4], and optimizing the cost and scalability of biomass utilization systems to enhance their economic viability for the petrochemical industry [5].

Concerning the multitubular ODH packed bed reactor, the reactor model developed in this thesis can be considered as one of the most consistent and generalized approximations to model heat transfer in the industrial-scale wall cooled packed bed reactor with a low tube-to-particle ratio overcoming historical limitations on the characterization of axial and radial heat transfer. The adequate characterization and prediction of both axial and radial temperature gradients is crucial in the simulation of the reactor performance for highly exothermic reactions in a packed bed with low d_t/d_p (<8), mainly near the reactor inlet, where hot spots/runaway typically develops. This indicates the opportunity areas where the contribution of this work can be applied. For example, with the recent industrialization of the multitubular ODH reactor, it is required a reliable reactor model accurately accounting for all the phenomena occurring during its performance, i.e., intrinsic kinetics and transport phenomena, as done in this work. This is crucial for its safe operation and design, control, optimization and intensification. Other opportunity areas are found on other industrial implemented highly exothermic reactions, such as the partial oxidation of o-xylene to phthalic anhydride [6–8], partial oxidation of methane to synthesis gas [9], hydrogenation of benzene [10], ethylene oxidation [11], among others.

5.3 References

- [1] P. Sharma, J. Sebastian, S. Ghosh, D. Creaser, L. Olsson, Recent advances in hydrogenation of CO₂ into hydrocarbons via methanol intermediate over heterogeneous catalysts, *Catal Sci Technol* 11 (2021) 1665–1697. <https://doi.org/10.1039/D0CY01913E>.
- [2] S. Cantera, R. Lebrero, L. Sadornil, P.A. García-Encina, R. Muñoz, Valorization of CH₄ emissions into high-added-value products: Assessing the production of ectoine coupled with CH₄ abatement, *J Environ Manage* 182 (2016) 160–165. <https://doi.org/10.1016/j.jenvman.2016.07.064>.
- [3] X. Papadopoulou, C., Matralis, H., Verykios, Utilization of Biogas as a Renewable Carbon Source: Dry Reforming of Methane, in: *Catalysis for Alternative Energy Generation*, Springer US, New York, 2012. https://doi.org/10.1007/978-1-4614-0344-9_3.
- [4] E. le Saché, T.R. Reina, Analysis of Dry Reforming as direct route for gas phase CO₂ conversion. The past, the present and future of catalytic DRM technologies, *Prog Energy Combust Sci* 89 (2022) 100970. <https://doi.org/10.1016/j.pecs.2021.100970>.
- [5] National Renewable Energy Laboratory, Hydrogen from Biomass State of the Art and Research Challenges, (2002). <https://www.nrel.gov/docs/legosti/old/36262.pdf> (accessed June 26, 2023).
- [6] C.O. Castillo-Araiza, F. López-Isunza, Modeling the partial oxidation of o-xylene in an industrial packed-bed catalytic reactor: The role of hydrodynamics and catalyst activity in the heat transport, *Ind Eng Chem Res* 49 (2010) 6845–6853. <https://doi.org/10.1021/ie901720z>.
- [7] P.H. Calderbank, K. Chandrasekharan, C. Fumagalli, The prediction of the performance of packed-bed catalytic reactors in the air-oxidation of o-xylene, *Chem Eng Sci* 32 (1977) 1435–1443. [https://doi.org/10.1016/0009-2509\(77\)80240-6](https://doi.org/10.1016/0009-2509(77)80240-6).
- [8] J.N. Papageorgiou, M.C. Abello, G.F. Froment, Kinetic modeling of the catalytic oxidation of o-xylene over an industrial V₂O₅-TiO₂ (anatase) catalyst, *Appl Catal A Gen* 120 (1994) 17–43. [https://doi.org/10.1016/0926-860X\(94\)80331-5](https://doi.org/10.1016/0926-860X(94)80331-5).
- [9] C.R.H. de Smet, M.H.J.M. de Croon, R.J. Berger, G.B. Marin, J.C. Schouten, Design of adiabatic fixed-bed reactors for the partial oxidation of methane to synthesis gas. Application to production of methanol and hydrogen-for-fuel-cells, *Chem Eng Sci* 56 (2001) 4849–4861. [https://doi.org/10.1016/S0009-2509\(01\)00130-0](https://doi.org/10.1016/S0009-2509(01)00130-0).
- [10] M.H. Karimi Darvanjooghi, M. Malakootikhah, S. Magdouli, S.K. Brar, Ethylene and cyclohexane co-production in the fixed-bed catalytic membrane reactor: Experimental study and modeling optimization, *J Memb Sci* 643 (2022) 120044. <https://doi.org/10.1016/j.memsci.2021.120044>.
- [11] Z. Nawaz, Heterogeneous Reactor Modeling of an Industrial Multitubular Packed-Bed Ethylene Oxide Reactor, *Chem Eng Technol* 39 (2016) 1845–1857. <https://doi.org/10.1002/ceat.201500603>.



Casa abierta al tiempo

UNIVERSIDAD AUTÓNOMA METROPOLITANA

ACTA DE DISERTACIÓN PÚBLICA

No. 00096

Matrícula: 2153804698

Innovations in Hydrocarbon Valorization: A Comprehensive Study of the Oxidative Conversion of Methane and the Oxidative Dehydrogenation of Ethane

En la Ciudad de México, se presentaron a las 8:00 horas del día 20 del mes de agosto del año 2024 en la Unidad Iztapalapa de la Universidad Autónoma Metropolitana, los suscritos miembros del jurado:

- DR. RICHARD STEVE RUIZ MARTINEZ
- DR. GAMALIEL CHE GALICIA
- DR. KAI OLAF HINRICHSEN
- DR. MARK SAEYS
- DR. HECTOR FERNANDO PUEBLA NUÑEZ

Bajo la Presidencia del primero y con carácter de Secretario el último, se reunieron a la presentación de la Disertación Pública cuya denominación aparece al margen, para la obtención del grado de:

DOCTOR EN CIENCIAS (INGENIERÍA QUÍMICA)

DE: ALEJANDRO ROMERO LIMONES

y de acuerdo con el artículo 78 fracción IV del Reglamento de Estudios Superiores de la Universidad Autónoma Metropolitana, los miembros del jurado resolvieron:

APROBADO

Acto continuo, el presidente del jurado comunicó al interesado el resultado de la evaluación y, en caso aprobatorio, le fue tomada la protesta.



ALEJANDRO ROMERO LIMONES
ALUMNO

REVISÓ

MTRA. ROSALIA SERRANO DE LA PAZ
DIRECTORA DE SISTEMAS ESCOLARES

DIRECTOR DE LA DIVISIÓN DE CBI

DR. ROMAN LINARES ROMERO

PRESIDENTE

DR. RICHARD STEVE RUIZ MARTINEZ

VOCAL

DR. GAMALIEL CHE GALICIA

VOCAL

DR. KAI OLAF HINRICHSEN

VOCAL

DR. MARK SAEYS

SECRETARIO

DR. HECTOR FERNANDO PUEBLA NUÑEZ